

# Physically-Based Realizable Modeling and Network Synthesis of Subscriber Loops Utilized in DSL Technology

by

**Jason Jon Yoho**  
**Time Domain & RF Measurement Laboratory**

Dissertation submitted to the Faculty of  
The Bradley Department of Electrical and Computer Engineering  
Virginia Polytechnic Institute and State University  
in partial fulfillment of the requirements for the degree of

Doctor of Philosophy

in

Electrical Engineering

APPROVED

Dr. Sedki M. Riad, Chairman

Dr. Ioannis M. Besieris

Dr. A. A. (Louis) Beex

Dr. Norris S. Nahman

Dr. Iman Salama

Dr. Sanjay Raman

Dr. Wayne A. Scales

Dr. Lee W. Johnson

Dr. William A. Davis

October 2001  
Blacksburg, Virginia

Keywords: Twisted-Pair Cable Models, Twisted-Pair Cable Measurements, DSL Feasibility Testing, Layer De-Embedding,  
POTS Topology Identification / Reconstruction

© 2001 by Jason Yoho

# Physically-Based Realizable Modeling and Network Synthesis of Subscriber Loops Utilized in DSL Technology

by

Jason Jon Yoho

Chairman: Dr. Sedki M. Riad  
Time Domain & RF Measurement Laboratory  
The Bradley Department of Electrical and Computer Engineering

## Abstract

Performance analysis of Digital Subscriber Line (DSL) technologies, which are implemented on existing telephone subscriber loops, is of vital importance to DSL service providers. This type of analysis requires accurate prediction of the local loop structure and precise identification of the cable parameters. These cables are the main components of the loop and are typically comprised of multi-conductor twisted pair type currently being used on existing telephone subscriber loops. This system identification problem was investigated through the application of single port measurements, with preference being placed on measurements taken from the service provider's end of the loop under investigation. Once the cabling system has been identified, the performance analysis of the loop was obtained through simulation.

Accurate modeling is an important aspect of any system identification solution; therefore, the modeling of the twisted pair cables was thoroughly investigated in this research. Early modeling attempts of twisted pair cabling systems for use with (DSL) technology has not been vigorously investigated due to the difficulty in obtaining wideband physical data necessary for the task as well as the limitations of simulators to accurately model the skin effects of the conductors. Models are developed in this research that produce a wideband representation of the twisted pair cables through the use of the data measured in high frequency spectra.

The twisted-pair cable models were then applied to the system identification problem through a de-embedding type approach. The identification process accurately characterizes the sections of the subscriber loop closest to the measurements node, and these identified sections were then modeled and de-embedded from the system measurement in a layer removing, or "peeling", type process. After each identified section was de-embedded from the system measurement, the process was repeated until the entire system was identified.

Upon completion of the system identification process, the resulting system model was simulated between the central office (CO) and resulting identified customer nodes for the evaluation of performance analysis. The performance analysis allows the providers to identify points where the DSL technology is feasible, and where so, the rates of the data transfer to the nodes that can be expected.

## ———— **Dedication** ————

Dedicated to my wife, Karen: My Love, My Support

Dedicated to my parents, Bud and Polly: My Guide, My Encouragement

Dedicated to my brothers, Aaron and Charley: My Best Friends

## ————— Acknowledgements —————

I would like to express my utmost gratitude to my advisor, Dr. Sedki M. Riad, for his guidance, support, and friendship. His words of encouragement and positive attitude throughout the many research projects we have worked on together were inspiring. I am greatly indebted to him for the many challenges he has placed upon me as well as his invaluable guidance and time he has so kindly offered me over the past several years. He will always be greatly appreciated..

My appreciation also extends to the others involved in this research project including my friends in the Time Domain & RF Measurement Laboratory including Ali Mugaibel and Yianni Antoniadis for their work and assistance towards the completion of this research; my friends in the Digital Signal Processing Research Laboratory including Dr. A. A. (Louis) Beex, Takeshi Ikuma, Visala Namburu, and Krishnaraj Varma; and finally, Acterna Corporation for their financial support during the course of this project.

I would also like to thank my other committee members consisting of Dr. Ioannis M. Besieris, Dr. Norris S. Nahman, Dr. Iman Salama, Dr. Sanjay Raman, Dr. Wayne A. Scales, and Dr. William A. Davis for their time and effort in reviewing this work.

I would like to express my appreciation to my family. I am extremely grateful to my wife, Karen, for her support and assistance during my work towards this goal. Her thoughtfulness and generosity motivate me to perform at my highest level. My parents, Bud and Polly, have been my greatest source of encouragement and good advice. I thank them for the opportunities they have given me to further my education. My brothers, Aaron and Charley, have always been supportive of my goals and the best of friends.

Finally, I would like to display my appreciation to the Bradley Department of Electrical Engineering at Virginia Polytechnic Institute and State University for the opportunity to study at such a prestigious university. I would also like to extend my thanks to the Bradley Endowment for offering me financial support during the course of my doctoral studies.

# Table of Contents

## Chapter 1: Introduction to DSL Technology

<b>1</b>	<b>Research Motivation and Objective</b>	<b>1</b>
1.1	DSL Technology	2
1.2	Subscriber Loop (Twisted Pair) Environment	5
1.2.1	<i>Twisted Pair Characteristics and Electrical Properties</i>	5
1.2.2	<i>Subscriber Loop Structure</i>	8
1.2.3	<i>Subscriber Loop Characteristics Used in Performance Analysis</i>	9
1.3	Subscriber Loop Modeling and Simulations	11
1.4	Methods of Subscriber Loop Synthesis	12
1.5	Summary and Organization	15

## Chapter 2: Introduction to Deconvolution and De-Embedding

<b>2</b>	<b>Introduction</b>	<b>17</b>
2.1	Deconvolution Schemes	17
2.2	Practical Application of Deconvolution	19
2.3	Acceptable Estimates of Deconvolution Solutions	20
2.4	Iterative Frequency Domain Deconvolution Techniques	21
2.4.1	<i>Optimal Compensation Technique</i>	22
2.4.2	<i>Regularization (Guillaume-Nahman) Technique</i>	22
2.5	Iterative Time Domain Deconvolution Techniques	23
2.5.1	<i>The Van-Cittert Deconvolution Technique</i>	23
2.5.2	<i>Discussion of Convergence of the Van-Cittert's Technique</i>	24
2.5.3	<i>Constrained Technique</i>	25
2.5.4	<i>Relaxation-Based Technique (Jansson's Technique)</i>	25
2.5.5	<i>Gold's Ratio Technique</i>	27
2.6	Optimization Criteria for Deconvolution Techniques	27
2.6.1	<i>Time Domain Optimization Criteria</i>	27
2.6.2	<i>Frequency Domain Optimization Criteria</i>	31
2.7	De-embedding Schemes	33
2.7.1	<i>Frequency Domain De-embedding</i>	34
2.7.2	<i>Time Domain De-embedding</i>	37
2.8	Comparison of Frequency and Time Domain Synthesis Schemes	37
2.8.1	<i>Time Domain Deconvolution</i>	37
2.8.2	<i>Frequency Domain Deconvolution</i>	38
2.9	Realizability Limitations and Accuracy of the Synthesis Problem	39
2.9.1	<i>Causality and Stability of Synthesis Problems</i>	39

2.9.2	<i>Realizability of Synthesis Problems</i> .....	40
2.9.3	<i>Identified Limiting Factors</i> .....	42
2.9.4	<i>Solutions to Truncation Discontinuities (Leakage Errors)</i> .....	45

---

### **Chapter 3: Layer De-Embedding Scheme Applied to DSL Subscriber Loops**

---

<b>3</b>	<b>Introduction</b> .....	<b>47</b>
3.1	Overall Reconstruction Procedure.....	47
3.2	De-Embedding Process Review.....	50
3.3	Windowing and Phase Shifting.....	53
3.3.1	<i>Pre-Processing of Time Domain Measurements</i> .....	54
3.3.2	<i>Windowing Functions</i> .....	54
3.3.3	<i>Linear Phase Component</i> .....	56
3.4	Structure Identification.....	57
3.4.1	<i>Topology Identification</i> .....	58
3.4.2	<i>Length Estimation</i> .....	63
3.5	Noise Reduction Schemes.....	69
3.5.1	<i>High Frequency De-Embedding Noise</i> .....	69
3.5.2	<i>Noise Introduced by Length Estimation Errors</i> .....	69
3.5.3	<i>Noise Reduction Using Different Window Functions</i> .....	70

---

### **Chapter 4: Twisted-Pair Cable Modeling for DSL Systems**

---

<b>4</b>	<b>Introduction</b> .....	<b>71</b>
4.1	High Frequency Approximation for Parallel Lines.....	72
4.1.1	<i>Method of Conformal Transformation Introduction</i> .....	72
4.1.2	<i>Properties of Analytic Functions of Complex Variables</i> .....	74
4.1.3	<i>Single Round Wire Analysis (Logarithmic Transformation)</i> .....	76
4.1.4	<i>Parallel Wire Topology Analysis</i> .....	78
4.1.5	<i>Parallel Wire Transmission Line Parameter Development</i> .....	80
4.1.6	<i>Capacitance Line Parameter</i> .....	81
4.1.7	<i>External Inductance Line Parameter</i> .....	82
4.1.8	<i>The Skin Effect (Planar Approximation) in Good Conductors</i> .....	83
4.1.9	<i>Resistance Line Parameter</i> .....	86
4.1.10	<i>Internal Inductive Line Parameter</i> .....	88
4.1.11	<i>Conductance Line Parameter</i> .....	90
4.1.12	<i>Summary of Line Parameters for Parallel Wires</i> .....	91
4.2	Skin Effect in Round Wires.....	92
4.2.1	<i>Wideband Current Distribution of Round Wires</i> .....	92
4.2.2	<i>Impedance of Round Wires</i> .....	94

4.2.3	<i>Relationship to Parallel Line Equations</i> .....	96
4.3	Modeling the Permittivity of the Insulating Material .....	97
4.4	Modeling of the Twisting Effects of Twisted Pair Cables.....	99
4.4.1	<i>Twisting Length Estimation</i> .....	99
4.4.2	<i>Fields of Helical Structures</i> .....	99
4.4.3	<i>Modeling of Helical Structures</i> .....	100
<hr/> <b>Chapter 5: Twisted-Pair Cable Measurements and Model Verification</b> <hr/>		
<b>5</b>	<b>Introduction/Overview</b> .....	<b>103</b>
5.1	Single Port Measurements (Frequency Domain).....	103
5.1.1	<i>Measurement Setup</i> .....	104
5.1.2	<i>Numerical Methods used to Obtain Primary Line Parameters</i> .....	105
5.2	Measurement Method and Results.....	108
5.2.1	<i>Measurement Repeatability</i> .....	108
5.2.2	<i>Measurement Variability</i> .....	109
5.2.3	<i>Variations Among Conductor Pairs</i> .....	109
5.2.4	<i>Length Estimation Error Measurements</i> .....	110
5.3	Secondary Line Parameters.....	112
5.4	Model Verification.....	112
5.4.1	<i>ANSI T1E1.4 Contribution Models</i> .....	113
5.4.2	<i>New Twisted Pair Models</i> .....	114
5.5	Model Comparisons (ANSI T1E1.4 Models versus Developed Models).....	116
5.6	Summary of Twisted Pair Line Parameter Models.....	117
<hr/> <b>Chapter 6: Layer De-Embedding Scheme Verification and Analysis</b> <hr/>		
<b>6</b>	<b>Introduction</b> .....	<b>124</b>
6.1	Gauge/Topology Detection and Length Estimation Verification .....	125
6.2	Topology Identification Using Ideal Length Estimation .....	126
6.3	Topology Identification Using Non-Ideal Length Estimation .....	127
6.4	Computation Noise Limitations.....	128
<hr/> <b>Chapter 7: Conclusion and Suggestion for Research Continuation</b> <hr/>		
<b>7</b>	<b>Conclusion</b> .....	<b>130</b>
7.1	Observation of Limitations .....	132
7.2	Suggestions for Research Continuation .....	133
	<b>References</b> .....	<b>134</b>
	<b>Appendix A: CSA Test Subscriber Loops</b> .....	<b>138</b>

<i>Appendix B: Layer De-Embedding Algorithm Flow Charts</i>	<i>141</i>
<i>Appendix C: Time and Frequency Domain Measurement Methods</i>	<i>146</i>
<i>Appendix D: Twisted Pair Cable Measurement Results</i>	<i>160</i>
<i>Vita</i>	<i>185</i>

## List of Figures

Figure 1.1	End to end system block diagram of a typical DSL system.	4
Figure 1.2	Transmission line model per unit length.	6
Figure 1.3	Typical structure of an end-to-end subscriber loop.	8
Figure 1.4:	(a) An ABCD two-port network (b) ABCD matrix representation.	9
Figure 1.5:	A generic end-to-end model of a subscriber loop using two-port parameters.	10
Figure 1.6:	(a) An example of a subscriber loop (b) Identical loop without the bridge tap.	12
Figure 1.7:	Characteristics of each of the two loops of Figure 1.6 (a) Real part of the input impedance (b) Imaginary part of the input impedance (c) Magnitude of the transfer function (d) The insertion loss in dB.	13
Figure 1.8:	Example measurements of the loop in Figure 1.6a (a) Magnitude of the input impedance from node 1 (b) Magnitude of the input impedance from node 3 (c) TDR response from node 1 (d) TDR response from node 3.	14
Figure 2.1	Time domain system diagram for convolution.	18
Figure 2.2	Frequency domain system diagram for convolution.	18
Figure 2.3	Algorithm of the time domain optimization techniques.	28
Figure 2.4:	Algorithm of the frequency domain optimization technique.	32
Figure 2.5:	Reflection coefficients and S-parameters of a multi-segment line.	35
Figure 2.6:	(a) Visualization of de-embedding process involving a single segment (b) Result after de-embedding process is completed.	36
Figure 2.7:	Block diagram for an ideal C/D converter.	43
Figure 2.8:	Nicolson Ramp method for leakage error correction.	45
Figure 2.9:	Nicolson Ramp method after subtraction.	46
Figure 2.10:	Nahman-Gans method for leakage error correction.	46
Figure 3.1:	Flow chart showing the process of the time-domain reconstruction algorithm.	48
Figure 3.2:	Visualization of de-embedding process involving a single segment.	51
Figure 3.3:	Reflection coefficients and S-parameters of a multi-segment line.	52
Figure 3.4:	a) FDR Response and Kaiser Window. b) FDR convolved with the Kaiser	

	Window.	55
Figure 3.5:	TDR Responses of CSA#4 and an open circuit prior to time shifting.	56
Figure 3.6:	TDR Responses of CSA#4 and an open circuit after time shifting.	57
Figure 3.7:	TDR Kaiser window responses contained within a typical reference database.	59
Figure 3.8:	Time duration used to compute the CSSE of the measurement with the database.	60
Figure 3.9:	Bridge tap possibilities to be considered when the gauges are unmatched.	61
Figure 3.10:	Description of an infinite bridge tap length adjustment.	63
Figure 3.11:	Plot of the weighted derivative of the NDR and the NDR for length detection.	64
Figure 3.12:	Background information for linear phase routine.	65
Figure 3.13:	Resulting linear phase component from the WGLPM.	66
Figure 3.14:	Typical phase velocity plot versus frequency.	67
Figure 3.15:	Typical relative permittivity plot calculated from the phase velocity.	67
Figure 3.16:	Leakage error and method of correction.	68
Figure 4.1:	(a) Z plane consisting of points from the x-y plane. (b) W plane consisting of points from the u-v plane.	73
Figure 4.2:	Coordinates for the flux function.	76
Figure 4.3:	Parallel wire topology.	79
Figure 4.4:	Magnetic flux lines in a parallel wire transmission line.	81
Figure 4.5:	A plane solid conductor with current flowing in the x-direction	85
Figure 4.6:	A circular conducting loop.	100
Figure 5.1:	Calibration setup for frequency domain measurements.	104
Figure 5.2:	Measurement setup for single port frequency domain measurements.	105
Figure 5.3:	General transmission line diagram.	106
Figure 5.4:	$R_{dc}$ measurement setup for length evaluation.	111
Figure 5.5:	Physical characteristics of a cross section the twisted pair cable.	114
Figure 5.6:	Model comparison to measured data of a 24 AWG SEALPIC cable.	118
Figure 5.7:	Model comparison to measured data of a 22 AWG SEALPIC cable.	119

Figure 5.8:	Model comparison to ANSI T1.601-1999 data of a 24 AWG SEALPIC cable.	120
Figure 5.9:	Model comparison to measured data of a 24 AWG SEALPIC cable.	121
Figure 5.10:	Model comparison to measured data of a 22 AWG SEALPIC cable.	122
Figure 5.11:	Time domain reflectometry waveforms simulated using each of the 24 AWG models.	123
Figure 6.1:	Termination topologies used for length estimation performance verification: (a) open circuit (b) gauge change (c) bridge tap.	125
Figure 6.2:	Length estimation performance verification of a bridge tap segment.	126
Figure 6.3:	Length estimation performance verification of a bridge tap segment.	127
Figure 6.4:	Computational noise resulting from first iteration of CSA #1 reconstruction.	129
Figure C.1:	Time Domain Reflectometry.	147
Figure C.2:	Frequency Domain Reflectometry.	148
Figure C.3:	Synthesis problem performed through different methods.	148
Figure C.4:	Time domain bounce diagram example.	149
Figure C.5:	General TDR and TDT measurement setup.	150
Figure C.6:	General FDR and FDT measurement setup.	151
Figure C.7:	Transfer function of a bandpass amplifier.	151
Figure C.8:	Time domain step response of a bandpass amplifier.	152
Figure C.9:	General network representation.	153
Figure C.10:	Effect of aliasing error on the time domain waveform.	154
Figure C.11:	Response of $X_o$ versus frequency and the truncation at the sampling frequency.	155
Figure C.12:	Response of $y(t)$ versus time and the truncation at the selected time duration.	156
Figure D.1:	Repeatability of Resistance ( $\Omega/m$ ) for Sample 3 of 22 AWG Cable.	161
Figure D.2:	Repeatability of Inductance ( $\mu H/m$ ) for Sample 3 of 22 AWG Cable.	162
Figure D.3:	Repeatability of Capacitance ( $pF/m$ ) for Sample 3 of 22 AWG Cable.	163
Figure D.4:	Repeatability of Conductance ( $\mu S/m$ ) for Sample 3 of 22 AWG Cable.	164

Figure D.5:	Variability of Resistance ( $\Omega/m$ ) for Samples 1 through 3 of 22 AWG Cable.	165
Figure D.6:	Variability of Inductance ( $\mu H/m$ ) for Samples 1 through 3 of 22 AWG Cable.	166
Figure D.7:	Variability of Capacitance (pF/m) for Samples 1 through 3 of 22 AWG Cable.	167
Figure D.8:	Variability of Conductance ( $\mu S/m$ ) for Samples 1 through 3 of 22 AWG Cable.	168
Figure D.9:	Resistance ( $\Omega/m$ ) of Tabulated and Measured Data for Different 22 AWG Twisted-Pairs Contained Within a Cable.	169
Figure D.10:	Inductance ( $\mu H/m$ ) of Tabulated and Measured Data for Different 22 AWG Twisted-Pairs Contained Within a Cable.	170
Figure D.11:	Capacitance (pF/m) of Tabulated and Measured Data for Different 22 AWG Twisted-Pairs Contained Within a Cable.	171
Figure D.12:	Conductance ( $\mu S/m$ ) of Tabulated and Measured Data for Different 22 AWG Twisted-Pairs Contained Within a Cable.	172
Figure D.13:	$\pm$ Relative Error of Resistance ( $\Omega/m$ ) Measurement Due to Length Estimation Errors.	173
Figure D.14:	$\pm$ Relative Error of Inductance ( $\mu H/m$ ) Measurement Due to Length Estimation Errors.	174
Figure D.15:	$\pm$ Relative Error of Capacitance (pF/m) Measurement Due to Length Estimation Errors.	175
Figure D.16:	$\pm$ Relative Error of Conductance ( $\mu S/m$ ) Measurement Due to Length Estimation Errors.	176
Figure D.17:	Real Intrinsic Impedance of Tabulated and Measured Data for Different Twisted-Pairs of a 22 AWG Cable.	177
Figure D.18:	Imaginary Intrinsic Impedance of Tabulated and Measured Data for Different Twisted-Pairs of a 22 AWG Cable.	178
Figure D.19:	Attenuation Constant of Tabulated and Measured Data for Different Twisted-Pairs of a 22 AWG Cable.	179
Figure D.20:	Phase Constant of Tabulated and Measured Data for Different Twisted-Pairs of a 22 AWG Cable.	180
Figure D.21:	Real Intrinsic Impedance of Tabulated and Measured Data for Different Twisted-Pairs of a 24 AWG Cable.	181

Figure D.22: Imaginary Intrinsic Impedance of Tabulated and Measured Data for Different Twisted-Pairs of a 24 AWG Cable.	182
Figure D.23: Attenuation Constant of Tabulated and Measured Data for Different Twisted-Pairs of a 22 AWG Cable.	183
Figure D.24: Phase Constant of Tabulated and Measured Data for Different Twisted-Pairs of a 22 AWG Cable.	184

## ————— **List of Tables** —————

Table 5.1	Color codes of the multiple cable pairs measured.	110
Table 5.2	Length evaluation measurement results.	111
Table 5.3	Typical model coefficients for 22 AWG and 24 AWG models.	117
Table 6.1	Results of length estimation algorithm performance given different terminations.	125
Table 6.2	Results of the application of the proposed identification scheme on portions of subscriber loops shown in Figure 6-3.	127
Table 6.3	Results of the application of the proposed identification scheme on CSA subscriber loops from the CO node (node 1).	128

# Chapter 1

## Introduction to DSL Technology

### 1 Research Motivation and Objective

The market for high-bandwidth access subscriptions is rapidly growing, and Digital Subscriber Line (DSL) technology is an attractive solution to meet the market demands. Since DSL technology can be deployed over the immense base of twisted pair cabling established by telephone companies, there is a high demand in the telecommunication industry for methods of accurately predicting the DSL access performance over this pre-existing infrastructure. The subscriber line, or set of twisted pair cables extending from the Central Office (CO) to the customer, needs to be tested for performance to assess the applicability of DSL technology on the loop as well as the obtainable access rate if the technology is feasible. Currently, there is DSL analysis equipment capable of assessing the performance rate of existing loops, but this equipment requires a two port measurement (taken between the CO port and the customer port). Though this method is viable, it requires a CO representative to travel to each of the sites where the customer port is located to perform the analysis through communication with the CO. A more cost effective solution would be to perform a single port measurement at the CO port for identification of the subscriber line; followed by simulations of the identified topology to assess the access performance of DSL technology to each of the customer ports. Higher identification accuracy can be obtained if the termination at the customer node is open-circuited due to the large impedance mismatch, though the developed algorithm has the provisions to account for

loaded terminations. The type of test equipment that can perform analysis based on single port measurements is not currently available on the market [1].

This work proposes a method of system identification that utilizes single port measurements for the use of performance analysis of DSL technology. An important aspect of any system identification problem is the development of accurate modeling techniques of the system components. In the DSL system, the precise modeling of the twisted-pair cables, the key components of the subscriber loops, has been thoroughly investigated. Another important aspect of system identification is the type of network synthesis implemented. There are several different techniques used in network synthesis, these methods will be presented as well as a detailed presentation of the implemented process.

The remainder of this chapter will present information pertaining to DSL technologies to develop a foundation of understanding for the system identification problem. This background information [2], [3] will include a description of DSL technology, an understanding of the DSL environment, a perspective of DSL performance analysis, and an introduction into types of network synthesis that may be used to solve this type of system identification. This chapter will conclude with an overview of the dissertation format.

## **1.1 DSL Technology**

The demand for high-speed data communications has been on the increase over the past several years due to drivers such as the internet, including the World Wide Web (WWW), video service, consumer services, and entertainment to name a few. Due to bandwidth limitations, high-speed voice band modems have reached a maximum transfer rate of 56 Kbps; therefore, new technologies are desired to exceed this limitation.

Integrated Services Digital Network (ISDN) was introduced in the early 1990s with access speeds reaching rates of 144 Kbps. ISDN technology, as with DSL technology, utilizes the twisted-pair infrastructure used by telephone companies, although some incompatibilities with the current phone system, such as co-existing simultaneously on the same cabling system, is a main factor in preventing widespread deployment of ISDN. Other factors preventing the increase in usage of ISDN technology include the lack of standardization throughout the industry along with the cost and difficulty of system installation. Therefore, several broadband access

technologies having faster data rates while avoiding the oversights of ISDN have emerged, including DSL technology. These new services have been gaining popularity over the past several years.

Several key attributes make DSL networks an attractive choice over other broadband technologies such as cable modems and wireless satellite systems. As mentioned earlier, DSL can be deployed over the existing infrastructure of existing twisted pair cables, requiring the inclusion of data switches and splitters to function. With cable modems, coaxial cable systems are generally a broadcast medium with a single line serving many subscribers; therefore, many subscribers will have to share the bandwidth of the cable interface. Also, most of the upload capabilities (data transfers from the subscriber to the CO) of the cable have not been conditioned for data transfers in many locations, and the addition of this infrastructure will be costly and time consuming.

Since the telephone switching centers are readily accessible and the fact that the installed base of twisted pair already exists, the simplicity of feasibility tests of DSL technology is obvious over some other technologies. For example, several wireless technologies also have the capabilities of transferring data to subscribers, and though most of these systems are used in broadcast applications, this technology could eventually become a competitor in the high-speed interactive data world. The main drawback to wireless satellite applications are the immense cost of the feasibility trials that would involve designing, building, and deploying the system before tests can even begin; assuming receivers and transmitters are readily available.

Various types of DSL technology have evolved over the past years depending on application and standardization. One of the most popular is ADSL, or Asymmetric Digital Subscriber Line, which is characterized by different data rates downstream (CO to subscriber) as compared to upstream (Subscriber to CO). Downstream data rates for ADSL can be as fast as 8 Mbps depending on the infrastructure length and quality; however, upstream rates are usually ten percent of this speed. An end-to-end system diagram of a typical ADSL system is shown in *Figure 1-1*. The subscriber end requires a telephone splitter to channel the voice and data information to their respected devices in the downstream direction, and combine the two classes of information in the upstream direction. The DSL modem can consist of an external modem, a network interface card, or a router in the case of small or home office applications. The

connection between the subscriber and the central office consists of twisted pair cable that generally has a maximum length of 5,500 meters in ADSL applications. The physical and electrical properties of these cables will be discussed in subsequent sections. At the CO, a splitter is again needed to combine or split the data and voice information. The voice data is routed to a telephone-switching center and the data is integrated into a DSL Access Multiplexer (DSLAM). The DSLAM aggregates subscriber line traffic into higher speed links for the backbone switching equipment.

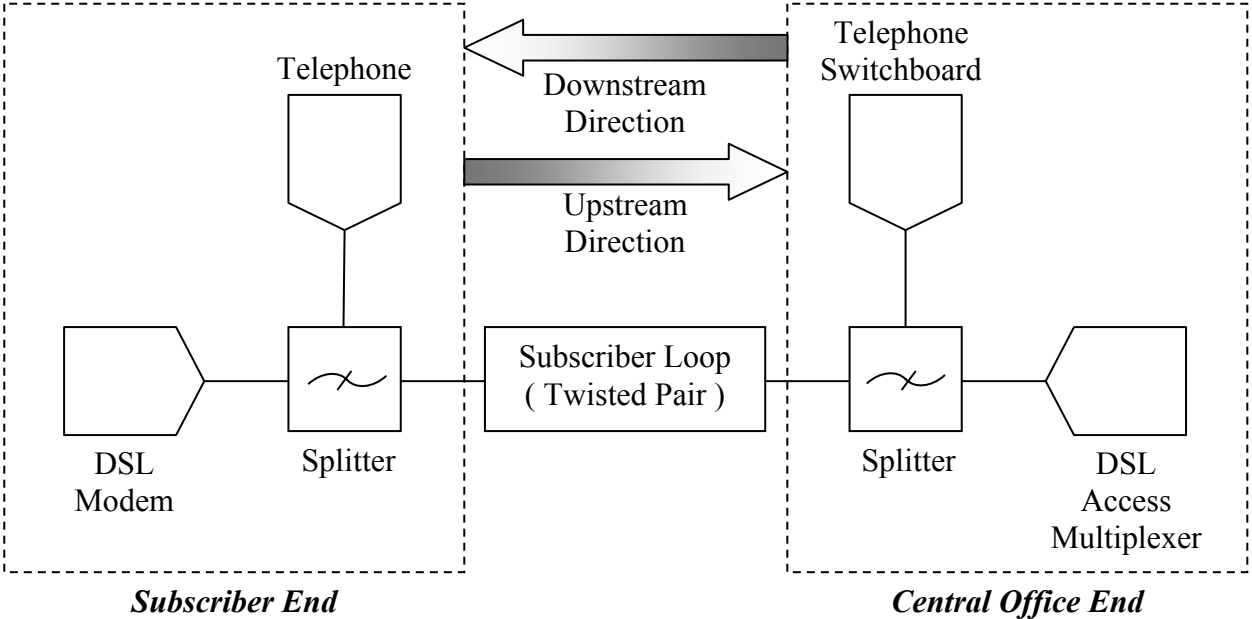


Figure 1-1: End to end system block diagram of a typical DSL system.

In terms of standardization, several different organizations govern this important aspect of the DSL marketplace to assure different vendors have compatible products. One of the bodies studying ADSL is committee T1, which is accredited by the American National Standards Institute (ANSI). This committee is broken down into several subcommittees that govern the standardization in different areas of ADSL. Other standards bodies include the International Telecommunications Union (ITU) and the European Technical Standards Institute (ETSI); these bodies facilitate the convergence of DSL technology and are largely based on the pre-existing ANSI standards.

The infrastructure of DSL technology, the telephone subscriber loop, is the key topic of investigation in this research. Since the telephone voice band has a narrowband nature (dc - 4

kHz), not all of the existing loops are conditioned for DSL networks due to limitations in cable quality or branching patterns. Adequate documentation is not always performed during expansion of the existing infrastructure, which prevents DSL providers from being able to calculate the feasibility and the obtainable data rate of the technology. This is the motivation for a system that detects subscriber loop topologies and performs throughput calculations of the resulting data rate between detected nodes.

## **1.2 Subscriber Loop (Twisted Pair) Environment**

The existing infrastructure of twisted pair cables on which DSL technology is deployed needs to be studied to produce accurate testing procedures and equipment. A twisted pair is simply made up of two cables twisted around one another that are electrically driven and sensed differentially to reduce the effects of outside influences such as crosstalk from other cables within the bundle or other outside interferences. Because the wires are physically close and symmetrical to one another, any outside influence on one of the cables will affect the other similarly; therefore, the interference will be subtracted out when the wires are driven using a differential mode. This section will expand on the characteristics of the twisted pair cables and the types of configurations that are applicable in telephony systems.

### **1.2.1 Twisted Pair Characteristics and Electrical Properties**

Many different types and qualities of twisted pair cable make up the existing telephone industry's cabling infrastructure. Twisted pair cables are usually bundled together in a cable sheath with 25 to 100 twisted pairs of cables in each bundle. Each wire is also coated with some type of insulating material such as a paper-based (PULP) or a plastic-based (PIC) material. The bundle of cables contains an outer shield that is grounded at the terminating blocks of the system to reduce the electromagnetic interference (EMI) from outside sources. The rate of twisting also varies among the pairs within each bundle to further reduce crosstalk between the cables. The rate of twisting is usually in the range of 12 to 40 turns per meter.

In addition to the insulation material used in production of the cables, twisted pair cables are also characterized by the diameter of the copper wire, or gauge, of the cable. The American Wire Gauge (AWG) designations are used and typical wire gauges include 19 AWG, 22 AWG, 24 AWG, and 26 AWG with diameters ranging from 0.912 mm to 0.404 mm, respectively.

Twisted pair cables are also defined by categories that specify electrical tolerances of the pair. These categories range from class 1 cables that have unspecified bit-rate capabilities (usually  $< 1\text{Mbps}$ ) to class 5 cables that have specified bit-rate capabilities of up to 100 Mbps. A minimum of class 3 cables (up to 16Mbps) is preferred for use in DSL technology. Most existing cabling in the telephone industry's infrastructure is as good as or better than this preferred class of cable.

The electrical characteristics of the twisted pair cables are defined using the classical transmission line model. This model incorporates a set of four parameters per unit length, including a series inductance and resistance and a shunt capacitance and conductance, also known as the *RLCG parameters* of the cable. The series inductance represents the total self-inductance of the two conductors, and the shunt capacitance is due to the close proximity of the two conductors. The series resistance is due to the finite conductivity of the conductors, and the shunt conductance is due to the dielectric loss in the material between the two conductors. *Figure 1-2* gives a graphic representation of a segment of twisted pair cable per unit length,  $dz$ .

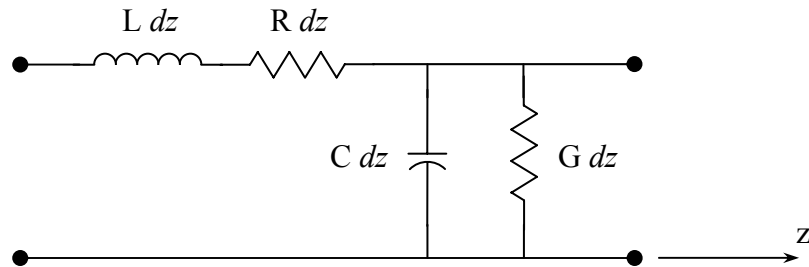


*Figure 1-2: Transmission line model per unit length.*

A literature review of the twisted pair models presently used to simulate the performance of DSL technology produced several models that were inadequate for time domain analysis, mainly due to their failure to adhere to the Kramers-Kronig causality relationships. For example, empirical models developed by British Telecommunications (BT) Laboratories, presented in the ANSI T1E1.4 contribution [4], were fit to data produced from performed measurements performed by the laboratories as described in [4]-[6]. These models are described below.

#### *Resistance*

$$R(f) = \left( r_{oc}^4 + a_c f^2 \right)^{0.25}, \quad (1-1)$$

where  $r_{oc}$  is the dc resistance and  $a_c$  is a constant that controls the onset of the  $\sqrt{f}$  factor.

### Inductance

$$L(f) = \frac{l_o + l_\infty \left( \frac{f}{f_m} \right)^b}{1 + \left( \frac{f}{f_m} \right)^b}, \quad (1-2)$$

where  $l_o$  is the low frequency inductance,  $l_\infty$  is the high frequency inductance, and  $f_m$  and  $b$  are parameters that control the transition between the two inductance parameters.

### Conductance

$$G(f) = g_o f^{g_c}, \quad (1-3)$$

where  $g_o$  and  $g_c$  allow fitting of the conductance measurements. Valid measurements of the conductance are difficult since the value of this shunt loss is small. The small conductance value is dominated by the higher series resistance value, making extraction of this parameter difficult.

### Capacitance

$$C(f) = C_\infty, \quad (1-4)$$

where  $C_\infty$  is a constant capacitance value, which assumes the relative permittivity of the dielectric surrounding the conductor is relatively constant over the frequency range of interest.

The problems resulting from the model's failure to comply with the Kramers-Kronig relationships will be presented in subsequent sections. New models that take this relationship into account as well as the physical characteristics and dimensions of the twisted pair cables will be introduced, verified, and applied to the network synthesis problem.

The RLCG parameters, also known as primary transmission line parameters, can be used to calculate the secondary line parameters, or the intrinsic impedance and propagation constant of the transmission line. These parameters are given respectively as

$$Z_o(f) = \sqrt{\frac{R(f) + j\omega L(f)}{G(f) + j\omega C(f)}}, \quad (1-5)$$

and

$$\gamma(f) = \alpha(f) + j\beta(f) = \sqrt{[R(f) + j\omega L(f)] \cdot [G(f) + j\omega C(f)]}. \quad (1-6)$$

The real and imaginary parts of the propagation function are the attenuation function,  $\alpha(f)$  (Np/m), and the phase function,  $\beta(f)$  (radians/m), respectively. These secondary line parameters will be used to model the twisted pair cables when the synthesis and performance analysis of the subscriber loops are processed.

### 1.2.2 Subscriber Loop Structure

Subscriber loops consist of sections of twisted pair cables usually of different gauges spanning from the central office to each subscriber. The subscriber loop structure is divided up into three main portions: the feeder cables, the distribution cables, and the drop wires. The feeder cables have the highest concentration (up to 2500 pairs) of twisted pairs within each bundle that connect the central office to the distribution cabinets. From these cabinets, the distribution cables connect the central office with current and potential customers. The drop wire is the final section of cable and connects the distribution cables to the subscriber. The connection of two or more sections of cables within each loop is referred to as a splice. A third cable spliced off of the main loop is called a bridge tap. The purpose of the bridge tap is to leave flexibility in the location of future subscribers on any given subscriber loop and is usually open circuited. The bridge tap length is limited to minimize adverse effects on the transmission characteristics of the loop. *Figure 1-3* shows the general structure of a subscriber loop and three sections of cable used to connect the central office to the subscriber.

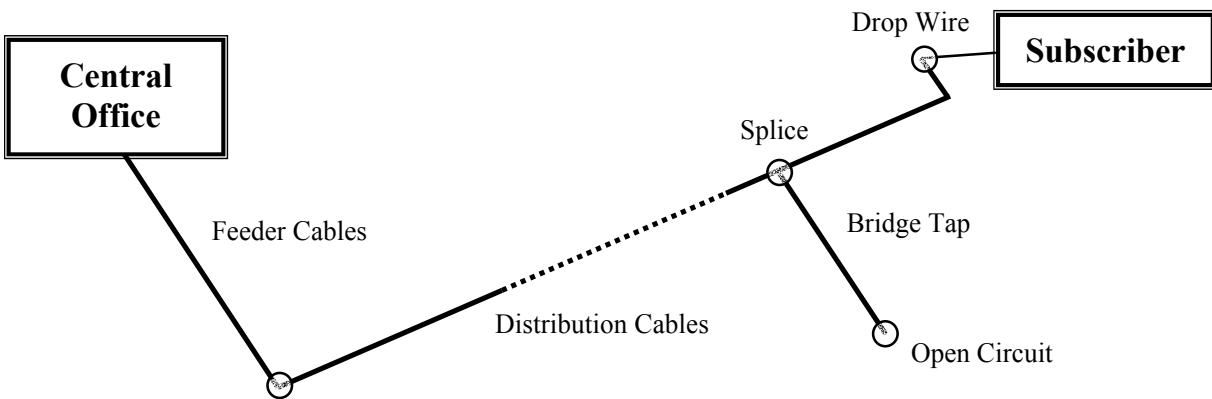


*Figure 1-3: Typical structure of an end-to-end subscriber loop.*

For the purpose of testing DSL technology on subscriber loops, several sets of test subscriber loops have been established. Telcordia Technologies developed a set of test loops [7] referred to as Carrier Servicing Area (CSA) loops; these are listed in Appendix A. These loops and portions of these loops will be used throughout this documentation to address the modeling aspects of the loops as well as the system identification procedures and performance analysis.

### 1.2.3 Subscriber Loop Characteristics Used in Performance Analysis

Items such as the loop length, loop topology, cable quality, and cable routing locations generate the characteristics of subscriber loops. Given that the twisted pair cables can be characterized in terms of a two-port system, the input impedance, transfer function, and insertion loss are important characteristics of any subscriber loop and will be discussed in this section.

The two-port parameters that are most convenient in characterizing twisted pair cables are the *ABCD transmission parameters* [8]. These parameters mathematically relate the voltage and current of the input port to the voltage and current of the output port (see *Figure 1-4*). A cascade connection of two or more two-port networks can be found by simply multiplying the *ABCD* matrices of each individual two-port network; this aspect of the *ABCD* parameters allows easy evaluation of subscriber loops due to the chain-type nature of the topologies.

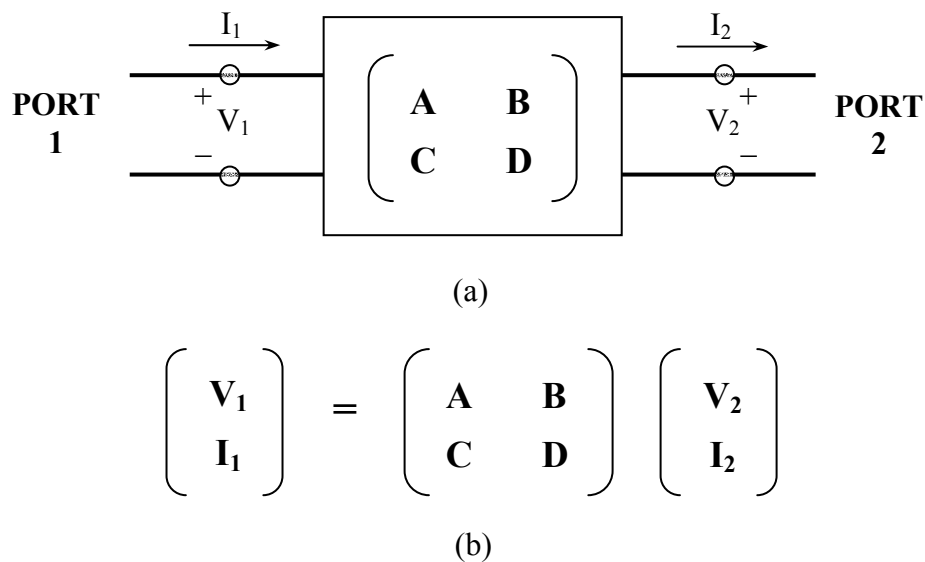


Figure 1-4: (a) An *ABCD* two-port network (b) *ABCD* matrix representation.

The  $ABCD$  parameters of a twisted pair cable segment that makes up the feeder or distribution lines are related to the secondary line parameters as follows (where  $\ell$  is the cable length):

$$\begin{bmatrix} A(f) & B(f) \\ C(f) & D(f) \end{bmatrix} = \begin{bmatrix} \cosh[\gamma(f) \cdot \ell] & Z_o(f) \sinh[\gamma(f) \cdot \ell] \\ Y_o(f) \sinh[\gamma(f) \cdot \ell] & \cosh[\gamma(f) \cdot \ell] \end{bmatrix}. \quad (1-7)$$

The  $ABCD$  parameters that model a bridge tap line relate to a shunt impedance referring to the secondary line parameters as follows:

$$\begin{bmatrix} A(f) & B(f) \\ C(f) & D(f) \end{bmatrix} = \begin{bmatrix} 1 & 0 \\ Y_o(f) \tanh[\gamma(f) \cdot \ell] & 1 \end{bmatrix}. \quad (1-8)$$

For analysis of a loop, some information is needed beyond the two-port  $ABCD$  parameters of the twisted pair segments. This information includes the source impedance that is usually the impedance of the data transmitter used when sending information or the measurement equipment if a subscriber loop analysis is in progress. The termination impedance,  $Z_L$ , of the distribution cable will be assumed open circuited throughout the research; this is due to the negligible impedance of the drop wires or the fact that the line could be disconnected during an analysis measurement. The open circuit terminations are an estimate though the developed software does have the provision for dealing with loaded terminations.

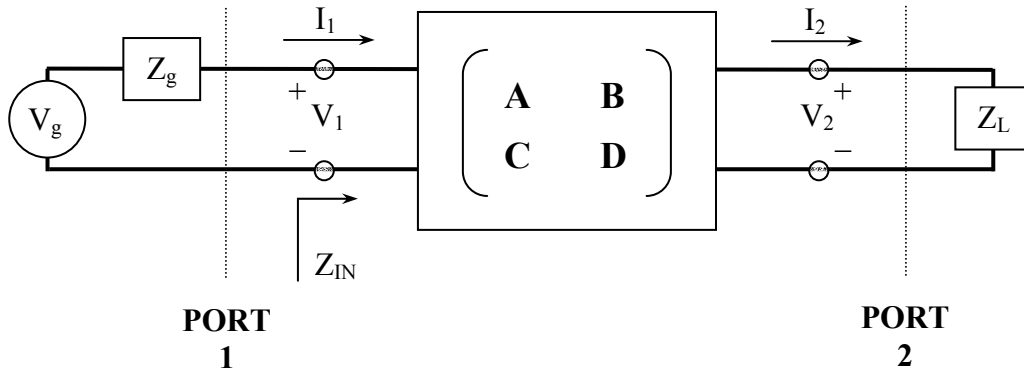


Figure 1-5: A generic end-to-end model of a subscriber loop using two-port parameters.

The input impedance of the subscriber loop is defined as the ratio of the voltage across the input port of the loop with the current inflowing into the input port. In terms of  $ABCD$  parameters, the input impedance is derived as:

$$Z_{IN} = \frac{V_1}{I_1} = \frac{A \cdot Z_L + B}{C \cdot Z_L + D}. \quad (1-9)$$

The transfer function of the subscriber loop will be defined as the ratio of the voltage across the output port of the loop with the voltage placed on the input port. In terms of  $ABCD$  parameters, the transfer function is derived as:

$$H = \frac{V_2}{V_g} = \frac{Z_L}{Z_g[C \cdot Z_L + D] + A \cdot Z_L + B}. \quad (1-10)$$

The insertion loss of the loop will be defined as the ratio of the power delivered to the load with the power delivered to the load had the loop not been present. This is basically the loss that is inserted between the central office and the subscriber due to the loop and is given in decibels as:

$$IL = 10 \log \left( \frac{P_{no\ loop}}{P_{loop}} \right) = 20 \log \left( \frac{A \cdot Z_L + B + Z_g[C \cdot Z_L + D]}{Z_g + Z_L} \right). \quad (1-11)$$

The insertion loss is one of the most important loop characteristics when discussing the performance capabilities of different DSL technologies on specific loop configurations.

### 1.3 Subscriber Loop Modeling and Simulations

A subscriber loop consists of several twisted pair segments connected together in what makes up the telephone industry's cabling infrastructure. *Figure 1-6* depicts a type of loop that could be seen in industry, with notation included to identify segment identification, gauge changes, node identifications, terminations, and bridge taps. Segment identification is used to classify each of the twisted pair sections of the loop during the reconstruction process. The nodes, or endpoints of each identified segment, will also be labeled as the loop identification scheme is processed. A node will be identified due to impedance mismatches such as those seen because of a gauge change (where two cables with different gauges are connected together), a bridge tap, or a mismatched termination.

The intrinsic impedance, transfer function, and insertion loss of the two loops shown in *Figure 1-6* are presented in *Figures 1-7* and *1-8*. It will be shown that the bridge taps, although providing greater flexibility for the telephone industry in terms of connecting future subscribers, have a negative impact on the insertion loss of a subscriber loop, and thus impose limitations on the upper limit of the estimated data rate. This aspect will be presented through simulations of the two loops shown in *Figure 1-6*, which are similar except the bridge tap is removed in the *Figure 1-6b*.

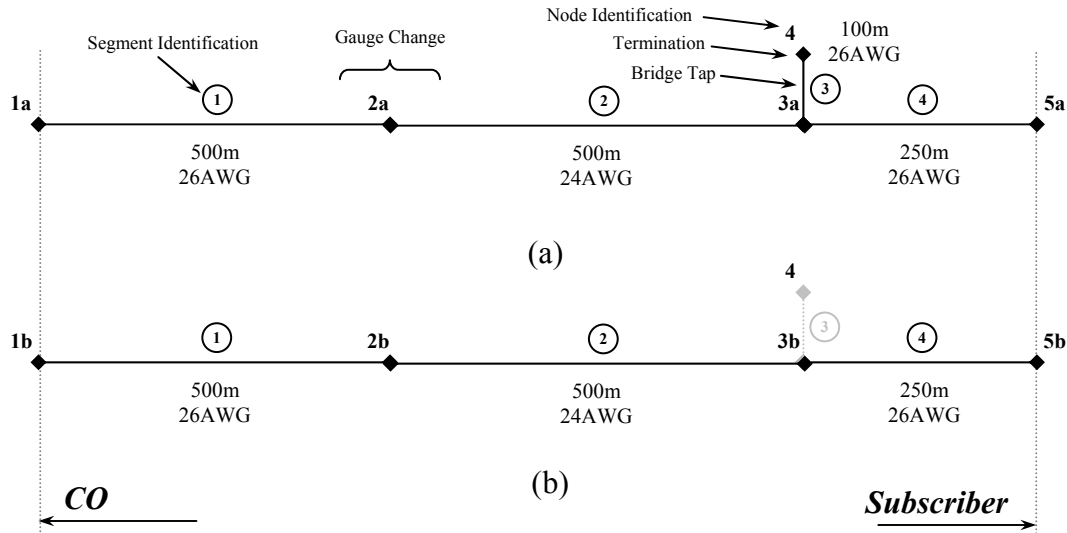


Figure 1-6: (a) An example of a subscriber loop (b) Identical loop without the bridge tap.

Figure 1-7 graphs the real and imaginary portions of the intrinsic impedance as well as the transfer function and insertion loss from node #1 to node #5 for both of the loops shown above. Figure 1-7c and d show the negative effects that a bridge tap can have on the transfer function and insertion loss of the loop. The standing waves, or multiple reflections, due to the bridge tap result in null values, or fluctuations, in the insertion loss. Since the addition of bridge taps causes degradation in the amount of power that can be transmitted through the subscriber loop, there are strict restrictions to the number of bridge taps allowed. It is obvious through this analysis that knowing the loop topology of a subscriber loop is of great importance to DSL providers for feasibility analysis as well as maintenance aspects of a given loop.

#### 1.4 Methods of Subscriber Loop Synthesis

Measurements of subscriber loops may be performed in either the time or frequency domain. Since this research investigates the feasibility of identifying the topology of the subscriber loop from the CO port, the measurement setup will be based on application to a single port; in other words, the transfer function, which is a two-port relationship, cannot be measured directly. The information of the subscriber loop is contained within both the time and frequency domain data. Figure 1-8 depicts typical results of the two types of measurements from nodes #1 and #3 based on the loop shown in Figure 1-6a.

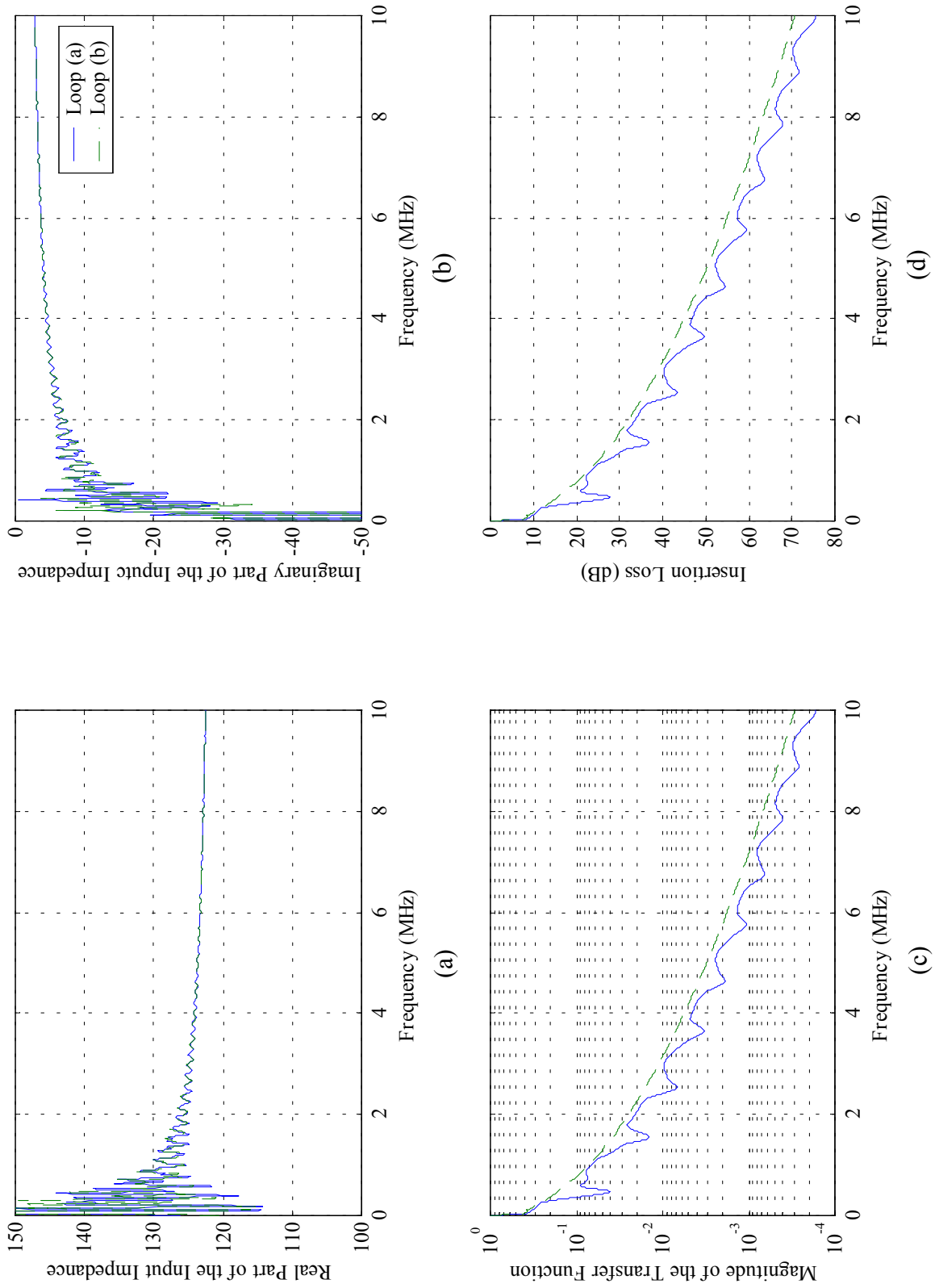


Figure 1-7: Characteristics of each of the two loops of Figure 1-6 (a) Real part of the input impedance (b) Imaginary part of the input impedance (c) Magnitude of the transfer function (d) The insertion loss in dB.

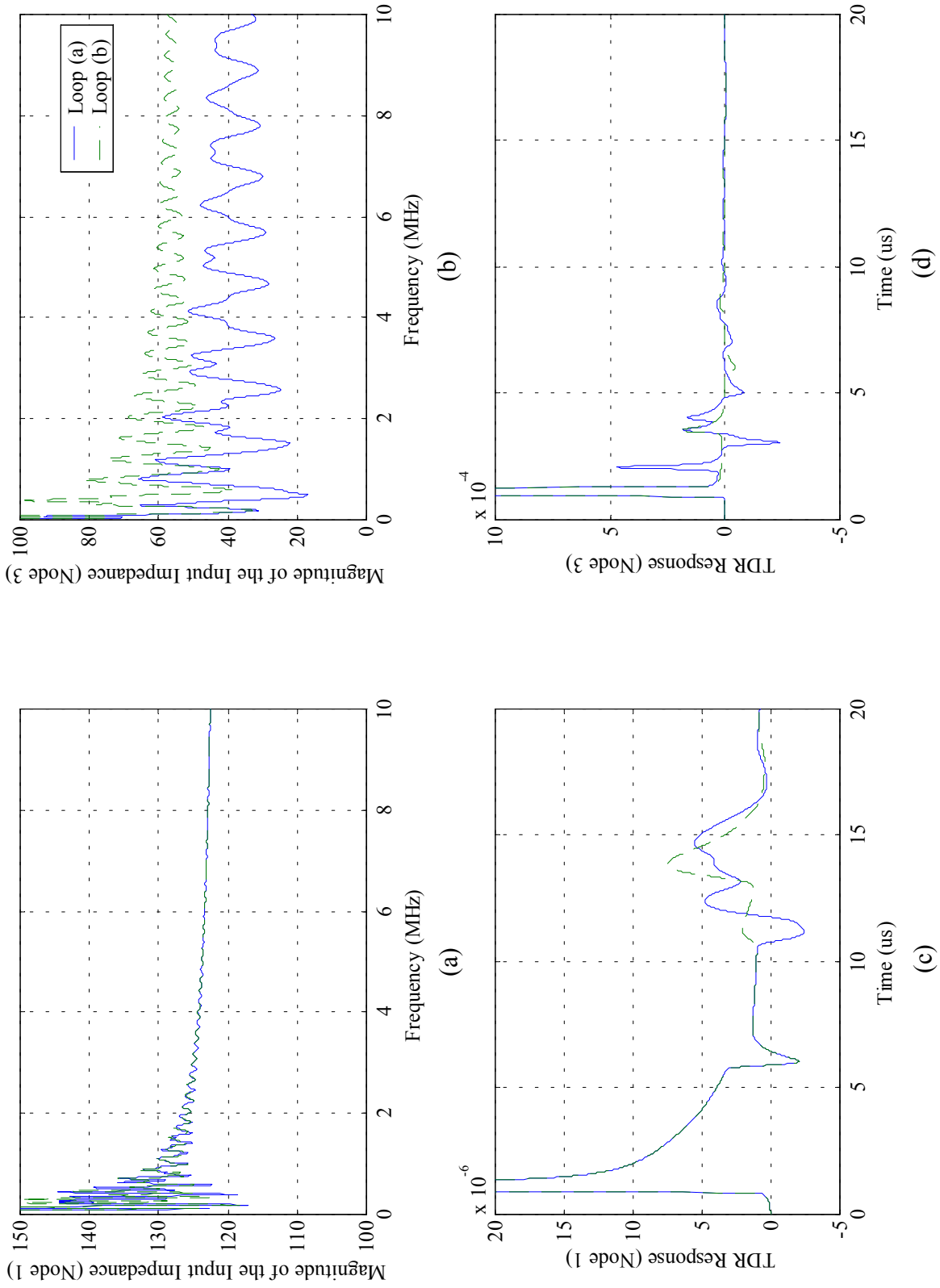


Figure 1-8: Example measurements of the loop in Figure 1-6a (a) Magnitude of the input impedance from node 1 (b) Magnitude of the input impedance from node 3 (c) TDR response from node 1 (d) TDR response from node 3.

Through the two types of measurements described, there are several methods for identifying the subscriber loop topologies. One of the methods that the synthesis problem can be solved is by a trial and error type approach. The trial and error type approach [9] simulates a number of different models and compares the results to the measured waveform (in the time or frequency domain). In an iterative scheme, the models are updated depending on specific criteria developed within the routine that adjusts the model until the simulated results match the measurements.

A second synthesis method that can be applied to the loop topology identification scheme is an optimization approach. The optimization approach uses a pre-programmed number of possible loop sections of different characteristics to perform the identification. This iterative approach continues under specific optimization schemes until the simulated results match the measured results.

Though the previously mentioned methods are viable approaches to the synthesis problem, this research will employ a method of layering. The layering, or “peeling” type, approach initially uses algorithms for detection of the characteristics of the loop structure connected to the measurement node. After identification of the initial portion of the subscriber loop, this portion is de-embedded, or removed from the measurement data. The process of de-embedding essentially moves the details of distant segments up to the location of the measurement node. This allows the de-embedding routine to work around some of the dispersion and attenuation properties of twisted pair cables.

## **1.5 Summary and Organization**

This chapter focused on background information about DSL technology and the presentation of subscriber loops that form the infrastructure of the telephone industry’s cabling system. Since DSL providers are interested in cost effective methods of predicting the throughput of these subscriber loops, this research proposes a method of single port identification. By performing identification of the subscriber loop at a single node and simulating the transfer function among the sets of nodes, the providers will be relieved from having to deploy an employee to the subscriber’s location to measure the transfer function directly.

Also presented in this section was the application of a layering type approach to accomplish the single port identification. This approach uses a technique called de-embedding as part of the identification process. Chapter 2 will present the theoretical background of this tool as well as the different types of de-embedding processes.

Chapter 3 will begin the presentation of original research including the detailed approach of the synthesis problem and the application of this approach to subscriber loops. The scheme will present algorithms for gauge detection of the twisted pair cables, length detection of the identified segments, and the de-embedding process as applied to the subscriber loops. An important property of the de-embedding tool is the user's ability to incorporate accurate models of the system components within the algorithm. Poor models of the twisted pair cables will introduce errors that will limit the ability of the de-embedding routine to identify the topology.

Chapter 4 will present the detailed development of the twisted pair cable models based on their physical and electrical properties. The modeling approach is based on the well-documented models developed for the parallel line cables. Aspects such as the skin effect within the conductor and the effects of the helical structure created due to the twisting will be presented.

Chapter 5 will present verification of the models based on actual measurements of the cables. The measurement setup as well as the numerical algorithms used to process the data into the primary line parameters will be presented.

Chapter 6 will incorporate all of the earlier chapters mentioned in verification of the subscriber loop reconstruction routine. The developed models, the de-embedding technique, and the algorithms for cable gauge and length detection will be combined together and applied to simulated data resulting from portions of typical subscriber loop topologies. Finally, Chapter 7 will discuss the results of the scheme as well as provide a conclusion and future areas of investigation regarding this research.

## Chapter 2

### Introduction to Deconvolution and De-Embedding

#### 2 Introduction

The characterization of linear systems from time and frequency domain measurements is of considerable interests in many applications. With prior knowledge of an applied excitation to a given linear system and an output measurement resulting from the excitation, these two sources of information can be processed to produce a response that completely describes the linear system. Deconvolution techniques are based on the separation of the excitation signal from the resulting output waveform, due to the fact that the system response has been convolved with the excitation in the performed measurement, in other words, it is a technique of separating known responses from a linear system response. This technique is sometimes used in error correction or system identification problems.

#### 2.1 Deconvolution Schemes

Since deconvolution is defined as the inverse of the convolution operation, the discussion of the convolution operation will be addressed foremost. The mathematical operation termed convolution is an operation that relates an input signal,  $x(t)$ , and an impulse response,  $h(t)$ , of a linear, time-invariant system to the resulting output signal,  $y(t)$ . Convolution in the time domain is defined by the following integrals referring to the system diagram shown in *Figure 2-1*:

$$y(t) = \int_{-\infty}^{\infty} x(\tau)h(t-\tau)d\tau = \int_{-\infty}^{\infty} x(t-\tau)h(\tau)d\tau , \quad (2-1)$$

or

$$y(t) = x(t) * h(t) = h(t) * x(t) . \quad (2-2)$$

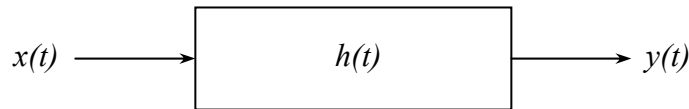


Figure 2-1: Time domain system diagram for convolution

The corresponding form in the frequency domain is given by the following equations referring to the system diagram in Figure 2-2:

$$Y(j\omega) = X(j\omega) \cdot H(j\omega), \quad (2-3)$$

or

$$Y(j\omega) = \int_{-\infty}^{\infty} y(t)e^{j\omega t} dt . \quad (2-4)$$

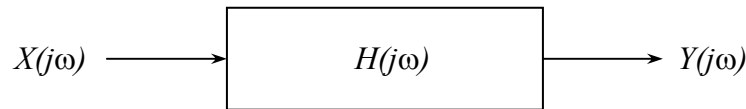


Figure 2-2: Frequency domain system diagram for convolution

Since deconvolution is the inverse process of the convolution operation, this inverse operation involves the determination of either  $x(t)$  or  $h(t)$  assuming there is adequate knowledge of the remaining two time functions. The process of determining  $h(t)$  through prior knowledge of  $x(t)$  and  $y(t)$  is a system identification process. The determination of  $x(t)$  through prior knowledge of  $y(t)$  and  $h(t)$  is a pulse measurement process. Without any loss of generality, only the deconvolution process for determination of  $h(t)$  will be referred to in the remainder of this solution.

In an ideal situation of one having exact and complete knowledge of  $x(t)$  and  $y(t)$ , deconvolution can be exactly performed to compute  $h(t)$  in either the time or frequency domains.

The time domain solution involves a set of linear simultaneous equations formed by using the discrete sequence representation of the time functions,  $x(t)$ ,  $y(t)$ , and  $h(t)$  in the integral form defined in (2-1). This set of equations is then solved to yield the time sequence of  $h(t)$  [10]. This type solution is typically achieved by using either matrix inversion or difference equation techniques. The frequency domain solution uses the Fourier transform to compute the frequency domain forms,  $X(j\omega)$  and  $Y(j\omega)$ , of the time functions. Next, (2-3) is used to compute  $H(j\omega)$  to which the inverse Fourier transform can be applied to yield  $h(t)$  [11].

Viewing the preceding discussion in a numerical sense, performing deconvolution in the time domain is similar to performing time domain differentiation. Both of these operations involve subtraction operations in the time domain [11]. It is obvious that errors may occur if the difference of two close values is taken. Any small errors in the processed data multiply significantly in the final result. The result will only be accurate if the processed data has absolute accuracy. In the frequency domain, the deconvolution operation involves a division operation, which is also sensitive to data errors (i.e. dividing by a small number). Consequently, in both the time and frequency domains it can be stated that the deconvolution operation is highly sensitive to noise and data errors. In practical applications, the deconvolution problem is mathematically classified as an ill-posed problem [11]. An ill-posed problem occurs when the information represented by the data (sequences), or the equations (continuous functions) are incomplete, or approximates. In the following section, the deconvolution operation will be investigated in practical applications where exact knowledge of the signals in the time or frequency domain is not possible. This discussion will be followed by methods of achieving acceptable estimates of the frequency domain solution along with surveyed techniques of frequency domain implementation.

## 2.2 Practical Application of Deconvolution

In a practical sense, deconvolution is referred to as an ill-posed problem and the topic of practical deconvolution is addressed in this section. In the opening section, the process of deconvolution was explained to yield  $h(t)$  exactly assuming exact knowledge of both  $x(t)$  and  $y(t)$ . However, in practical applications where  $x(t)$  and  $y(t)$  are obtained through measurements, obtaining exact knowledge of these signals is not realistic. Due to systematic limitations such as finite duration of the measured signals and finite distribution of the test signal, the acquired

waveform is different to a certain extent from the true time signal, resulting in only an estimate of the actual waveform. Designating measured waveforms by  $x_m(t)$  and  $y_m(t)$ , these waveforms are related to their exact time signals,  $x(t)$  and  $y(t)$ , by the following equations:

$$x_m(t) = x(t) + x_e(t), \text{ and} \quad (2-5)$$

$$y_m(t) = y(t) + y_e(t), \quad (2-6)$$

where  $x_e(t)$  and  $y_e(t)$  are unknown error components as a function of time.

The convolution in (2-2) using (2-5) and (2-6) takes the form:

$$y_m(t) - y_e(t) = h(t) * [x_m(t) - x_e(t)]. \quad (2-7)$$

The corresponding frequency domain form is given as:

$$Y_m(j\omega) - Y_e(j\omega) = H(j\omega) \cdot [X_m(j\omega) - X_e(j\omega)]. \quad (2-8)$$

Since the error quantities,  $x_e(t)$  and  $y_e(t)$ , including their transforms into the frequency domain,  $X_e(j\omega)$  and  $Y_e(j\omega)$ , are not known, it is not possible to obtain an exact solution for  $h(t)$  or  $H(j\omega)$  from (2-7) or (2-8). Instead, these equations can yield solutions for  $h_m(t)$  or  $H_m(j\omega)$  using:

$$y_m(t) = x_m(t) * h_m(t), \text{ and} \quad (2-9)$$

$$Y_m(j\omega) = X_m(j\omega) \cdot H_m(j\omega), \quad (2-10)$$

where  $h_m(t)$  is the inverse Fourier transform of  $H_m(j\omega)$ , and

$$H_m(j\omega) = H(j\omega) + H_e(j\omega). \quad (2-11)$$

It is shown that an error component will be introduced into the deconvolution solution. The error component initiates an investigation into methods for obtaining acceptable solutions.

### 2.3 Acceptable Estimates of Deconvolution Solutions

The approximation of the practical deconvolution problem in (2-10) fails by producing spurious components in the frequency regions where  $X(j\omega)$  is fairly small. In the rest of the frequency spectrum, where  $X(j\omega)$  is significant, the approximation is fairly accurate. The concept of achieving an acceptable solution for the deconvolution problem is to accept  $H_m(j\omega)$  as an initial approximation to  $H(j\omega)$  and try to minimize the content of the spurious components to enable a meaningful Fourier transformation [11].

Application of a properly designed filter to  $H(j\omega)$  can reduce the spurious components and produce an acceptable deconvolution estimate. The filter's stopband characteristics will be optimized to reduce the spurious components of  $H_m(j\omega)$ . Denoting the filter's transfer function by  $F(j\omega)$ , an acceptable deconvolution estimate,  $H_{est}(j\omega)$ , of  $H(j\omega)$  can be written as:

$$H_{est}(j\omega) = H_m(j\omega) \cdot F(j\omega). \quad (2-12)$$

Depending on the filter characteristics,  $F(j\omega)$  can be applied to either  $H_m(j\omega)$ ,  $Y_m(j\omega)$ , or  $X_m(j\omega)$  as shown in (2-13):

$$H_{est}(j\omega) = \left[ \frac{Y_m(j\omega)}{X_m(j\omega)} \right] F(j\omega) = \frac{[Y_m(j\omega) \cdot F(j\omega)]}{X_m(j\omega)} = \frac{Y_m(j\omega)}{[X_m(j\omega) \cdot F(j\omega)]}. \quad (2-13)$$

The main provision in designing the filter is how to reduce the noise and spurious components while preserving the majority of the signal information. Typically, this is where subjective judgment has to be used to decide the values of the filter's optimum parameters. In later sections of this solution, a variety of time and frequency domain criteria will be discussed. An optimum solution to the deconvolution would look as follows:

$$H_{opt}(j\omega) = H_m(j\omega) \cdot F_{opt}(j\omega). \quad (2-14)$$

In general, the optimization process is performed iteratively while monitoring some form of pre-developed criteria.

Filtering can also be performed in the time domain as shown in (2-15) and techniques include averaging [10], least squares [10], and conjugate gradient methods [22]:

$$h_{opt}(t) = h_m(t) * f_{opt}(t). \quad (2-15)$$

A presentation of iterative frequency domain and time domain techniques will follow with a review of different methods of time and frequency domain criteria analysis in the subsequent section.

## 2.4 Iterative Frequency Domain Deconvolution Techniques

The iterative frequency domain deconvolution techniques arise from the optimization of the filtering process explained in the previous section used to find acceptable solutions to the ill-posed deconvolution operation. The optimum filter interpolates  $H_m(j\omega)$  at the zeros of  $X_m(j\omega)$ ,

where it is indeterminate, to yield  $H_{opt}(j\omega)$ , the best estimate of  $H(j\omega)$ . The frequency domain techniques are based on the Wiener filtering theory. A class of these filters which has demonstrated quality performance are given by:

$$F(j\omega) = \frac{1}{1 + \frac{G(\omega)}{|X_m(j\omega)|^2}}, \quad (2-16)$$

where  $G(\omega)$  is a positive function of frequency. This filtering scheme is designed such that the quantity  $G(\omega)/|X_m(j\omega)|^2$  is small, and consequently,  $F(j\omega)$  is almost unity in the regions where  $X_m(j\omega)$  is not very small. However, when  $X_m(j\omega)$  is very small, the quantity  $G(\omega)/|X_m(j\omega)|^2$  should become significant and cause adequate filter attenuation to minimize the spurious components. Two cases of this type of filtering will be surveyed in this solution; the optimal compensation technique and the regularization technique (or the Guillaume-Nahman technique).

#### 2.4.1 Optimal Compensation Technique

The optimal compensation technique is presented as one of the iterative frequency domain deconvolution techniques. The filter definition of (2-16) is defined using the following:

$$G(\omega) = \lambda. \quad (2-17)$$

The resulting estimate of the deconvolution estimate is

$$H_{est}(j\omega) = Y_m(j\omega) \cdot \frac{X_m^*(j\omega)}{|X_m(j\omega)|^2 + \lambda}. \quad (2-18)$$

The characteristic of this filter is an adaptive type that is processed through a number of iterations until a specified criterion is obtained between accuracy and noise content indicators. These criteria will be presented in the following section.

#### 2.4.2 Regularization (Guillaume-Nahman) Technique

The regularization technique is presented as the second of the iterative frequency domain deconvolution techniques. The filter definition of (2-16) is defined using the following:

$$G(\omega) = \lambda\omega^4. \quad (2-19)$$

The resulting estimate of the deconvolution operation is

$$H_{est}(j\omega) = Y_m(j\omega) \cdot \frac{X_m^*(j\omega)}{|X_m(j\omega)|^2 + \lambda\omega^4}. \quad (2-20)$$

The characteristic of this filter is a low pass type that is processed through a number of iterations until a specified criterion for which the standard deviation in the imaginary part of the deconvolved impulse response is minimized [23]. As mentioned earlier, the deconvolution operation is ill-posed in both the frequency domain and time domain, therefore, iterative methods have also been developed in the time domain to achieve acceptable solutions; some of these methods are described in the following section.

## 2.5 Iterative Time Domain Deconvolution Techniques

There have been numerous forms of time domain iterative deconvolution techniques found in literature to determine acceptable estimates for the ill-posed deconvolution problem. Most of these techniques are a branch from or modification of Van-Cittert's technique. The Van-Cittert technique and others are presented in this section of the solution.

### 2.5.1 The Van-Cittert Deconvolution Technique

The Van-Cittert technique is an iterative time domain deconvolution technique based on forming successive approximations of the unknown system impulse response,  $h(t)$ , using the convolution equation [12]. The successive approximations are to converge to the unknown system impulse response, though this is not always possible when the technique is used without modifications [11]. In the technique, the initial approximation to  $h(t)$ ,  $h_1(t)$ , is chosen to be  $y(t)$ , and the  $h_i(t)$  term is obtained iteratively by adding an error correction term to the  $h_i(t)$  iteration:

$$h_{i+1}(t) = h_i(t) + [y(t) - h_i(t) * x(t)], \quad (2-21)$$

with

$$h_1(t) = y(t), \quad (2-22)$$

where  $i$  is the iteration number.

Ideally, the iterative process is ended whenever the following condition is achieved:

$$h_i(t) = h_{i+1}(t) = h(t). \quad (2-23)$$

This method requires extensive computational time due to the many numerical convolutions performed in the iteration. Also, the number of estimates needed to achieve an acceptable solution is not known.

As the iteration number,  $i$ , becomes large and an acceptable solution is obtained we can view the converged result as follows:

$$h(t) = F^{-1} \left\{ \frac{Y}{X} \right\}, \quad (2-24)$$

where  $Y$  and  $X$  are the Fourier transforms of  $y$  and  $x$ , respectively, and the  $F^{-1}$  is the inverse Fourier transform operator. Considering measurements that are bandlimited,  $X$  will have essentially zero values at some frequencies where, due to noise,  $Y$  may have finite values [13]. Therefore, estimates obtained with this method may contain a significant amount of spurious components. A review of different methods of criteria analysis that achieves a compromise between noise reduction and signal information preservation will be presented in a subsequent section of this chapter.

### 2.5.2 Discussion of Convergence of the Van-Cittert's Technique

The discussion of convergence of the time domain iterative techniques will be applied to the Van-Cittert deconvolution technique as discussed in [12]. If the Fourier transform is applied to the equations that define the technique, the conditions for convergence can then be obtained. Using the Fourier transform on (2-21) we obtain:

$$H_{i+1}(j\omega) = H_i(j\omega) + [Y(j\omega) - H_i(j\omega) \cdot X(j\omega)], \quad (2-25)$$

with

$$H_1(j\omega) = Y(j\omega). \quad (2-26)$$

After successive substitutions, (2-25) yields the sequence:

$$H_i(j\omega) = \left\{ 1 + [1 - X(j\omega)] + [1 - X(j\omega)]^2 + \dots + [1 - X(j\omega)]^i \right\} \cdot Y(j\omega). \quad (2-27)$$

The series in braces,  $\{ \}$ , consists of the first  $i^{\text{th}}$  terms of the binomial expansion of  $\{1 - [1 - X(j\omega)]\}^{-1}$ , provided that  $[1 - X(j\omega)] < 1$ . Hence, the sequence of  $H_i(j\omega)$  converges to the ratio of  $Y(j\omega) / X(j\omega)$  when  $[1 - X(j\omega)] < 1$ . The same result is exactly what one would

obtain from straightforward frequency domain division. It is important to notice that this conclusion is not valid for the frequencies at which  $X(j\omega) = 0$ .

For values of  $\omega$  where  $X(j\omega) = 0$ , or at frequencies outside the information band of the signal, and in the absence of noise,  $Y(j\omega) = 0$ . At these frequencies,  $H_i(j\omega)$  is undetermined; however, for a finite numerical answer, convergence is possible if and only if

$$\begin{aligned} |1 - X(j\omega)| < 1 &= \{\omega : X(j\omega) \neq 0\} \\ H(j\omega) = 0 &= \{\omega : X(j\omega) = 0\} \end{aligned} \quad (2-28)$$

The conditions in (2-28) are referred to as Bracewell's conditions for convergence and were first stated in [14] and were studied and reported in [15]. It was shown that if the observed response is known with an error, the noise content grows linearly with each iteration. This investigation leads to some modifications of the Van-Cittert technique which attenuate the noise effects. Some of these modified techniques are investigated in the next sections.

### 2.5.3 Constrained Technique

The constrained technique is used in systems where the data is generally non-negative. A non-negative constraint can be incorporated into Van Cittert's method in the following manner [16]:

$$h_{i+1}(t) = ph_i(t) + [y(t) - ph_i(t) * x(t)], \quad (2-29)$$

where

$$p = \begin{cases} 1, & h_i(t) \geq 0 \\ 0, & h_i(t) < 0 \end{cases} \quad (2-30)$$

The effect of the constraint operator,  $p$ , is to truncate the negative artifacts from the estimate during each iteration.

### 2.5.4 Relaxation-Based Technique (Jansson's Technique)

Relaxation-based iterative methods are another approach to constrained deconvolution where a relaxation function is incorporated into the correction factor. The relaxation factor would enable the correction factor to have zero or negative corrections to the new estimate if the

present estimate contained nonphysical values. One form of this type of relaxation factor is given as follows [17]:

$$h_{i+1}(t) = h_i(t) + r[y(t) - h_i(t) * x(t)], \quad (2-31)$$

where

$$r[h_i(t)] = \begin{cases} b, & h_i(t) \geq 0 \\ 0, & h_i(t) < 0 \end{cases} \quad (2-32)$$

The methods in (2-29) and (2-31) do cause the elimination of nonphysical artifacts from the estimate, but the methods use truncation to accomplish this elimination. It must be considered that truncation may have a detrimental effect of also eliminating important signal information.

Jansson developed a proposed method using an alternative technique, where successive estimates are constrained to occur between upper and lower bounds. Jansson modified Van Cittert's technique by introducing a relaxation that depends on the estimate which prevents truncation of any information. The upper and lower amplitude values correspond to the physical limits of the data. Jansson's method is given as follows [17]:

$$h_{i+1}(t) = h_i(t) + r[y(t) - h_i(t) * x(t)], \quad (2-33)$$

where

$$r[h_i(t)] = r_o \left[ 1 - 2 \left| h_i(t) - \frac{1}{2} \right| \right], \quad (2-34a)$$

or even more general as

$$r[h_i(t)] = b \left[ 1 - \frac{2}{c} \left| h_i(t) - \frac{c}{2} \right| \right]. \quad (2-34b)$$

where the evaluation function  $r[h_i(t)]$  constrains the estimate between the values of  $0$  and  $c$ . The relaxation function has a piece-wise linear shape and will perform corrections to the function in the following manner: (a) positive corrections if the estimate lies within the limits of  $0$  to  $c$ , (b) reverse corrections if the estimate lies outside this limits, and (c) varying positive corrections as a function of the estimate's signal-to-noise ratio [13]. Note that truncation of information is not performed in this method.

### 2.5.5 Gold's Ratio Technique

A technique referred to as Gold's ratio method is another iterative deconvolution technique, which is based on using Bayes theorem. It is given by

$$h_{i+1}(t) = \frac{h_i(t)y(t)}{y(t) * h_i(t)}, \quad (2-35)$$

and has been described by Gold [18], Siska [19], Richardson [20], and McNeil *et al.* [21].

This method has only been lightly investigated and no explicit constraints have been placed on (2-19). If the iteration of  $h_i(t)$  begins reasonably close to the true value then many of the non-physical components could cancel each other as long as there are no relatively large noise components.

The following section will present various optimization criteria for the frequency domain and time domain methods.

## 2.6 Optimization Criteria for Deconvolution Techniques

Optimization is the process of finding the highest quality estimate of  $H(j\omega)$ , or  $h(t)$  through the implementation of qualitative error function criteria. The optimization is carried out through iterations while monitoring some type of performance indicator. These criteria techniques can be performed in the time and frequency domains as will be described below.

### 2.6.1 Time Domain Optimization Criteria

An error function is first defined as

$$e(t) = y(t) - h_{est}(t) * x_m(t). \quad (2-36)$$

Different parameters must be defined to characterize the error function such as mean value, standard deviation, maximum value, etc.

The convergence of iterative techniques can be monitored by forming the root-mean square error of the estimate, given as

$$e_i = \sqrt{\frac{1}{N} \sum_{k=0}^{N-1} \left[ y(k) - \sum_{j=0}^k h_i(j) * x(k-j) \right]^2}, \quad (2-37)$$

where  $h_i(k)$  designates the  $i^{th}$  iterative estimate, and  $N$  designates the number of data points.

A model algorithm of the time domain optimization technique is given in *Figure 2-3*. The time domain functions of the measured input and output signals are transformed into the frequency domain by the Fourier transform operation. They are processed by the compensating filter and transformed to time domain functions by use of the inverse Fourier transform operation. The data is stored for each of the different values of filter parameters. After each of the filter parameters selected are processed, the application of the time domain quality criteria are performed for each of the filter parameters. The optimal filter parameter is selected, and hence, the optimal estimate of the deconvolution solution,  $H_{opt}(j\omega)$ , can be calculated. Surveys of some of the time domain quality criteria are described below [25].

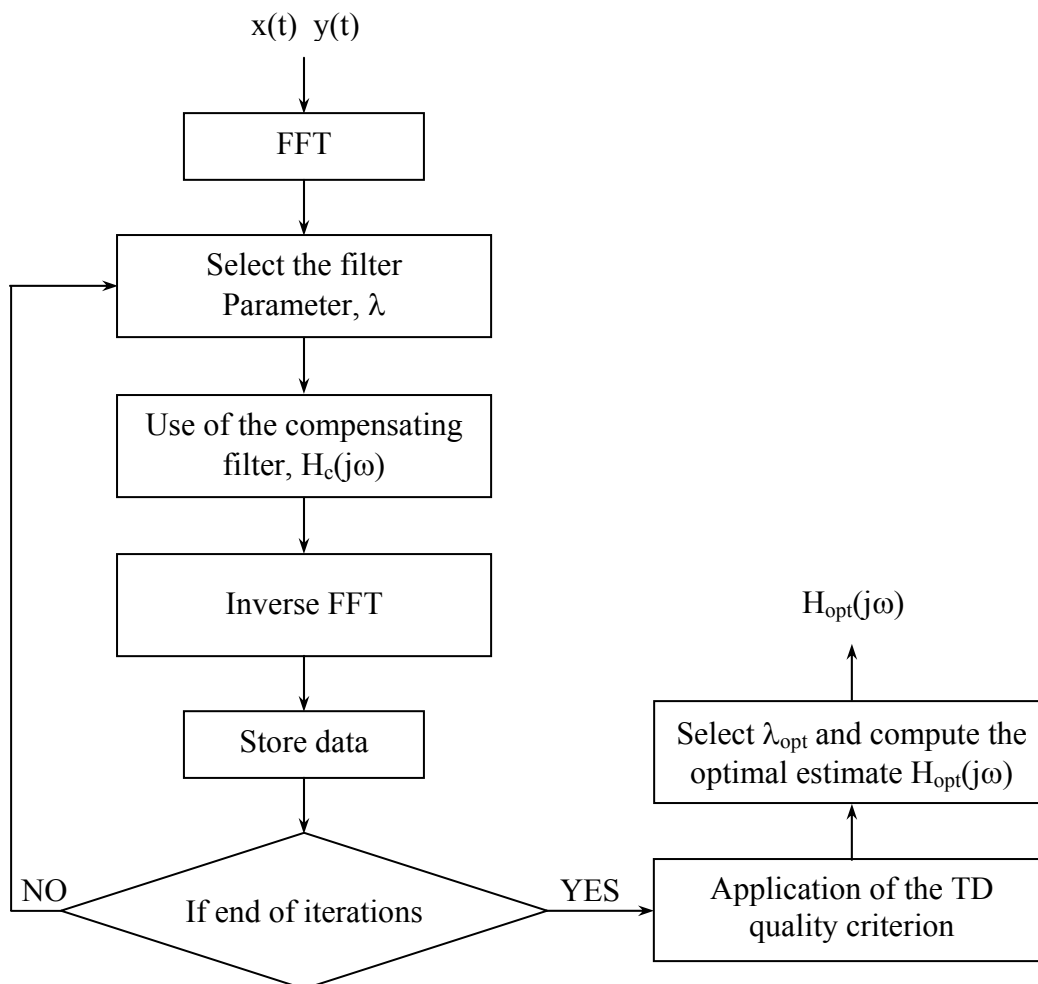


*Figure 2-3: Algorithm of the time domain optimization techniques.*

### 2.6.1.1 Guillaume-Nahman Criterion

The Guillaume-Nahman technique is a heuristic approach using frequency domain regularization. The optimum deconvolution result is obtained by monitoring when the standard deviation of the imaginary portion of the estimated solution is minimal [24] after the inverse Fourier transform operation is applied.

When deconvolving, it is found that  $h_{est}(t)$  has an imaginary part. This imaginary part is due to the presence of noise and computational errors occurring due to the deconvolution process. The estimate of the deconvolution result can then be written as follows:

$$h_{est}(t, \lambda) = h_{est}^r(t, \lambda) + j h_{est}^i(t, \lambda). \quad (2-38)$$

The power of the imaginary part is used as a measure of the quality result. This criteria quantity is calculated as follows:

$$\sigma_i(\lambda) = \sqrt{\frac{1}{N} \sum_{k=0}^{N-1} \{h_{est}^i(t, \lambda) - E[h_{est}^i(t, \lambda)]\}^2}, \quad (2-39)$$

where  $E[\cdot]$  represents the mean value.

### 2.6.1.2 Riad-Parruck Criterion

The Riad-Parruck technique is an approach to find the optimum deconvolution solution for impulse response data [26]. A steplike waveform is derived by integrating the impulse response, which yields a waveform with much less noise content. The optimum deconvolution result is obtained when the empirical mean value and the empirical standard deviation of the tail portion of the step response satisfy certain conditions. The resulting solution is not unique, requiring some non-automated interactions after the conditions are satisfied.

The technique states that for a duration limited  $h(t)$ , a time,  $T_1$ , exist such that:

$$h(t) = 0, \quad t > T_1. \quad (2-40)$$

A step response,  $w(t)$ , which is obtained by integrating the impulse response, must be flat for  $t > T_1$ . Using frequency domain regularization, it is known that as  $\lambda$  increases, the step response,  $w(t)$ , leads to a very small error content.

The accuracy,  $A(\lambda)$ , and noise content,  $N(\lambda)$ , are defined for the current iterative estimate as:

$$A(\lambda) = \text{Average}[w_{est}(t)], \quad t > T_1, \text{ and} \quad (2-41)$$

$$N(\lambda) = \text{RMS}[w_{est}(t) - A(\lambda)], \quad t > T_1. \quad (2-42)$$

The optimum value for the iteration parameter,  $\lambda$ , can then be defined such that

$$\frac{A(0) - A(\lambda_{opt})}{A(0)} \ll 1, \quad (2-43)$$

and

$$N(\lambda_{opt}) \ll N(0). \quad (2-44)$$

### 2.6.1.3 Bertocco Criterion

Bertocco *et al.*'s technique is a criterion proposed for step-like input signals using a single parameter regularization technique [27]. The technique is based on the idea that the output error introduced through deconvolution is uniformly distributed over the entire data sequence. The technique divides the time interval into two sections for optimization comparison.

The technique also states that for a duration limited  $h(t)$ , a time,  $T_1$ , exist such that:

$$h(t) = 0, \quad t > T_1. \quad (2-45)$$

The function, which gives the average squared output used in the technique's quality criteria, is given as follows:

$$\sigma(j, k) = \frac{1}{k - j + 1} \sum_{n=j}^k \{y_{est}(nT) - \hat{y}_{est}(nT)\}^2, \quad (2-46)$$

given in the interval from  $jT \leq nT \leq kT$ .

The average squared output is calculated at the front and tail end of the signal as the optimization parameter,  $\lambda$ , is modified. The optimum condition occurs when the two average squared error calculations are equal or

$$\sigma(0, L-1) = \sigma(L, N-1), \quad (2-47)$$

where  $\sigma(0, L-1)$  and  $\sigma(L, N-1)$  are the front and tail end of the average squared error, respectively, around point,  $L$ .

### 2.6.1.4 Youman Criterion

Youman *et al.*'s technique is a filtering technique used to smooth noisy data by implementing an adaptive, low pass filter [28]. The technique is based on the idea that when the randomness of the error signal reaches a maximum, the optimum deconvolution solution has been achieved. The noisy data can be written in discrete form as

$$x(n) = x_s(n) + x_n(n), \quad n = 0, 1, \dots, N-1, \quad (2-48)$$

where  $x_s$  is the noise-free signal and  $x_n$  is the noise sequence.

An estimate of the noise-free signal can be obtained by using the complex Fourier series expansion as follows:

$$x'_s = \sum_{k=0}^{M-1} C_m \exp\left[-j\left(\frac{2\pi mn}{N}\right)\right], \quad (2-49)$$

where  $M$  is the order of the harmonic expansion and  $C_m$  are the truncated complex Fourier series coefficients. The order is systematically increased and the serial correlation coefficients are calculated during each interval. The optimum order occurs whenever the randomness of the correlation of the error signal reaches a maximum.

## 2.6.2 Frequency Domain Optimization Criteria

The optimization criterion in the frequency domain establishes a technique for the selection of the iteration parameter. The application of the frequency domain optimization techniques partitions the transfer function into several frequency intervals to allow detection of the level of noise reduction and, if any, the level of signal distortion within each interval. The standard deviations of the magnitude of the transfer function within each of the intervals are monitored as the iteration parameter is varied. A criterion based on the standard deviation information is then used to select the optimum value for the iteration parameter. The optimum value will be determined by investigating the signal distortion and noise reduction within the different frequency bands as the iteration parameter is varied.

A model algorithm of the time domain optimization technique is given in *Figure 2-4*. The time domain functions of the measured input and output signals are transformed into the frequency domain by the Fourier transform operation. The functions are processed by the compensating filter and, in contrast to the time domain technique, the functions remain in the

frequency domain eliminating the use of the inverse Fourier transform. The data is stored for each of the different values of filter parameters. After each of the filter parameters selected are processed, the application of the frequency domain quality criteria are performed for each of the filter parameters. The optimal filter parameter is selected, and hence, the optimal estimate of the deconvolution solution,  $H_{opt}(j\omega)$ , can be calculated. Surveys of two of the frequency domain quality criteria are described below.

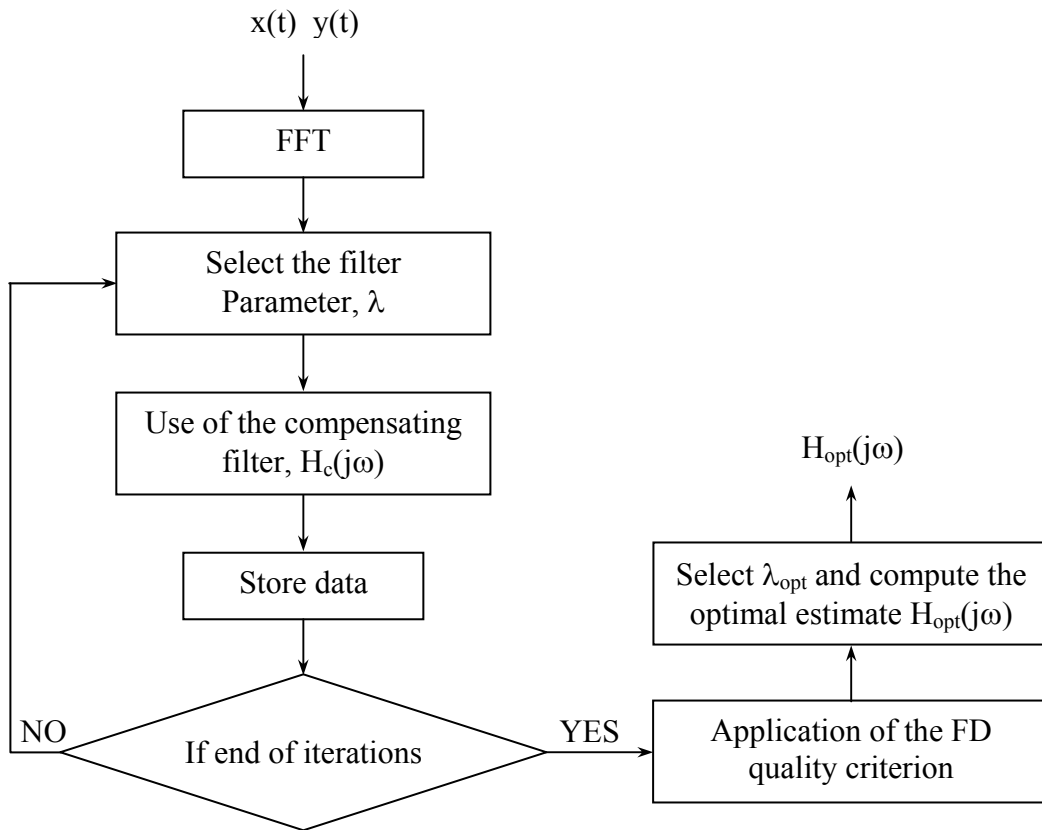


Figure 2-4: Algorithm of the frequency domain optimization techniques.

### 2.6.2.1 Riad-Bennia Criterion

The Riad-Bennia criterion employs the optimal compensation filtering technique discussed in an earlier section. The frequency range can be separated into different regions with various signal to noise ratios. The frequency range is divided into several frequency bands, in order to monitor the degree of noise reduction reached in each of the regions (not necessarily equal size). The criteria quantity is defined as the standard deviation of the transfer function

obtained for an optimal compensation filter parameter,  $\lambda$ , from the transfer function over the same interval with no filtering,  $\lambda=0$ . The standard deviation is defined over the  $i^{th}$  interval of frequency bands as follows [29]:

$$\sigma_i(\lambda) = RMS_i \left\{ \left| H^\lambda(j\omega) - H^0(j\omega) \right| \right\}, \quad (2-50)$$

where  $RMS_i$  refers to the root-mean-square operation over the  $i$ th frequency interval,  $H_\lambda(j\omega)$  is the transfer function obtained for a given  $\lambda$ , and  $H_0(j\omega)$  is the transfer function obtained for  $\lambda=0$ .

The choice of the optimum value is a compromise between avoiding signal distortion and attenuating the noise level in the frequency range of interest.

### 2.6.2.2 Extended Riad-Bennia Criterion

The Extended Riad-Bennia criterion employs both the optimal compensation filtering technique and the regularization technique, which were discussed in an earlier section. The process of partitioning the transfer function into different frequency bands still holds true in this technique. The criteria quantity is defined as the standard deviation of the transfer function obtained for an optimal compensation filter parameter,  $\lambda$ , and the regularization filter parameter,  $\gamma$ , from the transfer function over the same interval with no filtering,  $\lambda=0$ ,  $\gamma=0$ . The standard deviation is defined over the  $i^{th}$  interval of frequency bands as follows [30]:

$$\sigma_i(\lambda, \gamma) = RMS_i \left\{ \left| H(j\omega) [F(f, \lambda, \gamma) - F(f, \lambda_{min}, \gamma_{min})] \right| \right\}, \quad (2-51)$$

where  $RMS_i$  refers to the root-mean-square operation over the  $i$ th frequency interval,  $H_\lambda(j\omega)$  is the transfer function obtained for a given  $\lambda$ , and  $H_0(j\omega)$  is the transfer function obtained for  $\lambda=0$ ,  $\gamma=0$ , and initial values are  $\lambda_{min} \approx 0.0001\lambda_{init}$  and  $\gamma_{min} \approx 0.0001\gamma_{init}$ .

The choice of the optimum value is again a compromise between avoiding signal distortion and attenuating the noise level in the frequency range of interest.

## 2.7 De-embedding Schemes

De-embedding is a mathematical inverse operation that is used to remove the effects of a measured (or known) portion of a system to reveal the characteristics (or response) of the remainder of the system, which are typically referenced by, but not limited to, scattering parameters. De-embedding techniques, as with deconvolution techniques, can be applied in both

the frequency and time domains. Time and frequency domain data can also be de-embedded in the frequency and time domains, respectively, through the use of the Fourier and inverse Fourier transforms. The general frequency domain procedure will be developed and followed by an application towards network topology identification. Following the frequency domain discussion, the time domain procedure will be presented.

### 2.7.1 Frequency Domain De-embedding

Frequency domain de-embedding is produced by multiplying the inverse matrix of the desired change (calibration parameters, known system parameters, noise parameters, etc.) to the actual measurements resulting in an adjustment of the measurements [31]. Scattering parameters of the portion of the system may be obtained through processes such as measurement, system recognition, calculation from analytical models, or software simulation. In the next section, an application of the frequency de-embedding technique applied to network system identification is presented.

#### 2.7.1.1 Peeling-Type De-embedding Approach

The peeling-type de-embedding technique is the process of removing known segments (layers) of an unknown topology of a device or system. Once a set of identified segments is removed, the process can be repeated until the entire device or system is identified. All aspects of the segments to be removed need be accurately identified and modeled due to errors that will accumulate throughout the process, which will eventually cause the process to fail.

One method of the de-embedding process involves using the reflection coefficient of the entire network and the calculated S-parameters of the identified segment to obtain the loading reflection coefficient, or the reflection coefficient of the entire network excluding the identified segment. *Figure 2-5* shows a visual representation of the signal flowgraph using a scattering parameter, or S-parameter, model for each segment and the corresponding reflection coefficients encountered at each junction. Each segment of the network is represented by a set of S-parameters. The flowgraph also shows the interconnections of the segments.

This type of approach will be very useful in the system identification problem of the DSL subscriber loops. A general overview of this method will be presented followed by specific application to the DSL subscriber loops in the following chapter.

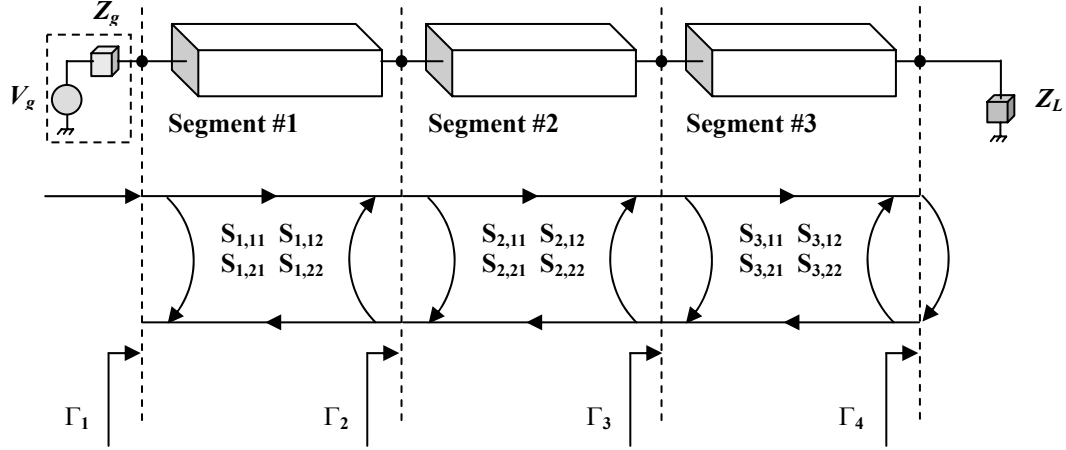


Figure 2-5: Reflection coefficients and S-parameters of a multi-segment line.

The loading reflection coefficient of the first segment is related to the measured reflection coefficient of the entire network loop and the identified S-parameters of the first line by the following equation:

$$\Gamma_i = S_{i,11} + \frac{S_{i,12}S_{i,21}\Gamma_{i+1}}{1 - S_{i,22}\Gamma_{i+1}}. \quad (2-52)$$

Rearranging Equation (2-52) for the loading reflection coefficient, we have the following solution:

$$\Gamma_{i+1} = \frac{S_{i,11} - \Gamma_i}{S_{i,22}(S_{i,11} - \Gamma_i) - S_{i,21}S_{i,12}}. \quad (2-53)$$

The frequency domain information of the network is processed and used in the de-embedding procedure. An example of removing a layer from a network topology consisting of series segments will now be presented. The S-parameters of the segment will be developed or measured making use of characteristics of the segment. The process of removing an identified segment is illustrated in *Figure 2-6*. The reflection coefficient is defined as the amplitude of the reflected voltage wave normalized to the amplitude of the incident voltage wave. The reflection coefficient,  $\Gamma$ , is a function of the source impedance,  $Z_g$  and the frequency domain input impedance,  $Z_{in\_loop}$ :

$$\Gamma = \frac{Z_{in\_loop} - Z_s}{Z_{in\_loop} + Z_s}. \quad (2-54)$$

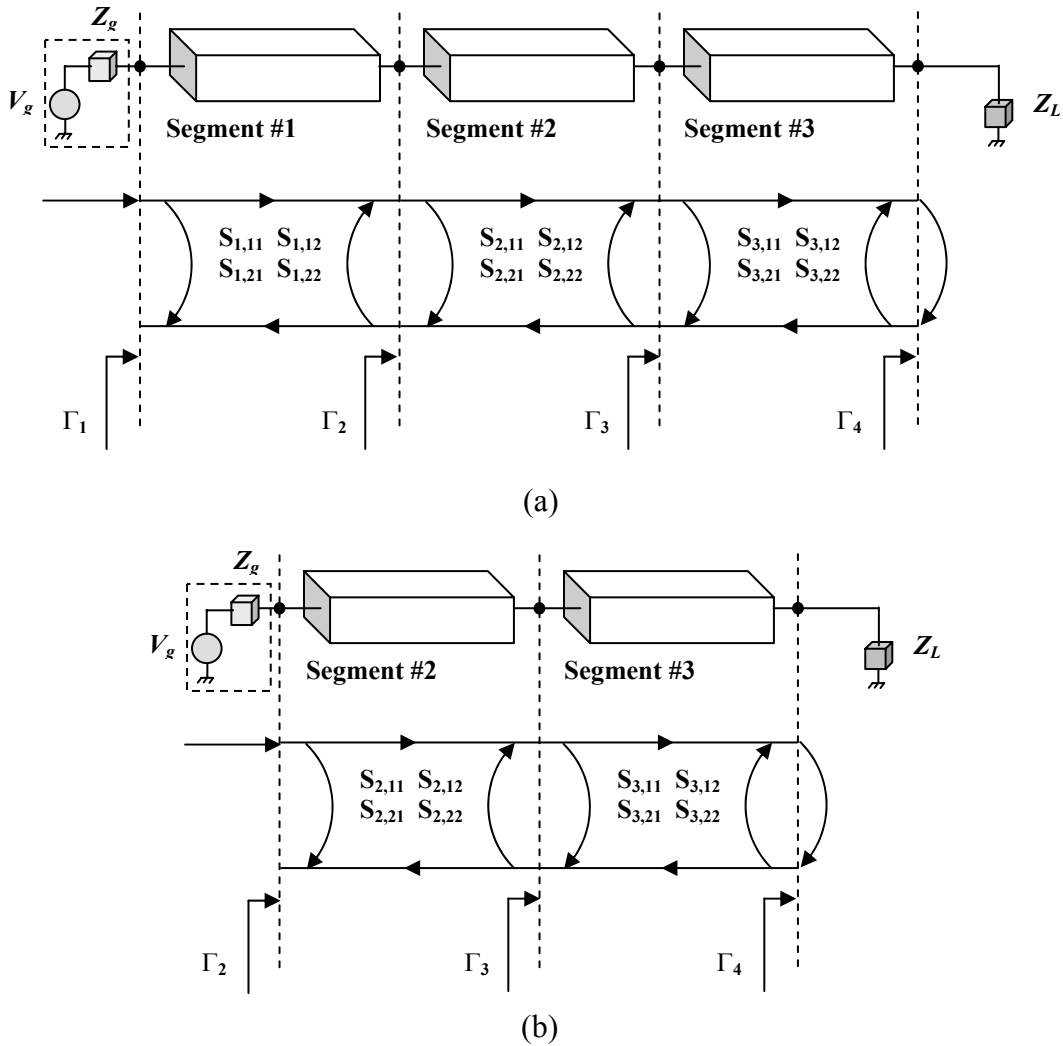


Figure 2-6: (a) Visualization of de-embedding process involving a single segment (b) Result after de-embedding process is completed.

Following the calculation of the reflection coefficient, the impulse (TDR) response of the network can be generated and the detection of the two-port scattering parameters is developed through a series of measurements or algorithms based on characteristics of the device. The S-parameters of the identified segment are used to calculate the loading reflection coefficient (2-53), and in turn the impulse response of the remaining network can be obtained and the process continued until all segments are identified. In the case of the DSL subscriber loops, some challenges could arise with identified bridge taps as they differ from the series nature of the example shown above. These challenges will be address in the following chapter.

### 2.7.2 Time Domain De-embedding

Time domain de-embedding is performed using a calibrated system of a high-speed automatic measurement system, such as a time domain reflectometry measurement system. In this type of system, real time measurements are performed and any perturbations of the device under test will be measured and extracted from the non-perturbed, or calibrated, measurement [32]. Time domain gating may also be employed to include only desired reflections occurring in the measured waveform. When a scan encompasses a single reflection, the specific gated waveform represents a reflection coefficient. Using the Fourier transform operation to transform the gated waveform into the frequency domain produces the reflection response of interest.

## 2.8 Comparison of Frequency and Time Domain Synthesis Schemes

The decision of whether the de-embedding or deconvolution is performed in the frequency or time domain is application and resource specific. There are advantages and disadvantages to the use of each method, which will be discussed in this section.

### 2.8.1 Time Domain Deconvolution

As mentioned previously, the time domain method produces  $h(t)$  by solving a set of linear simultaneous equations which is formed by using discrete sequence representations of the time functions. The advantages of this method will be presented followed by the disadvantages.

#### *Advantages*

- 1) The time domain methods presented in earlier sections of this solution are techniques that operate directly on the time domain data. The advantage of performing the convolution in the time domain is a reduction of error caused by the Fourier and inverse Fourier transform operations (algorithm and data processing).
- 2) The application of filters in the frequency domain as well as the Fourier transform errors could cause a non-causal response and instability. Time domain deconvolution can more easily achieve a causal and stable nature of the signal.
- 3) Another advantage is that the properties of the signal can be visualized during the iterative process. After each iteration (or series of iterations) the signal can be monitored to assist in choosing the optimum solution.

*Disadvantages*

- 1) The number of iterations could be immense until convergence is reached, as well as the number of calculations needed for comparison of the estimates, if the data being deconvolved is substantially large. With the applications consisting of large data point sequences requiring large amounts of calculations, the time domain applications would not be very practical in these situations.
- 2) As mentioned in the earlier sections, convergence is not always obtainable through time domain methods. Without modifications, the Bracewell's conditions for convergence may not be able to be met using time domain techniques.
- 3) A disadvantage, which is correlated to the initial disadvantage listed, is that the time domain techniques are very computationally extensive. The computational time it would take to iterate and compare for accurate results may not be justified in comparison with the accuracy obtained over more time efficient frequency domain methods.

**2.8.2 Frequency Domain Deconvolution**

Also mentioned previously, the frequency domain method arises from the optimization of a filtering process used for noise reduction. The optimum filter interpolates  $H_m(j\omega)$  at the zeros of  $X_m(j\omega)$ , where it is indeterminate, to yield  $H_{opt}(j\omega)$ , an acceptable estimate of  $H(j\omega)$ .

*Advantages*

- 1) One advantage of the frequency domain techniques was shown previously when the criteria for selecting the optimum filter parameter was by monitoring the spectral distribution of signal and noise. This process is a result of using a Wiener filter type of solution.
- 2) The algorithms of the frequency domain deconvolution are fairly simple and the iterative routines are easily implemented. This method allows for a choice of optimum solutions through an investigation of the noise and signal indicators used in the optimization routines. This gives a higher degree of freedom to the user on the topic of compromise between signal information and noise content.

3) In the case of optimization, the frequency domain method allows for convenient noise reduction algorithms to be used. Filtering algorithms may be application specific and can be easily implemented using frequency domain techniques.

### *Disadvantages*

1) One main disadvantage to performing deconvolution in the frequency domain is that the technique operates on transformed data when time domain data is available, which adds Fourier transform operator errors into the solution.

2) A wide variety of filtering methods have been proposed and their results are not always causal. The transforms and optimization routines can also have an ill effect on causality. This differs from the time domain techniques, whose output remains causal and stable. Both causality and stability of the synthesis problem are described in the following section.

3) Bandwidth limitations in the frequency domain prevent a portion of the spectral information in carrying over from the time domain. This limitation basically transforms as a truncation in the frequency domain, which may cause loss of signal information in the higher frequencies spectra. The effects of the loss of signal information can be viewed as a form of distortion.

## **2.9 Realizability Limitations and Accuracy of the Synthesis Problem**

In many practical applications the excitation response,  $x(t)$ , and the resulting system response,  $y(t)$ , are known. In these cases, the impulse response of the network or device under test,  $h(t)$ , is obtained through deconvolution techniques. After the deconvolution process has been applied to the pair of signals,  $x(t)$  and  $y(t)$ , the resulting impulse response,  $h(t)$ , must be checked for stability, realizability, causality, and accuracy (acceptable results) [33]. These characteristics of the resulting impulse response are reviewed, and the limiting factors are identified. In some cases, solutions to the identified limiting factors are proposed.

### **2.9.1 Causality and Stability of Synthesis Problems**

Before the excitation is applied to the network, it is assumed that the system is idle, or that the system response,  $y(t)$ , cannot be nonzero before the excitation response,  $x(t)$ , commences (becomes nonzero). This is the causal property one would expect of a network.

It was documented in [34] that in order for a network to be stable, it should not have any finite response when no excitation is applied to it, or

$$y(t) \equiv 0, \quad \text{for } x(t) \equiv 0. \quad (2-60)$$

For stability in the frequency domain, the necessary and sufficient condition for a network to be stable is that the network function has no right-half plane poles or poles positioned on the vertical axis. This condition can be written in the time domain as

$$\int_0^{\infty} |h(t)| dt < \infty. \quad (2-61)$$

The equation in (2-61) states that for  $x(t)$  and  $y(t)$  to be stable, their corresponding impulse response,  $h(t)$ , must be absolutely integrable.

### 2.9.2 Realizability of Synthesis Problems

The term realizability can be defined as whether  $h(t)$  (assuming stability) can be realized by a certain class of linear networks [33]. The realizability criteria of various classes of linear systems are well formulated in the frequency domain. Therefore the time domain synthesis problem will be transformed into the frequency domain for realizability consideration. A requirement for all classes of linear systems to be stable and realizable in the frequency domain is that  $H(j\omega)$  be a rational function with no right-half plane pole or multiple poles on the vertical axis.

This limits  $h(t)$  to have term of only the following type:

$$\left( A_0 + A_1 t + A_2 t^2 + \dots + A_n t^n \right) \exp(s_v t), \quad (2-62)$$

where

$$s_v = \sigma_v + j\omega_v, \quad \sigma_v \leq 0; \quad n = 0, \text{ if } \sigma_v = 0. \quad (2-63)$$

If  $h(t)$  contains terms that do not meet this restriction, then a stable network that will realize  $h(t)$  is not possible. If this occurs, an alternative is to find another estimate to the system impulse response,  $h(t)$ , that is realizable.

A rational function may be written as follows:

$$F(s) = \frac{a_m s^m + a_{m-1} s^{m-1} + \cdots + a_1 s + a_0}{b_n s^n + b_{n-1} s^{n-1} + \cdots + b_1 s + b_0}, \quad (2-64)$$

or

$$F(s) = K \frac{(s - s_{z1})(s - s_{z2}) \cdots (s - s_{zm})}{(s - s_{p1})(s - s_{p2}) \cdots (s - s_{pn})}, \quad (2-65)$$

where all of the coefficients of  $s$  are real. It is important to note that the polynomial expression may not be physically realizable or the order may be extremely large. Having some physical insight to the synthesis problem may allow the development of a different representation of the system.

It is necessary to first find a realizable rational approximation to a given sequence of data. Network functions, defined as the ratio of a response transform to an excitation transform, are analytic functions of a complex variable, and hence their real and imaginary parts are related by the Cauchy-Rieman relationship. For  $s = \sigma + j\omega$  and with  $F(s)$  written as  $R(\sigma, \omega) + jX(\sigma, \omega)$ , the relationship is defined as follows:

$$\frac{\partial R}{\partial \sigma} = \frac{\partial X}{\partial \omega}, \text{ and} \quad (2-66)$$

$$\frac{\partial X}{\partial \sigma} = -\frac{\partial R}{\partial \omega}. \quad (2-67)$$

The equations in (2-66) and (2-67) are implicit relationships and do not imply explicit formulas for computing one component from another. The relationships between the parts of a network function are well known in mathematics as Hilbert transforms.

By use of Cauchy's integral formula, given as:

$$F(s) = \frac{1}{j2\omega} \oint_C \frac{F(z)}{z - s} dz. \quad (2-68)$$

The relationships between the real and imaginary parts are as follows:

$$R(\omega) = R(\infty) = \frac{2}{\pi} \int_0^{\infty} \frac{\omega' X(\omega') - \omega X(\omega)}{\omega'^2 - \omega^2} d\omega', \text{ and} \quad (2-69)$$

$$X(\omega) = \frac{2\omega}{\pi} \int_0^{\infty} \frac{R(\omega') - R(\omega)}{\omega'^2 - \omega^2} d\omega' . \quad (2-70)$$

An important feature of the results established in [38] is the fact that it is not necessary to have the real (or imaginary) part as a realizable rational function. Corresponding to any given real part, whether in analytical or graphical form, an imaginary part can be computed from the integral.

Some of the identified problems associated with the characteristics mentioned above as well as accuracy in the deconvolution process will be presented in the next section. In some cases, methods of resolving or limiting the errors are presented.

### 2.9.3 Identified Limiting Factors

It has been explained in subsequent sections that the effects of small quantities of noise and error can have an undesirable effect on the results of the time and frequency domain deconvolution. Identified below are possible sources of these errors separated into measurement errors and limitations as well as sampling and computational errors and limitations.

#### 2.9.3.1 Measurement Errors

- 1) Imperfections of the system components used in the measurement process can result in errors. As an example, the calibration of the measurement system may require some type of interfacing with the system under test. The identical interfacing used to allow for the calibration standards will also be used to connect the system under test to the measurement system. Some effects of this interfacing will be included as part of the system components as an imperfection. Other imperfections could force a proposed deconvolution technique not to converge, or become unstable as the iterative process proceeds.
- 2) Another systematic measurement error, which is always common in measurements, is the noise content of the measured waveforms. Noise can result from imperfections in the calibration or from the effects of not calibrating all of the system error components within the system. Noise can also be introduced from external sources near the measurement system or the system under test. The effects of the noise can be seen, as described in earlier sections, as spurious components produced by the deconvolution routine.

3) The final identified measurement error seen, as a limiting factor in the synthesis problem, are the limitations of the measurement system. In the case of a transient signal with a wide bandwidth, if the bandwidth of the measurement equipment (waveform detector) is not large enough to obtain all of the relevant signal information, the observed waveform will be a distorted version of the actual signal, limiting the accuracy of the synthesis problem and possibility causing realizability errors as well as stability and causality problems. Limited dynamic range, sampling (or digitization) errors, and other limitations can also be restrictive factors in the synthesis problem.

### 2.9.3.2 Sampling and Digitization Errors

Discrete time signals used in deconvolution schemes most commonly occur as representations of sampled continuous time signals. The phenomenon of aliasing, which occurs when the sampling rate is insufficient or the signal is not bandlimited, will be presented [35].

Periodic sampling is a typical method of obtaining discrete time representation of a continuous time signal. A sequence of samples,  $x[n]$ , is obtained from a continuous time signal,  $x_c[n]$ , as

$$x[n] = x_c[nT], \quad -\infty < n < \infty, \quad (2-71)$$

where  $T$  is the sampling frequency and its reciprocal,  $f_s = 1 / T$ , is the sampling frequency in samples per second. A block diagram of this process, referred to as an ideal continuous-to-discrete-time (C/D) converter, is shown in *Figure 2-7*.

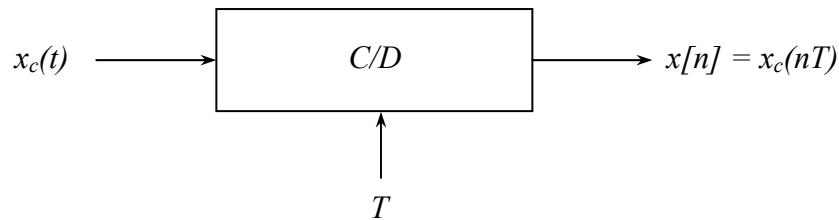


*Figure 2-7: Block diagram for an ideal C/D converter.*

Converting the frequency domain relationship of the output of an ideal C/D converter as described by (2-71) gives the following:

$$X(j\omega) = \frac{1}{T} \sum_{k=-\infty}^{\infty} X_c[j(\omega - k\omega_s)]. \quad (2-72)$$

where  $\omega_s$  is the sampling frequency in rads/s.

The result of  $H(j\omega)$  assumes a bandlimited Fourier transform whose highest nonzero frequency component is  $\omega_n$ . To prevent overlapping, it is obvious that the sampling frequency,  $\omega_s$ , would have to be twice the highest frequency component,  $\omega_n$ . The frequency,  $\omega_n$ , is commonly referred to as the Nyquist frequency and the frequency,  $2\omega_n$ , that must be exceeded by the sampling frequency is termed the Nyquist rate.

Aliasing, or fold-over errors are caused by not having a bandlimited signal, which causes  $\omega_n$  to be undefined, or sampled below the Nyquist rate which causes overlapping, and in turn an unrecoverable signal.

### 2.9.3.3 Signal Processing and Computational Errors

- 1) Quantization is an effect of transforming an analog signal to a digital signal, or quantized samples. In the case of using an ideal C/D converter, each sample is known with infinite precision, but in actual measurements, which make use of an analog-to-digital (A/D) converter, each sample will not have infinite precision. This is because the A/D converter is a physical device that converts a voltage or current amplitude at its input into a digital code representing a quantized amplitude closest to the amplitude of the input. Each time the input is sampled, the signal amplitude at that point is converted to the closest quantization level and held until the next sample is taken. This results in a step like waveform representation of the actual signal, the difference between these signals is referred to as the quantization error and could have an effect in the synthesis problem.
- 2) Numerical computational errors such as truncation and system limitation could also be causes of error in the synthesis problem. Even with the increasing power of computational devices, these errors could still cause potential difficulty.
- 3) Signal averaging is commonly used in measurement equipment to average out any of the time-varying components. Even though signal averaging is an acceptable method to reduce time-varying noise, it is not able to remove all aspects of the time-variations, which could lead to difficulties in the synthesis problem.
- 4) The effects of noise reduction filters were mentioned in previous sections and must be applied with acknowledgment of the destructive effects it could have on the signal. It is

important to monitor performance indicators while applying noise reduction filter, the optimum value between signal degradation and noise reduction is a subjective decision and a cause for errors leading to ill-effects in the synthesis problem.

5) Leakage errors are a redistribution of energy due to data windowing, which result from the Fourier or inverse Fourier transforms. Leakage error occurs when the values on each side of the time or frequency domain window are not continuous before performing the transformation operation. These discontinuities are normally caused by windowing of obtained data or by the time duration limitation or bandwidth limitation of the measurement equipment. Some solutions to leakage errors are found in the following section.

### 2.9.4 Solutions to Truncation Discontinuities (Leakage Errors)

Techniques have been developed to reduce the effects of leakage error when transforming data using the Fourier or inverse Fourier transforms when the data has discontinuous endpoints. In this section, two techniques for leakage error reduction will be presented.

#### 2.9.4.1 Nicolson-Ramp Method

The Nicolson method subtracts a ramp from the acquired data resulting in a waveform resulting in the two ends of the data sequence being continuous shown in *Figure 2-8* [36].

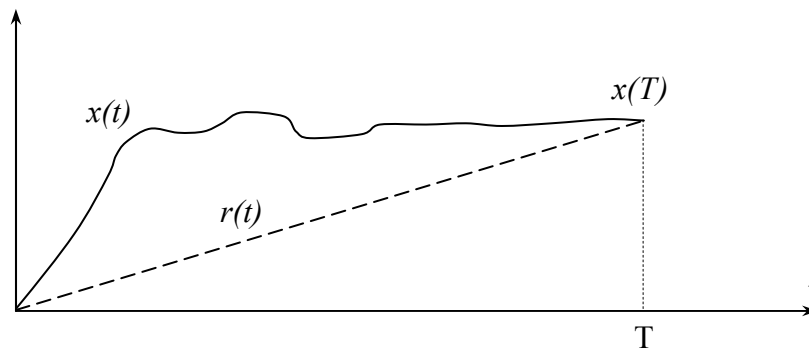


*Figure 2-8: Nicolson Ramp method for leakage error correction.*

The ramp,  $r(t)$ , is defined as

$$r(t) = \frac{x(T)}{T} t (u(t) - u(t - T)) \quad (2-73)$$

After subtraction, shown in *Figure 2-9*, the following result is obtained

$$x_2(t) = (x(t) - r(t))(u(t) - u(t - T)) \quad (2-74)$$

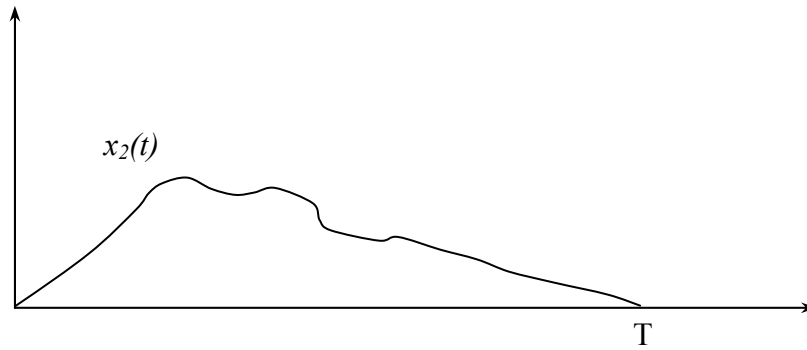


Figure 2-9: Nicolson Ramp method after subtraction

After applying the Fourier transform operator on  $x_2(t)$ , we obtain the transform of the original signal,  $X(j\omega)$ . The effects of the ramp are cancelled due to the odd harmonic content of the transformation of the ramp being combined with the zeros from the Nicolson method.

### 2.9.4.2 Nahman-Gans Method

The Nahman-Gans method consists of negating the signal and delaying the negated version by  $N$  points, and adding it to the original data sequence, see Figure 2-10 [37].

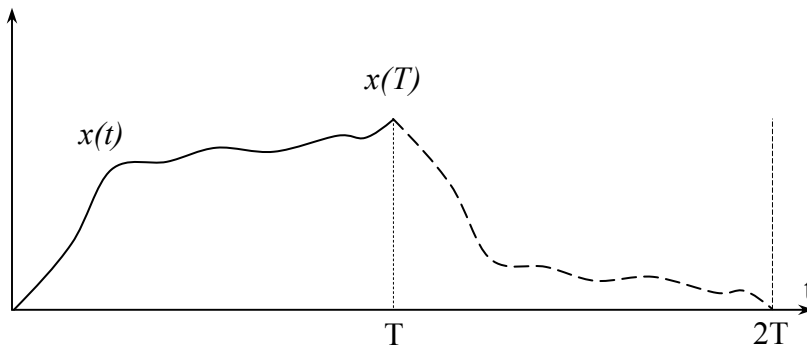


Figure 2-10: Nahman-Gans method for leakage error correction.

The resulting waveform is defined as

$$x_2(t) = x(t)(u(t) - u(t - T)) + (x(T) - x(t - T))(u(t - T) - u(t - 2T)) \quad (2-75)$$

The Nahman-Gans method results in the dc term and the odd harmonics of the Fourier transform solution.

## **Chapter 3**

### **Layer De-Embedding Scheme Applied to DSL Subscriber Loops**

#### **3 Introduction**

This chapter describes the original work on the time-domain network loop reconstruction algorithm. First, a global view of the entire reconstruction process will be presented; this will help the reader to understand the general flow of the algorithm as well as the reconstruction strategy. The subsequent sections present the secondary processes that run within the algorithm such as length estimation, structure/gauge identification, length refinement, and deconvolution filtering, with a focus on their implementation, theoretical background, and illustrations. Detailed flowcharts of the overall reconstruction process are presented in Appendix B. Also included with the flowcharts are comments to assist the understanding of certain topics.

In the early stages of using a time-domain based algorithm for network loop reconstruction, the causality of the models for twisted pair cables used within the algorithm was a limiting factor. In Chapter 4 new models will be presented and incorporated into the algorithm, and the results showed this method to be indeed viable.

#### **3.1 Overall Reconstruction Procedure**

The time-domain network loop reconstruction algorithm presented in this report focuses on the physical attributes of the problem. The physical attributes and phenomenon of these cables are used to accurately identify cabling structures without the application of a trial-and-error type

approach. The time-domain algorithm uses a single iteration to identify a network node based on the Time Domain Reflectometry (TDR) response of the network. Multiple iterations will be used in the length refinement routine and the deconvolution noise reduction routine. The identification of a network node in the time-domain algorithm consists of:

- Initial segment(s) identification through the use of database matching,
- Initial length estimation based on identified segment(s) gauge(s),
- De-embedding of identified segment(s) and the application of length refinement, and
- Iterative bridge-tap identification methods.

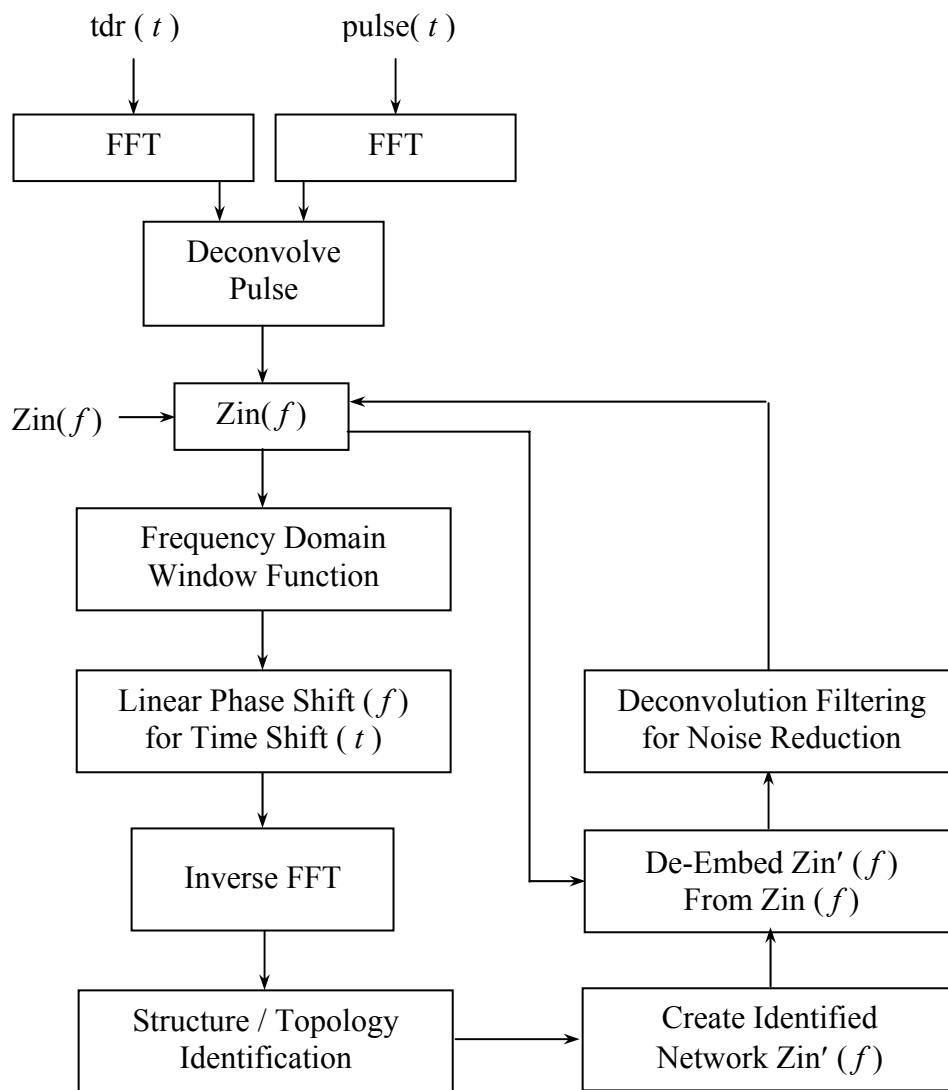


Figure 3-1: Flow chart showing the process of the time-domain reconstruction algorithm.

In this algorithm, segment identification precedes the length estimation; knowing the gauge(s) before proceeding with length estimation produces more accurate initial length estimations. The length estimation will then be refined through iterative techniques to minimize deconvolution noise. After deconvolution of identified segments, the process then determines the remaining topology and proceeds until all segments are identified. A flow chart showing the general procedure of the time-domain network reconstruction algorithm is shown in *Figure 3-1*.

The top-level algorithm is structured as follows:

- Step 1:** *Data pre-processing.* The algorithm begins processing on a frequency domain measurement of the input impedance of the network. The algorithm can accept the frequency domain input impedance directly or pre-process the TDR response along with the input pulse to obtain the frequency domain input impedance. (Appendix C outlines the methods of performing measurements in the time or frequency domains.)
- Step 2:** *Model initialization.* Create an empty network model (no segments; containing only the measurement node). Set the current node as the measurement node.
- Step 3:** *Window Function.* Apply a window function to the frequency domain input impedance. Incorporate a linear phase shift into the windowed result (based on the window independently) producing a shift the TDR waveform. This starts the TDR waveform at a known reference voltage and exposes the rising edge of the input pulse for gauge identification and length estimation references.
- Step 4:** *Nodal Structure Identification.* Using the database matching technique of the TDR waveform, identification of the current node's topology is identified. The gauges of the identified segments are noted. If no segment is found, EXIT.
- Step 5:** *Length Estimation.* Using a time delay / linear phase technique, the length estimation of the next shortest segment is identified using the TDR waveform and the identified gauge information. Application of this length could be applied to proceed further down the unknown topology or possibly applied to previously identified bridge taps of excessive length (Discussed in Section 3.4.1.3). If a single segment was detected in Step 4, the model is updated.

- Step 6:** *Topology Determination.* This is a procedure to determine the topology in the case of bridge-taps. Once the topology is determined, the result is documented within the algorithm. Depending on the result, infinite line segments may occur and will be dealt with using an iterative process the each time through the algorithm loop. The model is updated.
- Step 7:** *De-embedding Process.* The de-embedding process uses the detected gauge(s) and the length estimation already placed in the updated model to produce *ABCD* parameters of the identified topology. These two port parameters are used in conjunction with the initial frequency domain input impedance measurement to create a new input impedance consisting of the remaining network.
- Step 8:** *Noise Reduction Process.* The de-embedding procedure produces high frequency noise. This noise must be iteratively reduced to continue the algorithm to completion. Also contained in the noise reduction process is length refinement. Errors in length estimation cause noise in the de-embedding process, so iterative length refinement is included in this step. Return to Step 3.

There are two main areas of concern when processing the time-domain algorithm. First, the number of data points<sup>1</sup> and the sampling frequency<sup>2</sup> of the measured data need to be substantially large enough to give a high level of resolution in the TDR waveform resulting in accurate gauge and length estimation. This area of concern will be mentioned throughout this dissertation. The second area of concern is the effectiveness of the noise reduction techniques and length refinement. Failure of these noise reduction techniques will result is a drastic limitation of the overall reconstruction algorithm.

### 3.2 De-Embedding Process Review

The “Layer De-Embedding” technique is the process of removing identified segments of an unknown topology of a network loop. Once a set of identified segments is removed, the process can be repeated until the entire network loop is identified. The process of removing an identified segment is illustrated in *Figure 3-2*.

<sup>1</sup> To reduce complexity, 32,768 data points were used to process the ideas mentioned in this report, limitations of varying numbers of data points will be investigated at a later time.

<sup>2</sup> A sampling frequency of 125 MHz was used in this report unless otherwise stated. Modifying the sampling frequency will change the resolution of the time scale of the TDR waveform.

The frequency domain information of the network loop is processed and used in the de-embedding procedure. The reflection coefficient,  $\Gamma$ , is a function of the source impedance,  $Z_s$  and the frequency domain input admittance,  $Z_{in\_loop}$ .

$$\Gamma = \frac{Z_{in\_loop} - Z_s}{Z_{in\_loop} + Z_s} \quad (3-1)$$

$H_{RTF}$ , or the reflection transfer function, is the voltage divider formed by the source impedance of the measurement system and the input impedance of the loop under test. This quantity is defined as follows:

$$H_{RTF} = \frac{Z_{in\_loop}}{Z_{in\_loop} + Z_s} \quad (3-2)$$

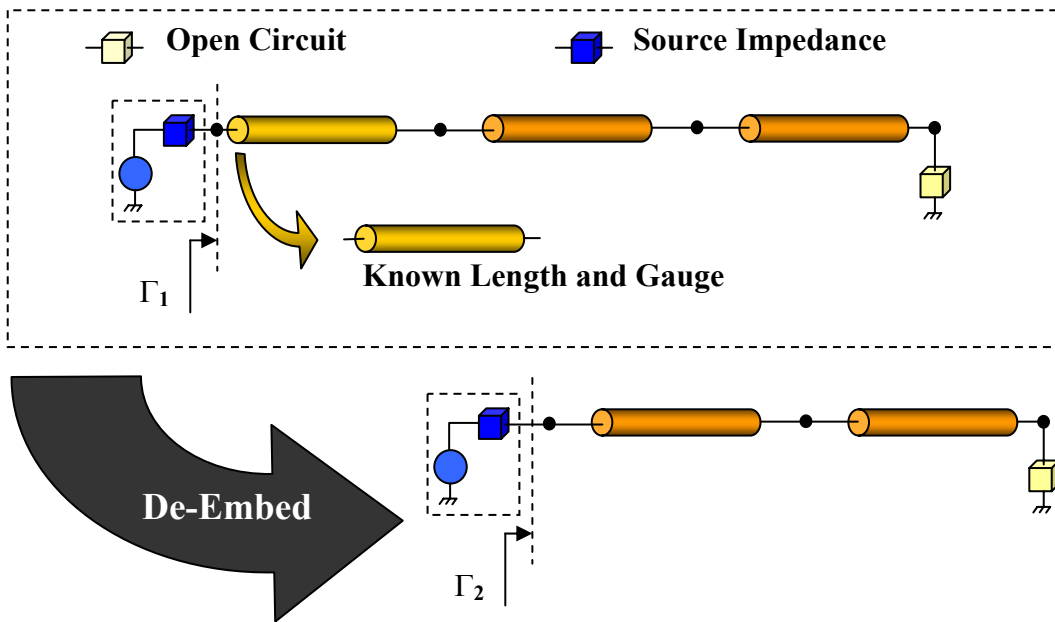


Figure 3-2: Visualization of de-embedding process involving a single segment<sup>3</sup>.

Following the calculation of the reflection coefficient, the impulse (TDR) response of the network loop is generated and the detection of the length and gauge of the segment closest to the generator is performed. This process is described in detail in later sections. The scattering

<sup>3</sup> The open circuit termination is used for illustrative purposes. The developed software contains code to account for any lumped element load.

parameters (S-parameters) or ABCD parameters of the identified segment will be calculated, using the detected length and gauge information, by use of the following equations (*Note:  $Z_o$  and  $\gamma$  are obtained through the gauge detection*):

$$\rho = \frac{Z_s - Z_o}{Z_s + Z_o}, \quad (3-3)$$

$$T = \exp(-\gamma\ell), \quad (3-4)$$

$$S_{11} = S_{22} = -\rho \frac{1 - T^2}{1 - \rho^2 T^2}, \text{ and} \quad (3-5)$$

$$S_{12} = S_{21} = T \frac{1 - \rho^2}{1 - \rho^2 T^2}. \quad (3-6)$$

The de-embedding process involves using the reflection coefficient of the entire network and the calculated S-parameters or ABCD<sup>4</sup> parameters of the identified segment to obtain the loading reflection coefficient, or the reflection coefficient of the entire network excluding the identified segment. *Figure 3-3* shows a visual representation of the signal flow graph using an S-parameter model for each segment showing the reflection coefficients at each junction.

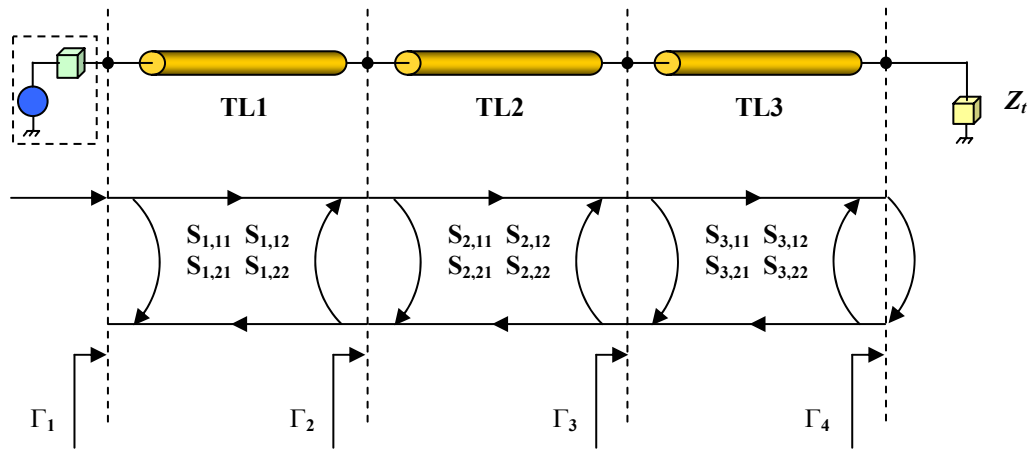


*Figure 3-3: Reflection coefficients and S-parameters of a multi-segment line.*

<sup>4</sup> It has been observed in noise reduction techniques that the ABCD calculations produce a lower amount calculation error than the S-parameter calculations, although S-parameters will be used in this chapter to define the process due to convenience.

The loading reflection coefficient of the first segment is related to the measured reflection coefficient of the entire network loop and the calculated S-parameters of the first line by the following equation:

$$\Gamma_i = S_{i,11} + \frac{S_{i,12}S_{i,21}\Gamma_{i+1}}{1 - S_{i,22}\Gamma_{i+1}}. \quad (3-7)$$

Rearrange (3-6) for the loading reflection coefficient, we have the following solution:

$$\Gamma_{i+1} = \frac{S_{i,11} - \Gamma_i}{S_{i,22}(S_{i,11} - \Gamma_i) - S_{i,21}S_{i,12}}. \quad (3-8)$$

The resulting updated frequency domain reflection transfer function,  $\tilde{H}_{RTF}$ , can be calculated from the loading reflection coefficient as follows:

$$\tilde{H}_{RTF} = \frac{\tilde{Z}_{in\_loop}}{\tilde{Z}_{in\_loop} + Z_s}, \text{ where } \tilde{Z}_{in\_loop} = Z_s \frac{1 + \Gamma_{i+1}}{1 - \Gamma_{i+1}}. \quad (3-9)$$

The de-embedding procedure allows one to process the identification routine on the node closest to the measurement equipment, which allows for higher levels of accuracy over trying to investigate the strongly degraded reflections due to attenuation and dispersion. The portion of the algorithm dealing with segment identification will be presented in the subsequent sections.

### 3.3 Windowing and Phase Shifting

The advantages of applying a window function and a linear phase shift in the frequency domain to the measured input impedance will be discussed in this section. The window will band limit the input impedance measurement and the linear phase shift in the frequency domain will result in a time delay of the waveform after the inverse Fourier transform is applied. These ideas will be discussed in detail in the following section. If time domain measurements are performed, pre-processing will need to take place before application of the window and phase shift; this topic will be addressed initially.

### 3.3.1 Pre-Processing of Time Domain Measurements

In the case that time-domain measurements are available instead of the frequency domain input impedance measurements, some pre-processing of the data will be required. Two time domain measurements are needed to extract the frequency domain input impedance; the input, or excitation pulse, and the output, or TDR response of the system. These two measurements will be processed in the frequency domain by using different degrees of filtering and iterative deconvolution schemes to extract the desired information. Candy, Clark, and Goodman explain this deconvolution procedure and list several references for the theory and application in [38] edited by Miller. Appendix C also presents some insight to the methods of time and frequency domain measurements.

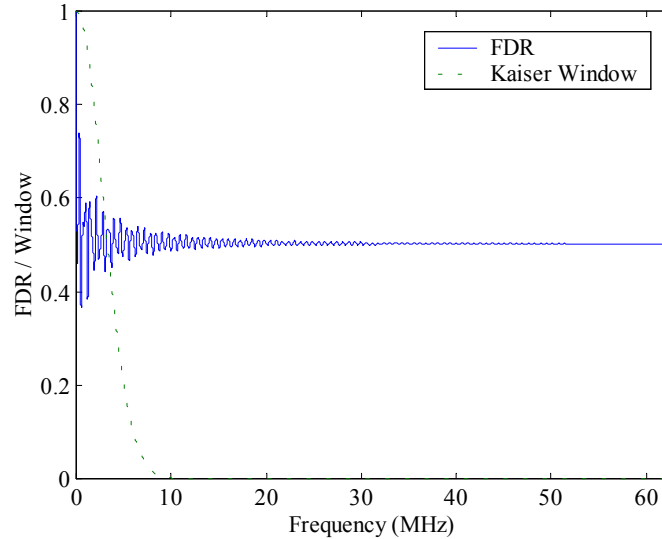
### 3.3.2 Windowing Functions

The process of windowing the frequency domain input impedance before application of the inverse Fourier transform results in two advantages. The first advantage results from the fact that the input impedance is not band limited. Applying the Fourier transform to a signal that is not band-limited results will result in violation of the Nyquist Sampling Theorem, which will in turn results in aliasing error after application of the inverse Fourier transform. Nyquist's theorem states that when sampling at a given rate, the highest frequency that can appear in the sampled signal is half the sampling frequency. In other words, the input impedance must be band limited at half the sampling frequency to not violate the theorem; a properly designed window will accomplish this desired band limitation. The second advantage to applying a window function to the frequency domain input impedance is that the rising slope of the window, after the linear phase component is applied, can be used for topology and gauge identification as well as a length estimation reference. This will be discussed in detail in Section 3.4.1.1.

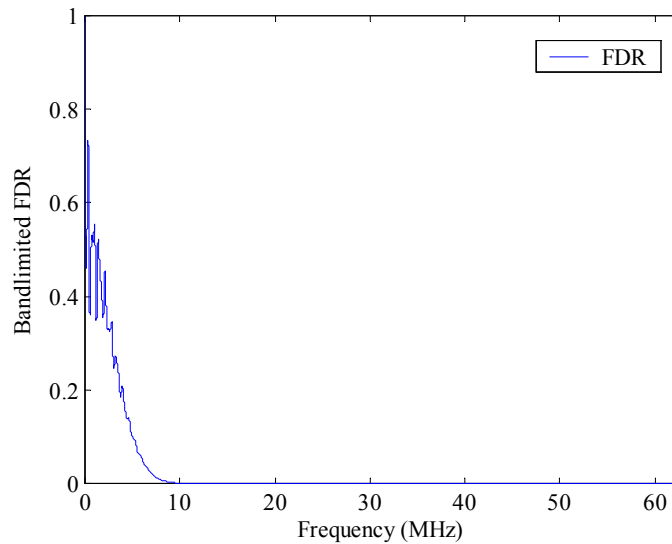
A Kaiser window function is one of several windows that may be applied to the input impedance measurement. The window is defined in (3-10) as follows:

$$Kaiser Window = \begin{cases} \frac{I_0[\beta(1 - [(n - \alpha)/\alpha]^2)^{0.5}]}{I_0(\beta)}, & 0 \leq n \leq M, \\ 0, & otherwise \end{cases}, \quad (3-10)$$

where  $\alpha = M/2$  and  $I_0(\cdot)$  represents the zeroth-order modified Bessel function of the first kind. There are a variety of windows having different properties such as main lobe width, side lobe level, etc. Many of these windows are discussed in [39]. An investigation into the application of these different windows will be addressed in the noise reduction section of this report.



a



b

Figure 3-4: a) FDR Response<sup>5</sup> and Kaiser Window. b) FDR convolved with the Kaiser Window.

<sup>5</sup> The Frequency Domain Reflectometry (FDR) response is created from loop CSA#4 of one of the sets of standard testing loops. The loop simulation was performed with a source impedance of 120Ω using the Cable Network Loop Simulation Toolbox, version 2.0.

To give an appreciation to the windowing application, *Figure 3-4 (a)* and *(b)* display the window along with the normalized voltage that is divided between the input impedance and the source impedance as shown in (3-11). The frequency domain reflectometry (FDR) response is termed the reflection transfer function impedance,  $Z_{RTF}$ , repeated here for convenience:

$$H_{RTF} = \frac{Z_{in\_loop}}{Z_{in\_loop} + Z_s}. \quad (3-11)$$

### 3.3.3 Linear Phase Component

Since the windowing function is applied similar to that of a low pass filter in the frequency domain, a linear phase component will need to be applied in the frequency domain to produce a time shift of the TDR response after the Fourier transform is performed. The relationship between the linear phase shift and the time delay is given in (3-12):

$$\phi_{LP} = e^{-j2\pi\left(\frac{F_s}{2}\right)t_s}, \quad (3-12)$$

where  $\phi_{LP}$  is the linear phase component,  $F_s$  is the sampling frequency, and  $t_s$  is the time delay.

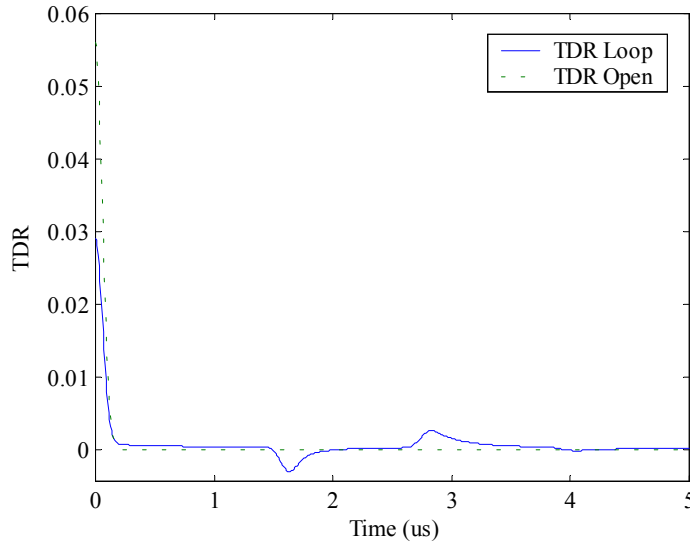


*Figure 3-5: TDR Responses of CSA#4 and an open circuit prior to time shifting.*

To illustrate this idea, the Fourier transform will be applied to the FDR waveform resulting from CSA#4 in *Figure 3-4(b)*. *Figure 3-5* shows the time domain waveform of the loop and of the window separately. It is obvious that the window function and resulting TDR response of the

loop are centered on zero. As stated earlier, the rising edge of the input pulse will be needed for topology identification as well as initialization of the length detection.

The process of time shifting the waveforms is based on a user-defined base level in terms of the windowing function used. The time shift produced by the window function will be applied to all other TDR waveforms created using the identical window. *Figure 3-6* shows the result of the time-shifted waveform using a base level of  $1 \times 10^{-8}$ . Using the same delay and window for all database waveforms and simulated waveforms will assist comparisons during the reconstruction process.

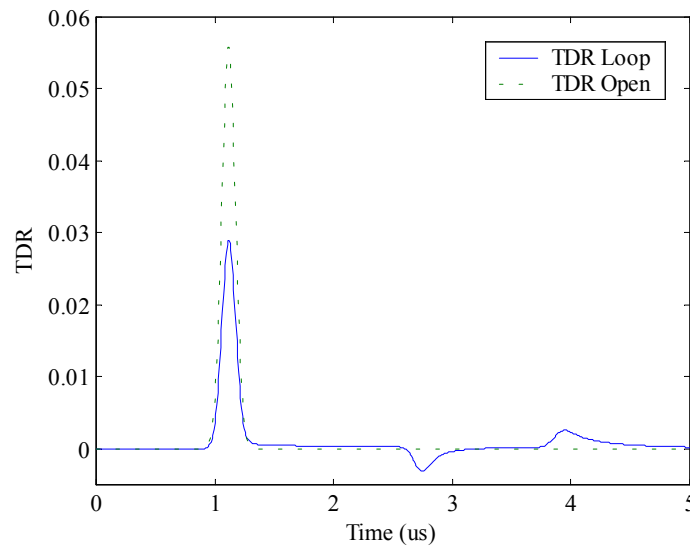


*Figure 3-6: TDR Responses of CSA#4 and an open circuit after time shifting.*

### 3.4 Structure Identification

This section will present the specifics regarding the time-domain reconstruction algorithm. The algorithm is applicable to the pre-processed data mentioned in an earlier section. The portion of the algorithm devoted to topology identification will be presented first. Discussed in this section will be the method of gauge identification, the method of dealing with bridge taps in a topology including the challenge of reconstructing relatively long bridge taps, which the algorithm will initially model as infinite line segments. Following the topology identification section, the length estimation process will be presented. The length estimation process is based on the time delay of specific reflections that occur in the time domain waveforms. The effects of

pulse dispersion, pulse attenuation, and leakage error resulting from the Fourier transforms are areas of focus concerning the length algorithm.

Appendix B contains a detailed flow chart of the time domain reconstruction algorithm<sup>6</sup>, which may be helpful when following the ideas presented in this section. Following this section will be a presentation concerning noise reduction including length refinement; the noise is a result of length estimation error and the de-embedding techniques used in the reconstruction algorithm.

### 3.4.1 Topology Identification

After pre-processing the measured input data, the resulting TDR response is input into a sub-process that detects the current node's topology (single segment or bridge-tap) and the gauge(s) of the detected segment(s). The algorithm has a unique process of detecting and dealing with bridge taps, and this process will also be detailed in this section. This section will also present the method of dealing with infinite line segments that can result from the modeling of relatively long bridge-taps detected during the reconstruction process.

#### 3.4.1.1 Gauge Detection

The process of gauge detection is a database-reference type algorithm. The algorithm contains a database of several different cable types and gauges, combinations of the cables, and the TDR response of the window (open circuit response). The database is created separately from the algorithm and is a function of the measurement specifics (sampling frequency, number of measurement points, etc.), the window function used (Kaiser, Blackman, etc.), and the cable models to be included in the reconstruction process. The cables in the database are simulated assuming to have an infinite length.

A typical database containing three different gauge wires will contain the following entries:

- TDR response of the window function (open circuit response),
- 22AWG cable of infinite length,
- 24AWG cable of infinite length,
- 26AWG cable of infinite length,

---

<sup>6</sup> MATLAB<sup>®</sup> 5.3 or higher was used as the programming language regarding of all the work mentioned in this research.

- Bridge tapped 22AWG and 22AWG cables of infinite length,
- Bridge tapped 22AWG and 24AWG cables of infinite length,
- Bridge tapped 22AWG and 26AWG cables of infinite length,
- Bridge tapped 24AWG and 24AWG cables of infinite length,
- Bridge tapped 24AWG and 26AWG cables of infinite length, and
- Bridge tapped 26AWG and 26AWG cables of infinite length.

This list is an example of three different gauge possibilities as well as the combination of any of these two cables that may happen to form a bridge tap.

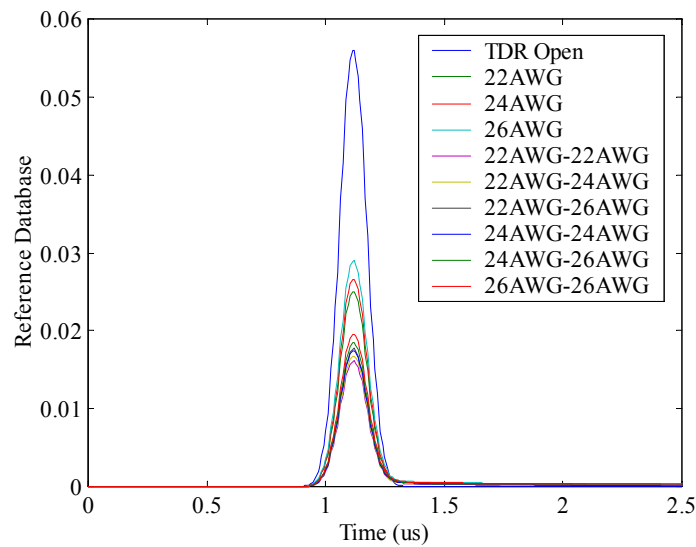


Figure 3-7: TDR Kaiser window responses contained within a typical reference database.

Figure 3-7 shows a plot of a typical database used by the algorithm. Depending on the application of the algorithm, the database may become more or less complex depending on the number of cable types needed for reconstruction.

The algorithm initially uses a peak detection command to calculate the time duration in which the gauge / topology detection will occur. The peak of the initial pulse is detected because the rising edges of the waveforms are reasonably undisturbed by the TDR simulation of a complex topology, leakage error does occur but can be kept minimal with long time durations. The measurement is then compared to each of the entries in the database using a cumulative sum squared error as follows:

$$CSSE_n = \sum_{i=1}^n (y_i - \hat{y}_i)^2, \quad (3-13)$$

where  $y(n)$  is the TDR response of the measured data to be identified,  $\hat{y}(n)$  is each separate entry in the database and  $n$  is the result of the peak detection.

The minimum CSSE computation is selected and the algorithm stores the corresponding gauge and topology of the selection. The resulting topology will decide the next step of the algorithm. *Figure 3-8* shows the time duration of the CSSE between the database and an actual measurement. There are three possible paths of the algorithm at this point; they are as follows:

1. the *TDR response of the window function* is detected, the reconstruction of the loop is complete, terminate algorithm and show final reconstruction results,
2. a *Single segment of cable* is detected, process length estimation and de-embed, and
3. a *Bridge tap of cable* is detected, process bridge tap identification procedure.

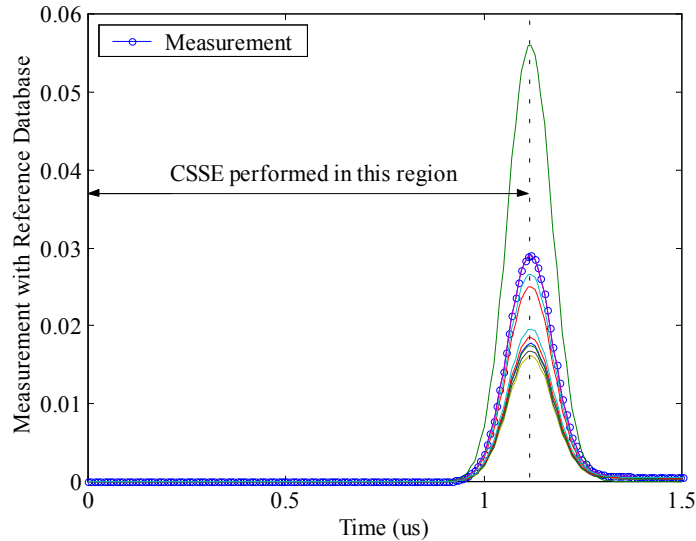


*Figure 3-8: Time duration used to compute the CSSE of the measurement with the database.*

The method used by the algorithm to reconstruct bridge taps will be discussed in the following sections. The special case of an infinitely long segment being modeled will also be addressed in a following section.

### 3.4.1.2 Bridge Tap Methodology

The methodology of the portion of the algorithm dealing with the reconstruction of bridge taps will be discussed in this section. The information obtained from the gauge detection process is input into this algorithm and the length estimation process is implemented to detect the length of the next closest segment. Following this procedure, the algorithm has three pieces of information from which to work; those are the gauges of each of the cables making up the bridge tap and the line as well as the length of one of the bridge tap segments. When the two gauges are not the same, or unmatched, this information leads to four possibilities of bridge tap information as depicted in *Figure 3-9*. Four possibilities occur because the gauge detection process can detect the gauges of the two cables forming the bridge tap, but the process cannot determine which cable gauge belongs to the line or the bridge tap, thus both cases must be considered as possibilities. In the case that the bridge tap is made up of two cables of the same gauge, the possibilities reduce to two, as the other two cases are redundant.

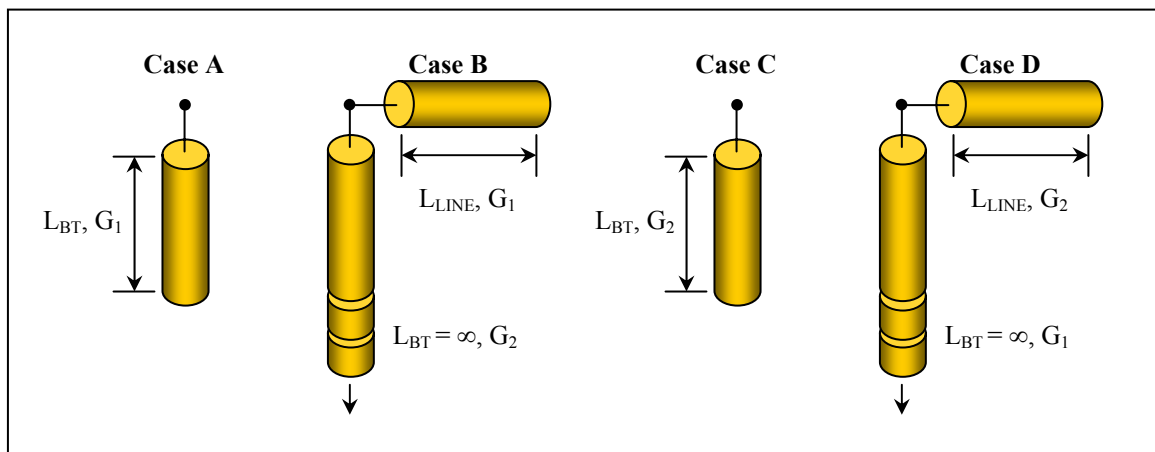


*Figure 3-9: Bridge tap possibilities to be considered when the gauges are unmatched.*

Each topology is created in the algorithm and simulated using the CNS Toolbox<sup>7</sup>. Each of the possible solutions is de-embedded from the measured data and the CSSE<sup>8</sup> is performed up to the detected peak of the open circuited response as mentioned in the gauge detection process.

<sup>7</sup> The Computer Network Simulation (CNS) Toolbox was developed by the researchers to be used in modeling an unlimited arrangement of subscriber loop topologies. The CNS toolbox is applicable to MATLAB<sup>®</sup> 5.3 or higher.

<sup>8</sup> The database CSSE comparison is not computed for the open circuited case because there will always be a undetected segment resulting from this process (recalling that an open circuit detection is the program termination flag).

One of the four cases will be result in the minimal CSSE and the other three cases will be eliminated.

In cases such as *B* and *D* shown in *Figure 3-9* there is an infinite line segment included in the reconstruction model because the length of the bridge tap exceeds the length of the next inline segment. The algorithm documents the node and gauge of the infinite line segment and sets a flag so that each subsequent length estimation is tested as a possible termination of the infinite line. The application of this process is defined and detailed in the following section.

### 3.4.1.3 Methodology for Infinite Segments

In the case that a bridge tap is longer than the following line segment, the length estimation routine will detect the length of the line segment. To de-embed the detected segment of the topology, the length of the bridge tap is de-embedded as a segment with infinite length as shown in cases *B* and *D*. The infinite line segment is documented by the algorithm and will be corrected on some subsequent iteration.

Referring to *Figure 3-10*, the length estimation process will return the length of segment #2, or  $L_{LINE\_1}$ . The bridge tap detection process will detect the bridge tap and model the length of the line to be infinitely long<sup>9</sup>, representing segment #1. The bridge tap will be de-embedded along with the segment in which the length was detected. In the subsequent iteration of this specific loop, the length estimation process will return the length  $L_{EST}$ . This length is applied to the infinite line bridge tap is compared to the database waveforms. In this case, the result will be found to be an acceptable match, the length of the bridge tap will be changed from an infinite length to the value of  $L_{LINE\_1} + L_{EST}$ . The bridge tap is now completely modeled and will be considered independent of any further loop iterations, though the bridge tap will still be considered for length refinement.

---

<sup>9</sup> De-embedding an infinitely long line from measurement of finite length results in a waveform that resembles a lossless line. De-embedding the infinitely long line removes the back-scattering, or decaying, portion of the waveform and adds a discontinuity at the location of the open circuited termination, which determines the exact length of the bridge tap.

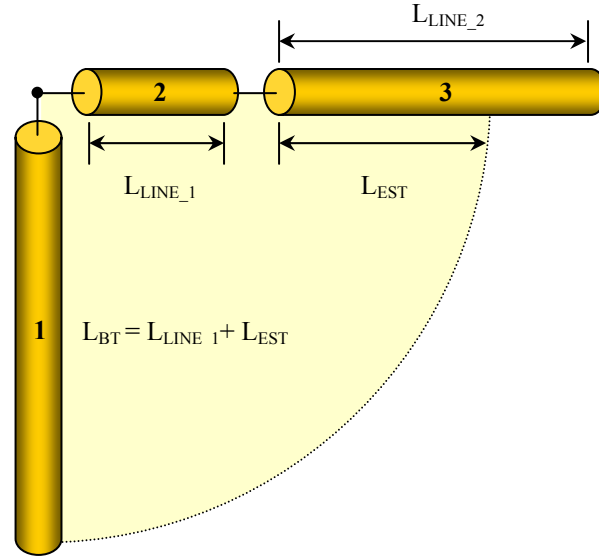


Figure 3-10: Description of an infinite bridge tap length adjustment.

In certain topologies, multiple infinitely long bridge taps may be modeled concurrently. In these cases, all the unknown bridge tap lengths are modified by the length estimation of the current iteration and compared using the CSSE method, any identified structures are updated and the process proceeds to the next iteration. In the case that the length estimation belongs to another line segment, that segment is processed and the bridge tap database remains unchanged.

### 3.4.2 Length Estimation

The length estimation process will be performed on the segment closest to the measurement node. After the gauge detection is processed, the difference between the TDR response and the infinite line corresponding to the *detected* gauge, termed the normalized difference response (NDR), is performed<sup>10</sup>.

$$NDR = y_i - \hat{y}_i, \quad (3-14)$$

where  $y(t)$  is the measured TDR response of the loop to be identified,  $\hat{y}(t)$  is the infinite line simulation using the detected gauge of the first segment.

<sup>10</sup> Due to the effects of leakage error, the detected gauge and measurement TDR waveforms are matched at the peak before the difference is taken. This makes the reference level the peak and not the erroneous baseline level.

The resulting waveform will be used in the estimation scheme termed the Weighted Gradient - Linear Phase Method (WGLPM). This length detection method will be described in detail as well as the correction scheme used to resolve leakage errors produced by the processing of the Fourier transforms.

### 3.4.2.1 Weighted Gradient - Linear Phase Method (WGLPM)

The weighted gradient linear phase method (WGLPM) incorporates the linear phase component (frequency domain) of the weighted derivative of the NDR with respect to time. After the peak detection of the time derivative of the NDR, an exponential weighting function is applied to the waveform after the detected peak ( $n_{peak}$ ) to minimize the effects of peaks later in time caused by discontinuities further down the network loop. *Figure 3-11* shows the weighted derivative of the NDR along with a plot of the NDR. The weighting function is defined as follows (note the weighting function continues through the entire series of discrete points that basically zero pads the time domain signal for more frequency domain detail):

$$w(n) = \exp(0.1 \cdot (n - (n + 1))), \quad n_{peak} < n \leq n_{max} \quad (3-15)$$

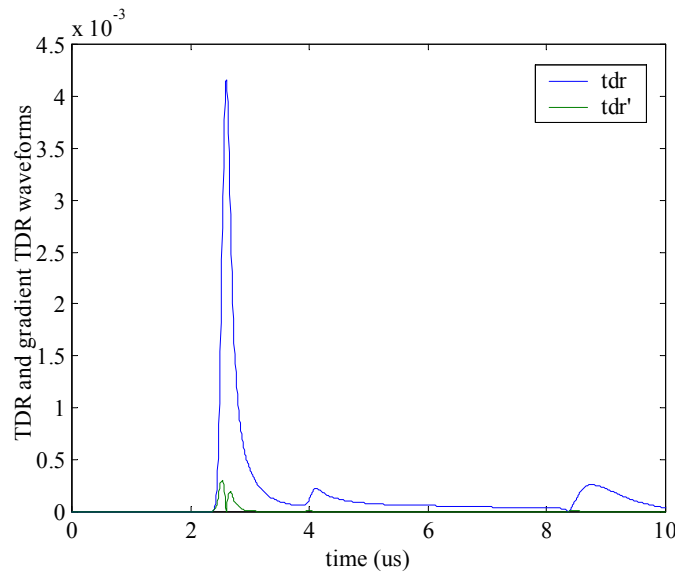


*Figure 3-11: Plot of the weighted derivative of the NDR and the NDR for length detection.*

Incorporating the weighting function along with the NDR, the WGLPM phase response is obtained from the following equation:

$$WGMPM = \angle \mathfrak{F} \left\{ w(n) \cdot \frac{d}{dt} |NDR(n)| \right\} . \quad (3-16)$$

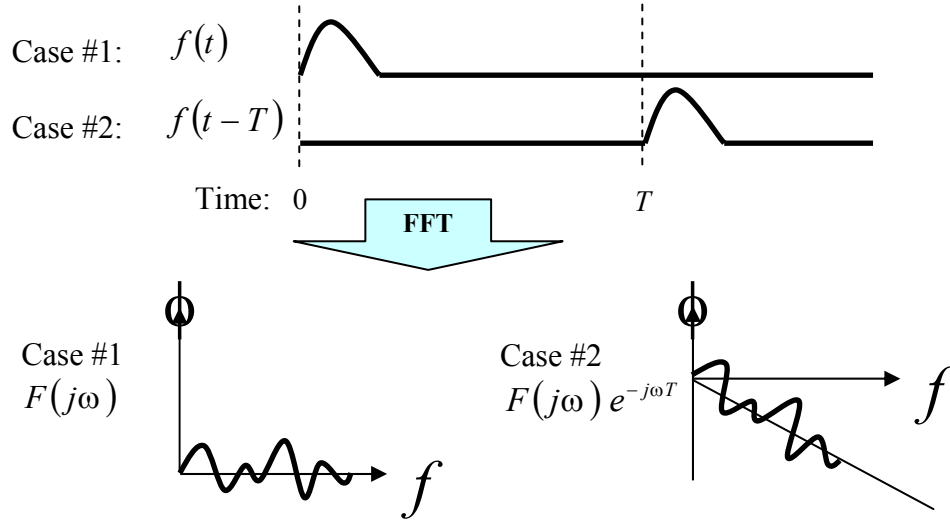


Figure 3-12: Background information for linear phase routine.

Figure 3-12 shows a graphical realization of the background methodology for the linear phase length detection routine. The difference between case #1 and case #2 is the delay  $T$ . After transforming the two waveforms to the frequency domain, the time delay,  $T$ , transforms in to a linear phase component as shown. The slope of the linear phase component is dependent on the length of the time delay. Keep in mind that the phase of the function,  $F(j\omega)$ , is also included in the phase component of (3-16), but the effect of the linear phase is dominant as can be seen in an example resulting linear phase component from the reconstruction routine in Figure 3-13. It is important to note that the derivative of the absolute value of the NDR is used to prevent problems resulting from possible negative slopes of the NDR.

The difference between time delays of the detected rising edge of the pulse and the first reflection are taken from a zero reference. This relates in an initial estimate of the actual time delay between the two responses, keeping in mind that the actual time delay is difficult to extract due to dispersion and attenuation.

The length is related to the calculated time delay using the following representation:

$$\text{length estimation} = \frac{c}{\sqrt{\epsilon_r}} \frac{(td_{REF} - td_{PUL})}{2}, \quad (3-17)$$

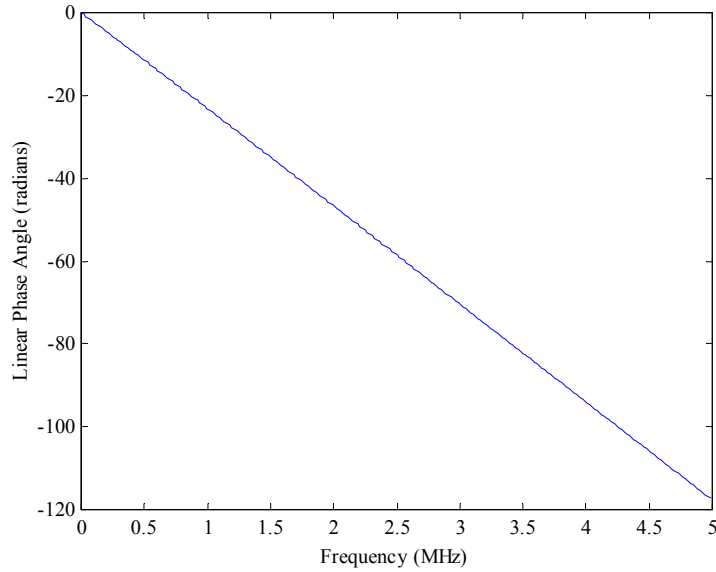


Figure 3-13: Resulting linear phase component from the WGLPM

where  $c$  is the speed of light,  $\epsilon_r$  is the relative permittivity of the insulation, and  $td$  is the time delay calculated using the linear phase routine. The only half of the time delay is desirable because the resulting reflection is due to the signal traveling to and back from the reflection, the reconstruction only needs the length from the input node to the reflection.

The relative permittivity is obtained from the models used in the reconstruction process. First, the phase velocity is calculated from the imaginary part of the propagation constant, or  $\beta$ , obtained from the models using the following equation:

$$v_{ph} = \frac{\omega}{\beta}, \quad (3-18)$$

where  $\omega$  is the radian frequency (radians/s).

The relative permittivity of the insulating material is calculated using the following:

$$\epsilon_r = \left( \frac{c}{v_{ph}} \right)^2. \quad (3-19)$$

The relative permittivity resulting from the highest phase velocity will be extracted and used in the length detection. The portion of the reflection we are most interested in is the rising edge, or beginning, of the reflection, and this corresponds to the portion with the highest phase velocity.

By plotting the phase velocity, *Figure 3-14*, and resulting relative permittivity, *Figure 3-15*, we can extract the corresponding information and apply it to the length estimation equation.

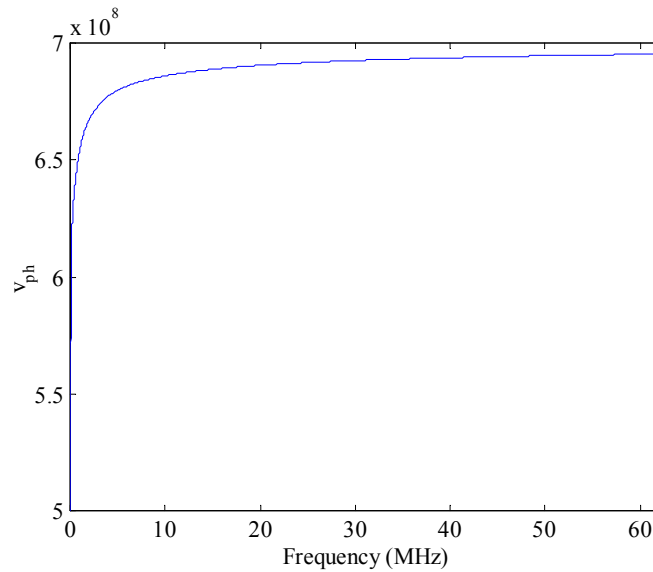


*Figure 3-14: Typical phase velocity plot versus frequency.*

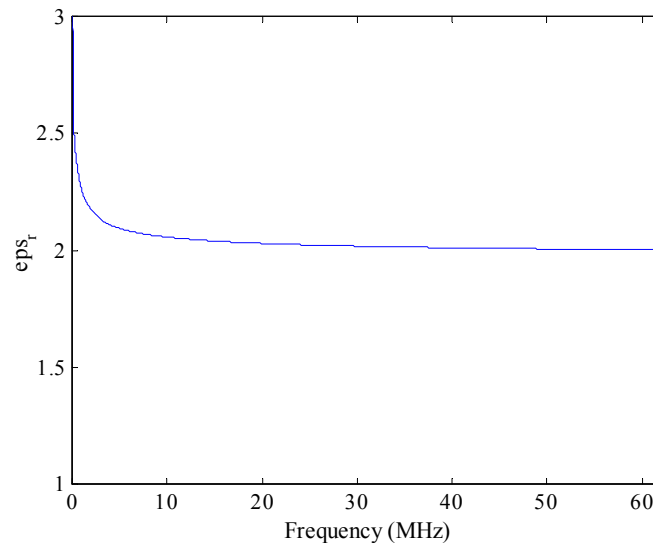


*Figure 3-15: Typical relative permittivity plot calculated from the phase velocity.*

### 3.4.2.2 Leakage Error Estimation

The leakage error investigated here is a result of a duration limited time domain response. The effects of the leakage error at shorter lengths are small in comparison with the attenuated response reflected from segments having a very long length.

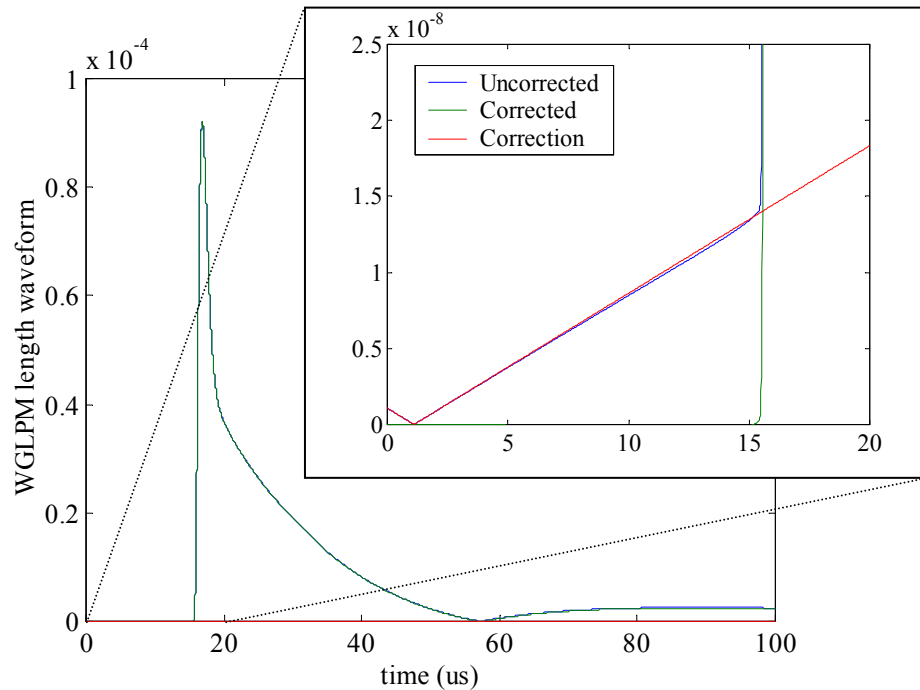


Figure 3-16: Leakage error and method of correction.

Shown in Figure 3-16 is a plot of the WGLPM waveform resulting from a 5000 ft. segment of 26 AWG cable. By viewing the subplot of the figure around 1.0  $\mu\text{s}$ , the location of the matched peak can be viewed resulting in a zero. The error of the match between the infinite line segment of the database and the 5000 ft. segment is a result of leakage error. By matching the peaks of the two waveforms one can see a linear representation of the error versus time. A linear equation is fit to this error and the fit is subtracted from the original waveform to remove a large portion of the leakage error. The waveform will now result in improved length detection by removing the possibility of this error being mistaken for a reflection from a discontinuity.

### 3.5 Noise Reduction Schemes

Possible noise sources and future investigations for solutions of noise reduction will be presented in this section. The noise source will be presented as well as an insight to possible solutions of this research difficulty.

#### 3.5.1 High Frequency De-Embedding Noise

The de-embedding process is subject to noise for some different reasons, and this fact makes noise reduction schemes an important factor to be considered. One source of error arises directly from the de-embedding equations and is the focus of the researcher's continuing efforts. The numerator of equation (3-20) shows a difference function of the scattering parameter,  $S_{11}$ , and the input reflection coefficient. At higher frequencies these values both approach zero and it is obvious that errors will occur when performing the difference function of two closely valued quantities.

$$\Gamma_{i+1} = \frac{S_{i,11} - \Gamma_i}{S_{i,22}(S_{i,11} - \Gamma_i) - S_{i,21}S_{i,12}} \quad (3-20)$$

One method being investigated to reduce this type of error is one of moving averages. By application of moving averages in the time domain before the Fourier transform is applied, the higher frequency response will have reduced amounts of noise. The idea is to overwrite the noisy high-frequency portion of original response with the response produced by the application of a moving average.

Other possible solutions are to perform some type of iterative noise reduction algorithm to reduce the noise content or extend the computational precision of the software used to extend the accuracy of the calculations.

#### 3.5.2 Noise Introduced by Length Estimation Errors

Another source of error results from length estimation errors within the length detection process. When de-embedding a segment with an incorrect length estimation, a portion of the error remains in the result of the de-embedding process and will eventually force the algorithm to fail without proper length refinement.

The desire for this research project is to develop a length refinement algorithm using optimization techniques. Length estimation is of high importance when dealing with reconstruction algorithms and refinement of previously detected segments. The research examined algorithms to optimize each detected segment identified all well as a global optimization of the entire reconstructed model.

### **3.5.3 Noise Reduction Using Different Window Functions**

Another possible source of error is the effects of the side lobes of the window function. The Kaiser window function has been used up to this point, but the investigation into the application of different type of windows with varying characteristics will be performed. Harris presents an extensive study of several different window functions in [39], some of which have been considered.

One implemented noise reduction technique was the development of causal modeling. The developed causal models reduced de-embedding errors and improved topology and length estimation algorithms. The development of these models is presented in the following chapter.

## Chapter 4

### Twisted-Pair Cable Modeling for DSL Systems

#### 4 Introduction

Current models of twisted pair cables used for Digital Subscriber Lines (DSL) involve empirical modeling of some type of measured data. Although these empirical formulas representing the line parameters of the DSL cable can be used in simulations to calculate frequency characteristics such as cross-talk and transfer functions, they fail to represent a physically realizable set of equations. They also include the inaccuracies of performing measurements of these cables at the lower frequency spectra. Since the high frequency data from DSL cables obtained through measurements is considered the most accurate, applying a broadband, physically realizable model to the high frequency data would produce the solution to the entire frequency spectra. An introduction to the process of developing a physically realizable model for cables used in DSL systems consisting of physical dimensions and material characteristics will be presented in this section. The well-documented high frequency parallel line approximation is an analytically realizable development involving physical parameters of the cables and will be presented in this section. The frequency limitation of this model is found to be caused by the uniform skin effect model used in the presentation. The skin effect of an infinite planar conducting slab is utilized and this model is only applicable at the higher frequencies. The broadband current distribution resulting from the skin effect in a round wire will then be presented and implemented in the model.

## 4.1 High Frequency Approximation for Parallel Lines

The physically realizable high frequency approximation for the parallel line topology is a very well documented problem. Since the DSL twisted pair topology is a variation of the parallel line topology, the parallel line equations will be discussed. The line parameters consisting of resistance,  $R$ , inductance,  $L$ , capacitance,  $C$ , and conductance,  $G$ , per unit length have been developed, and the derivation of these parameters will be presented in this section. To begin this discussion, the method of conformal transformations will be presented, followed by the properties of complex variables in analytic functions. Finally, the development of the line parameters is presented.

### 4.1.1 Method of Conformal Transformation Introduction

Considering the two-dimensional field distribution problem, a general mathematical approach utilizes the theory of functions of a complex variable. The analytical solutions to a wide variety of practical problems including the parallel wire topology can be developed using this approach [40]. The general method with application to the parallel wire problem will be presented in this section.

The complex variable,  $Z = x + jy$ , will be introduced where both  $x$  and  $y$  are real variables. It is convenient to associate the any given value of  $Z$  with a point location on the  $x$ - $y$  plane as shown in *Figure 4-1a*, and to call this plane the  $Z$  plane. One can also express the coordinates in polar form in terms of  $r$  and  $\theta$  as follows:

$$r = \sqrt{x^2 + y^2}, \theta = \tan^{-1}\left(\frac{y}{x}\right),$$

then

$$Z = x + jy = r(\cos\theta + j\sin\theta) = re^{j\theta}. \quad (4-1)$$

Suppose there is now a different complex variable,  $W$ , where:

$$W = u + jv = \rho e^{j\phi},$$

such that  $W$  is some function of  $Z$ . This means that, for each assigned value of  $Z$ , there is a rule specifying a corresponding value of  $W$ . The functional relationship is then written as:

$$W = f(Z). \tag{4-2}$$

If  $Z$  is to vary continuously, the corresponding point in the complex  $Z$  plane traces a curve,  $C$ . The values of  $W$  will vary corresponding to (4-2), tracing a curve,  $C'$ . To reduce misinterpretation, the values of  $W$  are usually shown on a separate graph, called the complex  $W$  plane, as shown in *Figure 4-1b*.

Now consider a small change,  $\Delta Z$ , in  $Z$  and the corresponding change,  $\Delta W$ , in  $W$ . The derivative of the function will be defined as the usual limit of the ratio of  $\Delta W$  to  $\Delta Z$  as the element  $\Delta Z$  becomes infinitesimal:

$$\frac{dW}{dZ} = \lim_{\Delta Z \rightarrow 0} \frac{\Delta W}{\Delta Z} = \lim_{\Delta Z \rightarrow 0} \frac{f(Z + \Delta Z) - f(Z)}{\Delta Z}. \tag{4-3}$$

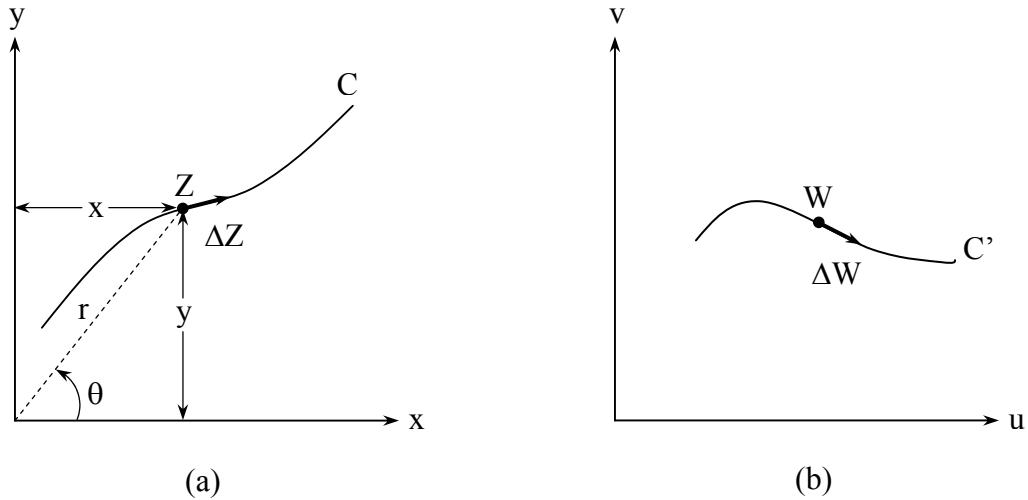


*Figure 4-1: (a) Z plane consisting of points from the x-y plane. (b) W plane consisting of points from the u-v plane.*

A complex function is said to be analytic whenever the derivative defined in (4-3) exists and is unique. The derivative may fail to exist at certain isolated (singular) points where it may be infinite or undetermined. It would appear that there is another ambiguity with respect to complex variables, since  $\Delta Z$  may be taken in any arbitrary direction in the  $Z$  plane from the

original point. For the derivative to be unique, the ratio of  $\Delta W$  to  $\Delta Z$  should end up being independent of this direction.

If this independence of direction is to result, a necessary condition is that one obtain the same result if  $Z$  is changed in the  $x$  direction alone or in the  $y$  direction alone. For a change in solely the  $x$  direction we have  $\Delta Z = \Delta x$  or:

$$\frac{dW}{dZ} = \frac{\partial W}{\partial x} = \frac{\partial}{\partial x}(u + jv) = \frac{\partial u}{\partial x} + j\frac{\partial v}{\partial x}. \quad (4-4)$$

For a change in solely the  $y$  direction we have  $\Delta Z = j\Delta y$  or:

$$\frac{dW}{dZ} = \frac{\partial W}{\partial(jy)} = \frac{1}{j} \frac{\partial}{\partial y}(u + jv) = \frac{\partial v}{\partial y} - j\frac{\partial u}{\partial y}. \quad (4-5)$$

The two complex quantities are equal if and only if their real and imaginary parts are separately equal. Hence, (4-4) and (4-5) result in equal quantities if:

$$\frac{\partial u}{\partial x} = \frac{\partial v}{\partial y}, \text{ and} \quad (4-6)$$

$$\frac{\partial v}{\partial x} = -\frac{\partial u}{\partial y}. \quad (4-7)$$

These conditions are known as the *Cauchy-Riemann equations* and are necessary conditions for  $\partial W/\partial Z$  to be unique at a point and the function  $f(Z)$  to be analytic at that point. It can be shown that if the *Cauchy-Riemann equations* are satisfied, the same result for  $\partial W/\partial Z$  is obtained for any arbitrary direction of the change  $\Delta Z$ , so they are sufficient conditions.

#### 4.1.2 Properties of Analytic Functions of Complex Variables

The properties of the analytic functions of complex variables will now be investigated with the objective of relating the previous development into an application such as the parallel wire problem [40].

If (4-6) is differentiated with respect to  $x$ , (4-7) is differentiated with respect to  $y$ , and the resulting equations added, there results the following:

$$\frac{\partial^2 u}{\partial x^2} + \frac{\partial^2 u}{\partial y^2} = 0. \quad (4-7)$$

Similarly, if the order of differentiation is reversed, there results the following:

$$\frac{\partial^2 v}{\partial x^2} + \frac{\partial^2 v}{\partial y^2} = 0. \quad (4-8)$$

These are recognized as the Laplace equations in two dimensions. Thus, both the real and imaginary parts of an analytic function of a complex variable satisfy Laplace's equation. As a result, they will be suitable for use as the potential functions for two-dimensional electrostatic problems. It will be shown that the real and imaginary portions will be acceptable to the development of the parallel line equations.

An investigation will now be performed to figure out which one of the two parts,  $u$  or  $v$ , is chosen as the potential function. The other part will become proportional to the flux function. To illustrate this, suppose  $u$  is the potential function in volts for a particular problem. The electric field, obtained as the negative gradient of  $u$  shows the following:

$$E_x = -\frac{\partial u}{\partial x}, E_y = -\frac{\partial u}{\partial y}. \quad (4-9)$$

Modifying the equation of the complete differential, the change in  $v$  corresponding to changes in the  $x$  and  $y$  coordinates of  $\partial x$  and  $\partial y$  gives:

$$dv = \frac{\partial v}{\partial x} dx + \frac{\partial v}{\partial y} dy. \quad (4-10)$$

But, the *Cauchy-Riemann* conditions from (4-6) and (4-7) give:

$$-dv = \frac{\partial u}{\partial y} dx - \frac{\partial u}{\partial x} dy = -E_y dx + E_x dy, \quad (4-11)$$

or

$$-\varepsilon dv = -D_y dx + D_x dy. \quad (4-12)$$

By inspection of *Figure 4-2*, this is recognized to be the electric flux,  $d\psi$ , between the curves  $v$  and  $v+dv$ , with the positive direction as depicted by the arrow. This gives:

$$-d\psi = \varepsilon dv. \quad (4-13)$$

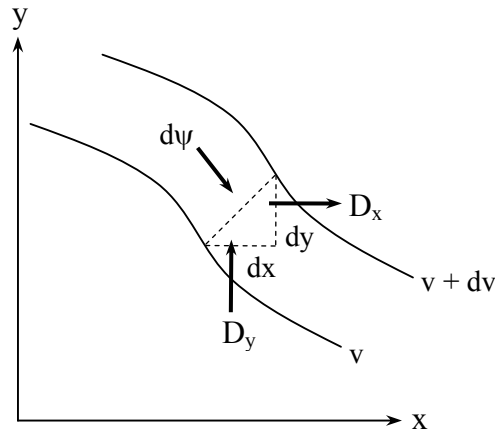


Figure 4-2: Coordinates for the flux function.

By choosing the reference for the flux at  $v = 0$ , the constant resulting from the integration is set equal to zero as follows:

$$-\psi = \epsilon v \quad \text{C / m.} \quad (4-14)$$

Likewise, if  $v$  is chosen as the potential function in volts for a problem,  $\epsilon u$  would be the flux function in coulombs per meter, with proper choice of the direction for positive flux.

From this discussion, it was shown that either  $u$  or  $v$  may be used as the potential function, resulting in the other being used as the flux function, since both satisfy Laplace's equation. However, the utility of the concept described in this section depends on being able to find the analytic function  $W = f(Z)$  such that  $u$  and  $v$  also satisfy the boundary conditions for the problem being considered. In the following sections, the development of the single round wire problem will be addressed, followed by the parallel wire problem, and concluding with the development of the line parameters of the parallel wire topology.

### 4.1.3 Single Round Wire Analysis (Logarithmic Transformation)

It is well known that an analytic equation employing the form of a logarithmic potential form is used for topologies such as line charges and charged cylinders [40], so we will consider the following logarithmic function:

$$W = C_1 \ln(Z) + C_2. \quad (4-15)$$

The logarithm of a complex number is readily found if the number is in the polar form as:

$$\ln(Z) = \ln(re^{j\theta}) = \ln r + j\theta, \quad (4-16)$$

so

$$W = C_1(\ln r + j\theta) + C_2. \quad (4-17)$$

By taking the constants,  $C_1$  and  $C_2$ , as real, the following results:

$$u = C_1 \ln r + C_2, \text{ and} \quad (4-18)$$

$$v = C_1\theta. \quad (4-19)$$

Considering  $u$  contains the logarithmic function, it will be chosen as the potential function. The flux function,  $\psi = -\epsilon v$ , is proportional to the angle,  $\theta$  (given by  $v$ ), as it should be for a problem with radial electric field lines.

To evaluate the constants for the single round wire problem in the form of a center conductor of a coaxial line, take the wire to have an inner radius  $a$  at potential  $V_o$  and outer radius  $b$  at zero potential. Substituting into (4-18) results in the following:

$$V_o = C_1 \ln a + C_2, \text{ and} \quad (4-20)$$

$$0 = C_1 \ln b + C_2. \quad (4-21)$$

Solving results in the following:

$$C_1 = \frac{V_o}{\ln\left(\frac{a}{b}\right)}, \text{ and} \quad C_2 = \frac{V_o \ln(b)}{\ln\left(\frac{a}{b}\right)}.$$

From this result, (4-15) can be written as:

$$W = V_o \left[ \frac{\ln\left(\frac{Z}{b}\right)}{\ln\left(\frac{a}{b}\right)} \right], \quad (4-22)$$

or

$$\Phi = u = V_o \left[ \frac{\ln\left(\frac{r}{b}\right)}{\ln\left(\frac{a}{b}\right)} \right] V, \text{ and} \quad (4-23)$$

$$\Psi = -\varepsilon v = \frac{-\varepsilon V_o \theta}{\ln\left(\frac{a}{b}\right)}. \quad (4-24)$$

#### 4.1.4 Parallel Wire Topology Analysis

In this section, the parallel wire topology will be address to forward the progress to the derivation of the line parameters, R, L, C, and G, of the transmission line. To begin one can consider the following analytic function which can represent the field about two line charges [40], one at location  $Z = a$  and the other at equal and opposite strength located at  $Z = -a$ :

$$W = K_1 \ln\left(\frac{Z-a}{Z+a}\right). \quad (4-25)$$

However, it is more general to write (4-25) so that it can yield the field about parallel cylinders of any radius.

Taking  $K_1$  as a real quantity results in the following:

$$u = \frac{K_1}{2} \ln\left[\frac{(x-a)^2 + y^2}{(x+a)^2 + y^2}\right], \text{ and} \quad (4-26)$$

$$v = K_1 \left[ \tan^{-1} \frac{y}{(x-a)} - \tan^{-1} \frac{y}{(x+a)} \right]. \quad (4-27)$$

The lines of constant  $u$  can be obtained from (4-26) by setting the argument of the logarithm equal to a constant as:

$$K_2 = \frac{(x-a)^2 + y^2}{(x+a)^2 + y^2}. \quad (4-28)$$

This may be rearranged to the following form:

$$\left[ x - \frac{a(1+K_2)}{1-K_2} \right]^2 + y^2 = \frac{4a^2 K_2}{(1-K_2)^2}, \quad (4-29)$$

so the curves of constant  $u$  are circles with centers at

$$x = \frac{a(1 + K_2)}{1 - K_2},$$

with a diameter of

$$d = \frac{4a\sqrt{K_2}}{1 - K_2}.$$

If  $u$  is taken as the potential function, any one of the circles of constant  $u$  may be replaced by an equipotential conducting cylinder. Thus, if  $d$  is the diameter of such a conductor with the center of  $D / 2$  (See *Figure 4-3*), the values of  $a$  and the particular value of  $K_2$  (denoted  $K_o$ ) may be obtained by setting the following:

$$D = \frac{2a(1 + K_o)}{1 - K_o}, \quad d = \frac{4a\sqrt{K_o}}{1 - K_o}.$$

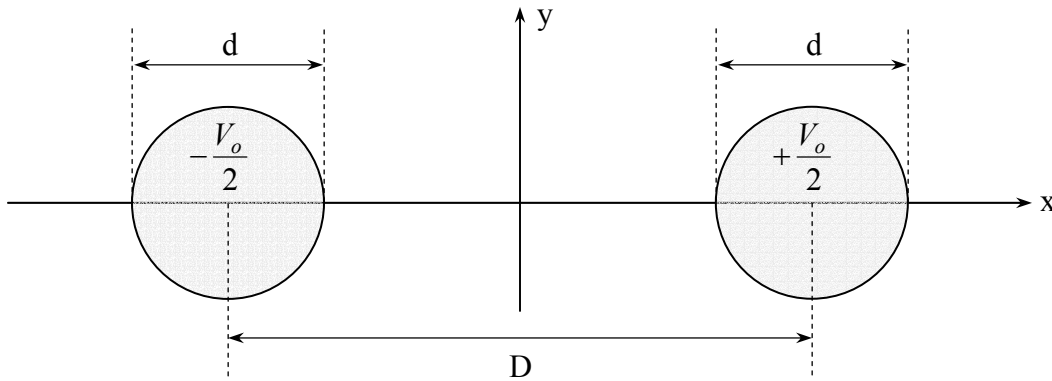


Figure 4-3: Parallel wire topology.

Solving we have:

$$a = \pm \frac{1}{2} \sqrt{D^2 - d^2}, \text{ and} \tag{4-30}$$

$$\sqrt{K_o} = \frac{D}{d} + \sqrt{\frac{D^2}{d^2} - 1}. \tag{4-31}$$

The constant  $K_1$  in the transformation depends on the potential of the conducting cylinder. Let this potential be  $V_o / 2$ . Then, by the definition of  $K_2$  (which is equal to  $K_o$  on the conducting cylinder) and by (4-31) one obtains:

$$\frac{V_o}{2} = K_1 \ln \sqrt{K_o} = K_1 \ln \left( \frac{D}{d} + \sqrt{\frac{D^2}{d^2} - 1} \right), \quad (4-32)$$

or

$$K_1 = \frac{V_o}{2 \ln \left( \frac{D}{d} + \sqrt{\frac{D^2}{d^2} - 1} \right)} = \frac{V_o}{2 \cosh^{-1} \left( \frac{D}{d} \right)}. \quad (4-33)$$

Substituting into (4-26), the potential at any point  $(x,y)$  is given as:

$$\Phi = u = \frac{V_o}{4 \cosh^{-1} \left( \frac{D}{d} \right)} \left[ \frac{(x-a)^2 + y^2}{(x+a)^2 + y^2} \right]. \quad (4-34)$$

For  $\Phi > 0$  with  $x > 0$ ,  $a < 0$  when  $K_1$  is positive so the negative sign must be chosen in (4-30).

The flux function,  $\psi = -\varepsilon v$ , results in the following:

$$\psi = -\varepsilon v = \frac{\varepsilon V_o}{2 \cosh^{-1} \left( \frac{D}{d} \right)} \left[ \tan^{-1} \frac{y}{(x+a)} - \tan^{-1} \frac{y}{(x-a)} \right]. \quad (4-35)$$

Although the left-handed parallel wire was not put in explicitly, the odd symmetry of the potential from (4-34) will cause this boundary condition to also be satisfied if the left-handed wire of diameter  $d$  with a center of  $-D / 2$  is at potential  $-V_o / 2$ . Therefore, the entire solution can be defined from the obtained result.

#### 4.1.5 Parallel Wire Transmission Line Parameter Development

This section describes the development of the R, L, C, and G line parameters for the parallel wire lines to be used as background material for the development of analytical equations for the twisted pair transmission lines.

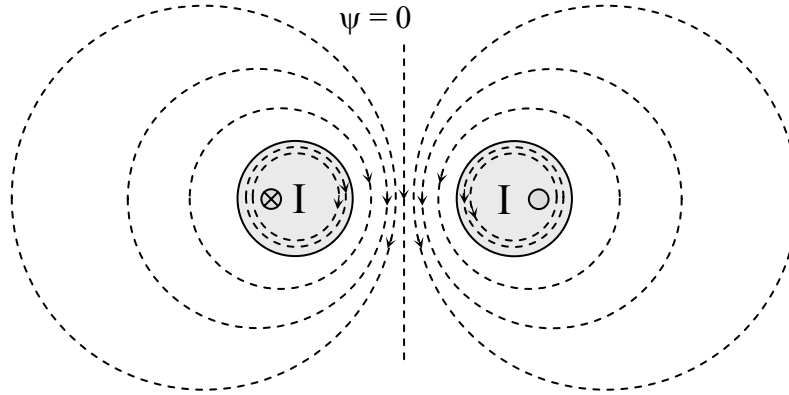


Figure 4-4: Magnetic flux lines in a parallel wire transmission line.

This section will begin with the calculation of the shunt capacitance line parameter, which is followed by the external inductance parameter, or the inductance due to the field lines external to the conductors. The skin effect of the conductors is then explained followed by the resistance line parameter. Following the explanation of the skin effect, the internal inductance, or the inductance due to field penetration of the conductors is described. Finally, the shunt conductance is derived.

#### 4.1.6 Capacitance Line Parameter

To obtain the capacitance per unit length of the parallel wire line, we first need to obtain the charge on the right hand conductor from Gauss's law by finding the total flux passing through the wire surface [41]. Integrating around the diameter of the wire changes the first term of (4-35) by  $2\pi$ , and the second term by zero. So

$$q = 2\pi \frac{\epsilon' V_o}{2 \cosh^{-1}\left(\frac{D}{d}\right)} \quad \text{C / m}, \quad (4-36)$$

or

$$C = \frac{q}{V_o} = \frac{\pi\epsilon'}{\cosh^{-1}\left(\frac{D}{d}\right)} \quad \text{F / m}, \quad (4-37)$$

where  $\varepsilon'$  is given by the real part of the complex permittivity and is related to the relative permittivity of the insulating (or dielectric) material as follows:

$$\varepsilon' = \varepsilon_r \varepsilon_o,$$

where  $\varepsilon_o$  is the permittivity of free space given by  $8.854 \cdot 10^{-12}$  (F/m) and  $\varepsilon_r$  is the relative permittivity of the insulating material. The final result of the capacitive derivation for a parallel wire is given in (4-37) and will be used in future development of the twisted pair equations.

#### 4.1.7 External Inductance Line Parameter

The external inductance, or the inductance due to the fields external to the wire, will be developed in this section. The internal portion of the inductance due to the skin effect or penetration of the field lines into the conductor will be developed after the skin effect is explained in the following section.

Using a similar procedure used to find the scalar electric potential (4-34) and the exact electric flux function (4-35), one can solve the magnetic field problem of the parallel wire topology. In this case, the roles of  $u$  and  $v$  are opposite from the electric field problem, with  $v$  being proportional to the magnetic scalar potential. The resulting scalar magnetic potential function and the exact magnetic flux function calculated for the parallel lines are as follows [40]:

$$\Psi_m = -\frac{\mu I_o}{4\pi} \ln \left[ \frac{(x-a)^2 + y^2}{(x+a)^2 + y^2} \right], \text{ and} \quad (4-38)$$

$$\Phi_m = \frac{I}{2\pi} \left[ \tan^{-1} \frac{y}{(x+a)} - \tan^{-1} \frac{y}{(x-a)} \right], \quad (4-39)$$

where

$$a = 0.5\sqrt{D^2 - d^2}. \quad (4-40)$$

Taking the flux difference at  $x = 0.5(D - d)$  and  $x = 0.5(-D + d)$  at  $y = 0$  and canceling the factor of  $\frac{1}{2}$  from the denominator and numerator, one obtains the following:

$$\Delta\Psi = \Psi(D - d, 0) - \Psi(-D + d, 0), \text{ and} \quad (4-41)$$

$$= -\frac{\mu I_o}{4\pi} \left\{ \ln \left[ \frac{(D-d-a)}{(D-d+a)} \right]^2 - \ln \left[ \frac{(-D+d-a)}{(-D+d+a)} \right]^2 \right\},$$

or

$$= -\frac{\mu I_o}{\pi} \ln \left| \frac{(D-d-a)}{(D-d+a)} \right| = -\frac{\mu I_o}{\pi} \ln \left| \frac{(D-d-\sqrt{D^2-d^2})}{(D-d+\sqrt{D^2-d^2})} \right|. \quad (4-42)$$

This term can be reduced to the following:

$$\Delta\psi_m = -\frac{\mu I_o}{\pi} \ln \left\{ \frac{D}{d} - \sqrt{\left(\frac{D}{d}\right)^2 - 1} \right\} = \frac{\mu I_o}{\pi} \cosh^{-1} \left( \frac{D}{d} \right). \quad (4-43)$$

So

$$L_{ext} = \frac{\Delta\psi_m}{I_o} = \frac{\mu}{\pi} \cosh^{-1} \left( \frac{D}{d} \right) \quad \text{H / m}, \quad (4-44)$$

where  $\mu$  is given by as permeability and is related to the relative permeability,  $\mu_r$  (assumed to be 1.0), of the insulating material as follows:

$$\mu = \mu_r \mu_o = \mu_o,$$

where  $\mu_o$  is the permeability of free space given by  $4\pi \cdot 10^{-7}$  (H/m). The final result of the external inductive derivation for a parallel wire is given in (4-44) and will be used in future development of the twisted pair equations.

#### 4.1.8 The Skin Effect (Planar Approximation) in Good Conductors

This section will present the investigation into the high frequency approximation of the penetration of electromagnetic fields into good conductors. The effects of this penetration into the conductors cause changes in the series inductance and resistance. The relationships between the skin effect and inductance and resistance equations will be developed.

At high frequencies the currents within a conductor tend to be restricted to the surface layer adjacent to the external electromagnetic fields. We will assume the conductor satisfies Ohm's Law as:

$$\vec{J} = \sigma \vec{E}, \quad (4-45)$$

where  $\sigma$  is the conductivity of the conductor. Substituting into one of Maxwell's equations gives the following:

$$\nabla \times \vec{H} = (\sigma + j\omega\epsilon)\vec{E}. \quad (4-46)$$

To show that the assumption of Ohm's Law implies the absence of charge density where we have assumed homogeneity of  $\sigma$  and  $\epsilon$ , take the divergence of (4-46) to give:

$$\nabla \cdot \nabla \times \vec{H} = (\sigma + j\omega\epsilon)\nabla \cdot \vec{E} = 0. \quad (4-47)$$

This results in the following:

$$\nabla \cdot \vec{D} = \rho = 0. \quad (4-48)$$

To derive the differential equation, which determines the penetration of the fields into the conductor, take the curl of the Maxwell curl equation for electric field to obtain:

$$\nabla \times \nabla \times \vec{E} = \nabla(\nabla \cdot \vec{E}) - \nabla^2 \vec{E} = -j\omega\mu\nabla \times \vec{H}. \quad (4-49)$$

For the transmission lines of good conductors under investigation, the displacement current is negligible in comparison with the current, or  $\omega\epsilon \ll \sigma$ . So, using (4-47) and substituting (4-48) into (4-49) one finds the following [40]:

$$\nabla^2 \vec{E} = -j\omega\mu\sigma \vec{E}. \quad (4-50)$$

Identical analysis can be performed for the magnetic field and current density resulting in the following:

$$\nabla^2 \vec{H} = -j\omega\mu\sigma \vec{H}, \text{ and} \quad (4-51)$$

$$\nabla^2 \vec{J} = -j\omega\mu\sigma \vec{J}. \quad (4-52)$$

Now consider the differential equations (4-50)-(4-52) in the example of a plane conductor of infinite depth, with no field variations along the width or length dimension. The analysis of this topology remains important to conductors with finite topology because the depth over which significant fields are concentrated is very small. Also, any field variations along the surface due to edge effects or curvature are small compared with the variations into the conductor and may be neglected.

For the uniform field situation shown in *Figure 4-5* with the electric field in the  $z$  direction assuming no variations in the  $y$  or  $z$  directions, (4-50) becomes:

$$\frac{d^2 E_z}{dx^2} = -j\omega\mu\sigma E_z = \tau^2 E_z, \quad (4-53)$$

where

$$\tau^2 = -j\omega\mu\sigma. \quad (4-54)$$

Taking the positive root of  $\sqrt{j}$  one obtains the following:

$$\tau = (1+j)\sqrt{\frac{\omega\mu\sigma}{2}} = \frac{1+j}{\delta}, \quad (4-55)$$

where

$$\delta = \sqrt{\frac{2}{\omega\mu\sigma}} \text{ m.} \quad (4-56)$$

The quantity  $\delta$  is called the depth of penetration, or skin depth.

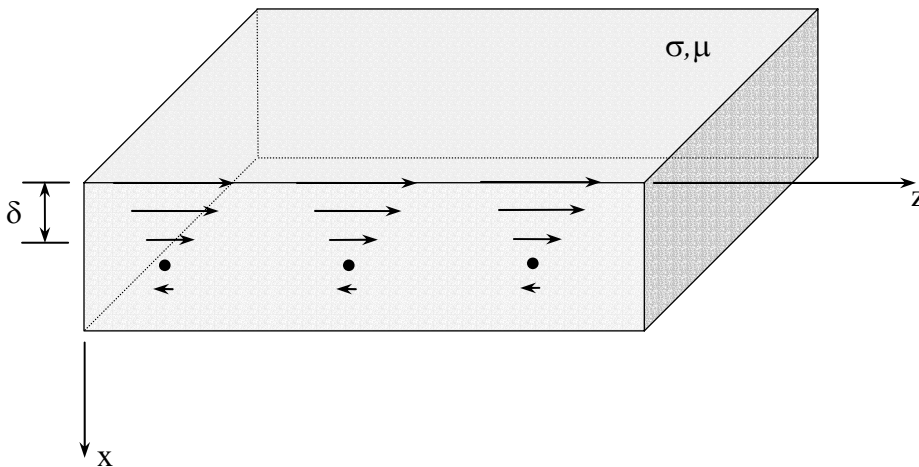


*Figure 4-5: A plane solid conductor with current flowing in the  $x$ -direction.*

Processing a complete solution to the differential equation in terms of exponentials results in the following:

$$E_z = C_1 e^{-\tau x} + C_2 e^{\tau x}. \quad (4-57)$$

The field will increase to infinity at  $x = \infty$  unless  $C_2$  is zero. The coefficient  $C_1$  may be written as the field at the surface if we let  $E_z = E_o$  when  $x = 0$ . This results in the following:

$$E_z = E_o e^{-\tau x} = E_o e^{-x/\delta} e^{-jx/\delta} . \quad (4-58)$$

Since the magnetic field and current density are governed by the same differential equation, this results in the following:

$$H_y = H_o e^{-x/\delta} e^{-jx/\delta} , \text{ and} \quad (4-59)$$

$$J_z = J_o e^{-x/\delta} e^{-jx/\delta} . \quad (4-60)$$

It is evident that the magnitudes of the fields and current decrease exponentially with penetration into the conductor.

#### 4.1.9 Resistance Line Parameter

The decay of fields into a good conductor may be looked at as the attenuation of a plane wave as it propagates into the conductor or from the point of view that induced fields from the time-varying currents tend to counter the applied fields. Currents concentrate near the surface and the ratio of the surface electric field to the current flow gives an internal impedance, the contribution to impedance from the fields penetrating the conductor.

The total current found flowing past a unit width on the surface of the plane conductor is found by integrating the current density (4-60) from the surface to an infinite depth [42] as:

$$I = \int_0^{\infty} J_z dx = \int_0^{\infty} J_o e^{-x/\delta} e^{-jx/\delta} dx = \frac{J_o \delta}{(1+j)} . \quad (4-61)$$

The electric field at the surface is related to the current density at the surface by the following:

$$E_o = \frac{J_o}{\sigma} , \quad (4-62)$$

so the effective internal impedance of the surface for unit width and unit length is given by:

$$Z_s = \frac{E_o}{I} = \frac{(1+j)}{\delta \sigma} = R_s + jX_s . \quad (4-63)$$

Therefore, the equivalent resulting surface resistance is given as:

$$R_s = \frac{1}{\delta \sigma} = \sqrt{\frac{\omega \mu}{2\sigma}}. \quad (4-64)$$

The surface reactance is equal in magnitude to the surface resistance from (4-63) as:

$$X_s = \omega L_s = \frac{1}{\delta \sigma} = \sqrt{\frac{\omega \mu}{2\sigma}}. \quad (4-65)$$

Therefore, the effective resistance for a surface can be determined if it is possible to calculate the surface reactance. So the surface inductance is given by:

$$L_s = \sqrt{\frac{\mu}{2\sigma \omega}} = \frac{\mu \delta}{2}, \quad (4-66)$$

which is in effect the inductance for a layer of thickness of  $\frac{1}{2} \delta$ . Suppose we consider that the magnetic field just outside the conductor is allowed to penetrate a distance of  $\frac{1}{2} \delta$  into the conductor, and that the dielectric outside the conductor has a permeability of free-space,  $\mu_o$ . The change in external inductance would be given by:

$$\Delta L = \frac{\mu}{\mu_o} \frac{\delta}{2} \frac{dL}{dz}. \quad (4-67)$$

Therefore, one can write the equivalent surface resistance for the conductor as:

$$R = \omega \Delta L = \omega \frac{\mu}{\mu_o} \frac{\delta}{2} \frac{dL}{dz} = \frac{R_s}{\mu_o} \frac{dL}{dz} \quad \Omega / \text{m}. \quad (4-68)$$

For the case of the parallel wire topology it can be found that:

$$R = -\frac{R_s}{\mu_o} \frac{\partial L}{\partial d} \quad \Omega / \text{m}. \quad (4-69)$$

Expressing the inductance (4-44) in logarithmic form, and keeping the assumption of  $\mu_r$  equal to unity for the dielectric, produces the following:

$$R = -\frac{R_s}{\mu_o} \frac{\partial}{\partial d} \left[ \frac{\mu_o}{\pi} \ln \left\{ \frac{D}{d} + \sqrt{\left( \frac{D}{d} \right)^2 - 1} \right\} \right] \quad \Omega / \text{m}, \quad (4-70)$$

so that

$$R = -\frac{R_s}{\pi} \left[ \frac{D}{d} - \sqrt{\left(\frac{D}{d}\right)^2 - 1} \right]^{-1} \left[ 1 + \frac{\left(\frac{D}{d}\right)}{\sqrt{\left(\frac{D}{d}\right)^2 - 1}} \right] \left[ -\frac{D}{d^2} \right] \Omega / \text{m}, \quad (4-71)$$

which reduces to

$$R = \frac{R_s}{\pi d} \frac{\frac{D}{d}}{\sqrt{\left(\frac{D}{d}\right)^2 - 1}} \Omega / \text{m}. \quad (4-72)$$

The first term is simply the resistance of the surface layers for a conductor, while the second term is the proximity factor. For the case of the parallel wire topology where there are two wires, the final result of (4-72) needs to be doubled resulting in the following:

$$R = \frac{2R_s}{\pi d} \frac{\frac{D}{d}}{\sqrt{\left(\frac{D}{d}\right)^2 - 1}} \Omega / \text{m}. \quad (4-73)$$

#### 4.1.10 Internal Inductive Line Parameter

The internal inductance due to the skin effect or penetration of the field lines into the conductor will be developed in this section. We will utilize the energy method to calculate the internal inductance. The magnetic energy may be found by integrating an energy density of  $\frac{1}{2}\mu H^2$  throughout the volume of significant fields. From a circuit point of view this is known to be  $\frac{1}{2}LI^2$ , where  $I$  is the instantaneous current flow through the inductance. Equating these two forms gives:

$$\frac{1}{2}LI^2 = \int_v \frac{\mu}{2} H^2 dV \quad (4-74)$$

The magnetic field distribution for a semi-infinite conductor with sinusoidally varying currents was found (4-59) to be:

$$H_y = -\frac{\sigma\delta E_o}{(1+j)} e^{-x/\delta} e^{-jx/\delta}, \quad (4-75)$$

where the coordinate system of *Figure 4-5* is used. The current per unit width,  $I$ , is just the value of  $H_y$  at the surface of the plane conductor and given by:

$$I = -H_y(0) = \frac{\sigma\delta E_o}{(1+j)}. \quad (4-76)$$

We may now apply (4-74) to the calculation of  $L$  although it is recognized that  $I$  and  $H$  in this case are written for instantaneous forms. Rewriting (4-74) for time-average stored energies we find

$$\frac{1}{4}L|I|^2 = \int_v \frac{\mu}{4}|H|^2 dV \quad (4-77)$$

Taking a width,  $w$ , so that the current is  $wI$ , and a length,  $l$ , and substituting (4-75) and (4-76) into (4-77) produces the following:

$$\frac{L}{4} \frac{\sigma^2 \delta^2 E_o^2}{2} w^2 = wl \int_0^\infty \frac{\mu}{4} \frac{\sigma^2 \delta^2 E_o^2}{2} e^{-\frac{2x}{\delta}} dx, \quad (4-78)$$

or

$$L = \frac{\mu l \delta}{2w}, \quad (4-79)$$

so

$$\omega L = \frac{l}{w} \frac{\mu \omega \sigma}{2\sigma} \sqrt{\frac{2}{\mu \omega \sigma}} = R_s \frac{l}{w}, \quad (4-80)$$

where relations for skin depth and surface resistivity have been substituted from earlier work. To correlate this result to the parallel wire topology, one can implement the proximity portion of the resistance from (4-72) as follows:

$$R_s \frac{l}{w} \Rightarrow \frac{R_s}{\pi d} \frac{\frac{D}{d}}{\sqrt{\left(\frac{D}{d}\right)^2 - 1}}, \quad (4-81)$$

or

$$L_{\text{int}} = \frac{R_s}{\omega \pi d} \frac{\frac{D}{d}}{\sqrt{\left(\frac{D}{d}\right)^2 - 1}} = \frac{R}{\omega}. \quad (4-82)$$

The final result of the internal inductive derivation for a parallel wire is given in (4-82) and will be used in future development of the twisted pair equations. The total inductance of the parallel wire topology is the sum of the internal and external resistance given as:

$$L = L_{\text{int}} + L_{\text{ext}}. \quad (4-83)$$

#### 4.1.11 Conductance Line Parameter

The conductance per unit length for the parallel line topology will be developed in this section. It has been assumed that the dielectric has a complex permittivity as  $\epsilon = \epsilon' - j\epsilon''$ , where  $\epsilon''$  includes the conductivity of the dielectric, assuming it is non-zero. The total shunt current consists of a displacement current,  $I_D$ , and a conduction current,  $I_S$ . The current leaving the conductor of positive potential is given by [41]:

$$I = I_D + I_S = j\omega\epsilon \oint_S \vec{e} \cdot \vec{n} dl = j\omega\epsilon' \oint_S \vec{e} \cdot \vec{n} dl + \omega\epsilon'' \oint_S \vec{e} \cdot \vec{n} dl, \quad (4-84)$$

where  $\vec{n}$  is the normal component and  $\vec{e}$  is the transverse component of the electric field with the  $z$  dependence separated. The first integral on the right gives the displacement current and the second integral gives the conduction current. The total shunt admittance is given by  $Y = j\omega C + G = (I_S + I_D)/V_o$  and it can be seen that:

$$G = \frac{I_S}{V_o} = \frac{I_S}{I_D} \frac{I_D}{V_o} = \frac{\omega\epsilon''}{\epsilon'} C, \quad (4-85)$$

since  $j\omega C = I_D/V_o$  and  $j\omega C / j\omega\epsilon' = C/\epsilon'$ . The relationship in (4-85) shows that the conductance can be calculated from the capacitance in (4-37) producing the following:

$$G = \frac{\pi\omega\epsilon''}{\cosh^{-1}\left(\frac{D}{d}\right)} \text{ S/m}. \quad (4-86)$$

The final result of the conductance derivation for a parallel wire topology is given in (4-86) and will be used in future development of the twisted pair equations.

#### 4.1.12 Summary of Line Parameters for Parallel Wires

To conclude the derivation of the parallel wire line parameters, a summary of each parameter is given below.

*Capacitance:*

$$C = \frac{\pi \epsilon'}{\cosh^{-1}\left(\frac{D}{d}\right)} \quad \text{F / m}, \quad (4-87)$$

where  $\epsilon'$  is the real part of the complex permittivity including the dielectric constant of the insulating material,  $D$  is the center-spacing between the parallel wires, and  $d$  is the diameter of the conductor.

*Inductance:*

$$L = \frac{\mu}{\pi} \cosh^{-1}\left(\frac{D}{d}\right) + \frac{R_s}{\omega \pi d} \frac{\frac{D}{d}}{\sqrt{\left(\frac{D}{d}\right)^2 - 1}} \quad \text{H / m}, \quad (4-88)$$

where  $\mu$  is the permeability of air (assuming  $\mu_r$  is unity),  $R_s$  is the surface resistance given in (4-64), and  $\omega$  is the radian frequency.

*Resistance:*

$$R = \frac{2R_s}{\pi d} \frac{\frac{D}{d}}{\sqrt{\left(\frac{D}{d}\right)^2 - 1}} \quad \Omega / \text{m}, \quad (4-89)$$

where  $\sigma$  is the conductivity of the conductor used in the parallel wire topology.

*Conductance:*

$$G = \frac{\pi\omega\varepsilon''}{\cosh^{-1}\left(\frac{D}{d}\right)} \text{ S / m,} \quad (4-90)$$

where  $\varepsilon''$  is the imaginary part of the complex permittivity and includes the conductivity of the dielectric.

## 4.2 Skin Effect in Round Wires

The uniform current distribution of a plane conductor was presented in an earlier section and used for the high frequency approximation of the resistance and internal inductance. In this section the non-uniform current distribution such as that found in a round wire will be presented. From the developed current distribution, the impedance of the round wire will be recalculated resulting in new models for the resistance and internal inductance. Finally, the resulting line parameters will be incorporated with the proximity portion of the parallel line equations. This analysis will produce a wideband representation of the parallel line models developed in the earlier section.

### 4.2.1 Wideband Current Distribution of Round Wires

To perform this analysis for good conductors of round wires, it is first recalled that for good conductors, the displacement current is negligible in comparison with the conduction current so recall that:

$$\nabla \times \vec{H} = \vec{J} = \sigma \vec{E}. \quad (4-91)$$

Faraday's law equation in phasor form is given as:

$$\nabla \times \vec{E} = -j\omega\mu \vec{H}. \quad (4-92)$$

From (4-91) and (4-92) the differential equation for the current density was derived as in (4-52):

$$\nabla^2 \vec{J} = -j\omega\mu\sigma \vec{J}. \quad (4-93)$$

Taking the current in the  $z$  direction with no variations with  $z$  or the angle,  $\phi$ , around the diameter of the cable, equation (4-93) expressed in cylindrical coordinates is then:

$$\frac{d^2 J_z}{dr^2} + \frac{1}{r} \frac{dJ_z}{dr} + T^2 J_z = 0, \quad (4-94)$$

where

$$T^2 = -j\omega\mu\sigma, \quad (4-95)$$

or

$$T = j^{-\frac{1}{2}} \sqrt{\omega\mu\sigma} = j^{-\frac{1}{2}} \frac{\sqrt{2}}{\delta}, \quad (4-96)$$

where  $\delta$  is the parameter called the skin depth. The equation in (4-94) is a Bessel equation. The resulting two independent solutions are as follows:

$$J_z = AJ_0(Tr) + BH_0^{(1)}(Tr), \quad (4-97)$$

where  $J_0$  is the zeroth order Bessel function of the first kind and  $H_0^{(1)}$  is the zeroth order Hankel function of the first kind.

For a solid wire,  $r = 0$  is included in the solution, and it is necessary that  $B = 0$  since a study of the Hankel function,  $H_0^{(1)}$ , shows that this is infinite @  $r = 0$ . Therefore,

$$J_z = AJ_0(Tr). \quad (4-98)$$

The arbitrary constant  $A$  can be evaluated in terms of the current density at the surface of the round wire. This boundary condition is given as follows:

$$J_z = \sigma E_0, \quad \text{at } r_0, \quad (4-99)$$

where  $E_0$  is the surface electric field, and  $r_0$  is the radius of the round wire, or  $d = 2 \cdot r_0$ .

Equation (4-98) then becomes the following:

$$J_z = \frac{\sigma E_0}{J_0(Tr_0)} J_0(Tr). \quad (4-100)$$

A study of the series definitions of the Bessel functions with complex arguments shows that  $J_0$  is complex. It will be convenient to break the complex Bessel function into real and imaginary parts shown as:

$$Ber(v) \stackrel{\Delta}{=} \text{real part of } J_0(j^{-\frac{1}{2}}v), \text{ and}$$

$$Bei(v) \stackrel{\Delta}{=} \text{imaginary part of } J_0(j^{-\frac{1}{2}}v).$$

The definitions result in the following:

$$J_0(j^{\frac{1}{2}}v) = Ber(v) + j Bei(v). \quad (4-101)$$

The resulting current density is given as:

$$J_z = \sigma E_0 \frac{Ber\left(\sqrt{2} \frac{r}{\delta}\right) + j Bei\left(\sqrt{2} \frac{r}{\delta}\right)}{Ber\left(\sqrt{2} \frac{r_0}{\delta}\right) + j Bei\left(\sqrt{2} \frac{r_0}{\delta}\right)}. \quad (4-102)$$

#### 4.2.2 Impedance of Round Wires

As described earlier, the internal impedance of the round wire includes the resistance and the internal inductance contribution of the overall inductance parameter. The impedance is calculated from the total current in the wire and the electric intensity at the surface [40]. The total current may be obtained from the magnetic field at the surface of the wire, since the line integral of the magnetic field around the outside of the wire must be equal to the total current inside the wire given as:

$$\oint \vec{H} \cdot d\vec{l} = I, \quad (4-103)$$

or

$$2\pi r_0 H_\phi \Big|_{r=r_0} = I. \quad (4-104)$$

The magnetic field is obtained from the electric field using Maxwell's equations as:

$$\nabla \times \vec{E} = -j\omega\mu \vec{H}. \quad (4-105)$$

Only the fields  $E_z$  and  $H_\phi$  are present due to no variations in the  $z$  or  $\phi$  directions for the round wire resulting in only  $r$  derivatives remaining shown as:

$$H_\phi = \frac{1}{j\omega\mu} \frac{dE_z}{dr}. \quad (4-106)$$

From the previous section, the current density is related to the electric field by the conductivity, or

$$E_z = \frac{J_z}{\sigma} = E_0 \frac{J_0(Tr)}{J_0(Tr_0)}. \quad (4-107)$$

Substituting into (4-106) and recalling from the previous discussion that  $T^2 = -j\omega\mu\sigma$  gives:

$$H_\phi = \frac{E_0 T}{j\omega\mu} \frac{J'_0(Tr)}{J_0(Tr_0)} = -\frac{\sigma E_0}{T} \frac{J'_0(Tr)}{J_0(Tr_0)}, \quad (4-108)$$

where  $J'_0(Tr)$  is the derivative of  $J_0(Tr)$  with respect to  $Tr$ .

Solving for  $I$  from (4-104) results in the following:

$$I = -\frac{2\pi r_0 \sigma E_0}{T} \frac{J'_0(Tr)}{J_0(Tr_0)}. \quad (4-109)$$

The internal impedance per unit length is obtainable by the following:

$$Z_{\text{int}} \triangleq \frac{E_z(r_0)}{I} = \frac{T J_0(Tr_0)}{2\pi r_0 \sigma J'_0(Tr)}. \quad (4-110)$$

To interpret (4-110) for arbitrary, or wideband, frequencies, we need to break the Bessel functions into real and imaginary parts, recall that:

$$J_0(j^{-\frac{1}{2}}v) = \text{Ber}(v) + j \text{Bei}(v),$$

and note the derivative as

$$\text{Ber}'(v) + j \text{Bei}'(v) = \frac{d}{dv} [\text{Ber}(v) + j \text{Bei}(v)] = j^{-\frac{1}{2}} J'_0(j^{-\frac{1}{2}}v). \quad (4-111)$$

The impedance can now be rewritten as follows:

$$Z_{\text{int}} = R + j\omega L_{\text{int}} = \frac{jR_s}{\sqrt{2\pi r_0}} \left[ \frac{\text{Ber}(q) + j \text{Bei}(q)}{\text{Ber}'(q) + j \text{Bei}'(q)} \right], \quad (4-112)$$

where

$$R_s = \frac{1}{\delta \sigma} = \sqrt{\frac{\omega \mu}{2\sigma}}, \text{ and } q = \frac{\sqrt{2}r_0}{\delta}.$$

This produces the internal resistance and inductance equations as follows:

$$R = \frac{R_s}{\sqrt{2\pi r_0}} \left[ \frac{Ber(q)Bei'(q) - Bei(q)Ber'(q)}{[Ber'(q)]^2 + [Bei'(q)]^2} \right], \text{ and} \quad (4-113)$$

$$\omega L_{\text{int}} = \frac{R_s}{\sqrt{2\pi r_0}} \left[ \frac{Ber(q)Ber'(q) + Bei(q)Bei'(q)}{[Ber'(q)]^2 + [Bei'(q)]^2} \right], \quad (4-114)$$

or

$$L_{\text{int}} = \frac{R_s}{\omega \sqrt{2\pi r_0}} \left[ \frac{Ber(q)Ber'(q) + Bei(q)Bei'(q)}{[Ber'(q)]^2 + [Bei'(q)]^2} \right]. \quad (4-115)$$

### 4.2.3 Relationship to Parallel Line Equations

This section will evaluate the revised resistance and inductance equations for the wideband parallel line equations incorporating the results from the round wire current distribution discussion in the previous section.

*Inductance:*

The actual internal inductance needs to be multiplied by two to account for the two wires and also included is the proximity factor as shown in (4-116):

$$L_{\text{int}} = \frac{2R_s}{\omega \sqrt{2\pi r_0}} \left[ \frac{Ber(q)Ber'(q) + Bei(q)Bei'(q)}{[Ber'(q)]^2 + [Bei'(q)]^2} \right] \frac{\frac{D}{d}}{\sqrt{\left(\frac{D}{d}\right)^2 - 1}} \text{ H / m.} \quad (4-116)$$

The resulting overall inductance is the sum of the internal inductance and external inductance (4-44) (which remains the same from the previous evaluation) as follows:

$$L = \frac{\mu}{\pi} \cosh^{-1}\left(\frac{D}{d}\right) + \frac{2R_s}{\omega \sqrt{2\pi r_0}} \left[ \frac{Ber(q)Ber'(q) + Bei(q)Bei'(q)}{[Ber'(q)]^2 + [Bei'(q)]^2} \right] \frac{\frac{D}{d}}{\sqrt{\left(\frac{D}{d}\right)^2 - 1}} \text{ H / m.} \quad (4-117)$$

*Resistance:*

The resulting resistance found in the previous section and shown in (4-113) also needs to be multiplied by two to account for both wires. This result then needs to be multiplied by the same proximity factor as the inductance resulting in the following:

$$R = \frac{2R_s}{\sqrt{2\pi r_0}} \left[ \frac{Ber(q)Bei'(q) - Bei(q)Ber'(q)}{[Ber'(q)]^2 + [Bei'(q)]^2} \right] \frac{\frac{D}{d}}{\sqrt{\left(\frac{D}{d}\right)^2 - 1}} \quad \Omega / \text{m}. \quad (4-118)$$

### 4.3 Modeling the Permittivity of the Insulating Material

The real and imaginary parts of the admittance function have to be related by a pair of Hilbert transforms [43]. This will assure that the resulting network is causal. The causality of relationship between the conductance and capacitance lies in the causality of the model relating the real and imaginary parts of the complex permittivity. The relationship between these parameters is shown again for convenience.

$$G = \frac{\omega \varepsilon''}{\varepsilon'} C \quad (4-119)$$

The well-known model developed by Debye<sup>1</sup> for the complex permittivity satisfies the Hilbert transform pairs and is written as follows:

$$\varepsilon^*(\omega) = \varepsilon_o \left[ \varepsilon'_{r\infty} + \frac{\varepsilon'_{rs} - \varepsilon'_{r\infty}}{1 + j\omega\tau_e} \right], \quad (4-120)$$

where  $\varepsilon'_{rs}$  and  $\varepsilon'_{r\infty}$  are the relative permittivities at zero and infinite frequencies, respectively.  $\tau_e$  is the new relaxation time constant related to the original relaxation time,  $\tau$ , by:

$$\tau_e = \tau \left[ \frac{\varepsilon'_{rs} + 2}{\varepsilon'_{r\infty} + 2} \right]. \quad (4-121)$$

From (4-120),  $\varepsilon'_r(\omega)$  and  $\varepsilon''_r(\omega)$  are obtained as follows:

$$\varepsilon'_r(\omega) = \frac{\text{Re}[\varepsilon^*(\omega)]}{\varepsilon_o} = \varepsilon'_{r\infty} + \frac{\varepsilon'_{rs} - \varepsilon'_{r\infty}}{1 + \omega^2\tau_e^2}, \quad (4-122)$$

and

$$\varepsilon''_r(\omega) = -\frac{\text{Im}[\varepsilon^*(\omega)]}{\varepsilon_o} = \frac{(\varepsilon'_{rs} - \varepsilon'_{r\infty})\omega\tau_e}{1 + \omega^2\tau_e^2}. \quad (4-123)$$

<sup>1</sup> The Debye model is used here for convenience to implement the Kramers-Kronig causality relationships.

The equations for the capacitance and conductance as developed for the parallel lines, re-written for convenience are given as:

$$C = \frac{\pi\epsilon'}{\cosh^{-1}\left(\frac{D}{d}\right)} \quad \text{F / m,} \quad (4-124)$$

and

$$G = \frac{\pi\omega\epsilon''}{\cosh^{-1}\left(\frac{D}{d}\right)} \quad \text{S / m.} \quad (4-125)$$

A common method for transmission line models using the insulating material found in the twisted pair cables is to assume the capacitance is constant, arbitrary of frequency range. For this to be possible  $\epsilon'$  would need to be constant, re-writing (4-122) so that it is independent of frequency forces the following equality:

$$\epsilon'_{rs} = \epsilon'_{r\infty}, \quad (4-126)$$

resulting in

$$\epsilon'_r = \epsilon'_{r\infty}, \quad (4-127)$$

and

$$\epsilon''_r = 0. \quad (4-128)$$

Finally solving for the capacitance and inductance using (4-127) and (4-128) gives:

$$C = \frac{\pi\epsilon'}{\cosh^{-1}\left(\frac{D}{d}\right)} \quad \text{F / m,} \quad (4-129)$$

and

$$G = 0 \quad \text{S / m.} \quad (4-130)$$

It is appropriate to apply different models to fit the measured data as accurately as possible, though obtaining quality measurements of the small conductance parameter is difficult. This may include using one of the above models, developing a new model, or performing material characterizing measurements on the insulation to obtain wideband permittivity characteristics.

## 4.4 Modeling of the Twisting Effects of Twisted Pair Cables

The effects of twisting the parallel line model will be investigated in this section. Through cable measurements, it was found that the twisting effects on the line parameters involved mainly the reactance parameters, the inductance and capacitance. Some proposed modeling techniques regarding the effects of the cable twisting are presented in the following discussion.

### 4.4.1 Twisting Length Estimation

As the parallel line cable model is twisted it becomes a helical structure. The resulting helical structure [44], due to the physical shape of the structure, will have a different physical length than the length of the parallel wire topology, or axial length. The relationship between these two lengths will be developed.

The parameters of the helix will first be given as follows:

$D_h$  = Outer diameter of the helix,

$C_h$  = Circumference of the Helix =  $\pi D_h$ ,

$S_h$  = Spacing between turns =  $C_h \tan(\alpha)$ ,

$\alpha$  = Pitch angle =  $\tan^{-1} \frac{S_h}{C_h}$ ,

$L_h$  = Length of one turn =  $\sqrt{C_h^2 + S_h^2}$ ,

$N_h$  = Number of turns, and

$A_h$  = Axial Length =  $N_h S_h$ .

It can be seen through the equations that if the pitch angle extends to  $90^\circ$ , the helical structure becomes a linear structure, or the parallel line topology.

The resulting new length estimation needs to be incorporated into the developed models to view if the effects of this relationship compensates completely for the cable twisting.

### 4.4.2 Fields of Helical Structures

Another investigation into the effects of the twisting of the parallel line cables is to examine the analysis of helical structures such as helical antennas [44], [45] and slow wave structures

[40]. The field analysis, development of the propagation constant, and other details have been documented for these structures and may be useful in adapting the model to cables of different twisting rates.

#### 4.4.3 Modeling of Helical Structures

The last mentioned investigation is the application of known models to represent the twisting effects of the cable. A method for helical structures proposed in [46] relates the twisted pair cables to model consisting of sets of series models of the parallel transmission line model followed by that of a circular ring. Models have been previously developed for ring structures such as ring antennas. The possibility of incorporating these two models together to model the twisted pair cable is plausible.

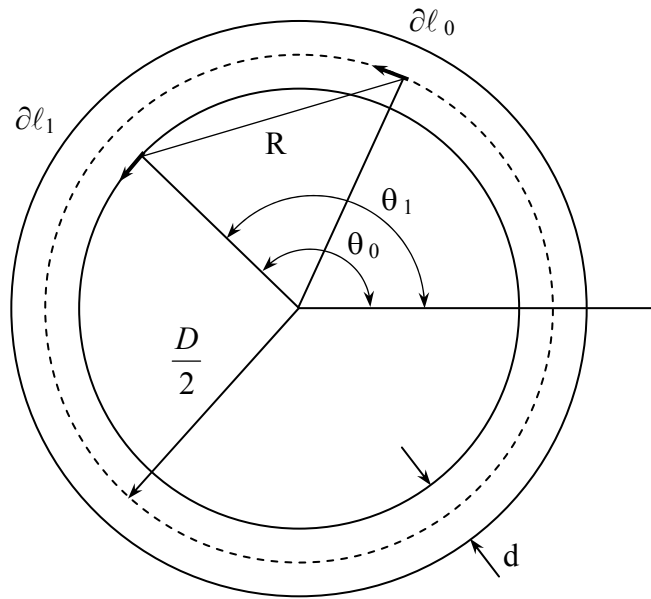


Figure 4-6: A circular conducting loop.

To further this discussion, an investigation in the self-inductance of a circular conducting loop will be discussed. Following the derivation in [47], consider a conductor of diameter,  $d$ , bent into a circular loop of mean diameter,  $D$ , as shown in Figure 4-6. The magnitudes of  $\partial l_1$  and  $\partial l_0$  are given by

$$2|\partial l_0| = D\partial\theta_0, \text{ and } 2|\partial l_1| = (D-d)\partial\theta_1 \approx D\partial\theta_1. \quad (4-131)$$

The angle between of  $\partial \ell_1$  and  $\partial \ell_0$  is  $\theta_1 - \theta_0$ , and hence:

$$\partial \ell_0 \cdot \partial \ell_1 = \frac{D^2}{4} \cos(\theta_1 - \theta_0) \partial \theta_0 \partial \theta_1. \quad (4-132)$$

The distance,  $R$ , between the two elements of arc length is given by:

$$R^2 = \frac{1}{4} \left[ D^2 + (D-d)^2 - 2D(D-d) \cos(\theta_1 - \theta_0) \right]. \quad (4-133)$$

Hence the external inductance is given by:

$$L_{coil\_ext} = \frac{\mu_o D^2}{4\pi} \int_0^{2\pi} \int_0^{2\pi} \frac{\cos(\theta_1 - \theta_0) \partial \theta_0 \partial \theta_1}{[2D(D-d) + d^2 - 2D(D-d) \cos(\theta_1 - \theta_0)]^{0.5}}. \quad (4-134)$$

Through integrating over  $\theta_1$  first, perform a change of variables by replacing  $\theta_1 - \theta_0$  with  $\theta$  and  $\partial \theta_1$  with  $\partial \theta$  resulting in the following:

$$L_{coil\_ext} = \frac{\mu_o D^2}{4\pi} \int_0^{2\pi} \int_0^{2\pi} \frac{\cos(\theta) \partial \theta \partial \theta_0}{[d^2 - 2D(D-d)(1 - \cos \theta)]^{0.5}}. \quad (4-135)$$

The limits of the integrals do not need to be altered because the origin in  $\theta_1$  is arbitrary in view of the circular symmetry. Since the result of the integration of  $\theta$  is independent of  $\theta_0$ , we may perform the integration over  $\theta_0$  at once, resulting in a factor of  $2\pi$ . We now have the following result:

$$L_{coil\_ext} = \frac{\mu_o D^2}{2} \int_0^{2\pi} \frac{\cos(\theta) \partial \theta}{[d^2 - 2D(D-d)(1 - \cos \theta)]^{0.5}}. \quad (4-136)$$

This expression can be evaluated using elliptic integrals. The resulting expression from this process is given as:

$$L_{coil\_ext} = \frac{\mu_o D}{2} \left[ \left( \frac{2}{k} - k \right) K - \frac{2}{k} E \right], \quad (4-137)$$

where

$$k^2 = \frac{4D(D-d)}{(2D-d)^2}, \quad (4-138)$$

and  $K$  and  $E$  are elliptic integrals given as follows:

$$E = \int_0^{2\pi} (1 - k^2 \sin^2(\alpha))^{0.5} \partial\alpha, \text{ and} \quad (4-139a)$$

$$K = \int_0^{2\pi} \frac{\partial\alpha}{(1 - k^2 \sin^2(\alpha))^{0.5}}. \quad (4-139b)$$

After the above integrals are calculated, the result reduces to the following:

$$L_{coil\_ext} = \frac{\mu_o D}{2} \left( \ln \frac{8D}{d} - 2 \right). \quad (4-140)$$

The resulting overall inductance of the twisted pair cable per unit length sums the external inductance (4-44), the internal inductance (4-116), and the just derived external coil inductance (4-140) given as

$$L = L_{ext} + L_{int} + n \cdot L_{coil\_ext}. \quad (4-141)$$

where  $n$  is the number of coils per unit length.

## Chapter 5

### Twisted Pair Cable Measurements and Model Verification

#### 5 Introduction/Overview

This chapter will summarize the processes and procedures used to characterize the SEALPIC<sup>®</sup> twisted-pair communication cables manufactured by Superior Essex as well as provide verification of the designed twisted pair models (from Chapter 4) using the measurement results. The primary line parameters (resistance, inductance, conductance, and capacitance per unit length) were extracted from open and short-circuited frequency domain measurements on the cables. The measurements were performed on 22 and 24 AWG cables over the frequency range of 100 kHz to 10 MHz.

All measurements were performed using the Hewlett Packard HP4195A network analyzer. The lower frequency limit (100 kHz) of the measurement in all cases was due to the Hewlett Packard impedance test adapters (HP41951-61001) used to interface the network analyzer to the cable under test.

#### 5.1 Single Port Measurements (Frequency Domain)

Single port measurements are simply impedance measurements performed over a specified frequency domain. Two measurements using different terminations are needed to extract the primary line parameters (R, L, C, and G) of each of the cables under test: an open-circuited termination impedance measurement,  $Z_{oc}$ , and a short-circuited termination impedance

measurement,  $Z_{sc}$ . The numerical methods used to extract the line parameters from these two measurements will be explained in detail along with the measurement setup resulting in the line parameter values.

### 5.1.1 Measurement Setup

The measurement setup used to perform the single port impedance measurements as well as the calibration procedure will be described in this section. The required equipment for the calibration procedure and measurements are listed below:

- HP 4195A Network/Spectrum Analyzer,
- 0311LB North Hills Balanced Transformer,
- 41951-69001 Impedance Test Adapter,
- Low noise coax 50  $\Omega$ ,
- Calibration standards: Load, Open and Short, and
- Coax to banana type converters and connectors.

The network analyzer is connected to the balun through the impedance test set using the 50  $\Omega$  coax as shown in *Figure 5-1*. In the single port measurements, the balun is used in both the calibration and measurement process as a transition between an unbalanced coaxial line and the balanced twisted-pair cable under test. Because balun is a 50  $\Omega$  to 100 $\Omega$  transformer, on the measurement side of the transformer, two 10  $\Omega$  resistors were added to more closely match the intrinsic impedance of the twisted-pair cable ( $\sim 120 \Omega$ ) for impedance mismatch reduction, or more descriptively to reduce standing waves between the transformer and the cable under test. On the network analyzer side of the balun there is no impedance mismatch with the 50  $\Omega$  coax.

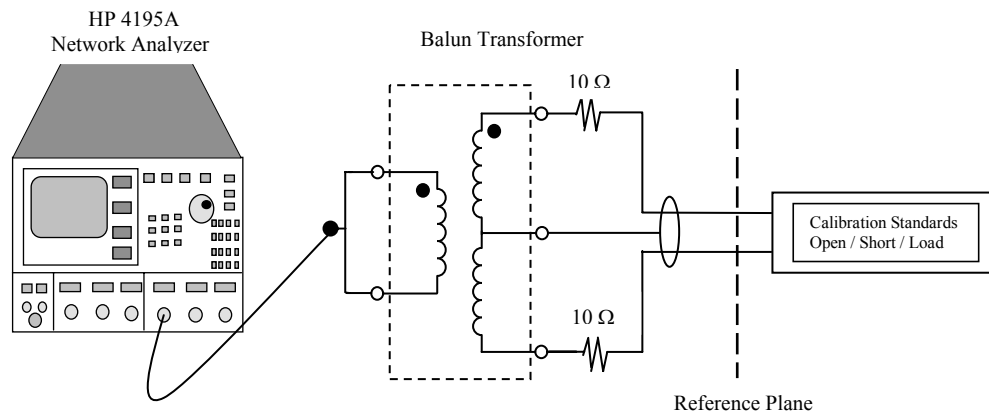


*Figure 5-1: Calibration setup for frequency domain measurements.*

The balun is then connected to a set of banana plug type connectors that will be used to interface the measurement setup to the cable under test.

*Figure 5-1* shows the calibration setup of the single port impedance measurements. The single port full calibration option is used which requires open, short, and load measurement standards. The calibration procedure is performed at the reference plane of the measurement setup to reduce the majority of effects caused by the connections and the small mismatches with the balun. The calibration is also performed over the frequency range between 100 kHz and 10 MHz.

The single port measurement setup, including the cable under test, is shown in *Figure 5-2*. As shown, the cable under test is connected to the balun through the use of the banana type connectors at the reference plane and is also connected through the use of banana type connectors at the termination plane to the open or short-circuited loads. The two measurements consisting of the open-circuited termination impedance measurement,  $Z_{oc}$ , and a short-circuited termination impedance measurement,  $Z_{sc}$  are now performed. The following section will describe the numerical methods used to transform these two measurements to the primary line parameters.

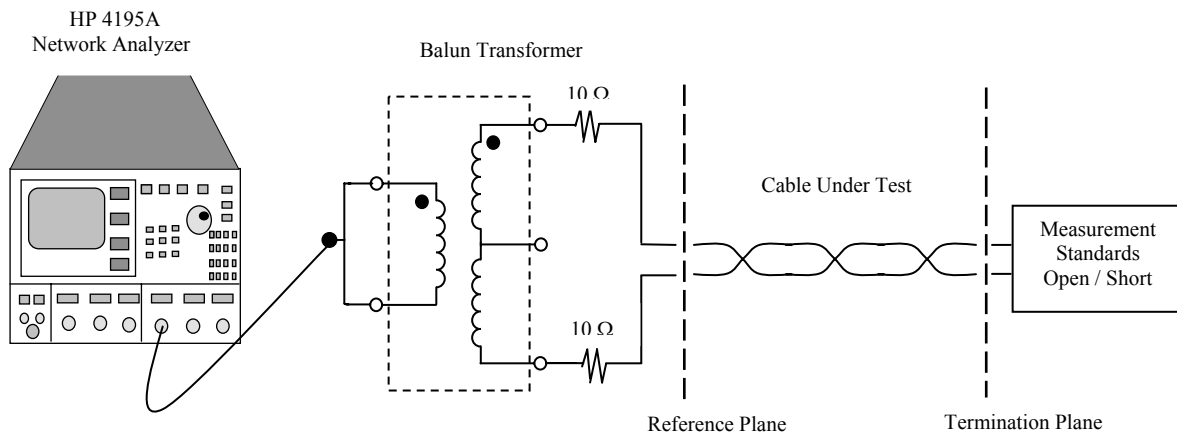


*Figure 5-2: Measurement setup for single port frequency domain measurements.*

### 5.1.2 Numerical Methods used to Obtain Primary Line Parameters

This section introduces the method of extracting the transmission line parameters from the two measurements mentioned in the previous section. This method is used to obtain  $Z_o$ , and  $\gamma$ , and essentially R, L, C, and G of the twisted-pair cable.

Consider the following transmission line diagram,

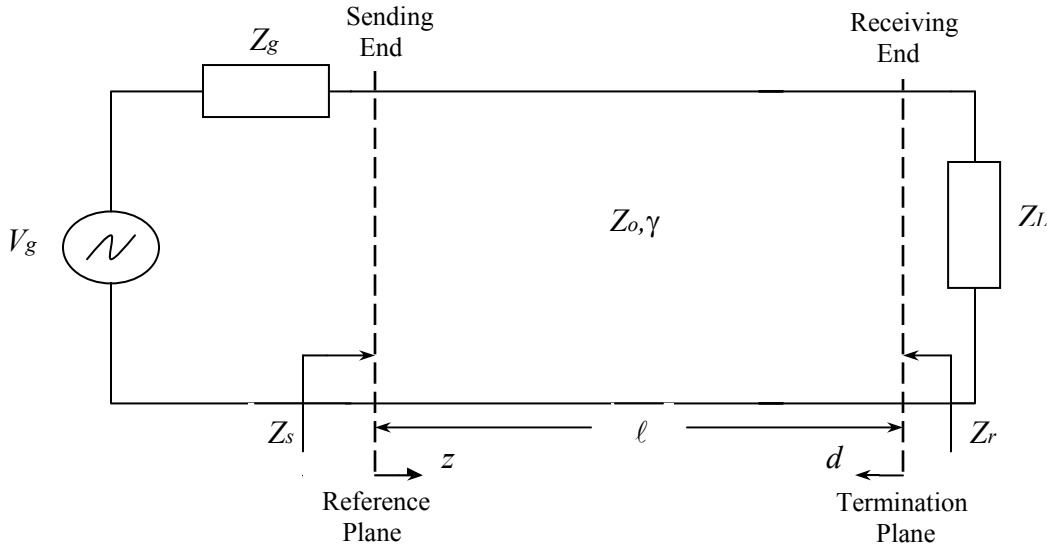


Figure 5-3: General Transmission Line Diagram.

In general, the line impedance computed from the receiving end (or output port) in terms of load impedance,  $Z_L$  and  $Z_o$  is given as:

$$Z = Z_o \frac{(Z_L + Z_o)e^{\gamma d} + (Z_L - Z_o)e^{-\gamma d}}{(Z_L + Z_o)e^{\gamma d} - (Z_L - Z_o)e^{-\gamma d}} \quad (5-1)$$

This impedance in terms of hyperbolic functions using  $e^{\pm\gamma d} = \cosh(\gamma d) \pm \sinh(\gamma d)$  is given as:

$$Z = Z_o \frac{Z_L + Z_o \tanh(\gamma d)}{Z_o + Z_L \tanh(\gamma d)}. \quad (5-2)$$

As mentioned earlier, a common procedure for determining the characteristic (or line) impedance and the propagation constant,  $\gamma$ , of a given transmission line, in our case the twisted-pair cable, is to make an open and a short-circuited measurement.

First, we measure the sending end impedance with the receiving end short-circuited and this is by letting  $d = \ell$  and  $Z_L = 0$  in Equation (5-2).

Then, Equation (5-2) becomes:

$$Z_{sc} = Z_o \tanh(\gamma \ell) \quad (5-3)$$

Second, we measure the sending end impedance with the receiving end open-circuited and this is by letting  $d = \ell$  and  $Z_L = \infty$ .

Then, Equation (5-2) becomes:

$$Z_{oc} = Z_o \coth(\gamma \ell) = \frac{Z_o}{\tanh(\gamma \ell)} \quad (5-4)$$

Solving Equation (5-3) and (5-4) for  $Z_o$  and  $\gamma$  results in:

$$Z_o = \sqrt{(Z_{oc})(Z_{sc})} = R_o + jX_o \quad (5-5)$$

and,

$$\gamma = \sqrt{\frac{(Z_{sc})}{(Z_{oc})}} = \alpha + j\beta \quad (5-6)$$

The characteristic impedance,  $Z_o$ , and the propagation constant,  $\gamma$ , of a transmission line are defined in general as functions of the line parameters as given below:

$$Z_o = \sqrt{\frac{R + j\omega L}{G + j\omega C}} = \sqrt{\frac{Z}{Y}}, \text{ and} \quad (5-7)$$

$$\gamma = \sqrt{(R + j\omega L)(G + j\omega C)} = \sqrt{Z \cdot Y}. \quad (5-8)$$

Then solving (5-8) for  $Z$  and substituting the result into (5-7) produces the following:

$$Z_o = \sqrt{\frac{\gamma^2}{Y^2}} \Rightarrow Y = \frac{\gamma}{Z_o} = G + j\omega C. \quad (5-9)$$

Also, by substituting  $Y$  from (5-9) into (5-7) produces the following:

$$Z_o = \sqrt{\frac{Z}{\gamma} Z_o} \Rightarrow Z = Z_o \cdot \gamma = R + j\omega L. \quad (5-10)$$

Finally, from (5-9) and (5-10),  $R$ ,  $L$ ,  $C$ , and  $G$  of the transmission line model are determined as:

$$R = \text{Re}\{Z_o \cdot \gamma\}, \quad (5-11)$$

$$L = \frac{1}{\omega} \text{Im}\{Z_o \cdot \gamma\}, \quad (5-12)$$

$$G = \operatorname{Re}\left\{\frac{\gamma}{Z_o}\right\}, \text{ and} \quad (5-13)$$

$$C = \frac{1}{\omega} \operatorname{Im}\left\{\frac{\gamma}{Z_o}\right\}. \quad (5-14)$$

## 5.2 Measurement Method and Results<sup>1</sup>

The measurement setup used to characterize the twisted-pair cables was described in Section 5.1. The only task to be performed before proceeding with the measurements is a decision of the length of the cable under test. A problem with resonances occurs at longer cable lengths within the frequency range of interest. Multiple cable lengths between 1.8 m and 12.8 m were initially measured to be able to piecewise the data together surrounding the different resonances. After this investigation, it was found that the shorter length cables give accurate low frequency results (~100 kHz) and a single length cable was chosen for all measurements. The length of 3.0 m was chosen because the low frequency results are highly comparable to the longer length cables and the resonance occurs outside the frequency range of interest ( $f_r > 10\text{MHz}$ ).

This section also contains measurement results concerning the repeatability of the measurements, the variability between different sections of cable, the differences between the different twisted-pairs within the same section of cable, and an investigation into the length errors due to variable twist rates between the different twisted pairs housed within the same cable sheath. An explanation of each of the results will be given in this section of the dissertation. Figures showing the resulting data from each of the measurements are located in Appendix D at the end of this document.

### 5.2.1 Measurement Repeatability

Repeatability is a term describing the process of investigating the precision of measurements taken at different instances in time. Measurements that have high precision are referred to as repeatable. In the case of the cable measurements, three complete measurements (including calibration) were taken at different intervals in time to test the repeatability of the

---

<sup>1</sup> Cross-talk analysis was performed and showed the crosstalk between cable pairs had little effect on the parameter measurements. The effect of crosstalk on the reconstruction routine is planned in the ideas for future research.

single port measurement technique. The results of these measurements can be viewed in Appendix D for the 22AWG cables. The plot of the tabular data from ANSI T1.601-1999 [48] that was previously used in the simulator before this investigation is plotted along with the measurement results.

Investigating the plots will lead to the conclusion that the measurements are repeatable given the minor differences in the measurement results. The differences noticed in the plots must be included as a tolerance level of the measurement setup.

### 5.2.2 Measurement Variability

Variability is a term describing the process of investigating the precision of measurements of different sections of the same cable. Different measurements of different sections that have high precision are referred to as having low variability. In the case of the cable measurements, three measurements (using the same calibration) were taken of three different sections of the 22AWG and the 24AWG cables using the single port measurement technique. The results of these measurements can be viewed in Appendix D. The plot of the tabular data from ANSI T1.601-1999 [48] that was previously used in the simulator before this investigation is plotted along with the measurement results.

Investigating the plots will lead to the conclusion that the cables have a low variability given the minor differences in the measurement results. The differences noticed in the plots show that there are some sign of variability in the cable sections, but this is to be expected due to abnormalities such as a length difference due to variable twisting rates or the position of the cable pair within the metallic sheath.

### 5.2.3 Variations Among Conductor Pairs

Measurements were taken to compare the variations between different conductor pairs among the multiple pairs contained within the cable. This investigation was processed due to the fact that the pairs are known to have different rates of twisting, and the effects of the variable twisting on the measurements needs to be investigated. Using the single port measurement technique (with the same calibration), four different conductor pairs were measured of both the 22 AWG and the 24 AWG cables. The legend of the resulting figures given in Appendix D uses the references listed in *Table 5.1* to define the cable color codes.

Table 5-1: Color codes of the multiple cable pairs measured.

Legend Code	Cable Color
RB	Red / Blue
GnW	Green / White
OW	Orange / White
GW	Gray / White

The results show the variation between the different cable pairs to be small. The differences noticed show that there are some signs of differences between the cable pairs, which brings about the investigation into various twisting rates resulting in different cable lengths.

#### 5.2.4 Length Estimation Error Measurements

The length of the cable under test is required in the evaluation of the RLCG parameters as can be seen from the equations presented in earlier sections. In the investigations involving different twisted-pairs within the same cable, there are some noticeable differences in the results. The difference in the results could be due to the difference in the length of the cables under test. This section is devoted to evaluate this assumption and confirm this possible source of deviation. Single port measurements were again used for this evaluation.

There are two possible sources of variation in determining the length of the cable under test. The first difference between conductor pairs is possibly due to twisting rates as well as the placement within the conducting shield. With an increase in twisting, the resulting variation will also be increased. The second source of variation is introduced by the cutting of the cable and length estimation of the leads involving the connectors and soldering. Assuming enough care was taken in preparing the cables for measurement, the later source of variation should be consistent among the different cable pairs, so the investigation will focus on the source mentioned initially.

##### 5.2.4.1 Measurement Setup

Low frequency measurements will be used to measure the dc resistance,  $R_{dc}$ , which will be related it to the length of the cable. Given that the cable is consistent in physical structure and

electrical properties (i.e., wire diameter and conductivity), the length of the cable will be proportionate to  $R_{dc}$ . The measurement setup consists of a dc or a low frequency resistance meter and a short termination. The measurement frequency in this investigation was 5 Hz using the HP4192A Low Frequency Impedance Meter.

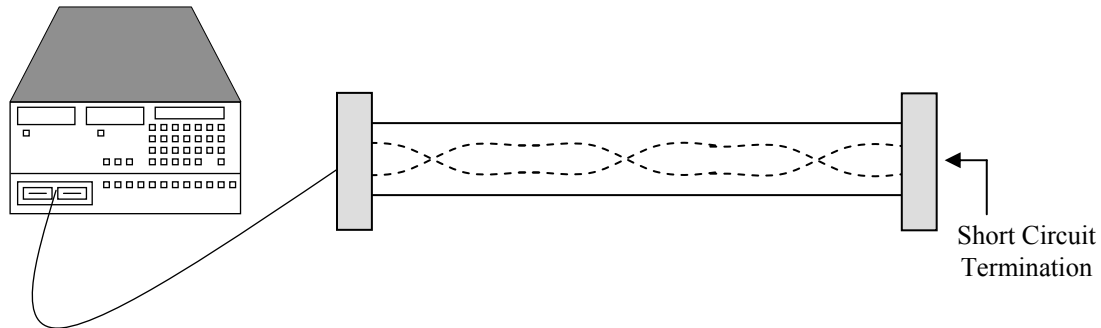


Figure 5-4:  $R_{DC}$  measurement setup for length evaluation.

Six different twisted-pairs with a length of 31.63 meter (63.25 meter round trip, 24AWG cable) were measured. The shorts of each of the cable were implemented using the same procedure on each of the twisted-pairs. Table 5-2 tabulates the results of this analysis by showing the resulting  $R_{dc}$  of each of the twisted pairs. By taking the maximum and minimum values of  $R_{dc}$  we can calculate the percentage deviation between the resistance values. This percentage difference is then related to the length of the 31.63 meter cable in centimeters. Finally, the maximum difference in centimeter per meter of cable is displayed.

Table 5-2: Length evaluation measurement results.

Twisted-Pair	$R_{DC}$ ( $\Omega$ )	Analysis	
		Gray / White	5.536
Orange / White	5.522	$R_{dc}$ min	5.522
Green / White	5.537	% Difference	.307859
Brown / White	5.522	Deviation (m) measured	0.09735
Blue / White	5.538	Deviation (cm) measured	9.735
Blue / Red	5.539	Deviation (cm/m) normalized	0.30778

The maximum percentage deviation in the measurements of the resistance can be found from the minimum and maximum measured  $R_{dc}$  results as:

$$\%Deviation = \frac{R_{dc\ max} - R_{dc\ min}}{R_{dc\ min}} \times 100, \quad (5-15)$$

which corresponds to .30778 cm/m.

To investigate the effect of this maximum possible normalized variation on the line parameters of the cables, the length input into the software used to evaluate the measured data was adjusted by this amount as follows.

$$L_{ADJUSTED} = L_{MEASURED} \pm \frac{Deviation_{NORM}}{2} \quad (5-16)$$

The results of this investigation can be viewed in Appendix D. From this investigation, it is shown that within a specific section of cable, the length of the conductor pairs (due to twisting or placement within the cable itself) may be of slightly different. The results of the length evaluations, through the use of dc measurements, are shown to be a very plausible explanation for some of the measurement differences seen in the earlier sections.

### 5.3 Secondary Line Parameters

The secondary line parameters are examined consisting of the intrinsic impedance,  $Z_o$ , plotted in real,  $R_o$ , and imaginary,  $X_o$ , values along with the propagation constant,  $\gamma$ , plotted in real,  $\alpha$ , and imaginary,  $\beta$ , values. Appendix D contains the plots for both the 22AWG and the 24AWG cables. These values were calculated using the measured parameters of the primary line parameters, R, L, C, and G.

### 5.4 Model Verification

This section will provide validation of the model development presented in Chapter 4 for the twisted-pair communication cables. The initial models used in the system identification routine were developed and published in the ANSI T1E1.4 [4] contribution by British Telecommunications (BT) Laboratories. It was discovered that the developed algorithm, which makes use of these models, produced a non-causal time domain response. Acknowledging the importance of causality when dealing with a modeling process, the research group investigated

methods of producing realizable, causal models. The BT models and the new models will be compared through the use of the time domain reflectometry (TDR) output of the developed system identification algorithm as well as the RLCG parameters.

First, the models reported in the ANSI T1E1.4 contribution will be summarized followed by the summary of the developed models of this research. The empirical models developed by BT Laboratories were empirical formulas fit to data produced through measurements performed by the BT researchers. Conversely, the new models presented in this research were formulated from the parallel line analytical models, which have been described thoroughly in literature. The presented models will be evaluated through an investigation of their accuracy in comparison to measurements performed by the researchers ( $100 \text{ kHz} \leq f \leq 10 \text{ MHz}$ ) and tabulated data presented in ANSI T1.601-1999 ( $10 \text{ Hz} \leq f \leq 5 \text{ MHz}$ ).

#### 5.4.1 ANSI T1E1.4 Contribution Models

The corresponding empirical models for the primary transmission line parameters developed in [4] are as follows:

$$R(f) = \left( r_{oc}^4 + a_c f^2 \right)^{0.25}, \quad (5-17)$$

where  $r_{oc}$  is the dc resistance and  $a_c$  is a constant that controls the onset of the  $\sqrt{f}$  factor.

$$L(f) = \frac{l_o + l_\infty \left( \frac{f}{f_m} \right)^b}{1 + \left( \frac{f}{f_m} \right)^b}, \quad (5-18)$$

where  $l_o$  is the low frequency inductance,  $l_\infty$  is the high frequency inductance, and  $f_m$  and  $b$  are parameters that control the transition between the two inductance parameters.

$$G(f) = g_o f^{g_c}, \quad (5-19)$$

where  $g_o$  and  $g_c$  allow fitting of the conductance measurements. Valid measurements of the conductance are difficult since the value of the conductance loss is small resulting in the series resistance,  $R(f)$ , dominating the overall loss.

$$C(f) = C_\infty, \quad (5-20)$$

where  $C_\infty$  is a constant capacitance value, which assumes the relative permittivity of the dielectric surrounding the conductor is relatively constant over the frequency range of interest.

### 5.4.2 New Twisted Pair Models

The models developed in Chapter 4 will be summarized in this section for convenience; *Figure 5-5* shows the physical dimensions of the twisted pair cable as a reference.

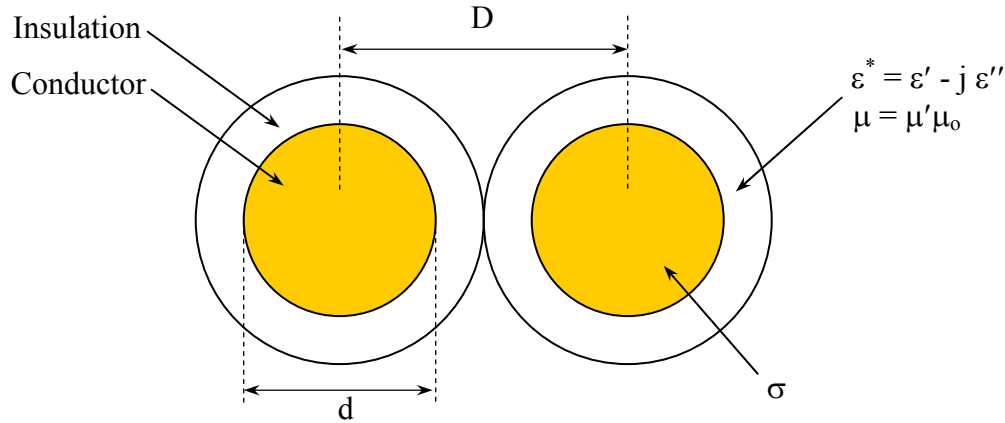


*Figure 5-5: Physical characteristics of a cross section the twisted pair cable.*

The series resistance of the transmission line model was developed and is given as:

$$R = \frac{2R_s}{\sqrt{2\pi r_0}} \left[ \frac{Ber(q)Bei'(q) - Bei(q)Ber'(q)}{[Ber'(q)]^2 + [Bei'(q)]^2} \right] \frac{\frac{D}{d}}{\sqrt{\left(\frac{D}{d}\right)^2 - 1}} \quad \Omega / \text{m} \quad (5-21)$$

$$R_s = \frac{1}{\delta \sigma} = \sqrt{\frac{\omega \mu}{2\sigma}} \quad (5-22)$$

where  $q = \frac{\sqrt{2}r_0}{\delta}$ ,  $r_0 = \frac{d}{2}$  m, and  $\delta = \sqrt{\frac{2}{\omega\mu\sigma}}$  m and,

$r_0$  = wire conductor radius (m),

$d$  = wire conductor diameter (m),

$D$  = wire diameter including dielectric material (m),

$\delta$  = conductor skin depth (m),

$\sigma$  = conductivity of the metallic conductor (S / m),

$\mu$  = permeability of the insulating material (H / m),

$\omega$  = radian frequency (rads / s), and

The series inductance is given as:

$$L = L_{ext} + L_{int} + n \cdot L_{coil\_ext} \quad \text{H / m}, \quad (5-23)$$

where  $n$  is the number of turns per meter, and

$$L_{ext} = \frac{\mu_o}{\pi} \cosh^{-1}\left(\frac{D}{d}\right) \quad \text{H / m}, \quad (5-24)$$

$$L_{int} = \frac{2R_s}{\omega\sqrt{2\pi r_0}} \left[ \frac{Ber(q)Ber'(q) + Bei(q)Bei'(q)}{[Ber'(q)]^2 + [Bei'(q)]^2} \right] \frac{\frac{D}{d}}{\sqrt{\left(\frac{D}{d}\right)^2 - 1}} \quad \text{H / m}, \quad (5-25)$$

$$L_{coil\_ext} = \frac{\mu_o \eta D}{2} \left( \ln \frac{8\eta D}{d} - 2 \right) \quad \text{H / m}, \quad (5-26)$$

where  $\eta$  is an adjustment on the diameter of the coil in the loop's self inductance equation resulting from the estimation of using spaced loops to model a helical structure;  $R_s$  is given in equation (5-22).

The capacitance is estimated to be a constant over the desired bandwidth resulting in the following equations:

$$C = \frac{\pi \varepsilon'}{\cosh^{-1}\left(\frac{D}{d}\right)} = \text{Constant} \quad \text{F / m}, \quad (5-27)$$

where  $\varepsilon'$  = real part of the permittivity of the insulating material, and

$$G = \frac{\pi \omega \varepsilon''}{\cosh^{-1}\left(\frac{D}{d}\right)} = 0 \quad \text{S / m}, \quad (5-28)$$

where  $\varepsilon''$  = imaginary part of the permittivity of the insulating material.

## 5.5 Model Comparisons (ANSI T1E1.4 Models versus Developed Models)

Comparisons of the models with the data sets from the ANSI T1.601-1999 data and the measured data produced by the research group are shown graphically in this section. The models of the primary line parameters (RLCG) and the secondary line parameters, the intrinsic impedance and propagation constant, will be displayed.

All of the TDR responses presented in this report were generated using the developed CNS toolbox (Version 2.0). The TDR simulation was acquired over a 40- $\mu$ sec sampling duration for a 40-MHz sampling frequency. The input pulse was a 10 V raised-cosine pulse with a 2- $\mu$ sec duration having a source impedance of 120 $\Omega$ . The pulse was input into a 1000 m - 50  $\Omega$  lossless line followed by a 300 m segment of the modeled transmission line. Additionally, all network loop nodes were assumed to be open-circuited.

Both models were fit to the measured data described earlier in this chapter and the model comparisons are displayed in *Figure 5-6* for 24 AWG and *Figure 5-7* for 22 AWG. It is observed that the low frequency data points were not available due to the bandwidth limitations of the measurement equipment. For this reason, the data fitting of the two models are relatively different in this frequency range. The resulting intrinsic impedances and propagation constants produced by the two models are shown in *Figure 5-9* and *Figure 5-10* for 24 AWG and 22 AWG, respectively. The models show excellent correlation to the measured data.

A second investigation graphically compares the match of the models to the ANSI T1.601-1999 data in *Figure 5-8*. As mentioned earlier, it has been investigated that the conductance value is negligible with respect to the TDR waveforms. The only parameter of concern in the figure is that of the inductance. The mismatch of the model developed by the researchers to the data reported in the ANSI standard can be due to several items. One possibility is that the data recorded in the standard is not valid over the entire frequency range because of the difficulties in measuring the primary transmission line parameters at very low frequencies (due to equipment accuracy and bandwidth limitations).

It is understood that large differences in the intrinsic impedances will cause more significant mismatches, resulting in larger fluctuations in the TDR waveform. However, the intrinsic impedances that were calculated from the models are very similar. This results in the

conclusion that the non-causality of the empirical model is the cause of the differences in the TDR waveforms produced by the two models, shown in *Figure 5-11*.

## 5.6 Summary of Twisted Pair Line Parameter Models

Typical model coefficients of the new line parameter models for the twisted pair lines of 22 AWG and 24 AWG are given in *Table 5-3*.

*Table 5-3: Typical model coefficients<sup>2</sup> for 22 AWG and 24 AWG models.*

Parameter	24 AWG Cable	22 AWG Cable
$d$ (m)	$5.4459 \cdot 10^{-4}$	$6.6472 \cdot 10^{-4}$
$D$ (m)	$8.8901 \cdot 10^{-4}$	$10.9699 \cdot 10^{-4}$
$\sigma$ (S/m)	$5.9225 \cdot 10^7$	$5.8034 \cdot 10^7$
$n$	14.0573	14.0015
$\eta$	3.7015	0.8466
$\epsilon_r$	1.7823	2.0326
$\epsilon''$	0	0

This chapter summarized the processes and procedures used to characterize the SEALPIC<sup>®</sup> twisted-pair communication cables manufactured by Superior Essex for 22 AWG and 24 AWG. The primary line parameters (resistance, inductance, conductance, and capacitance per unit length) were extracted from frequency domain measurements on the cables.

Comparisons between the non-causal ANSI T1E1.4 models and the models developed by the researchers were presented. The effects of the non-causality of the ANSI T1E1.4 models showed a cumulative effect of errors over the entire TDR waveform. In an actual measurement environment, the measured TDR waveform will be causal, so the models used to identify the system will also need to be causal. The developed models characterize the cables over a sufficient wideband response to obtain an accurate and causal time domain waveform.

<sup>2</sup> Measured physical values of these cables are as follows: (24 AWG)  $d = 5.080 \cdot 10^{-4}$  m,  $D = 8.890 \cdot 10^{-4}$  m; (22 AWG)  $d = 6.350 \cdot 10^{-4}$  m,  $D = 10.9220 \cdot 10^{-4}$  m; Conductivity of copper is documented [8],  $\sigma = 5.813 \cdot 10^7$ .

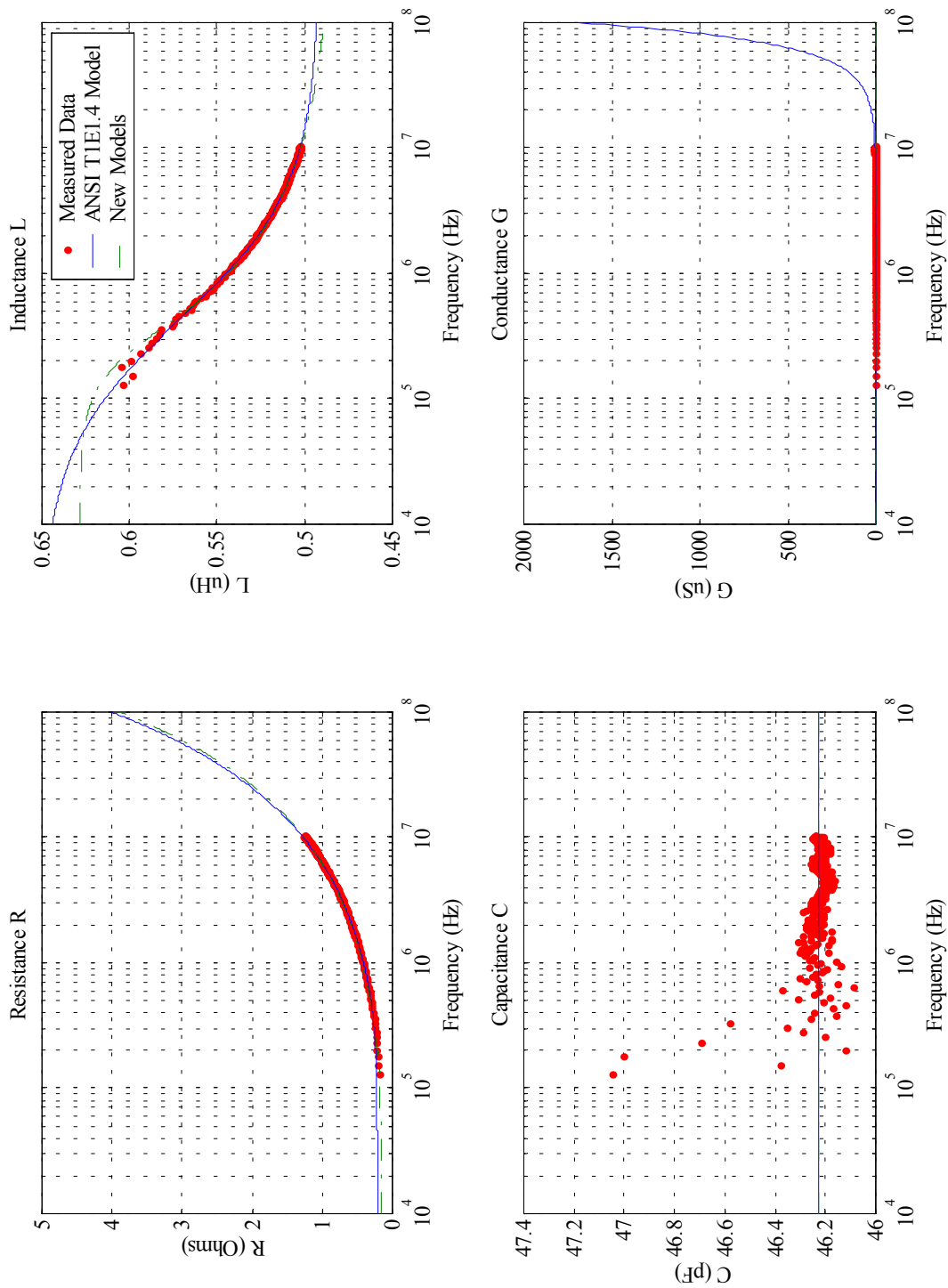


Figure 5-6: Model comparison to measured data of a 24 AWG SEALPIC cable.

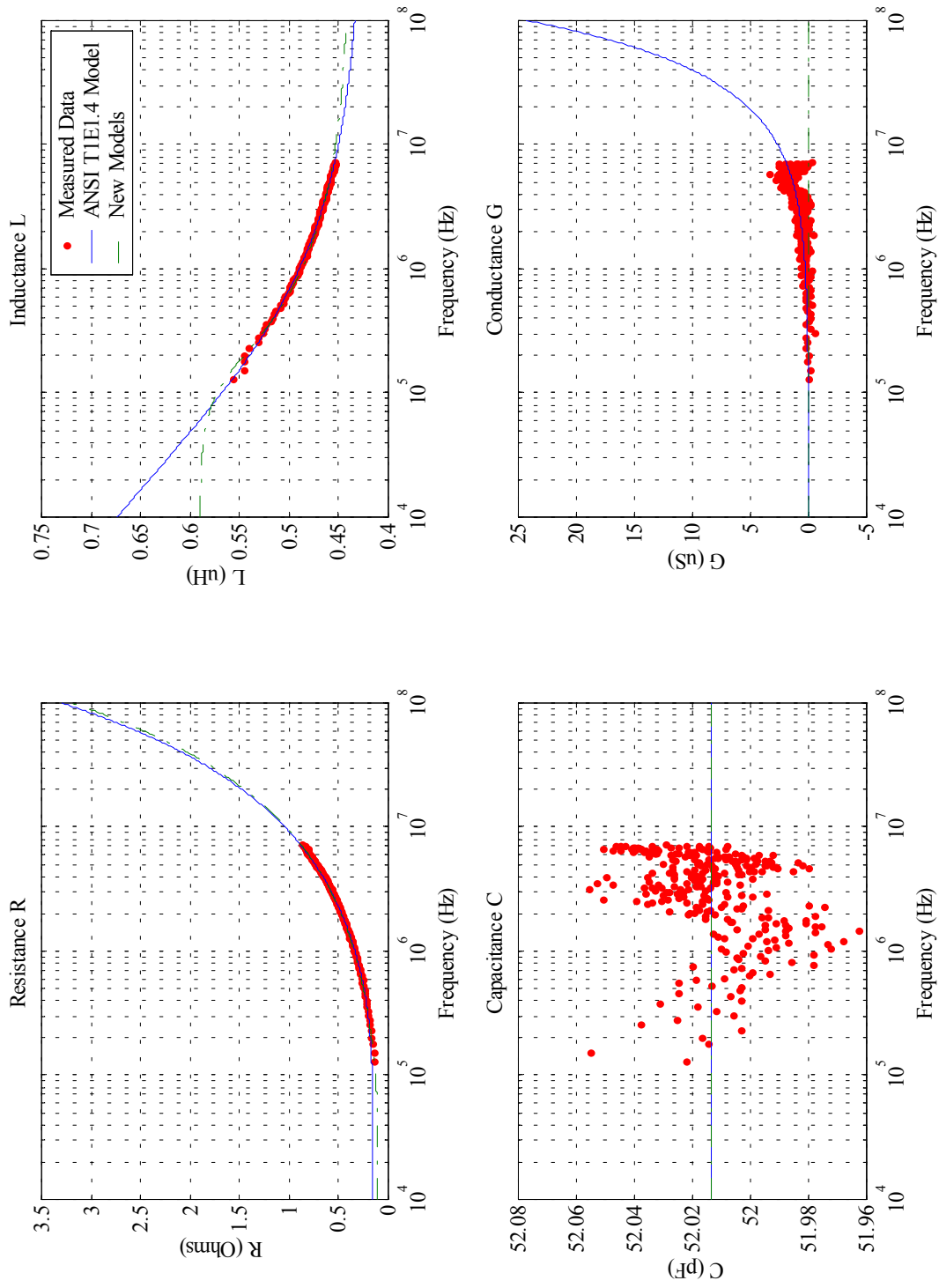


Figure 5-7: Model comparison to measured data of a 22 AWG SEALPIC cable.

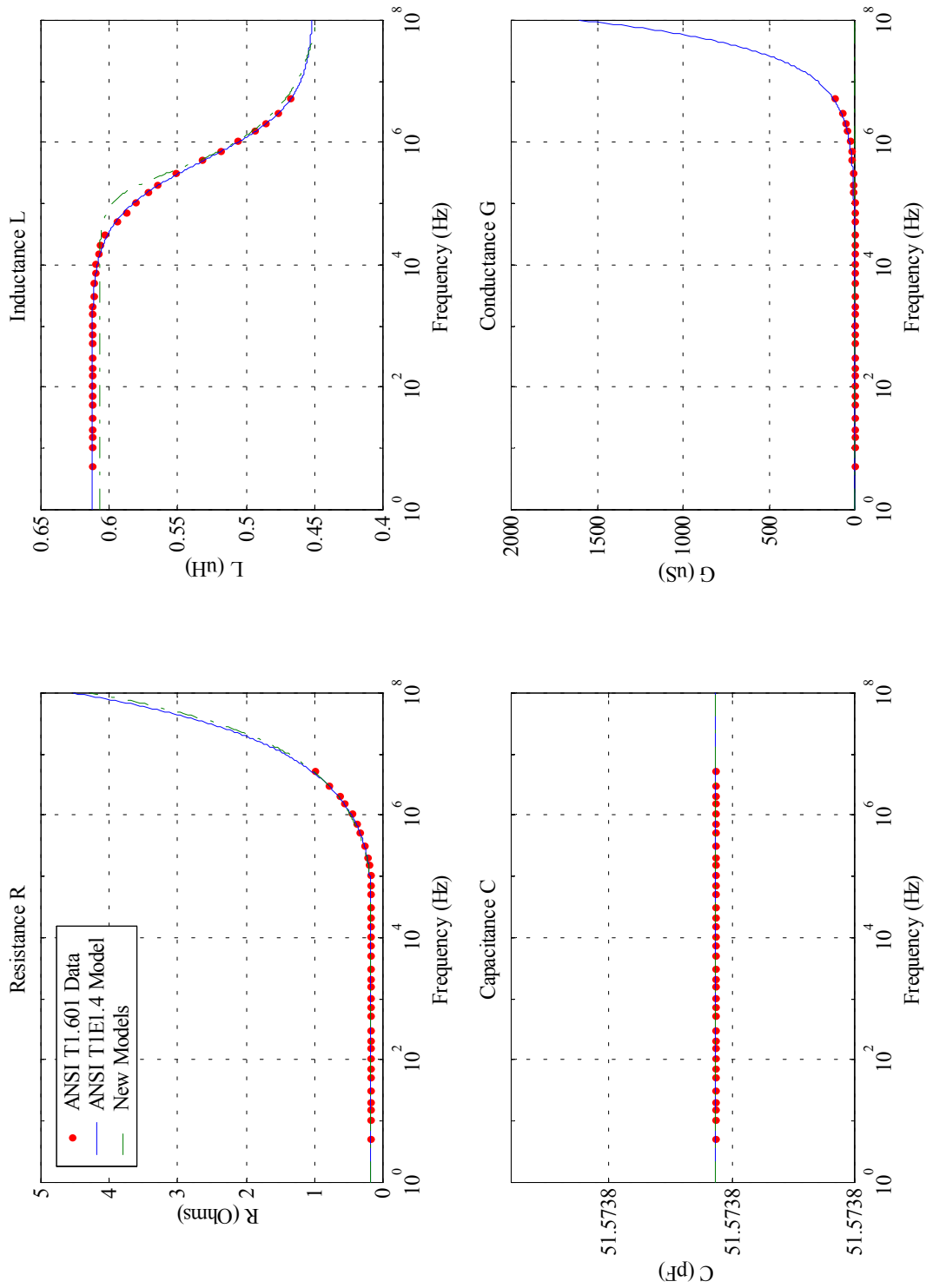


Figure 5-8: Model comparison to ANSI T1.601-1999 data of a 24 AWG SEALPIC cable.

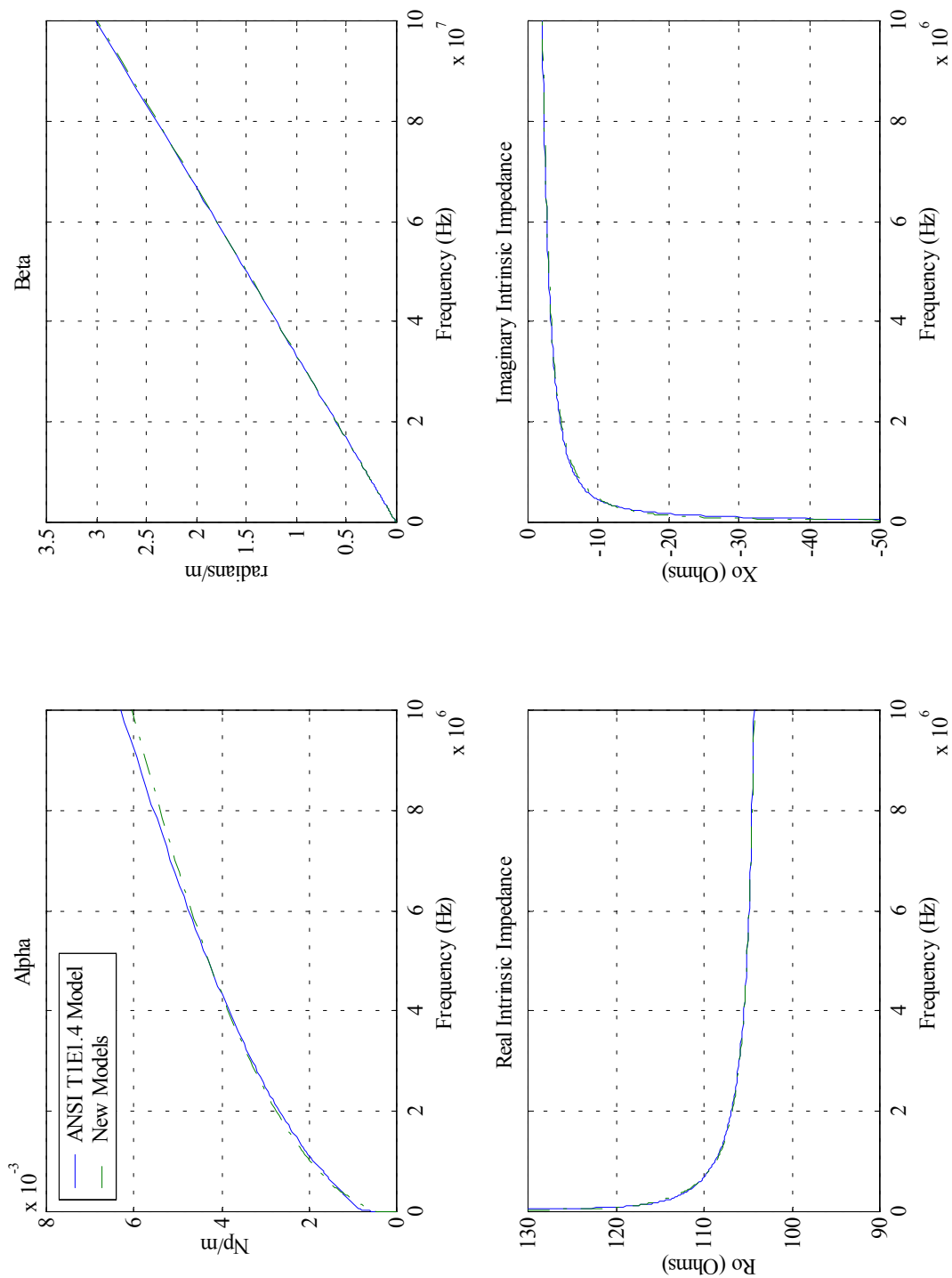


Figure 5-9: Model comparison to measured data of a 24 AWG SEALPIC cable.

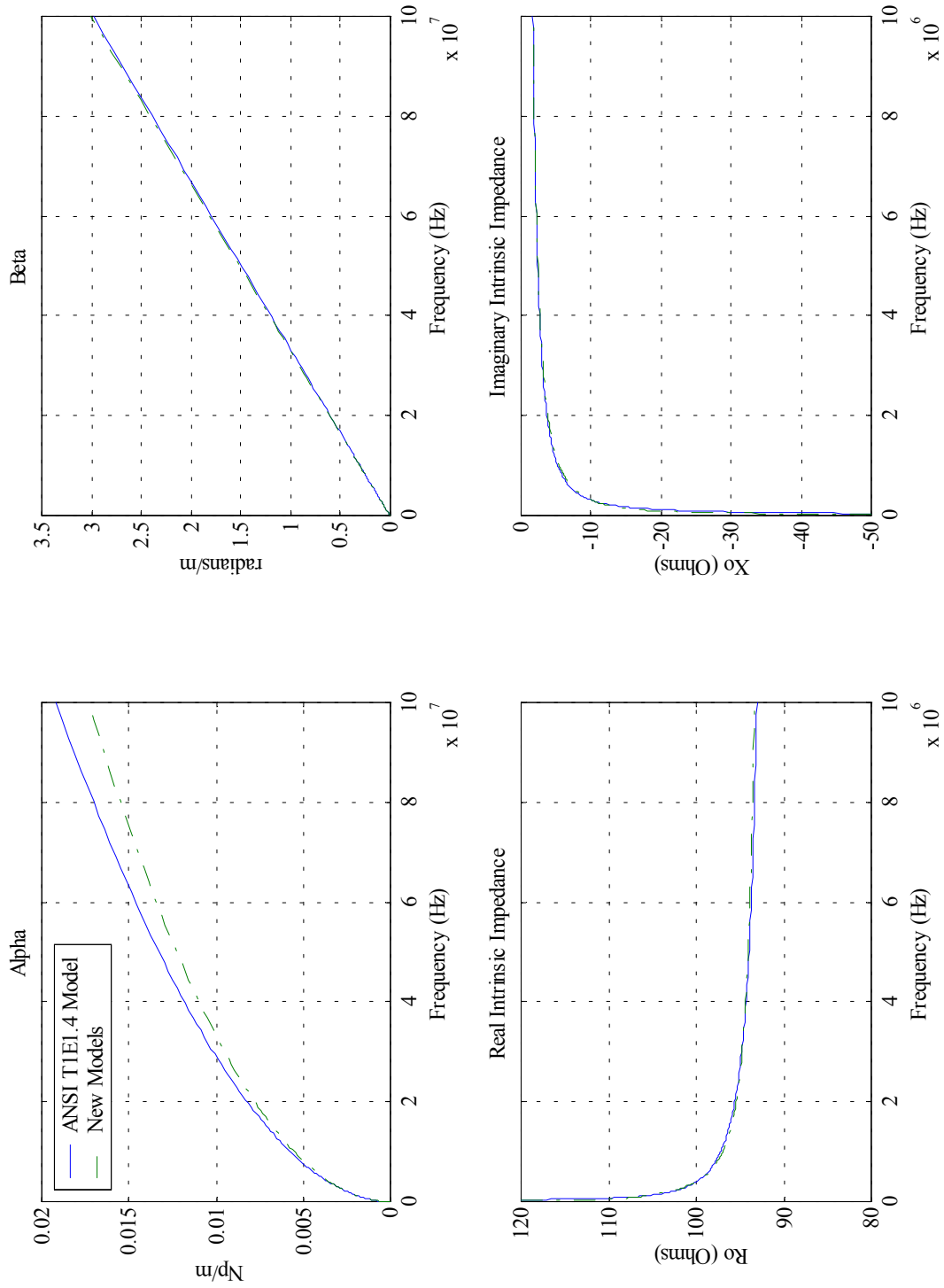


Figure 5-10: Model comparison to measured data of a 22 AWG SEALPIC cable.

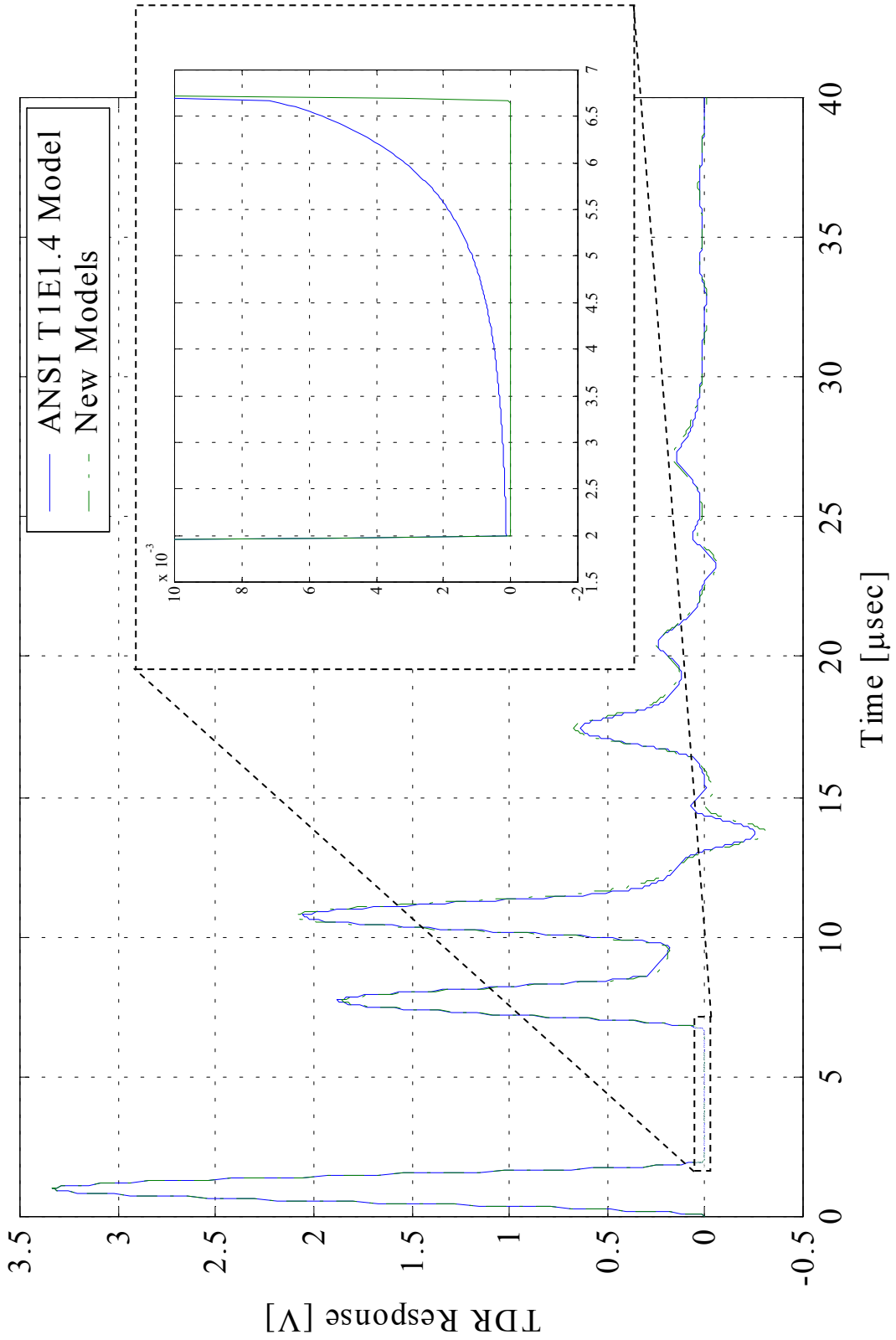


Figure 5-11: Time domain reflectometry waveforms simulated using each of the 24 AWG models.

---

## Chapter 6

### Layer De-Embedding Scheme Verification and Analysis

#### 6 Introduction

This chapter will present verification of the subroutines used in the layer de-embedding scheme as well as some of their limitations. The topology and gauge identification subroutine will be discussed along with the verification of the length estimation algorithm. In each case, examples of the subroutine implementation will be presented along with a performance analysis.

Following this presentation, the performance analysis of the layer de-embedding identification algorithm applied to selected topologies will be evaluated and discussed. This scheme will be evaluated using two methods; the first technique will incorporate the length estimation subroutine described above and the second technique will present the scheme assuming ideal length estimation. By presenting the layer de-embedding technique with the assumption that ideal length estimations are obtainable will allow the complete verification of the scheme and a more robust verification process.

Finally this chapter will conclude by presenting the limitations that occur due to computational errors resulting from the double precision standards developed by IEEE. The developed routine, during the identification process, will eventually have to perform evaluations on numbers having very similar values. The occurrence of these types of computations will

result in the inclusion of noise in the resulting de-embedded data causing failure of the identification scheme.

### 6.1 Gauge/Topology Detection and Length Estimation Verification

As mentioned previously, the gauge/topology detection and the length estimation algorithms are implemented in the time domain using the response of the Time Domain Reflectometry (TDR) waveform. An impedance change in the subscriber loop topology is detected and processed by the algorithm for length estimation; therefore, the performance of the length algorithm based on three terminations that are typically found in subscriber loops (an open circuit, a gauge change, and a bridge tap) is presented in this section.

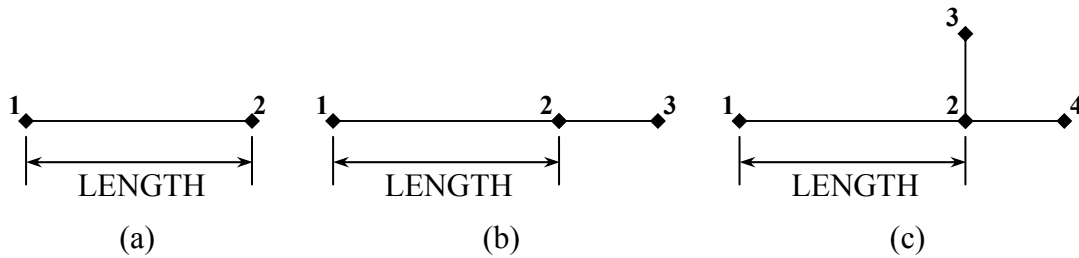


Figure 6-1: Termination topologies used for length estimation performance verification: (a) open circuit (b) gauge change (c) bridge tap.

Figure 6-1 depicts the topologies used in the verification process. The length of the segment between nodes one and two are adjusted between 50 and 2000 meters and detected by the estimation algorithm in each of the termination cases. The initial line is a 24 AWG cable followed by a 22 AWG cable in (b) and a combination of two 26 AWG cables in (c).

Table 6-1: Results of length estimation algorithm performance given different terminations.

Length	Open Circuit	Gauge Change	Bridge Tap
50 m	49.83 m	49.83 m	49.83 m
100 m	100.26 m	100.26 m	100.26 m
500 m	500.69 m	500.68 m	499.86 m
1000 m	999.55 m	1000.40 m	999.55 m
2000 m	2000.50 m	2006.60 m	1998.2 m

Table 6-1 presented the results of the length estimation verification given the three different topologies listed in Figure 6-1. The results show the length estimation algorithm is robust over a wide range of lengths and unaffected by the different reflections created due to various terminations.

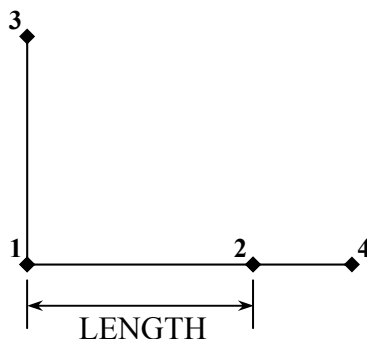


Figure 6-2: Length estimation performance verification of a bridge tap segment.

The case displayed in Figure 6-2 will have similar results of the various termination topologies displayed in Figure 6-1 as long as the gauge detection is correct. If the two segments spanning from node one are of different gauges, there is a possibility that the incorrect gauge may be applied to the initial length estimation. This will cause a length error that could result in the premature failure of the algorithm. The development and application of a segment length optimization routine will need to be implemented to advance beyond this limitation.

## 6.2 Topology Identification Using Non-Ideal Length Estimation

As mentioned previously, the length estimation algorithm is an initial estimate of the line length. Optimization schemes will need to be applied to the current segment's length as well as the length of previously detected segments to reduce computational errors resulting from incorrect length estimates. This type of optimization scheme will allow the overall length of subscriber loop detection to be increased.

This section will present the proposed reconstruction algorithm on some portion of subscriber loop segments using the initial length detection scheme without any optimization routines. Figure 6-3 displays the topology portions that the algorithm will be reconstructing and Table 6-2 shows the result of the reconstruction process. The results show the success of the algorithm for gauge detection and length estimation. With the use of an optimization scheme to

minimize the length errors resulting from the initial length estimation algorithm, the reconstruction abilities of the algorithm will be significantly improved.

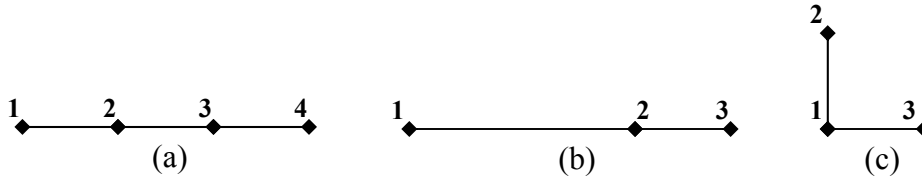


Figure 6-3: Length estimation performance verification of a bridge tap segment.

Table 6-2: Results of the application of the proposed identification scheme on portions of subscriber loops shown in Figure 6-3.

Loop (a)	Length	Gauge	Detected Length	Detected Gauge
1	200 m	24 AWG	200.13 m	24 AWG
2	200 m	22 AWG	190.63 m	22 AWG
3	200 m	26 AWG	215.38 m	24 AWG
Loop (b)	Length	Gauge	Detected Length	Detected Gauge
1	1500 m	24 AWG	1501.9 m	24 AWG
2	200 m	22 AWG	187.66 m	22 AWG
Loop (c)	Length	Gauge	Detected Length	Detected Gauge
1	1000 m	26 AWG	997.61 m	26 AWG
2	1000 m	24 AWG	1002.20 m	24 AWG

The following section will perform the verification of the subscriber loop identification algorithm as if the length optimization scheme were already developed.

### 6.3 Topology Identification Using Ideal Length Estimation

In this section the proposed identification scheme will be applied to the CSA test subscriber loops listed in Appendix A using ideal length identification. As depicted in Table 6-3, CSA loops #1 - #5 are successfully reconstructed while CSA loops #6 - #10 could not be reconstructed past node two due to the long length of the initial segment. After the detection and de-embedding of these long segments, computational noise is introduced in the resulting input

impedance of the remaining portion of the subscriber loop. The computational noise will be addressed in the following section.

Table 6-3: Results of the application of the proposed identification scheme on CSA subscriber loops from the CO node (node 1).

Loop		Loop	
CSA #1	success	CSA #6	fail
CSA #2	success	CSA #7	fail
CSA #3	success	CSA #8	fail
CSA #4	success	CSA #9	fail
CSA #5	success	CSA #10	fail

#### 6.4 Computational Noise Limitations

The numerator of equation (6-1) shows a difference function of the scattering parameter,  $S_{11}$ , and the input reflection coefficient. At higher frequencies these values both approach zero, it is obvious that errors will occur when performing the difference function of two closely valued quantities.

$$\Gamma_{i+1} = \frac{S_{i,11} - \Gamma_i}{S_{i,22}(S_{i,11} - \Gamma_i) - S_{i,21}S_{i,12}} \quad (6-1)$$

Computational limitations restrict the overall detected length. This limitation is due to the double precision computational standard that has been implemented by IEEE. During the de-embedding process, this limitation causes computational noise to enter the routine due to performing mathematical operations on numbers with similar values. *Figure 6-4* shows the result of de-embedding the initial segment (~ 1800 meters) of CSA #1 depicted in Appendix A. A collection of shorter segments will also cause this computational problem.

The computational restriction of the double precision standard cannot be overcome without the use of symbolic, or Maple, based programming using MATLAB. This type of programming is very slow and unpractical in this application. However, it has been found that algorithms exist

in the C programming language that combine multiple double precision numbers together to create algorithms that can handle a higher number of significant digits. The re-development of this research in the C language along with the application of these algorithms could be a solution to the computational limitation.

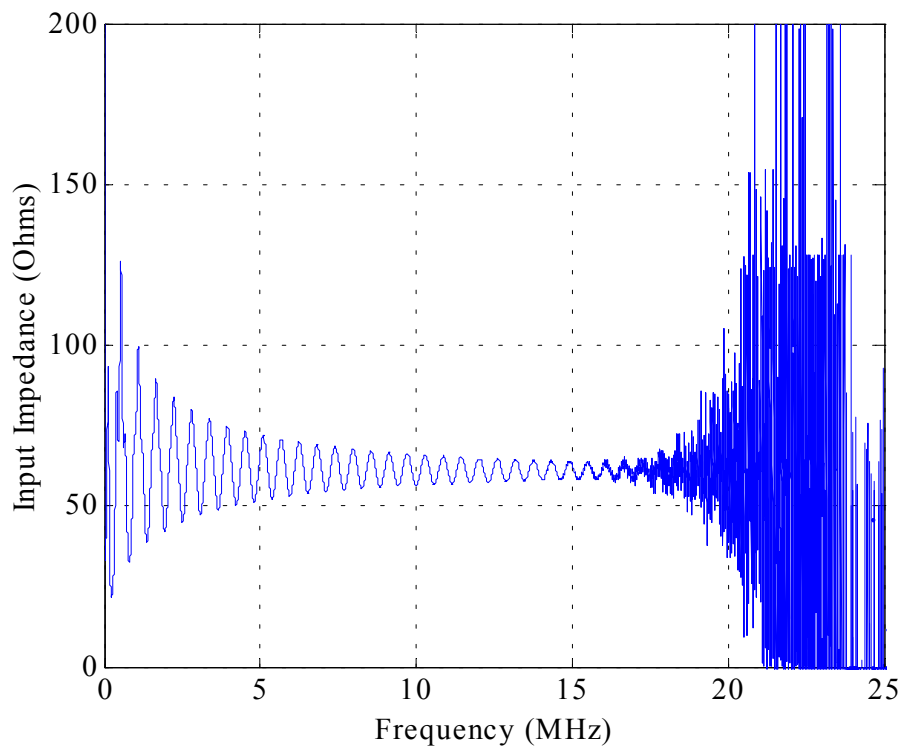


*Figure 6-4: Computational noise resulting from first iteration of CSA #1 reconstruction.*

## Chapter 7

### Conclusion and Suggestions for Research Continuation

#### 7 Conclusion

A solution to the identification problem of estimating the telephone industry's subscriber loop infrastructure has been proposed. The proposed solution would allow high-speed DSL access providers to perform topology identification of a given subscriber loop from the central office through data obtained from a single port measurement, preventing the provider from having to send an employee to the subscriber node to perform two port evaluations. The details of the identified subscriber loop can be used to simulate the two port transfer function between different nodes. The transfer function is then used to calculate loop characteristics such as insertion loss to determine performance and feasibility investigations of DSL technology on the identified topology. The development of the algorithm to perform the described system identification was divided into the following phases:

- Understanding of the subject to be identified,
- Development of a simulator to model the subscriber loop system,
- Development of twisted pair cable models that are valid in the time and frequency domains,
- Identification of subscriber loop segments using the time-domain characteristics of the loop based on the time-domain reflectometry (TDR) response, and
- De-embedding identified segments from the performed single port measurement.

The initial phase in any system identification process is to develop an understanding of the system including detailed characteristics of the system components. The subscriber loop is made up of a network of twisted pair cables extending from the central office to each DSL subscriber. The twisted pairs are classified based on the physical characteristics such as gauge, cable length, and insulating material. Knowledge of the response of each of these characteristics with respect to measurements performed in either the time and frequency domain were investigated to reach the overall objective of topology identification.

The proposed solution to the identification process is model based, in other words, each identified system component is modeled and the resulting collection of identified models is referenced to the actual measurement to determine the accuracy of detection. The task of referencing the identified segments to the actual measurements requires the ability to perform simulations on the segments as well as the complete measurement setup. With this in mind, the second phase of this research was the development of a simulator that incorporates the models of the twisted pair segments that make up the subscriber loop as well as the measurement setup in the time or frequency domain used to collect data of the loop. The initial version of the simulator incorporated models from the ANSI T1E1.4 contribution, although these models gave an accurate account of frequency domain measurements, they produced a non-causal response in the time domain.

Since the models produced a non-causal response when simulating the time domain measurements, it caused difficulty in detection of the characteristics of the cables and placed a limitation on the initial trials for the de-embedding attempts. The non-causal models limited the de-embedding routine because of the inclusion of errors into the process. After an identified segment was removed from performed measurements, traces of the errors due to the insufficient time domain model were left behind, eventually causing failure of the identification routine. Causal models were investigated and developed due to these limitations, and after verification the models were included in the simulator as well as the system identification process

Since the new twisted pair models produced a realizable time domain response, the resulting TDR waveform produced through measurements can be analyzed to determine the characteristics of the twisted pair segments located closest to the measurement nodes. Gauge and topology detection is performed through comparisons with a cable database containing

information of cables with known characteristics. Cable length is determined using the time delay, or linear phase technique to relate the length of the segment through the time delay of discontinuities found in the TDR waveform. The fact that the twisted pair cables have lossy and dispersive characteristics forces the development of algorithms to deal with these cable qualities while processing detection.

Using the mentioned processes for simulation, modeling, and detection of the twisted pair cables, an iterative algorithm for system identification can be produced. This algorithm is defined in the frequency domain and involved the modeling of the detected twisted pair segments as a two port device. Then using a system of two port parameters for the cable, the characteristics of the cable are mathematically removed using a process termed de-embedding. This identification and de-embedding process continues until the subscriber loop is determined or a process limitation is reached.

### **7.1 Observation of Limitations**

The resolution of length estimation algorithm is proportional to the number of points, or the time spacing, in the TDR waveform. Therefore, the detected length will fall into a tolerance band that is around the exact value of the length. In the case a certain topology has several segments; these errors could possibly accumulate causing a limitation of the algorithm.

Computational limitations restrict the overall detection length to about 1500 meters. This limitation is due to the double precision computational standard that has been implemented by IEEE. During the de-embedding process, this limitation causes computational noise to enter the routine due to performing mathematical operations on numbers with similar values. Considering Asymmetric Digital Subscriber Lines (ADSL) technology can be deployed on subscriber loops reaching lengths of greater than 4500 meters, this research will only be applicable to sections of the subscriber loops that handle ADSL. However, Very High Speed Digital Subscriber Line (VDSL) technology is only applicable to subscriber loops that have lengths as long as 1400 meters. Identification of loops employing VDSL technology would be a valid application of this research in the current state of the algorithm.

As mentioned previously, the algorithm is model based, which means that the measured data of a specific topology will have to be compared to a database of pre-programmed cable models during some portions of the reconstruction algorithm. If the exact model for the

measured is not found within the database, the closest model will be implemented. This procedure will cause errors that could eventually accumulate and cause failure of the algorithm.

Finally, some topologies will result in reflections that occur simultaneously on the TDR response. In these cases, it is possible that the algorithm may detect the wrong model during the database comparison with the TDR response.

## 7.2 Suggestions for Research Continuation

The computational restriction of the double precision standard (as found in MATLAB) cannot be overcome without the use of symbolic, or Maple, based programming. This type of programming is very slow and unpractical in this application. However, it has been found that algorithms exist in the C programming language that combine multiple double precision numbers together to create algorithms that can handle a higher number of significant digits. The re-development of this research in the C language along with the application of these algorithms could be a solution to the computational limitation.

Optimization of the detected segment lengths needs to be developed and incorporated into the system identification algorithm. Through an iterative length optimization scheme, more accurate length estimations will be obtained that will allow the system identification algorithm to be more successful. This step would best be performed after actual field measurements are performed so the algorithms can take into account of the accumulation of the additional complexities that will arise.

It has also been mentioned that errors can occur when the models stored in the database do not exactly match the measured waveforms. Investigations in adaptive modeling based on modifications of the stored model parameters could be investigated. The systematic modification of the most accurate model's parameters to more closely match the actual measurement would reduce resulting errors significantly.

Investigations of electromagnetic interference of cables deployed in the actual subscriber loop infrastructure and these effects on this algorithm could be investigated. Under practical circumstances there will be a larger number of discontinuities and temperature changes, which will modify actual measurements from what would be found in the model database. Cable crosstalk models may also need to be incorporated into the algorithm.

## References

- [1] C. Dunford and R. Fitts, "xDSL Service Testing: White Paper for Telecommunications Service Providers and Local Exchange Carriers," Concord, Ontario: Consultronics, White Paper CBX80WN2, 2000.
- [2] D. Rauschmayer, *ADSL/VDSL Principles: A Practical and Precise Study of Asymmetric Digital Subscriber Lines and Very High Speed Digital Subscriber Lines*. Macmillan Technology Series, Indianapolis: Macmillan Technical, 1999.
- [3] W. Y. Chen, *DSL: Simulation Techniques and Standards Development for Digital Subscriber Line Systems*. Macmillan Technology Series, Indianapolis: Macmillan Technical, 1998.
- [4] J. Cook, "Parametric Modeling of Twisted Pair Cables for VDSL," ANSI Contribution T1E1.4/96-15, January, 1996.
- [5] J. Cook, "Minor Corrections to doc. T1E1.4/96-15, Parametric Modeling of Twisted Pair Cables for VDSL," ANSI Contribution T1E1.4/96-073, April, 1996.
- [6] A. Pickering, "Parametric Modeling of US 24 and 26 American Wire Gauge (AWG) Cables," ANSI Contribution T1E1/96-074, April, 1996.
- [7] K Sistanizadeh and R. C. McConnell, "Generic Requirements for High-Bit-Rate Digital Subscriber Lines," Telcordia Technologies, Technical Advisory TA-NWT-001210, 1991.
- [8] D. M. Pozar, *Microwave Engineering*. Reading: Addison-Wesley Publishing Company, 1990.
- [9] T. Ikuma, "Model-Based Identification of POTS Local Loops for DSL Connectivity Prediction," Virginia Polytechnic Institute, 2001.
- [10] N. S. Nahman and M. E. Guillaume, "Deconvolution of time domain waveforms in the presence of noise," NBS Tech. Note 1047, October 1981.
- [11] S. M. Riad, "The deconvolution problem: An overview," *Proceedings of the IEEE*, Vol. 74, No. 1, January 1986.
- [12] A. Bennis and S. M. Riad, "Filtering capabilities and convergence of the Van-Cittert deconvolution technique," *IEEE Transactions on Instrumentation and Measurement*, Vol 41, No. 2, April 1992.
- [13] P. B. Crilly, "A quantitative evaluation of various iterative deconvolution algorithms," *IEEE Transactions on Instrumentation and Measurement*, Vol 40, No. 3, June 1991.
- [14] R. N. Bracewell and J. A. Roberts, "Aerial smoothing in radio astronomy," *Australian J. Physics.*, Vol. 7, pp.615-640, 1954.
- [15] N. R. Hill and G. E. Ioup, "Convergence of the Van-Cittert iterative method of deconvolution," *J. Optical Society of America*, Vol. 66, No. 5, pp. 487-489, May 1976.

- [16] R. Schafer, R. Mersereau, and M. Richards, "Constrained iterative restoration algorithms," *Proceedings of the IEEE*, Vol. 69, pp. 298-308, 1931.
- [17] P. A. Jansson, *Deconvolution With Applications in Spectroscopy*, New York: Academic, ch. 3-4, pp. 67-134, 1984.
- [18] R. Gold, "An iterative unfolding method for response matrices," Argonne, IL: AEC Research and Development Report ANL-6984, Argonne National Lab., 1964
- [19] P. E. Siska "Iterative unfolding of intensity data, with application to molecular beam scattering," *J. Chem. Phys.*, Vol. 59, pp. 6052-6060, December 1973.
- [20] W. Richardson "Bayesian-based iterative method of image restoration," *J Opt. Soc. Amer.*, Vol. 62, pp. 55-59, January, 1972.
- [21] K MacNeil and R. Dixon, "High-resolution photoelectron spectroscopy of methanol and its deuterated derivatives: Internal rotation in the ground ionic state," *J. Electr. Spectroscopy and Related Phenomena*, Vol. 11, pp. 315-331, 1977.
- [22] T. K. Sarkar, F. I. Tseng, S. A. Dianat, and B. Z. Hollmann, "L2-approximation of impulse response from time limited input and output: Theory and experiment," presented at URSI, U. S. National Radio Science Meet., Boulder, CO, January 1983.
- [23] N. S. Nahman and M. E. Guillaume, "Some results using the Guillaume-Nahman automated deconvolution method," presented at URSI, U. S. National Radio Science Meet., Boulder, CO, p. 149, January 1983.
- [24] N. S. Nahman, "Software correction of measured pulse data." *Fast Electrical and Optical Measurements*, NATO ASI Series, T. E. Thompson and L. H. Lucssen Eds. Dordrecht, The Netherlands: Martin Nijhoff, pp. 351-417, 1986.
- [25] T. Dabóczy and I. Kollár, "Multiparameter optimization of inverse filtering algorithms," *IEEE Transactions on Instrumentation and Measurement*, Vol 45, No. 2, pp. 417-420, April 1996.
- [26] B. Parruck and S. M. Riad, "An Optimization Criterion for Iterative Deconvolution," *IEEE Transactions on Instrumentation and Measurement*, Vol IM-32, No. 1, pp. 137-140, March 1983.
- [27] M. Bertocco, C. Narduzzi, C. Offelli, and D. Petri, "An improved method for iterative identification of bandlimited linear systems," *IEEE Instrumentation and Measurement Technol. Conf.*, Atlanta, GA, CH2940-5/91, pp. 368-372, May, 1991.
- [28] N. H. Youman, A. B. Kopp, D. B. Miller, and C. D. Taylor, "On correcting HV impulse measurements by means of adaptive filtering and deconvolution," *IEEE Trans. Power Delivery*, Vol. 6, No. 2, pp. 501-506, 1990.
- [29] A. Bennis and S. M. Riad, "An optimization technique for iterative frequency-domain deconvolution," *IEEE Transactions on Instrumentation and Measurement*, Vol 39, No. 2, April 1990.

- [30] T. Dhaene, L. Martens, and D. De Zutter, "Extended Bennia-Riad Criterion for interactive frequency domain deconvolution," *IEEE Transactions on Instrumentation and Measurement*, Vol 42, No. 2, April 1994.
- [31] R. L. Vaitkus, "Wide-band de-embedding with a short, an open, and a through line," *Proceedings of the IEEE*, Vol. 74, No. 1, pp. 71-74, January 1986.
- [32] H. E. Stinehelfer Sr., "Discussion of de-embedding techniques using time domain analysis," *Proceedings of the IEEE*, Vol. 74, No. 1, pp. 90-94, January 1986.
- [33] K. L. Su, *Time Domain Synthesis of Linear Networks*, Prentice-Hall Inc., New Jersey, 1971.
- [34] K. L. Su, *Active Network Synthesis*, McGraw-Hill Inc., New York, 1965.
- [35] A. V. Oppenheim and R. W. Schaffer with J. R. Buck, *Discrete-Time Signal Processing*, Prentice-Hall Inc., New Jersey, 1999.
- [36] A. M. Nicolson, "Forming the fast Fourier transform of a step response in time domain metrology," *Elec. Tran. Lett.*, Vol. 9, p. 317, 1973.
- [37] W. L. Gans and N. S. Nahman, "Continuous and discrete Fourier transforms of steplike waveforms," *IEEE Transactions on Instrumentation and Measurement*, Vol IM-31, p. 97, 1982.
- [38] Harris, F. J., "On the Use of Windows for Harmonic Analysis with the Discrete Fourier Transform," *Proceedings of the IEEE*, Vol. 66 No. 1, January 1978, pp. 51-83.
- [39] Miller, E. K., *Time Domain Measurements in Electromagnetics*. New York: Van Nostrand Reinhold Publishing Company, 1986.
- [40] S. Ramo, J. R. Whinnery, and T. Van Duzer, *Fields and Waves in Communication Electronics*, John Wiley and Sons, Inc., New York, 1994.
- [41] R. E. Collins, *Foundation for Microwave Engineering*, McGraw-Hill Book Co., New York, 1966.
- [42] C. W. Davidson, *Transmission Lines for Communications*, The MacMillan Press, Ltd., London and Basingstoke, 1978.
- [43] K. M. Fidanboyly, *Time Domain Synthesis Applied to Modeling of Microwave Structures and Material Characterization*, Dissertation, Virginia Polytechnic Institute and State University, 1991.
- [44] W. L. Stuzman and G. A. Thiele, *Antenna Theory and Design*, John Wiley and Sons, Inc., New York, 1981.
- [45] D. H. Werner and R. Mittra, *Frontiers in Electromagnetics*, IEEE Press on Microwave Technology and RF, New York, 2000.
- [46] R. W. P. King and S. Prasad, *Fundamental Electromagnetic Theory and Applications*, Prentice-Hall Inc., New Jersey, 1986.

- [47] R. Plonsey and R. E. Collin, Principles and Applications of Electromagnetic Fields, McGraw-Hill, New York, 1961, p 280.
- [48] “American National Standard for Telecommunications – Integrated Service Digital Network (ISDN) – Basic Access Interface for Use on Metallic Loops for Application on the Network Side of NT (Layer 1 Specification),” ANSI T1.601-1999, New York: American National Standards Institutes, 1999.
- [49] G. H. Bryant, Principle of Microwave Measurements, IEE Electrical Measurement Series 5, Peter Peregrinus Ltd., London, U. K., 1993.
- [50] M. N. O. Sadiku, Elements of Electromagnetics, Sanders College Publishing, Fort Worth, TX, 1989.
- [51] J. Millman, Microelectronics: Digital and Analog Circuits and Systems, McGraw Hill Inc., New York, 1979.

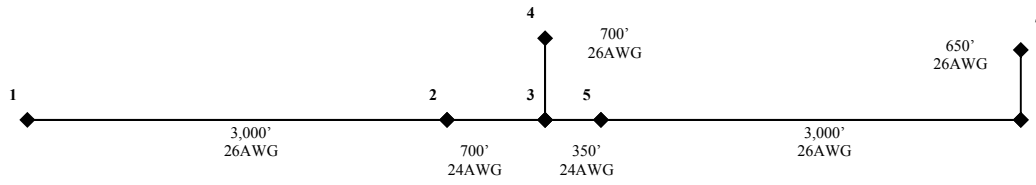
# **Appendix A**

## **CSA Test Subscriber Loops**

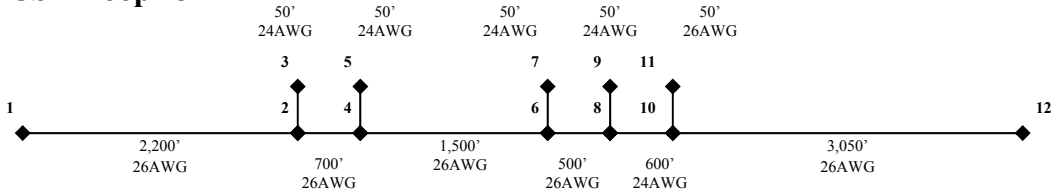
**CSA Loop #1**



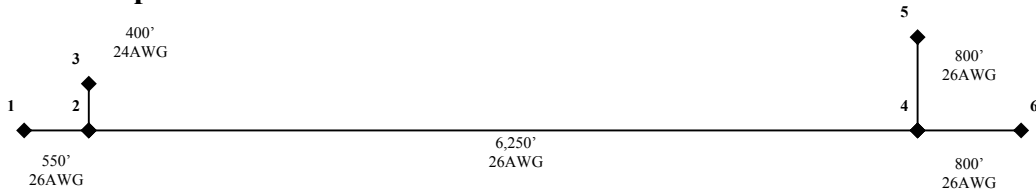
**CSA Loop #2**



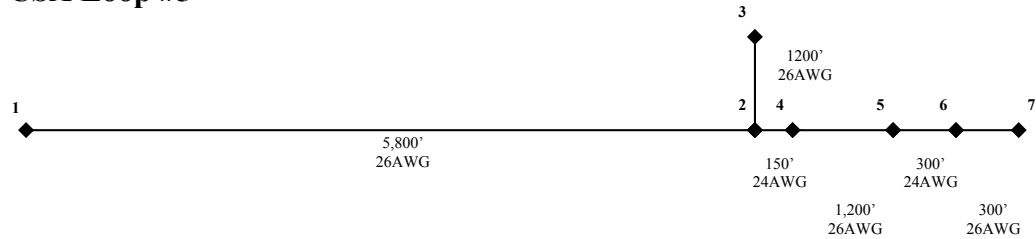
**CSA Loop #3**



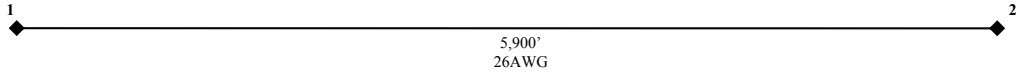
**CSA Loop #4**



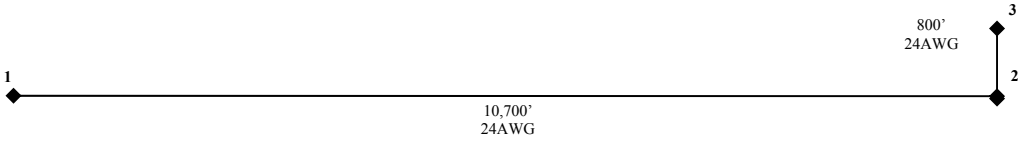
**CSA Loop #5**



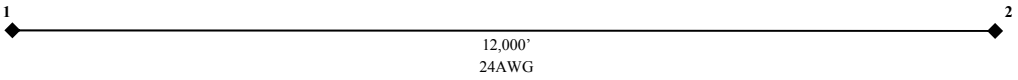
**CSA Loop #6**



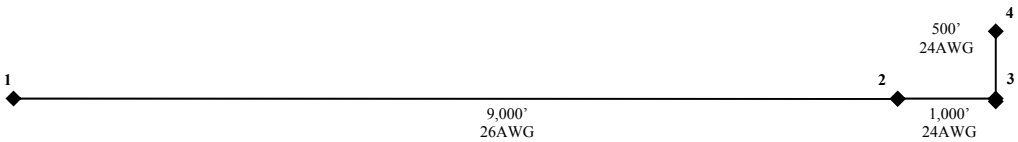
**CSA Loop #7**



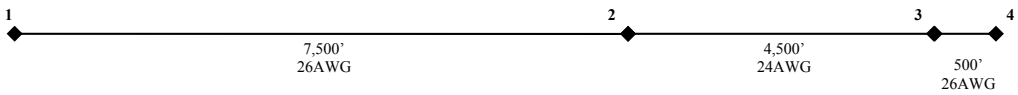
**CSA Loop #8**



**CSA Loop #9**

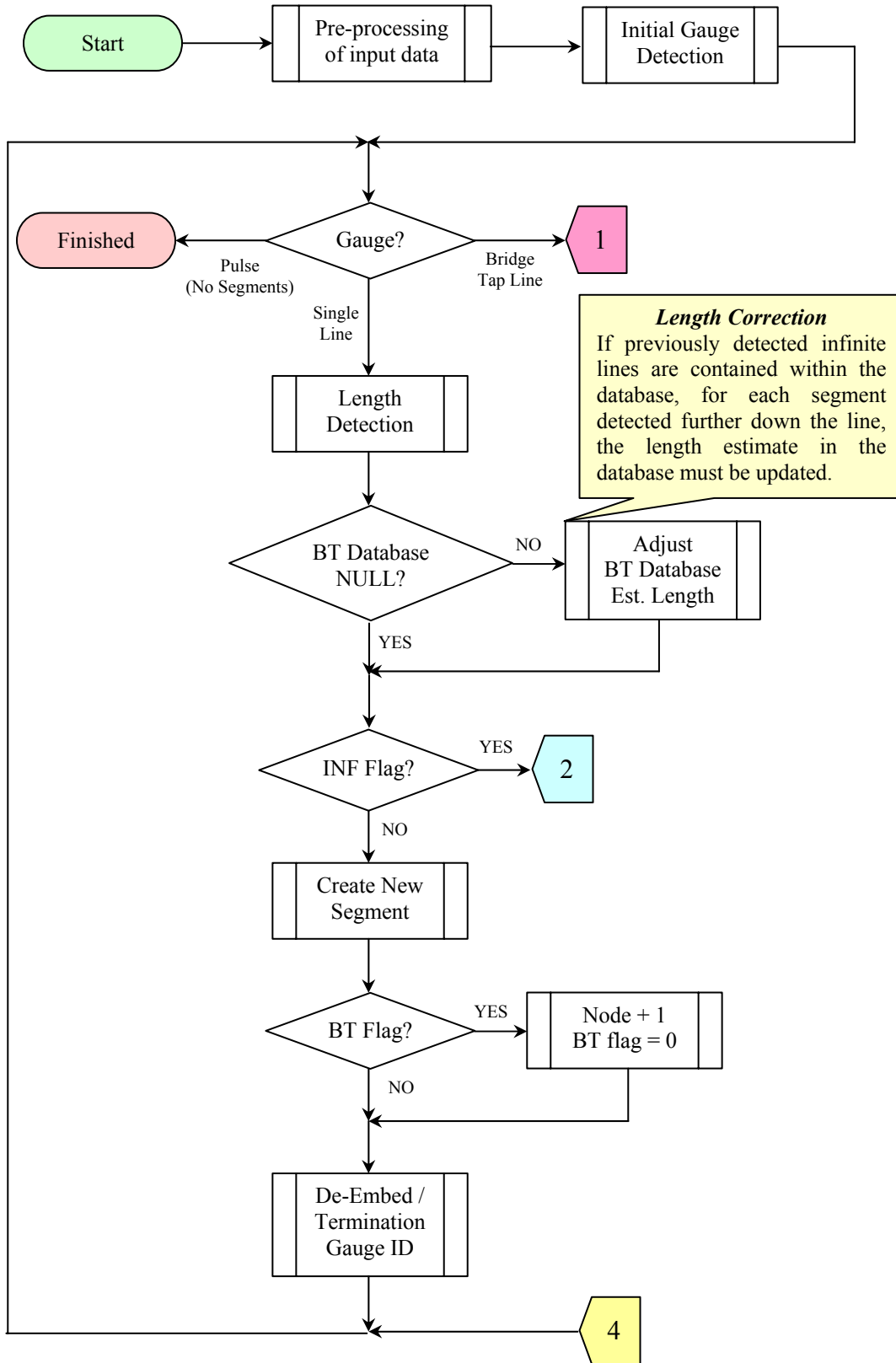


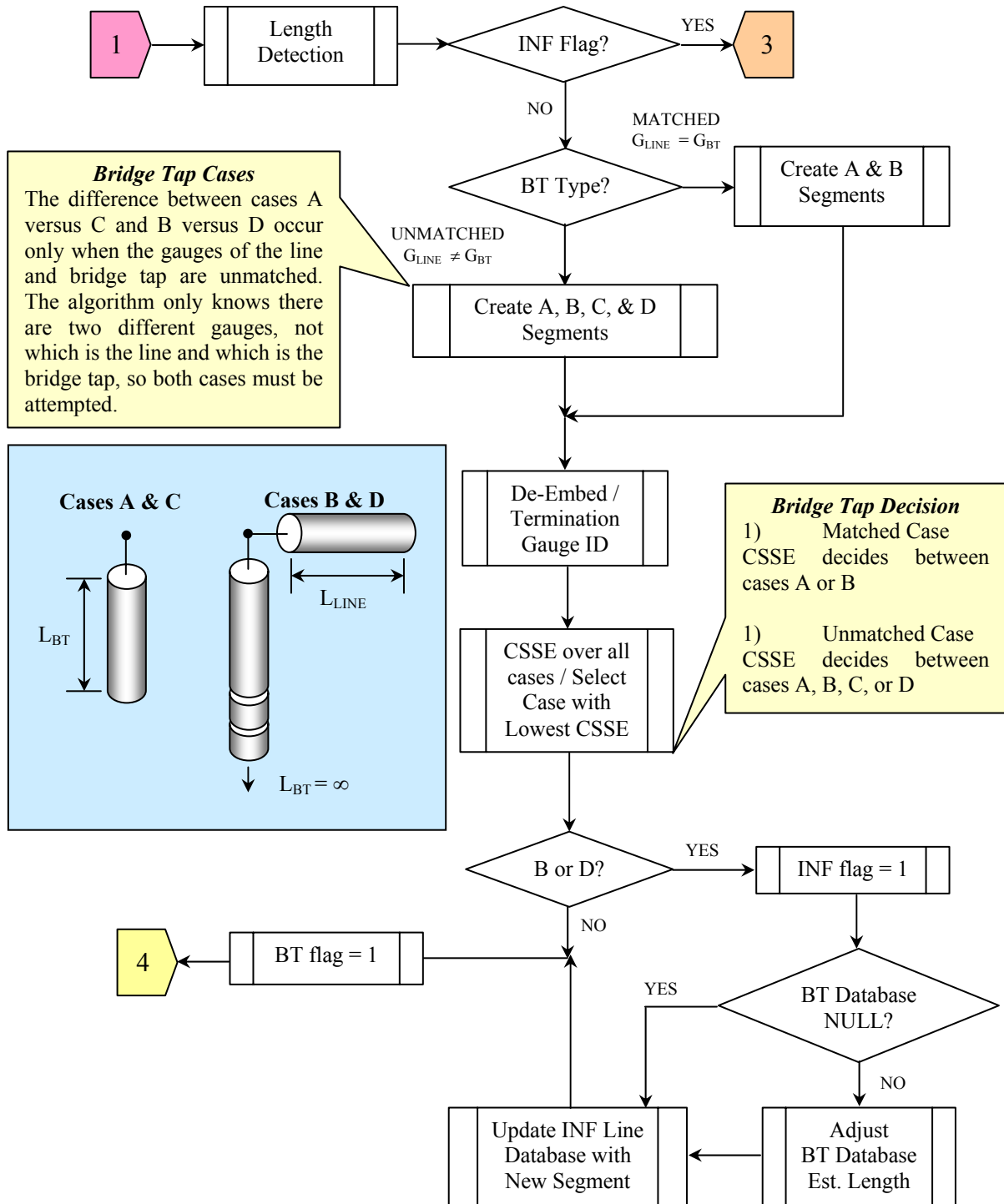
**CSA Loop #10**

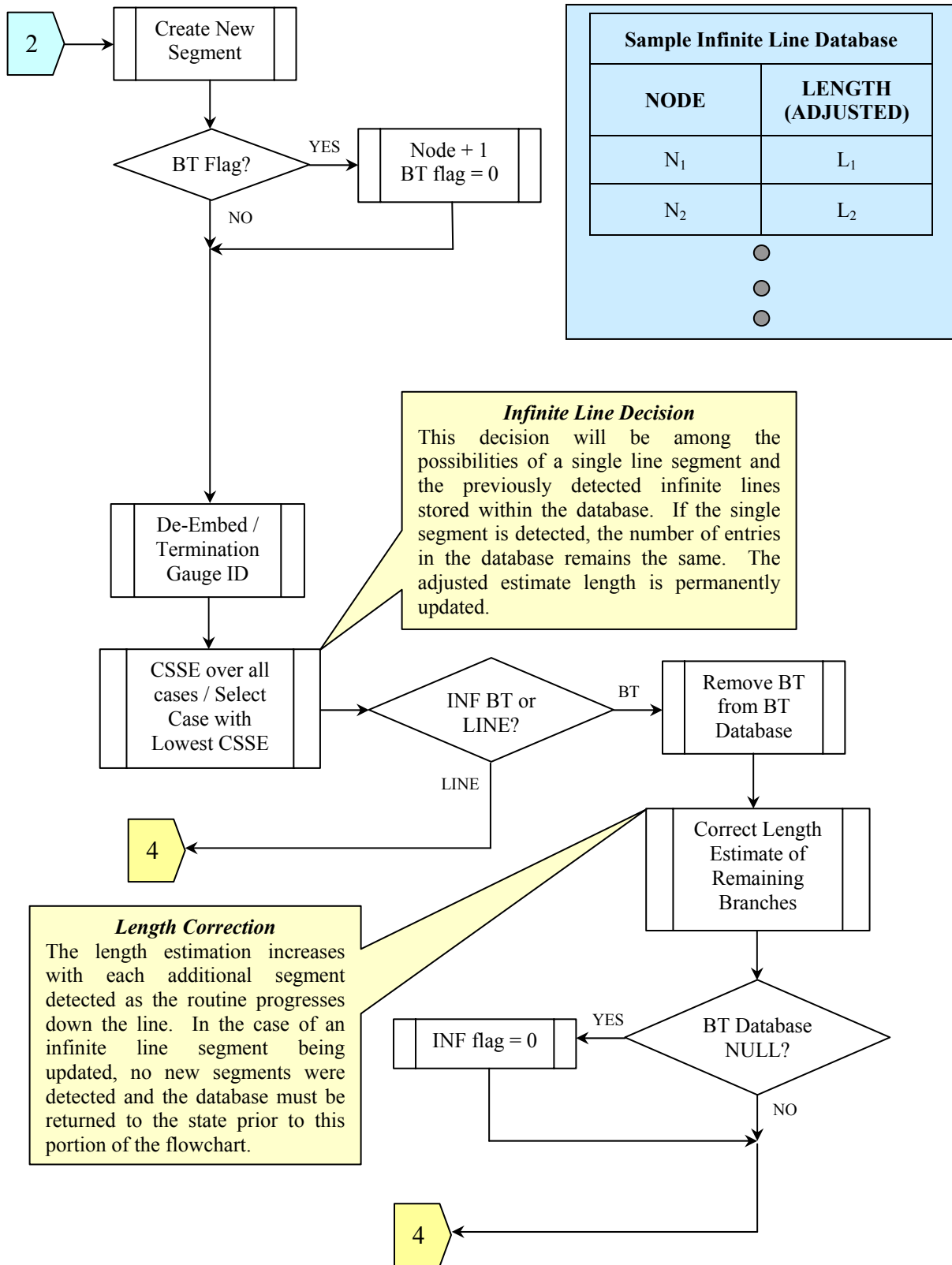


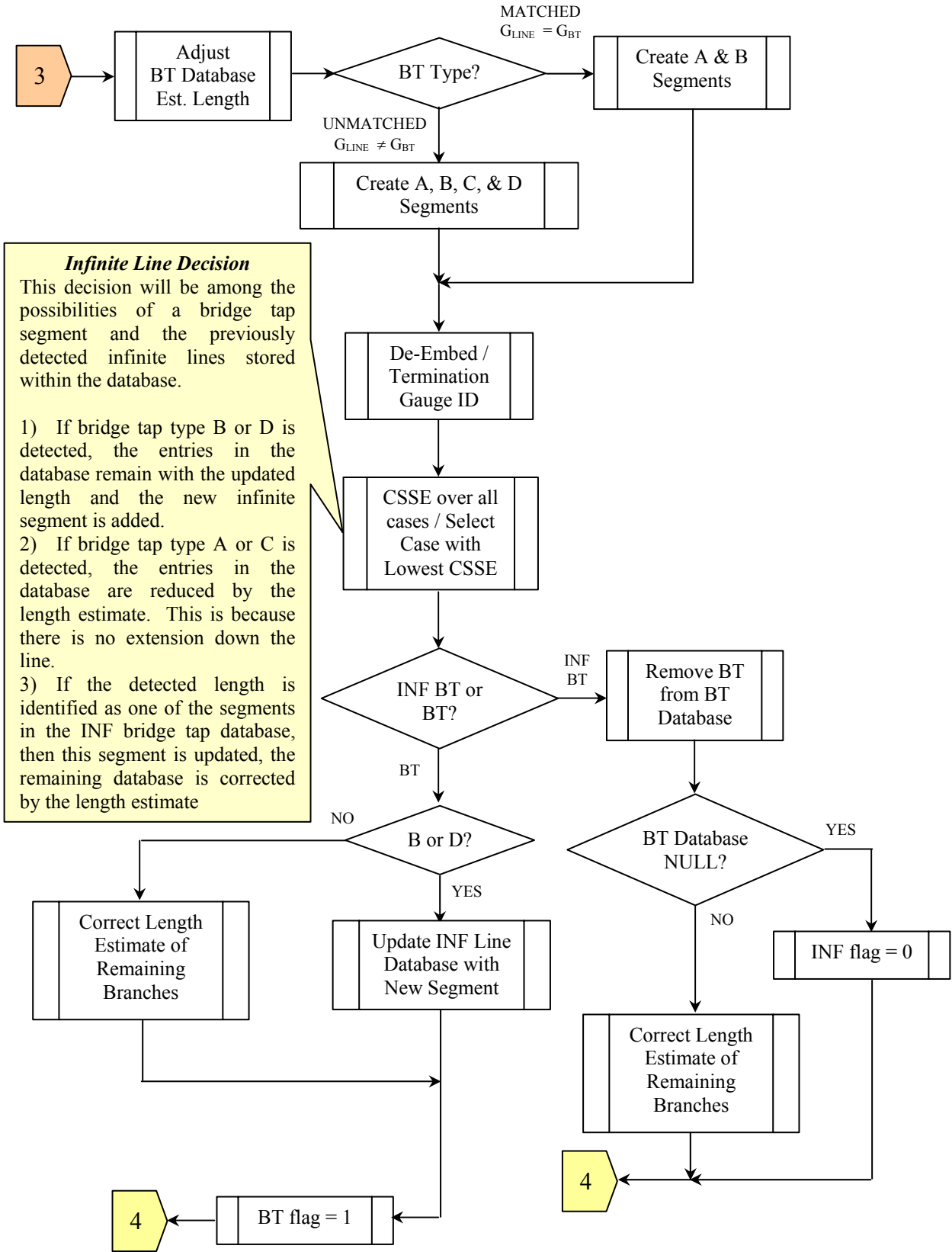
## **Appendix B**

### **Layer De-Embedding Algorithm Flow Charts**









## **Appendix C**

### **Time and Frequency Domain Measurement Methods**

## C Introduction to Methods of Time and Frequency Domain Measurements

Time Domain Reflectometry (TDR) is the systematic method of sending a RF pulse into a system and measuring the reflections at the input port to determine information about the system content, such as length to an impedance change, values of the reflection coefficients and impedances at the discontinuities. It is convenient to launch a pulse or step function as that shown in *Figure C-1* [49]. The resulting input and output waveforms have an equivalent spectral description, which can be simulated as a set of discrete spectral lines with appropriate amplitudes and phases. This is accomplished by performing the inverse Fourier transform operation on the reflected time domain spectra obtained through the measurement system; we will define this frequency spectra as Frequency Domain Reflectometry (FDR) information.

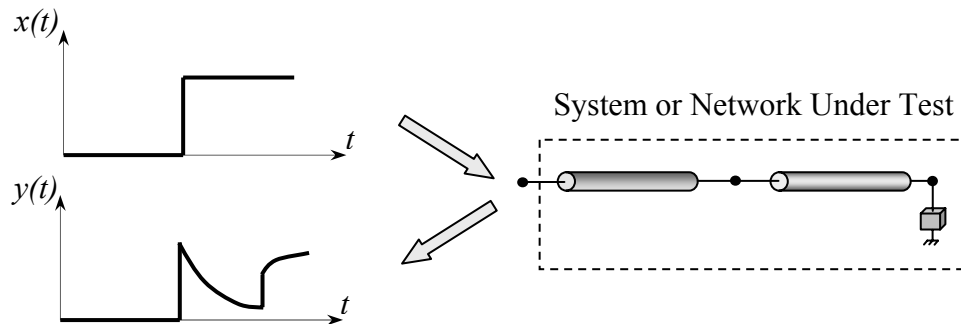


*Figure C-1: Time Domain Reflectometry*

FDR can be taken directly by launching discrete sampled spectra components of the desired time domain pulse and noting the modified amplitudes and phases of the reflected waveform. Another approach is to perform the measurement using a network analyzer over the frequency spectra to produce the reflected transfer function,  $H(j\omega)$ , as shown in *Figure C-2* [49]. In the case where the spectral information of the step function was input into the system, the time domain information is obtained by taking the Fourier transform of the spectral returns, thus resulting in the same information as sending a step function in the time domain. In the case where the transfer function was measured directly, there is the advantage of being able to try an unrestricted number of different pulse types through convolution in the frequency domain. After the desired pulse is applied, the Fourier transform is applied to obtain the frequency domain data. Pulses with different spectra components can be applied to obtain a broad information set of the system.

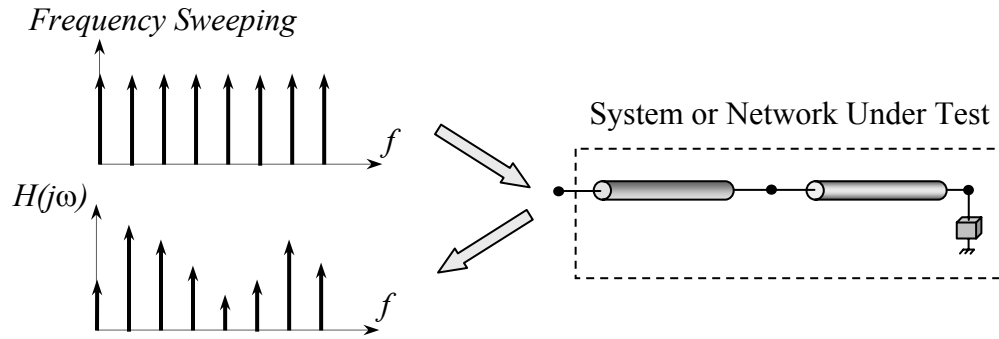


Figure C-2: Frequency Domain Reflectometry

The ideas of TDR and FDR have been initially discussed in the following section and an in depth review of these methods will be presented as well as measurement setups and techniques. On the focus of device and network synthesis, the modeling process can be performed in either the time and frequency domains. Figure C-3 graphically depicts the options of network characterization in the time and frequency domains using time or frequency domain measurements.

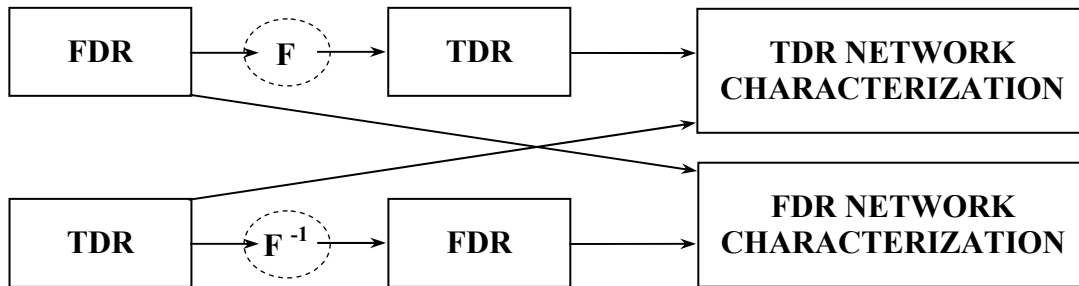


Figure C-3: Synthesis problem performed through different methods

### Bounce Diagrams

From Fourier analysis a pulse can be regarded as the superposition of waves of many frequencies. Thus, sending a pulsed signal on the line may be regarded as the same as simultaneously sending waves of different frequencies [50]. For the sake of convenience, the problem will be analyzed in the time domain.

Consider two transmission lines in series with different intrinsic impedances,  $Z_1$  and  $Z_2$ , lengths,  $\ell_1$  and  $\ell_2$ , and propagation constants,  $\gamma_1$  and  $\gamma_2$  as shown in Figure C-4. If the source impedance is matched to the initial line, the reflection coefficient is equal to unity. The other reflection coefficients are calculated from the intrinsic impedances at the discontinuities. The

delays,  $T_1$  and  $T_2$ , are a function of the propagation delay and the length of the line. The input pulse,  $A$ , is reflected at the different discontinuities of the transmission lines. The TDR response is equivalent to the summation of the infinite reflections at the input terminal.

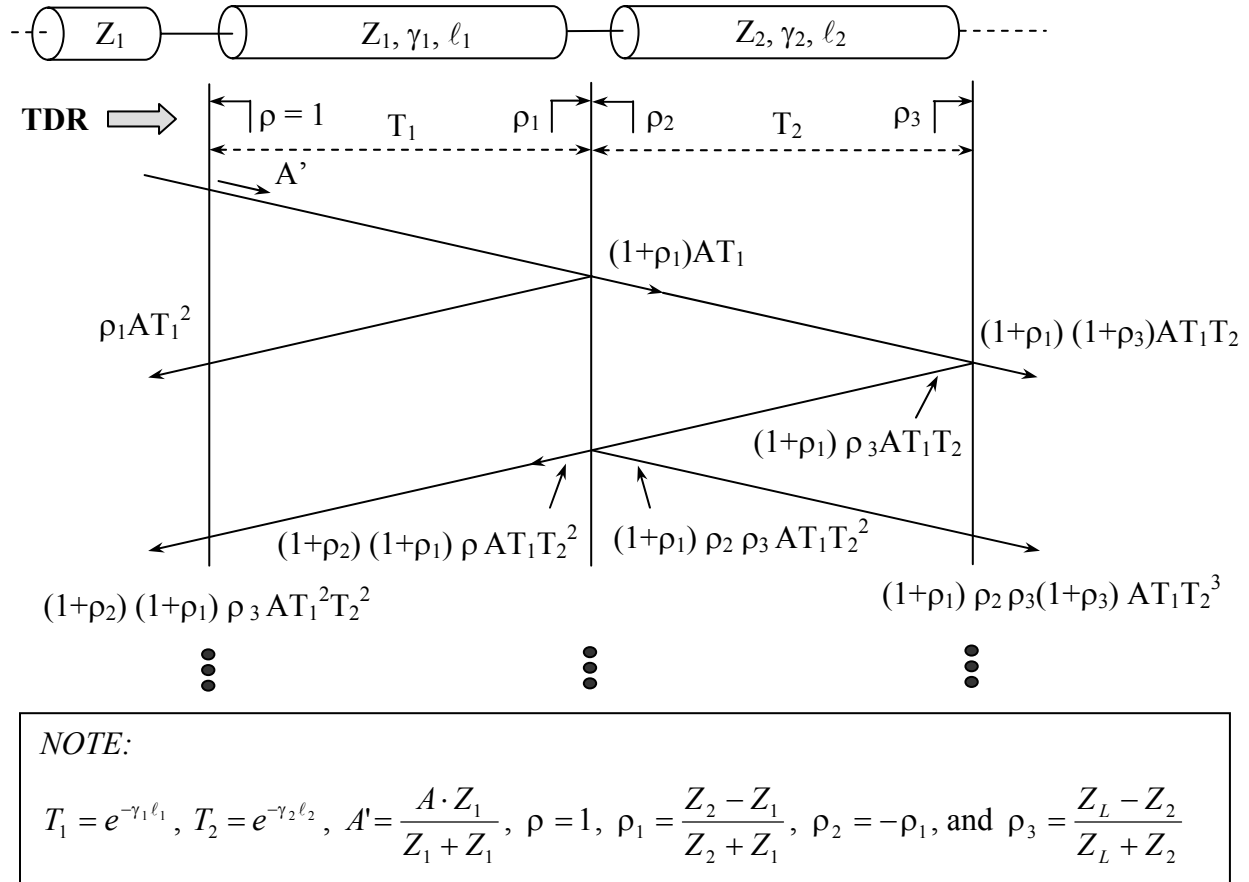


Figure C-4: Time domain bounce diagram example.

### Time Domain Measurements

The essential property of time domain reflectometry techniques is the ability to distinguish discontinuities and the time separation between them. A schematic illustration of the components of a time domain measurement system is shown in *Figure C-5*. The RF pulse generator triggers a sampling oscilloscope as the pulse enters the system under test. The figure displays the measurement locations of both the reflection and transmission, Time Domain Transmission (TDT), measurements. In the case of the stepped pulse input, which is typically used because the pulse's frequency spectra extends to dc, the time domain resolution depends on the risetime of the step, which is inversely related to the step function's bandwidth.

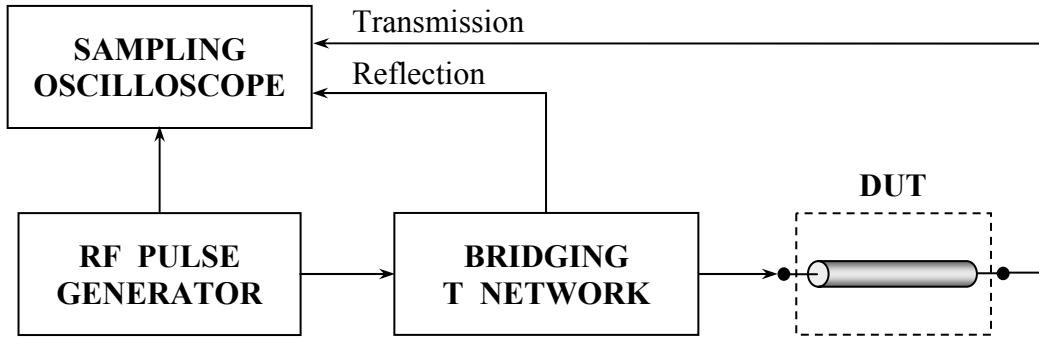


Figure C-5: General TDR and TDT measurement setup

One advantage of time domain measurements is that they require only a single measurement where the frequency domain techniques require frequency sweeping, which involves a measurement at each discrete frequency. Another advantage of TDR is that the resulting waveform immediately gives a physical insight into the characterization problem, whereas calculations (i.e. pulse development, convolution, Fourier transforms) need to be performed to the FDR equivalent measurement before information is visually realizable by the user. A problem associated with TDR is that the method is more susceptible to noise due to the wide variety of noise reducing algorithms in the frequency domain. Also, the method is limited by the pulse generating equipment with respect to the number of pulses and the pulse characteristics that may be used.

### Frequency Domain Measurements

The measurement system used to perform frequency domain measurements is displayed in *Figure C-6*. It is important to note the presence of the vector analyzer, which is needed to recover the amplitude and phase of the system response. The sweeper is synthesized for accurate phase determination, but phase lock and roll can also be used if greater speed is essential. Vector analyzers employ calibration standards to reduce the reflection and transmission errors at the expense of an increased number of measurements resulting in increased measurement time. System bandwidth determines the limits to pulse and spectral line widths as well as line separation in the frequency spectra, which determines the aliasing time, or time duration.

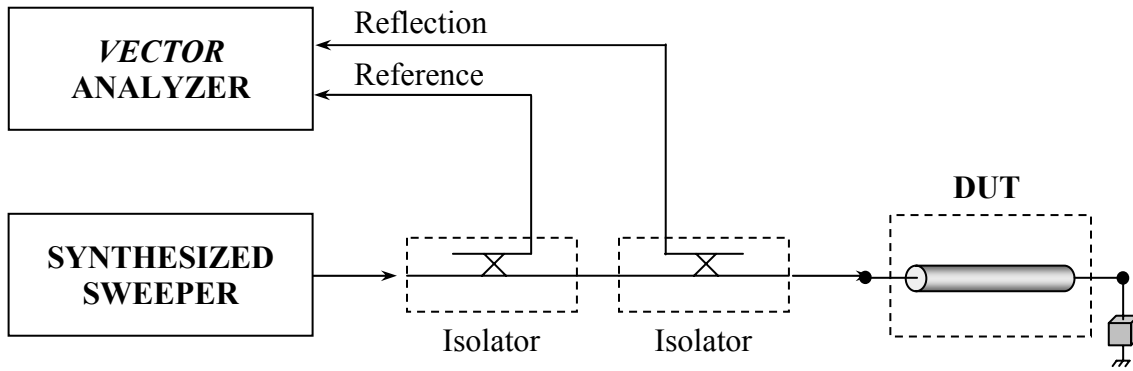


Figure C-6: General FDR and FDT measurement setup

As mentioned earlier, FDR has the advantage of improvement in signal noise and jitter due to the ease of application of noise reduction algorithms and the use of calibration techniques. Another advantage is that the limitation on waveforms is reduced; waveforms can be created and applied through frequency domain convolution prior to the Fourier transformation operation.

### Equivalences Between Time and Frequency Domain Measurements

To support the discussion and increase the understanding between the time and frequency domain measurement techniques, some correspondences between the two methods will be presented in this portion of the discussion [39].

#### Dispersion and Bandwidth

The relationship between frequency domain bandwidth and time domain dispersion will be presented in this section. Assume the frequency domain transfer function of a bandpass amplifier is measured. A typical response of this type of amplifier is shown in *Figure C-7*.

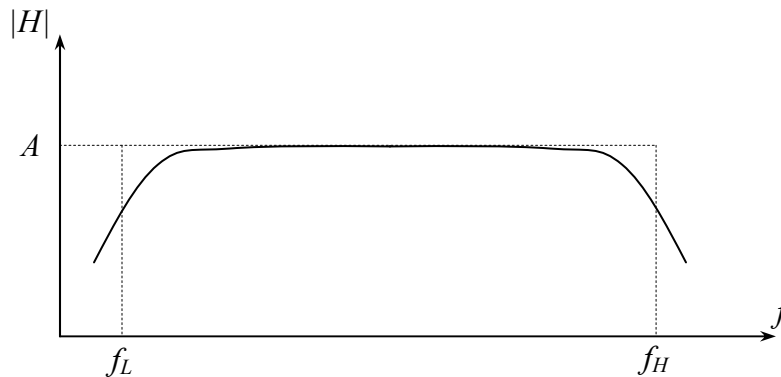
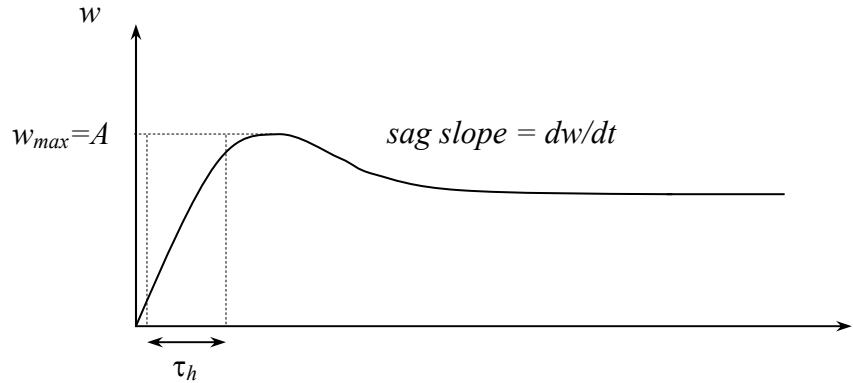


Figure C-7: Transfer function of a bandpass amplifier

Several parameters can be obtained from the frequency domain measurement to help characterize the amplifier's performance such as the midband gain,  $A$ , the low frequency cutoff,  $f_L$ , the high frequency cutoff,  $f_H$ , as well as how the amplifier behaves over the frequency band.

These parameters can also be determined using time domain techniques. By using a step waveform excitation into the input of the amplifier, the resulting output response will look similar to the waveform found in *Figure C-8*.



*Figure C-8: Time domain step response of a bandpass amplifier.*

The amplitude response,  $w_{max}$ , is equal to the midband gain of the amplifier, the cutoff frequencies can be determined from the transition duration,  $\tau_h$ , and the sag slope is calculated from the following [51]:

$$f_H - f_L = \frac{0.35}{\tau_h}, \quad (\text{C-1})$$

$$\text{sag slope} = -2\pi A \cdot f_L. \quad (\text{C-2})$$

This shows the midband gain and the cutoff frequencies can be obtained through time domain techniques. Since these values are frequency domain quantities, they are more directly obtained through frequency domain measurements. However, only a single time domain measurement is needed to obtain these quantities whereas several measurements are needed in the frequency domain as the measurement equipment sweeps through the desired frequency range. Other information obtained through the use of the time domain techniques include the fact that the waveform dispersion becomes more evident.

### Time Delay and Phase

If we consider the measurement system in *Figure C-9*, let a time delay,  $T_d$ , be applied to either the excitation,  $x(t)$ , or the system response,  $h(t)$ , by introducing a delay network between the pulse network and the system. If the delay is considered as part of the pulse generator, the excitation pulse can be written as  $x(t - T_d)$ . The delay can also be considered as part of the network resulting in system's impulse response to become  $h(t - T_d)$ .

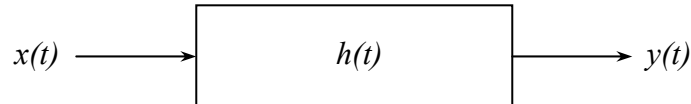


*Figure C-9: General network representation*

In either case the response of the altered system takes the form:

$$y(t - T_d) = x(t - T_d) * h(t) = x(t) * h(t - T_d). \quad (\text{C-3})$$

The resulting frequency domain response is as follows:

$$Y(j\omega) \cdot \exp(j\omega T_d) = X(j\omega) \cdot \exp(j\omega T_d) \cdot H(j\omega). \quad (\text{C-4})$$

The resulting function will have the exactly the same magnitude function as  $Y(j\omega)$ , the same response as the old system. The only difference between the two functions is the linear phase component,  $\omega T_d$ . This demonstrates the ability to relate the time delay to a phase component in the frequency domain.

### Problems of Transforming Data Between the Domains

Examples of problems associated with transformations from the time domain to the frequency domain and vice versa will be presented in a practical sense in this section. During characterization, it is usually necessary to convert the information from one domain to the other to obtain the benefits of each domain. When processing this transformation, leakage errors and aliasing errors can be encountered in the time and frequency domains. Examples of these errors will be presented in this section along with possible solutions and methods of error quantification.

### Aliasing Error

Aliasing, or fold-over errors are caused by not having a bandlimited signal, which causes the Nyquist rate to be undefined, which in turn causes overlapping and an unrecoverable signal. The effect of aliasing in a TDR waveform is shown in *Figure C-10*. In this case the sampling frequency is increased from 40MHz to 120MHz and the reduction of aliasing is clearly shown. Bandlimiting the input pulse would also have an effect on the desired sampling frequency needed. It has also been proposed during simulations of TDR pulses to sample at a high frequency then downsample the waveform to obtain a number of points that is computationally acceptable.

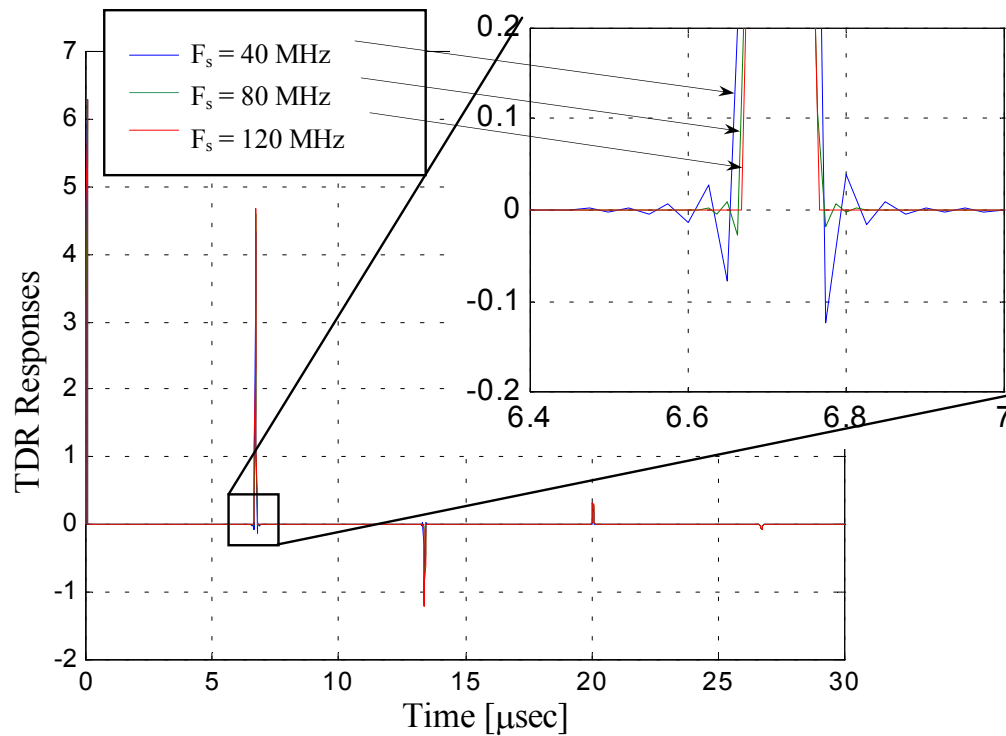


*Figure C-10: Effect of aliasing error on the time domain waveform*

### Frequency Domain Leakage Error

Frequency domain leakage error is a source of error resulting when the waveform is not bandlimited within the frequency under investigation. It can also be defined as an error which results when the sampling frequency is not sufficient to capture the full amount of information needed to produce an ideal response. In a sample case of modeling transmission lines, the

imaginary portion of the intrinsic impedance,  $X_o$ , may not be given enough time to reach zero at the specified sampling frequency. This frequency domain truncation of  $X_o$  is incorporated in the calculated time domain reflected admittance as leakage error. A plot of an imaginary portion of the intrinsic impedance versus frequency is shown in *Figure C-11*.

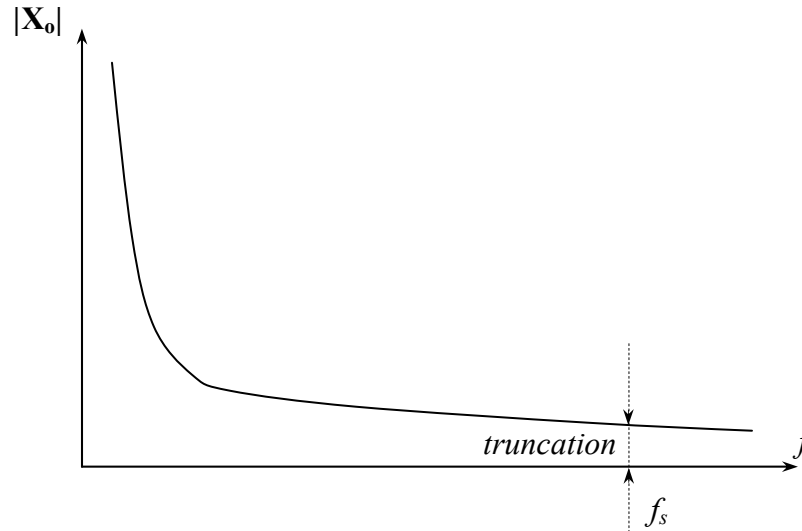


*Figure C-11: Response of  $X_o$  versus frequency and the truncation at the sampling frequency.*

The input pulse used in the calculation of the time-reflected voltage waveform must be bandlimited to reduce the effects of the frequency domain leakage error. When convolving in the frequency domain, if the pulse or the system information is bandlimited, then the result of the frequency domain convolution will be bandlimited. The time domain data will show no effects of the removed leakage error.

Investigating the frequency domain response of the generated waveforms, it is discovered that the response is usually not completely band-limited. A proposed method to determine the amount of error is to use a window function in the frequency domain to force a completely band-limited response. A Kaiser Window function [35] can be applied to the frequency domain response of the input pulse. The Kaiser Window uses zeroth-order modified Bessel functions of the first kind to produce the window function. The Kaiser window is defined as follows:

$$w[n] = \begin{cases} \frac{I_o[\beta (1 - [(n-\alpha)/\alpha]^2)^{0.5}]}{I_o(\beta)}, & 0 \leq n \leq M \\ 0, & \text{otherwise} \end{cases} \quad (\text{C-5})$$

Another typical proposed filter method is using the Blackman filter [35] to accomplish the band-limiting task. The Blackman filter is defined as follows:

$$w[n] = \begin{cases} 0.42 - 0.5 \cos(2\pi n/M) + 0.08 \cos(4\pi n/M), & 0 \leq n \leq M \\ 0, & \text{otherwise} \end{cases} \quad (\text{C-6})$$

### Time Domain Leakage Error

Time domain leakage errors are a redistribution of energy as a result of time gating, which results from the inverse Fourier transforms. Leakage error is encountered because the waveform may not have a limited time duration and the gating function used on the data is not continuous before performing the transformation operation. An example of a limited time duration causing truncation and resulting in time domain leakage error is shown in *Figure C-12*. Methods for correcting leakage errors were presented in the Chapter 2.

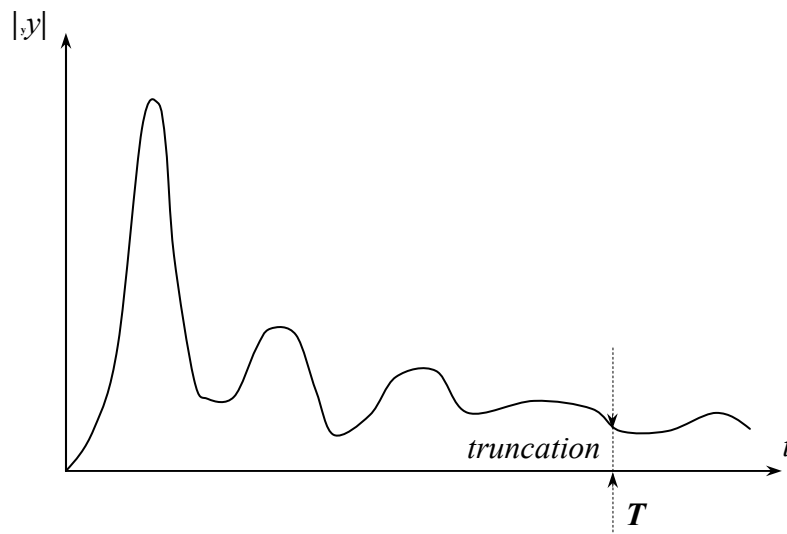


*Figure C-12: Response of  $y(t)$  versus time and the truncation at the selected time duration.*

## Time and Frequency Domain Measurement Critical Comparison

It has been demonstrated that the measurements for device and network characterization can be performed in the time and frequency domain. In this section, the system comparisons between the two methods will be discussed.

### *Transition Duration and Frequency Band Limitations*

The relationship between limited transition duration,  $\tau$ , and frequency band limitations,  $BW$ , will be presented in this section. It will be shown that the bandwidth is a reciprocal of the time duration. The number of points in the time domain transition duration,  $N_\tau$ , and the number of points in the frequency domain bandwidth,  $N_{BW}$ , are given as:

$$N_\tau = \frac{\tau}{\Delta T}, \text{ and} \quad (\text{C-7})$$

$$N_{BW} = \frac{BW}{\Delta f}, \quad (\text{C-8})$$

where  $\Delta T$  is the time spacing, or time resolution, and  $\Delta f$  is the frequency spacing, or frequency resolution.

Multiplying  $N_\tau$  and  $N_{BW}$  results in the following:

$$N_\tau N_{BW} = \frac{\tau \cdot BW}{\Delta T \Delta f}. \quad (\text{C-9})$$

From the familiar expression [35] for passive networks which are not underdamped, the following is given:

$$\tau = \frac{2.2}{\omega_{3dB}} = \frac{0.35}{f_{3dB}} = \frac{0.35}{BW}, \quad (\text{C-10})$$

or

$$\tau \cdot BW \cong 0.35 \pm 10\%. \quad (\text{C-11})$$

Applying the same methodology to the number of points results in the following:

$$N_\tau N_{BW} \cong 0.35 N. \quad (\text{C-12})$$

Substituting (C-10) and (C-11) into (C-9), the number of points is related to the time and frequency domain resolution as follows:

$$\Delta T \Delta f = \frac{1}{N}. \quad (\text{C-13})$$

In (C-11), the time duration is shown to be related to the reciprocal of the bandwidth. It is obvious that a higher speed transition duration results in a wideband signal in the frequency domain. Therefore, faster pulses are required to increase the bandwidth of the input signal in time domain measurements. The relationship between the time and frequency domain resolution in (C-13) will be discussed in the following section.

### *Time and Frequency Resolution*

In the case of time and frequency domain resolution, the ideal situation is to have the time spacing,  $\Delta T$ , equal to zero which resulting in an infinite time duration,  $T = \infty$ , and an infinite number of samples,  $N = \infty$ . This unrealistic situation is even more noticeable noting that the measurement equipment would have to have an infinite bandwidth. The equation that relates the time and frequency domain resolution to the number of samples is shown in (C-13) where  $\Delta T$  is the time spacing, or time resolution, and  $\Delta f$  is the frequency spacing, or frequency resolution. The time resolution depends on the risetime, which is inversely related to the bandwidth of the step excitation function. A faster excitation risetime gives higher time resolution while compromising the frequency domain resolution as a result of the corresponding increase in bandwidth. The number of samples,  $N$ , is limited by the measurement equipment, so through investigating (C-13), there is an obvious trade off between frequency domain resolution and time domain resolution. Higher frequency domain resolution will result in lower time domain resolution and vice versa. The application will determine the weight of the resolution of each domain and will need to be modified to obtain desired results.

Some methods to increase time and frequency domain resolution, which are usually limited by the measurement equipment, will be investigated. The obvious method of increasing the resolution is by increasing the number of points, which will result in higher resolutions in both domains. An increase in the time domain resolution can be obtained by increasing the sampling frequency. As the relationship in (C-14) will increase the time domain resolution by an increase in the sampling frequency, the frequency domain resolution will be compromised.

$$\Delta T = \frac{1}{f_s} \quad (\text{C-14})$$

Another method of increasing resolution is through interpolation. Interpolation can be accomplished through zero padding before the Fourier or inverse Fourier transform, this process manually increases the number of points which increases resolution.

### *Dynamic Range*

Dynamic range is defined as the ratio between the maximum input level of a system by the minimum input level which the system provides reasonable signal quality. The input pulse of the system compromises the dynamic range in the time domain. The power applied by the input pulse is non-uniform or spread throughout the frequency range, which restricts the amount of power applied over the frequency spectra of the input pulse. At frequencies where the power of the input pulse is compromised, the system noise could cause measurement difficulties. The level of power supplied by the input pulse generator is also limited by the tolerances of the sampling head, therefore, introducing a high powered pulse to increase the dynamic range of the time domain measurement system is limited. Since the frequency measurements are taken using discrete methods, or taking one frequency at a time, the amount of power applied for each frequency point is fairly uniform with respect to the system noise. Since uniform power can be applied at all frequencies, the dynamic range of the frequency domain measurement system is much greater than that of the time domain counterpart.

## **Appendix D**

### **Twisted Pair Cable Measurement Results**

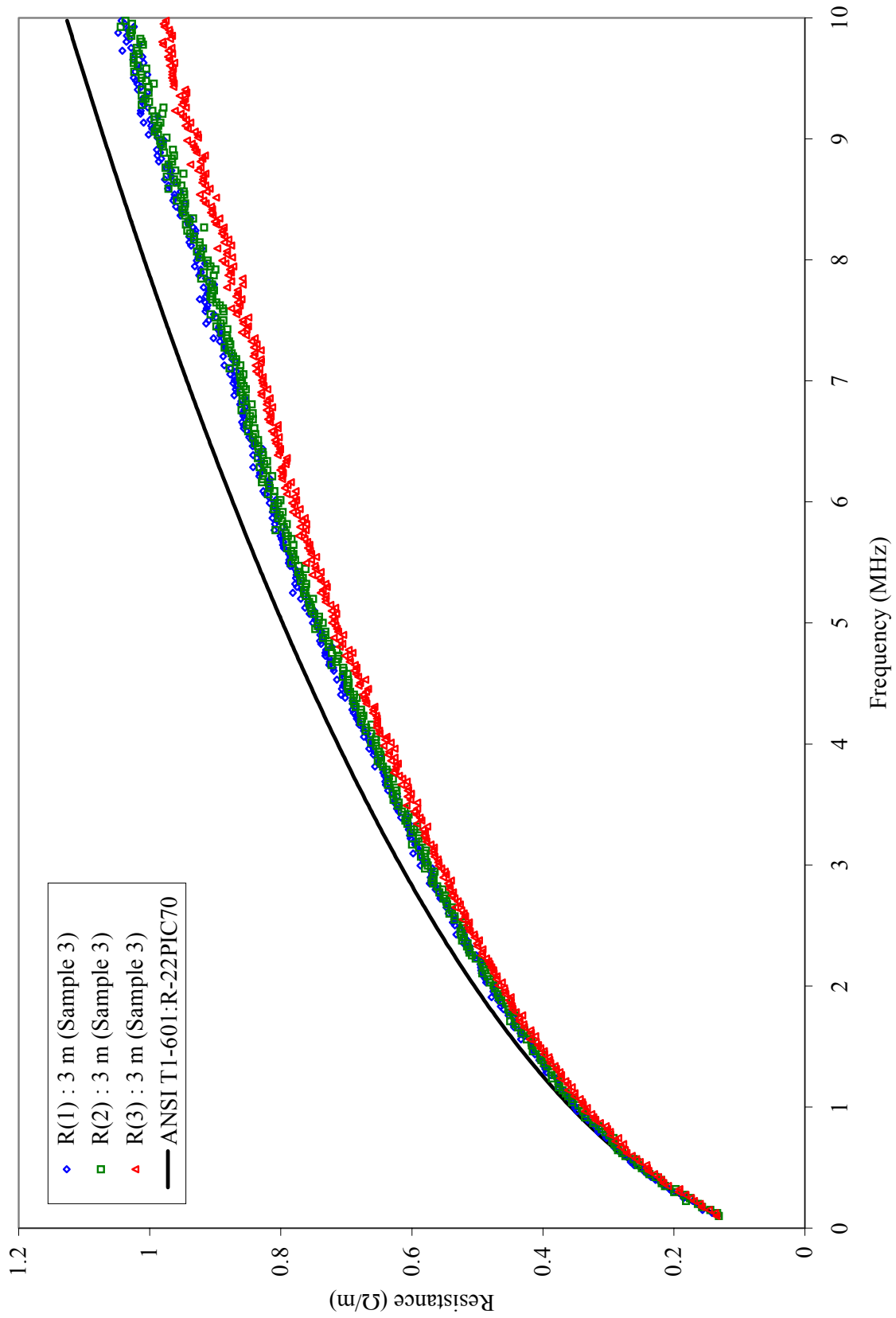


Figure D-1: Repeatability of Resistance ( $\Omega/m$ ) for Sample 3 of 22 AWG Cable.

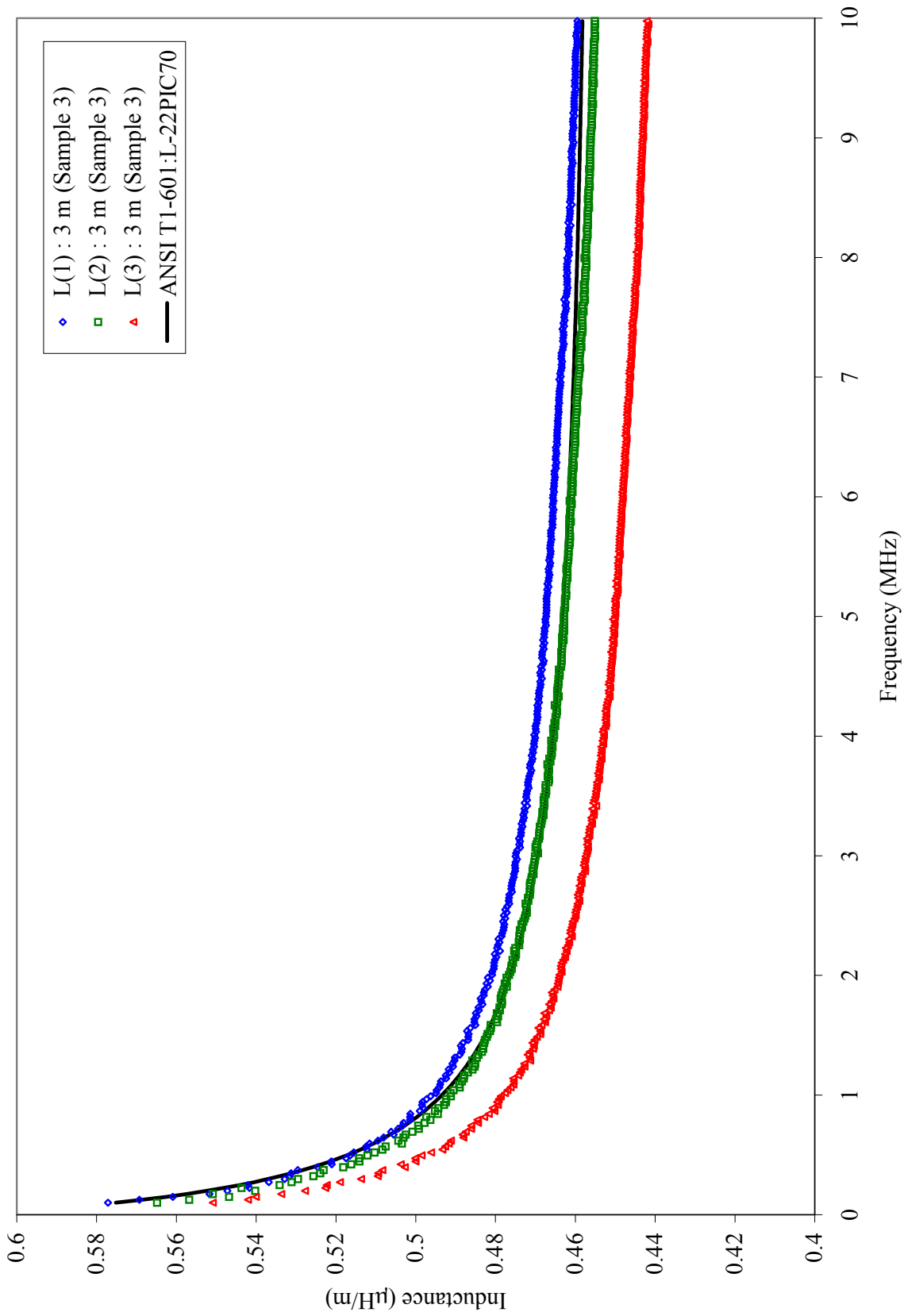


Figure D-2: Repeatability of Inductance (µH/m) for Sample 3 of 22 AWG Cable.

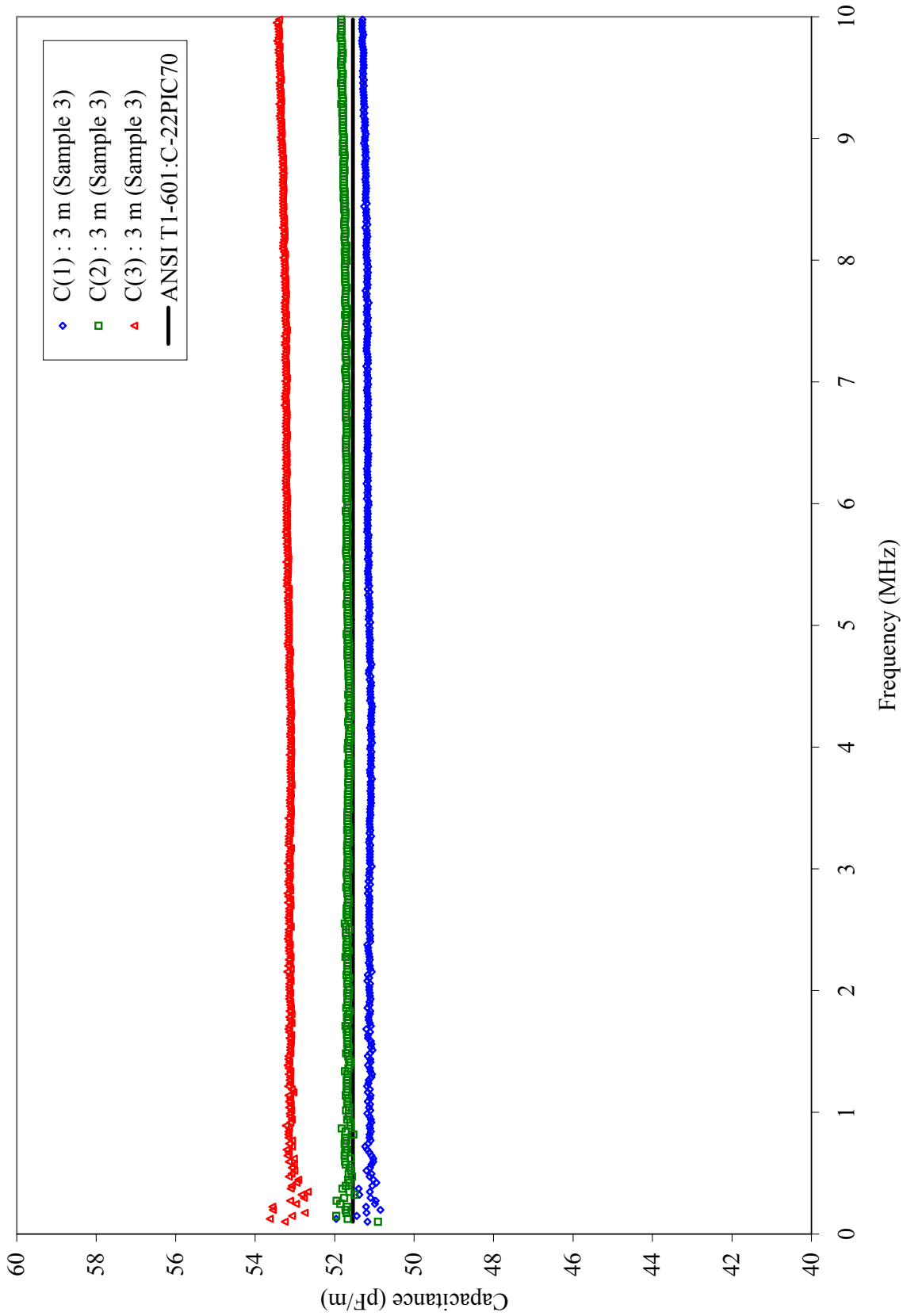


Figure D-3: Repeatability of Capacitance (pF/m) for Sample 3 of 22 AWG Cable.

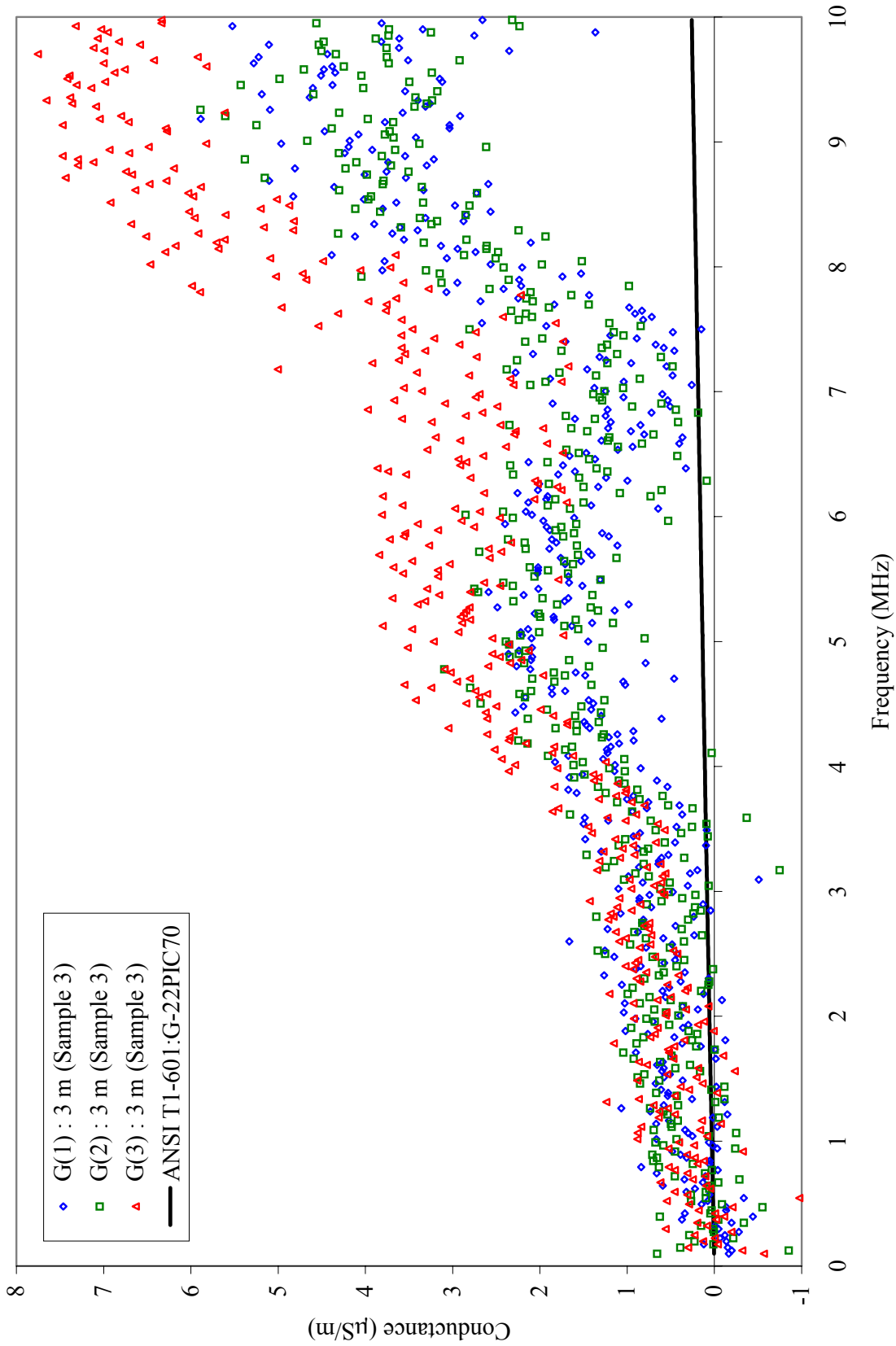


Figure D-4: Repeatability of Conductance ( $\mu\text{S}/\text{m}$ ) for Sample 3 of 22 AWG Cable.

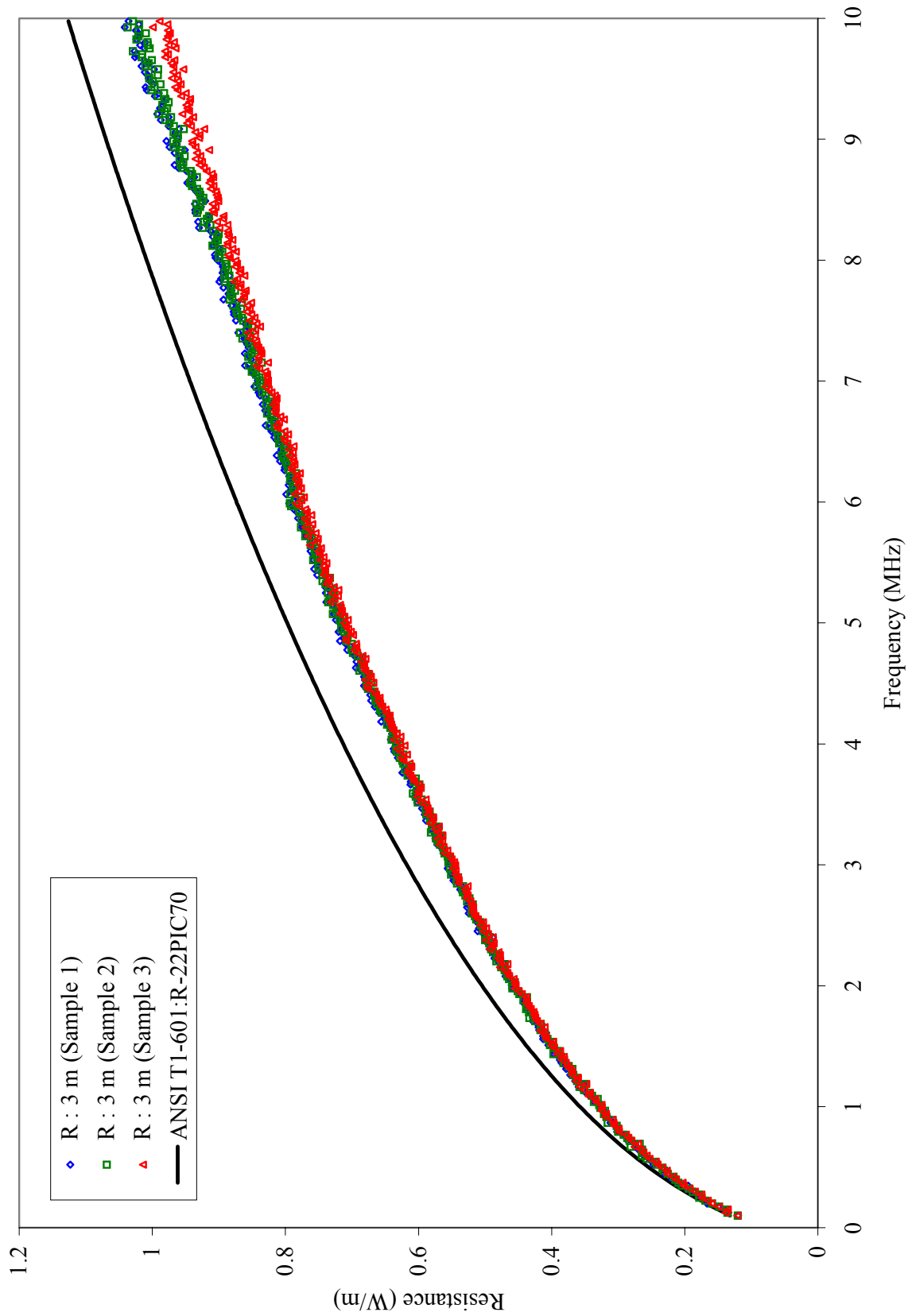


Figure D-5: Variability of Resistance ( $\Omega/m$ ) for Samples 1 through 3 of 22 AWG Cable.

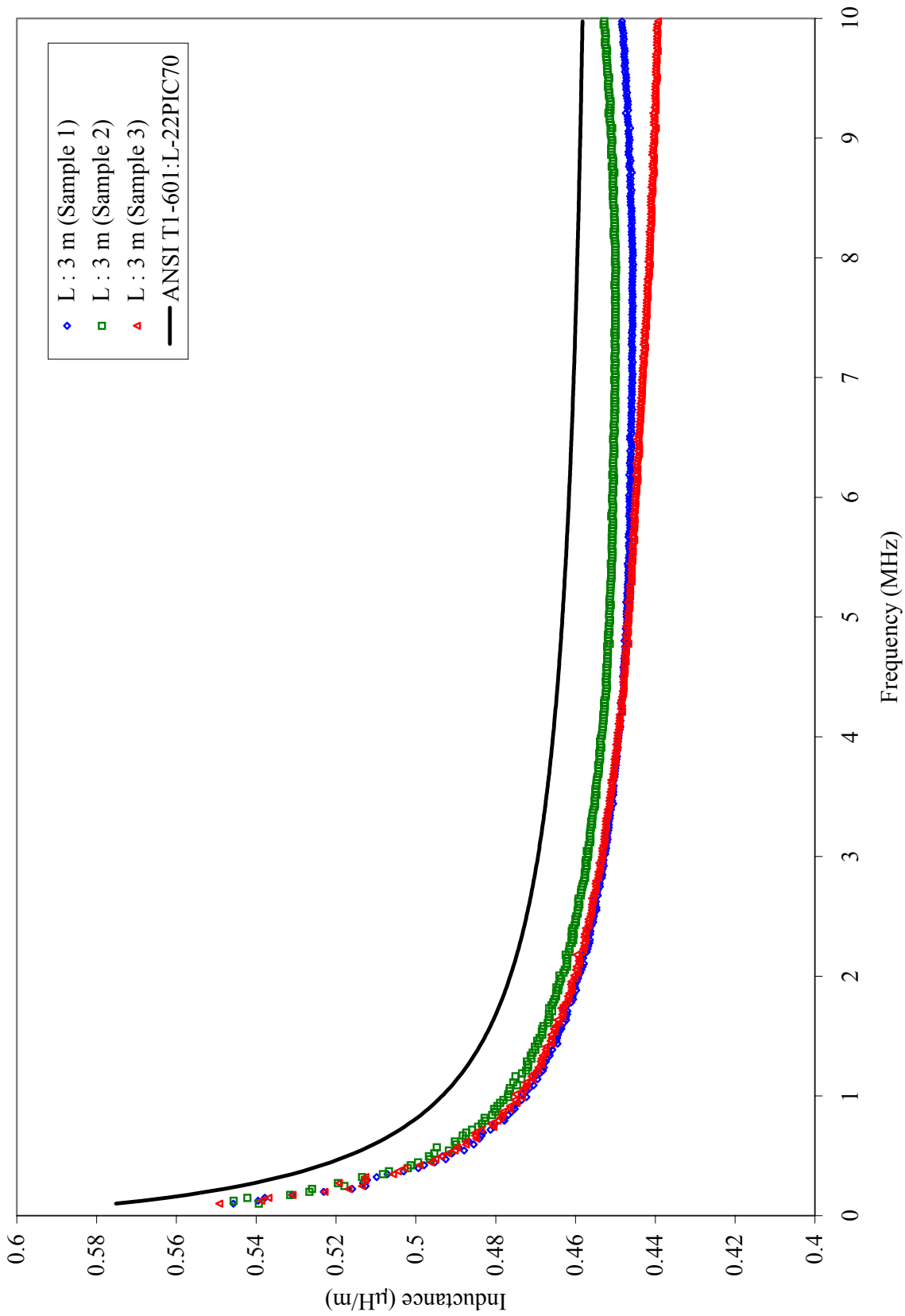


Figure D-6: Variability of Inductance ( $\mu\text{H/m}$ ) for Samples 1 through 3 of 22 AWG Cable.

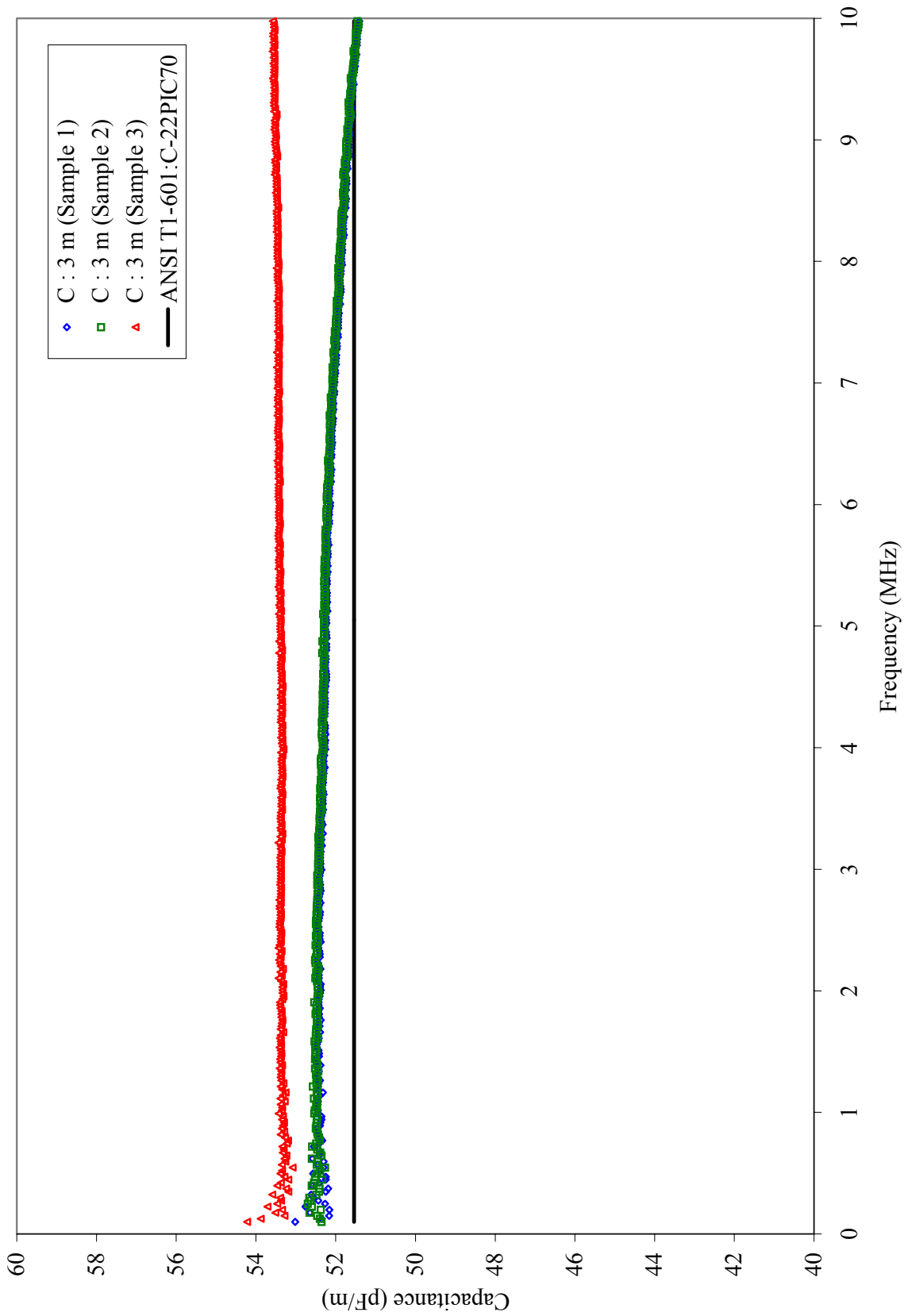


Figure D-7: Variability of Capacitance (pF/m) for Samples 1 through 3 of 22 AWG Cable.

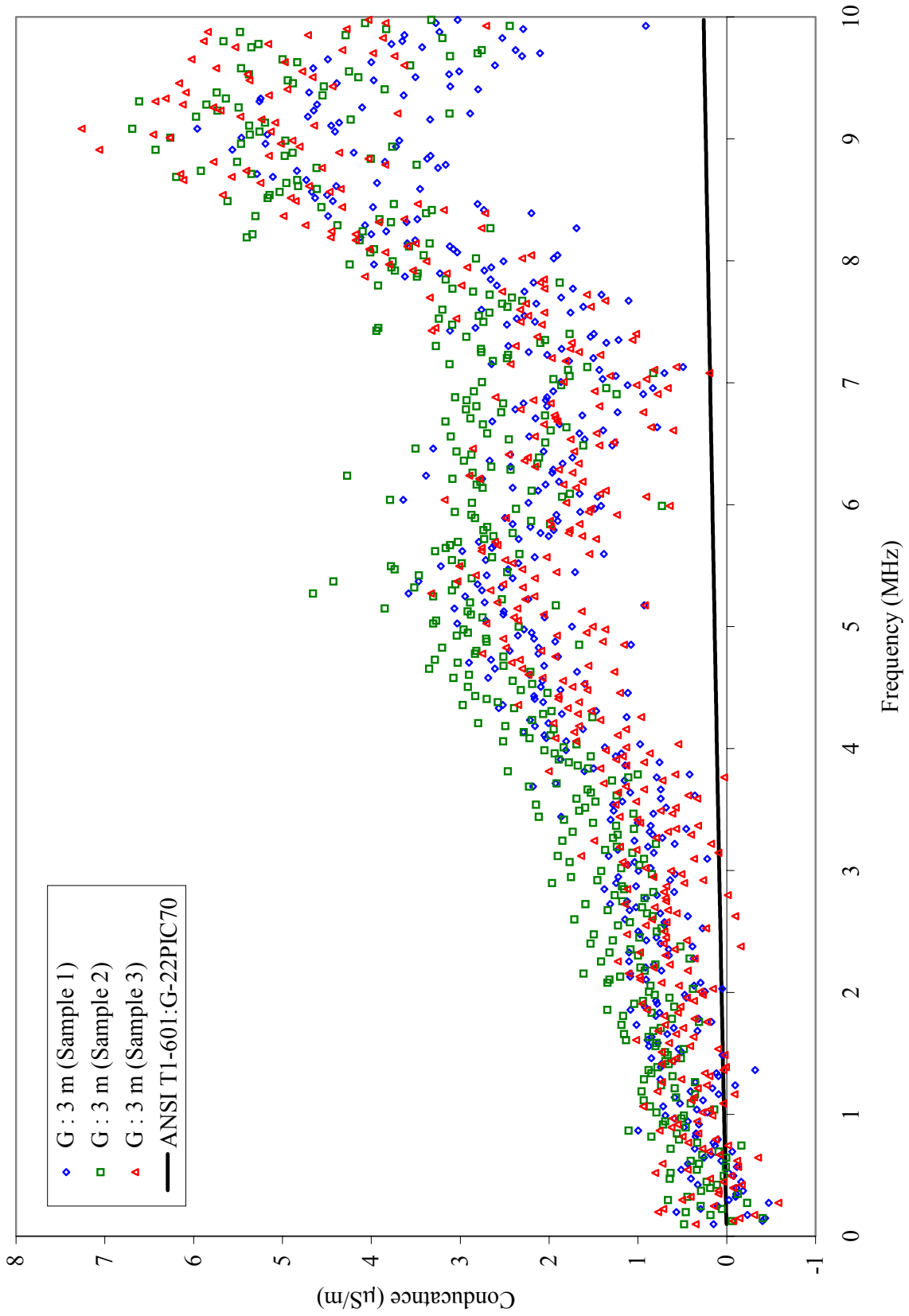


Figure D-8: Variability of Conductance ( $\mu\text{S/m}$ ) for Samples 1 through 3 of 22 AWG Cable.

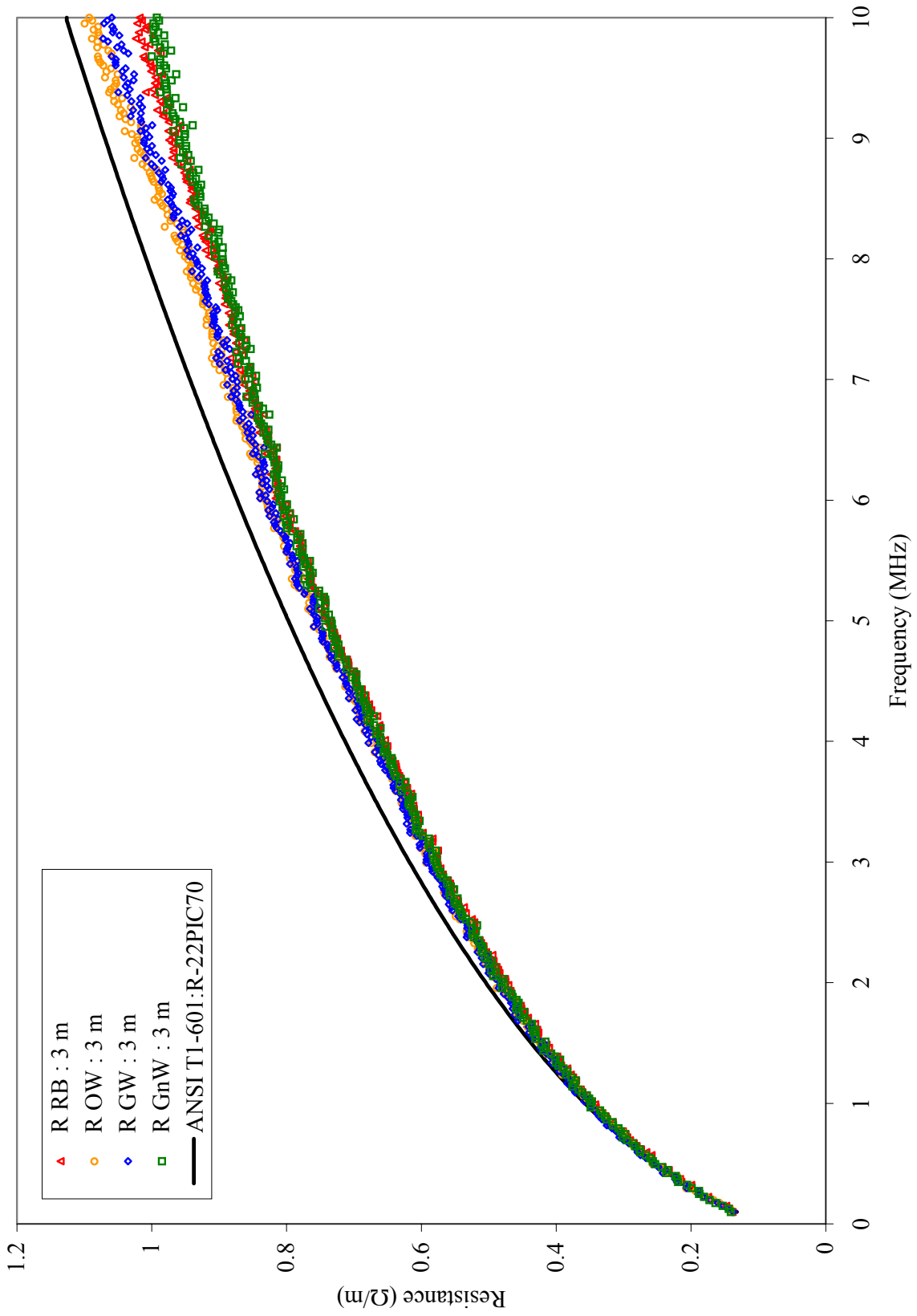


Figure D-9: Resistance ( $\Omega/m$ ) of Tabulated and Measured Data for Different 22 AWG Twisted-Pairs Contained Within a Cable.

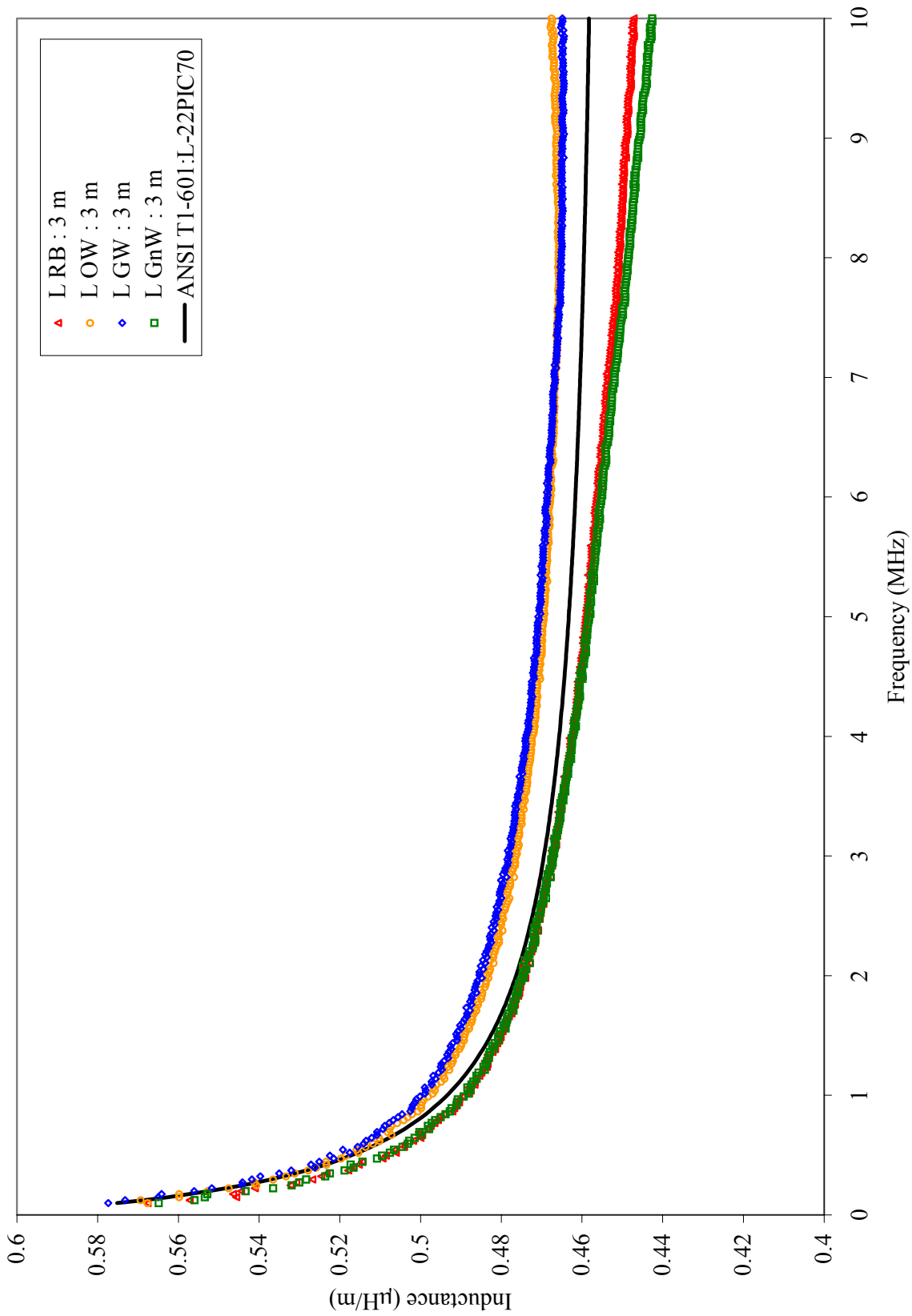


Figure D-10: Inductance ( $\mu\text{H}/\text{m}$ ) of Tabulated and Measured Data for Different 22 AWG Twisted-Pairs Contained Within a Cable.

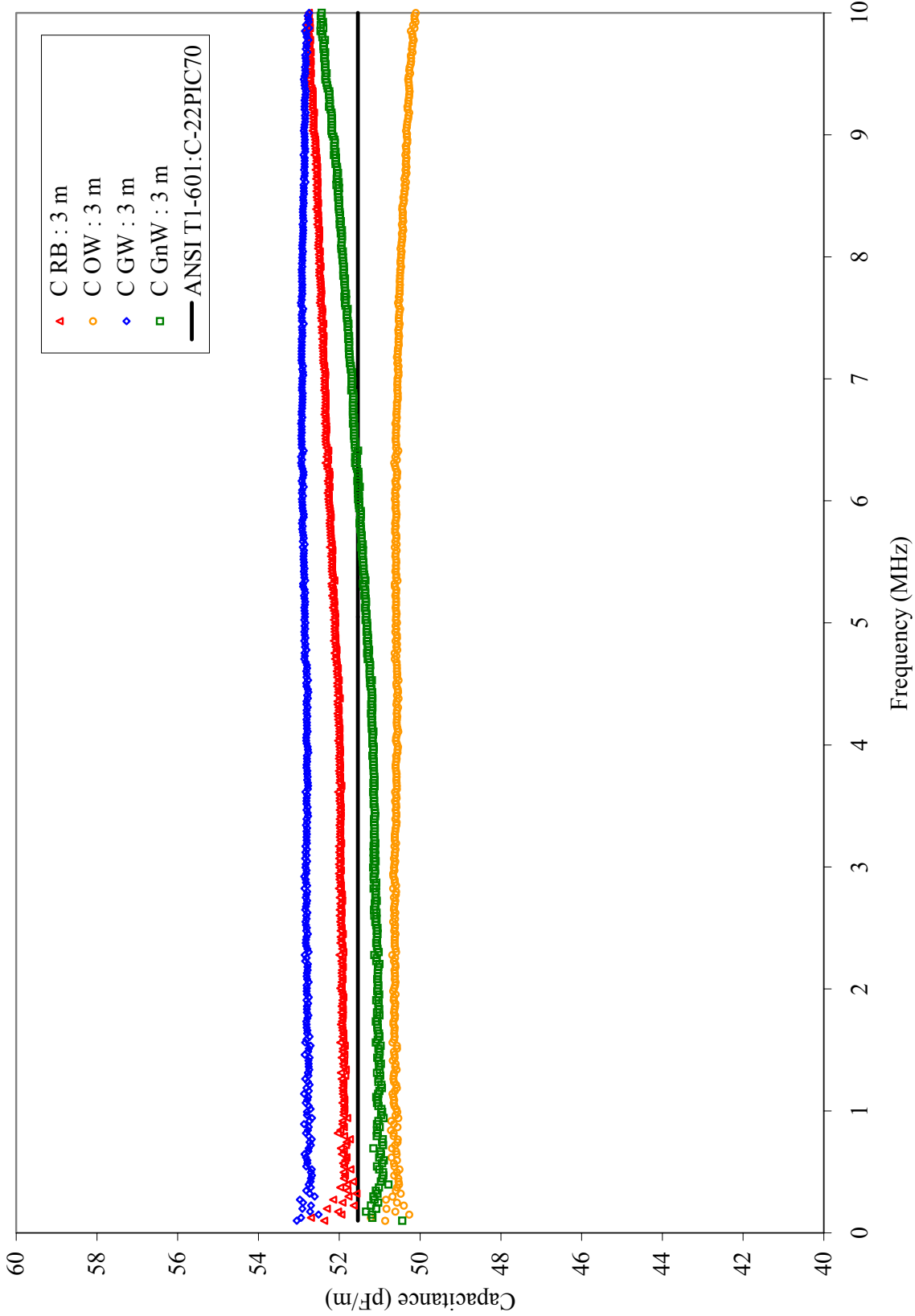


Figure D-11: Capacitance (pF/m) of Tabulated and Measured Data for Different 22 AWG Twisted-Pairs Contained Within a Cable.

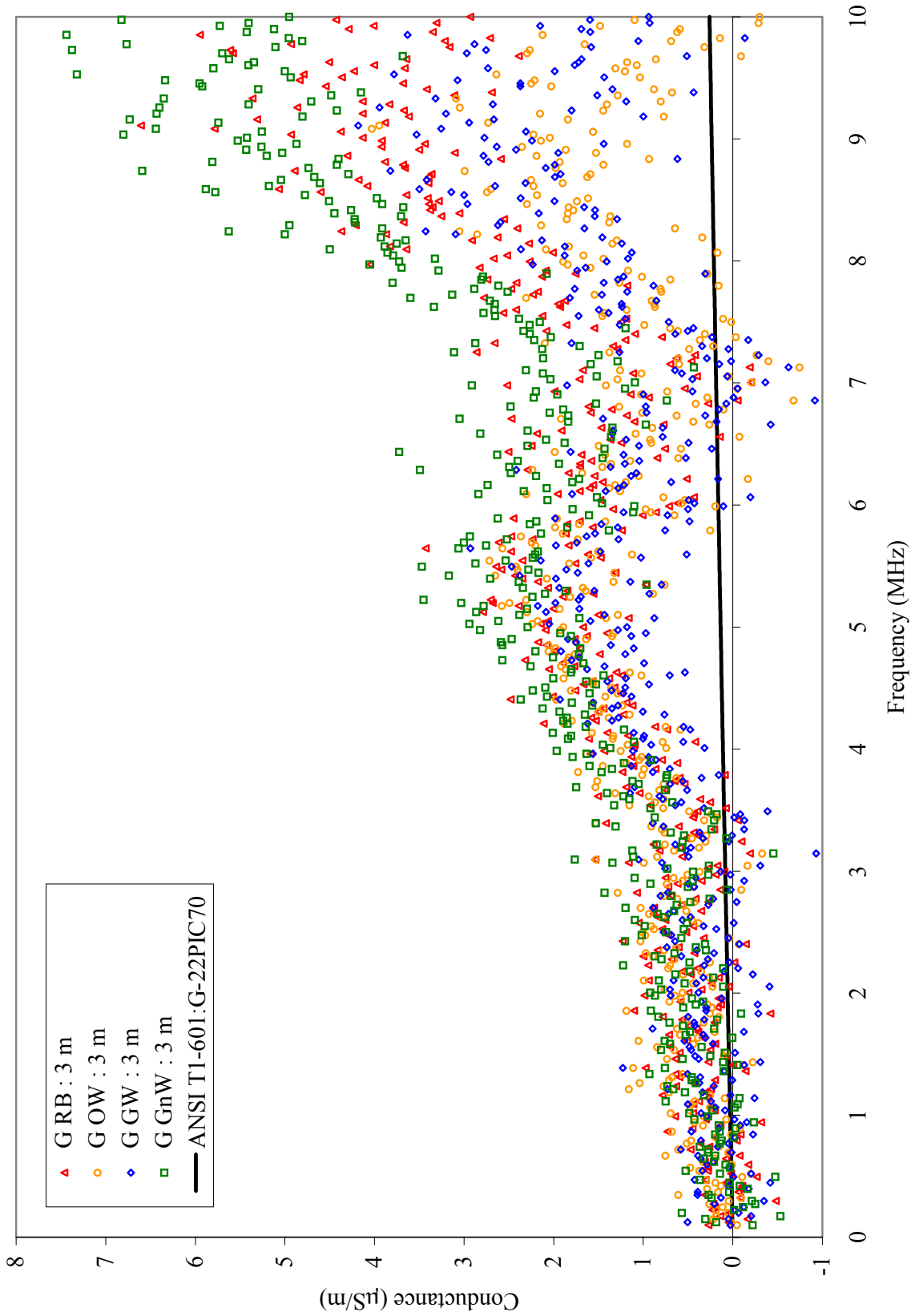


Figure D-12: Conductance ( $\mu\text{S/m}$ ) of Tabulated and Measured Data for Different 22 AWG Twisted-Pairs Contained Within a Cable.

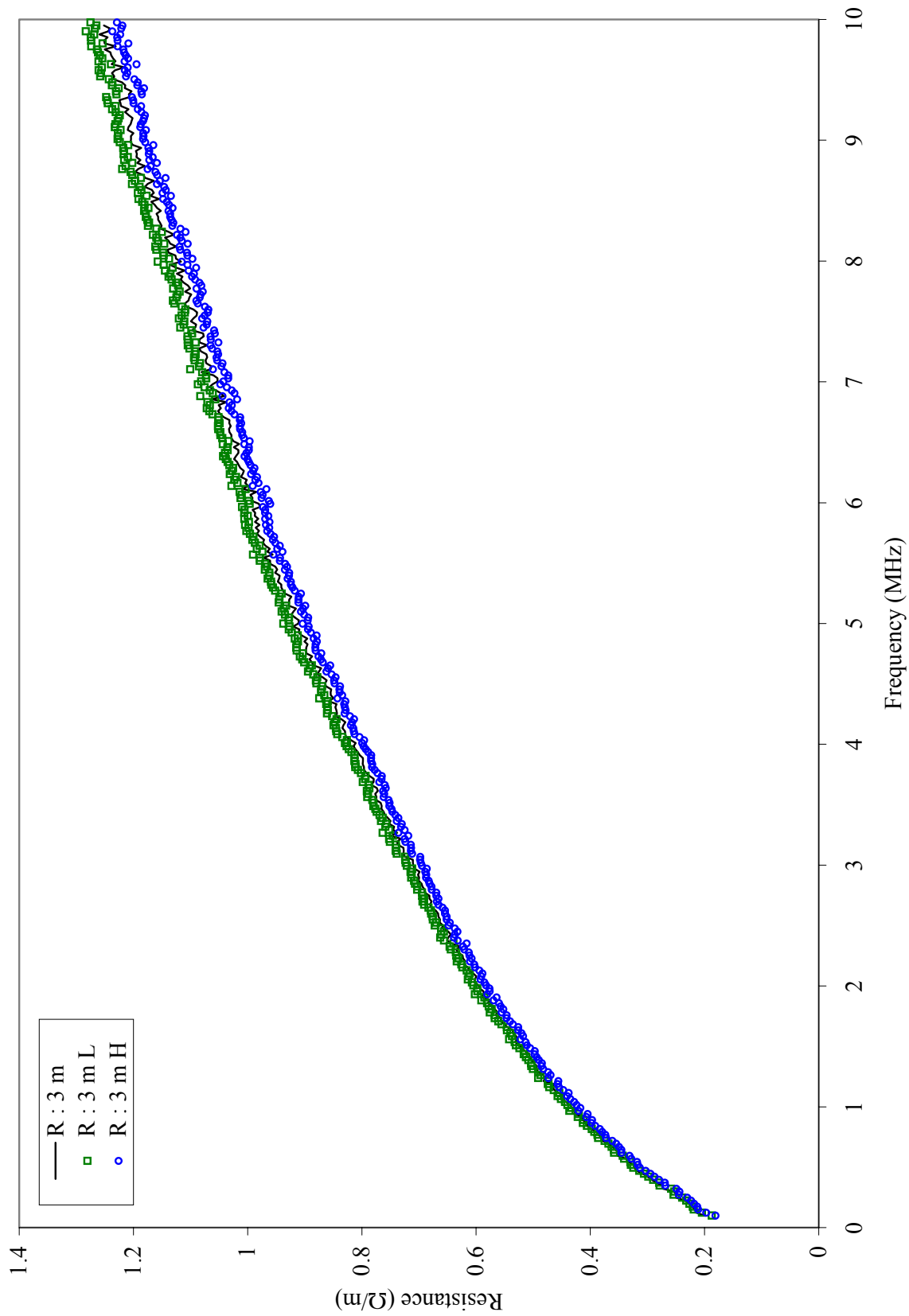


Figure D-13: ±Relative Error of Resistance (Ω/m) Measurement Due to Length Estimation Errors.

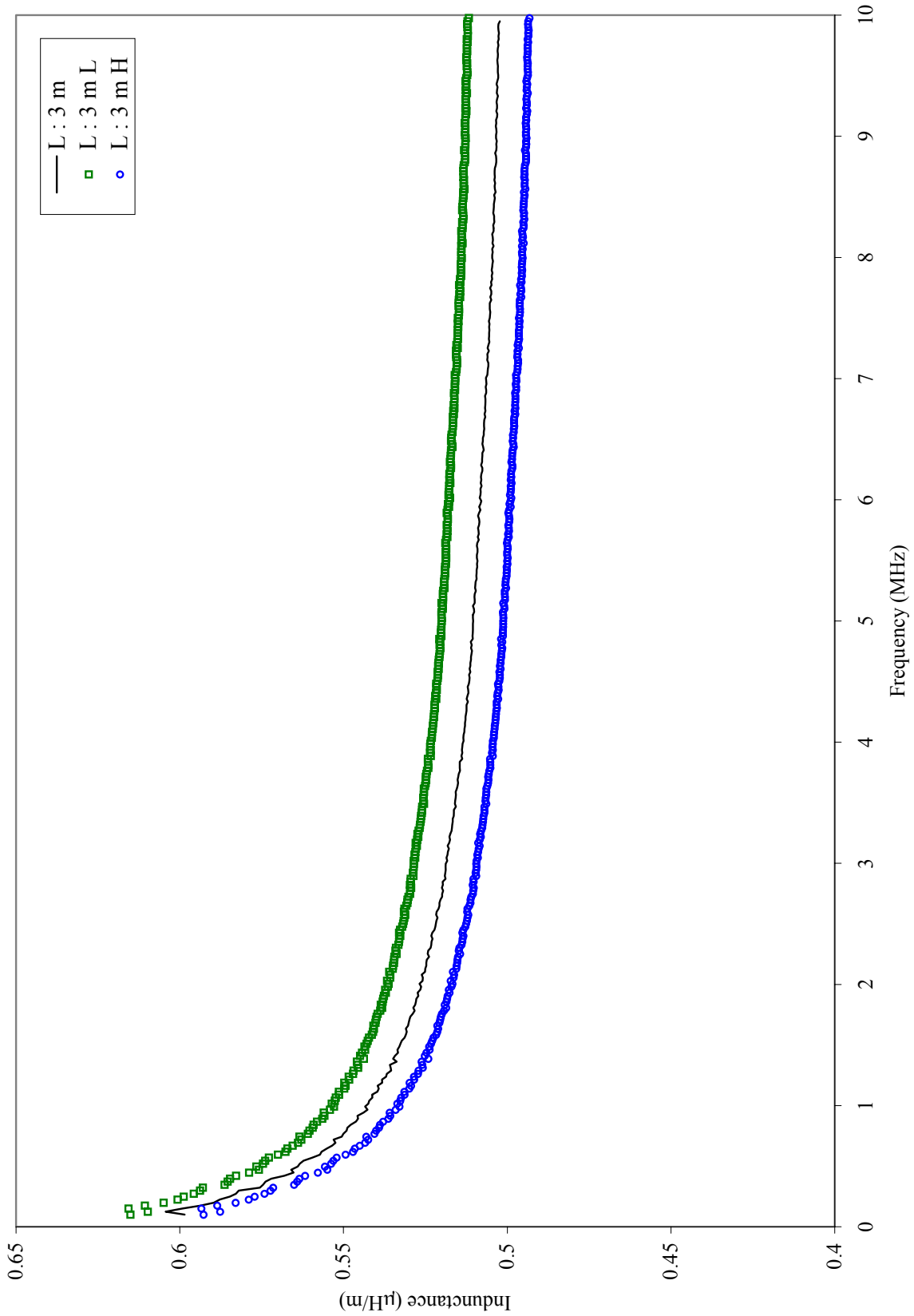


Figure D-14:  $\pm$ Relative Error of Inductance ( $\mu\text{H/m}$ ) Measurement Due to Length Estimation Errors.

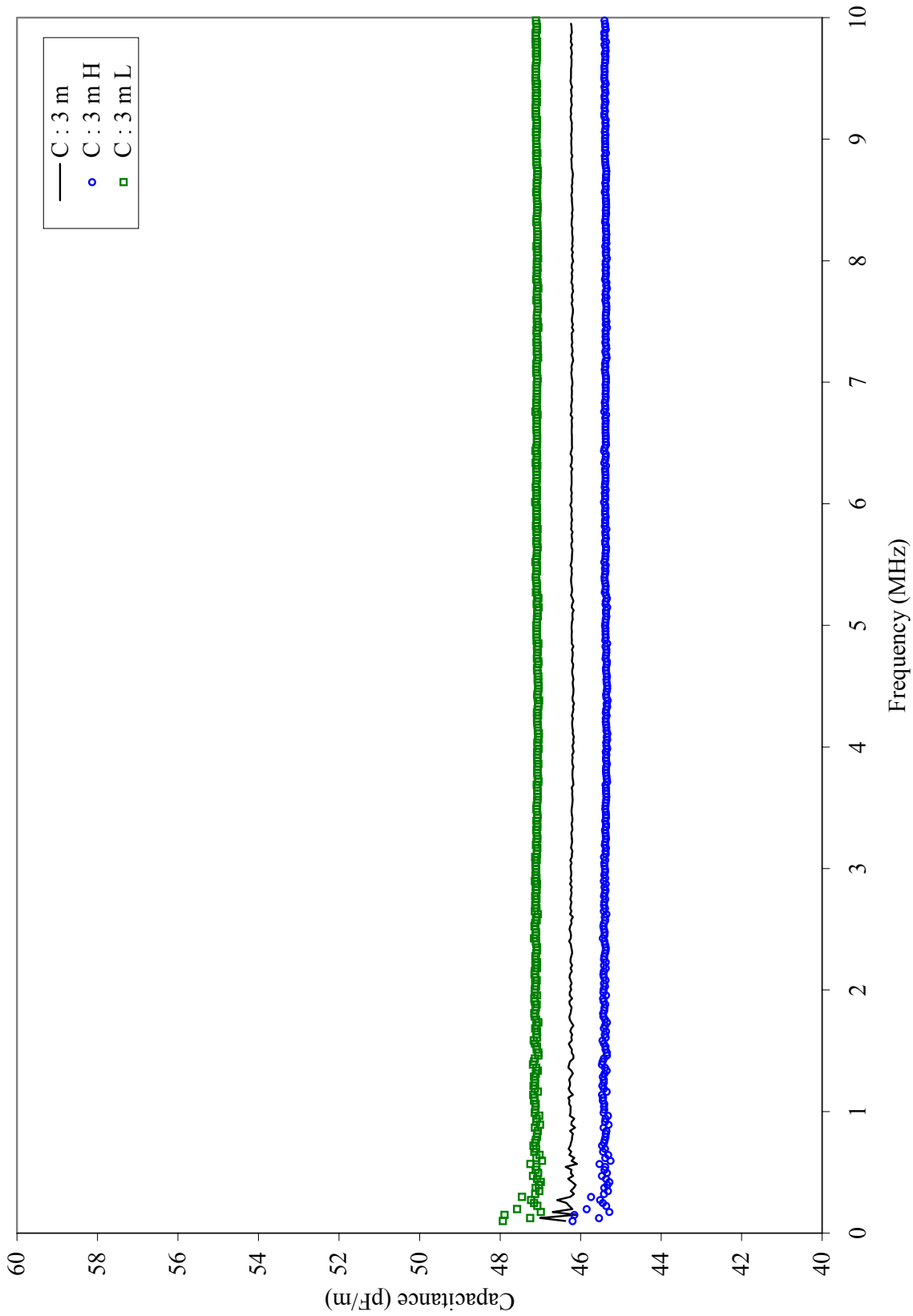


Figure D-15:  $\pm$ Relative Error of Capacitance (pF/m) Measurement Due to Length Estimation Errors.

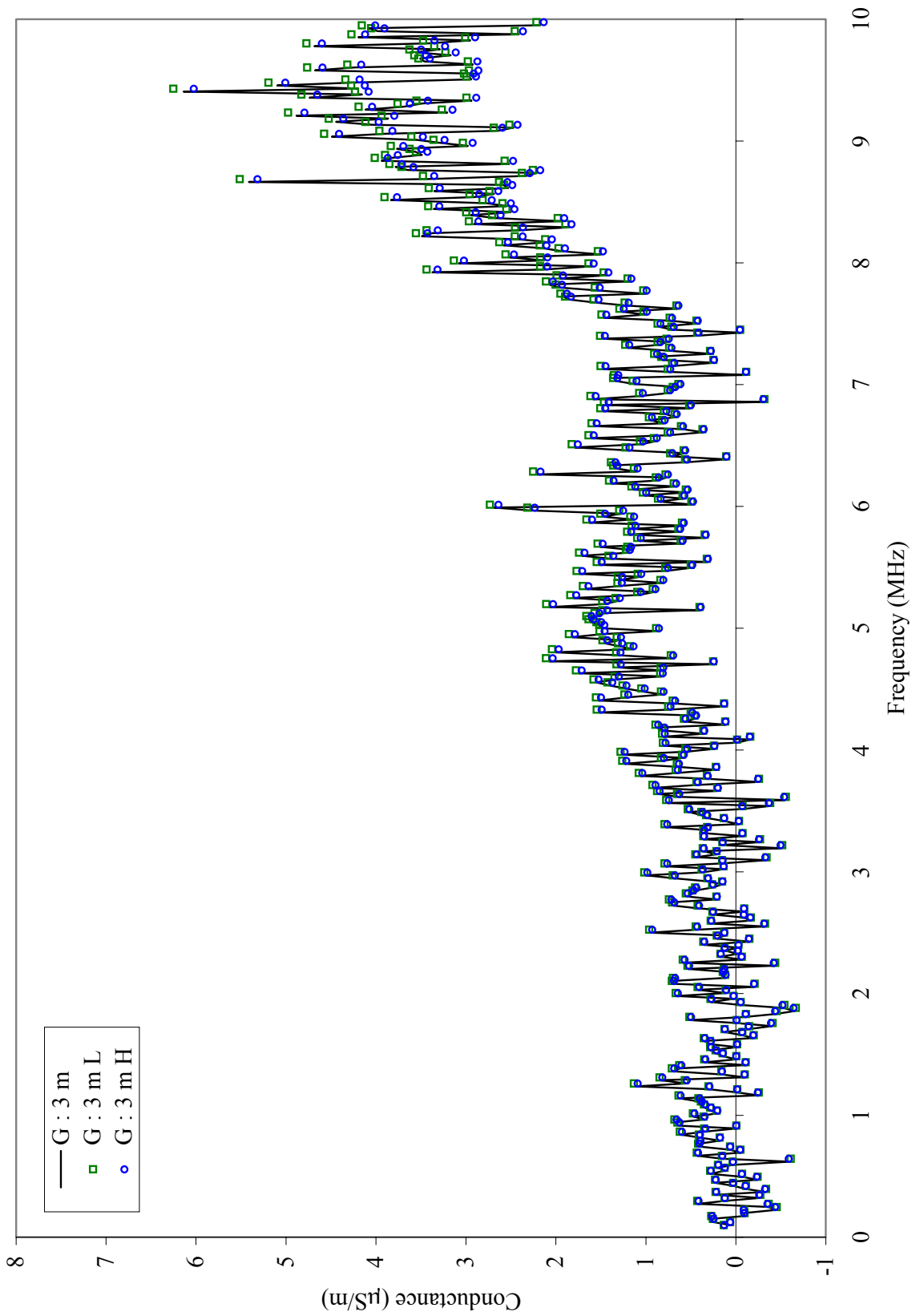


Figure D-16:  $\pm$ Relative Error of Conductance ( $\mu\text{S/m}$ ) Measurement Due to Length Estimation Errors.

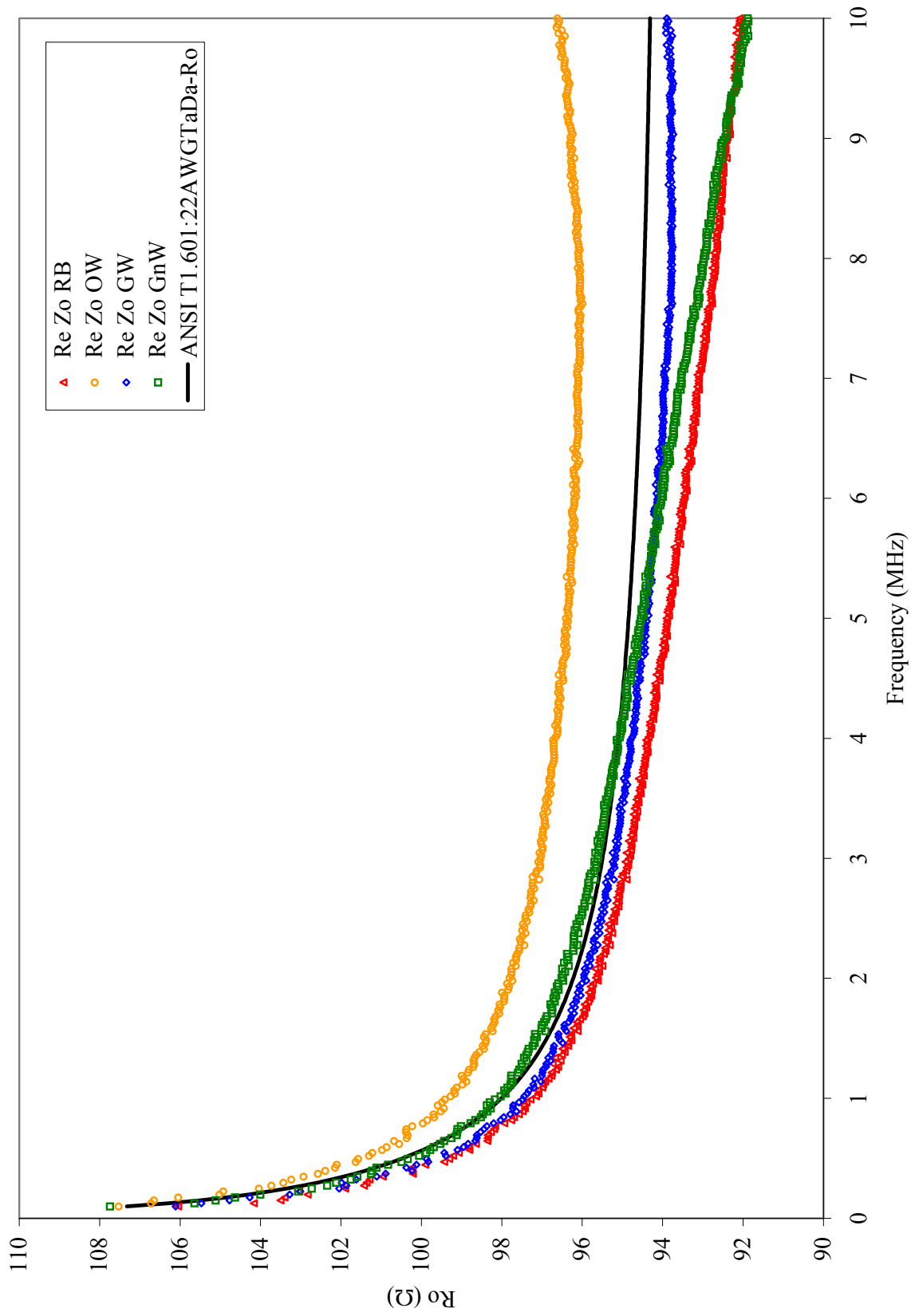


Figure D-17: Real Intrinsic Impedance of Tabulated and Measured Data for Different Twisted-Pairs of a 22 AWG Cable.

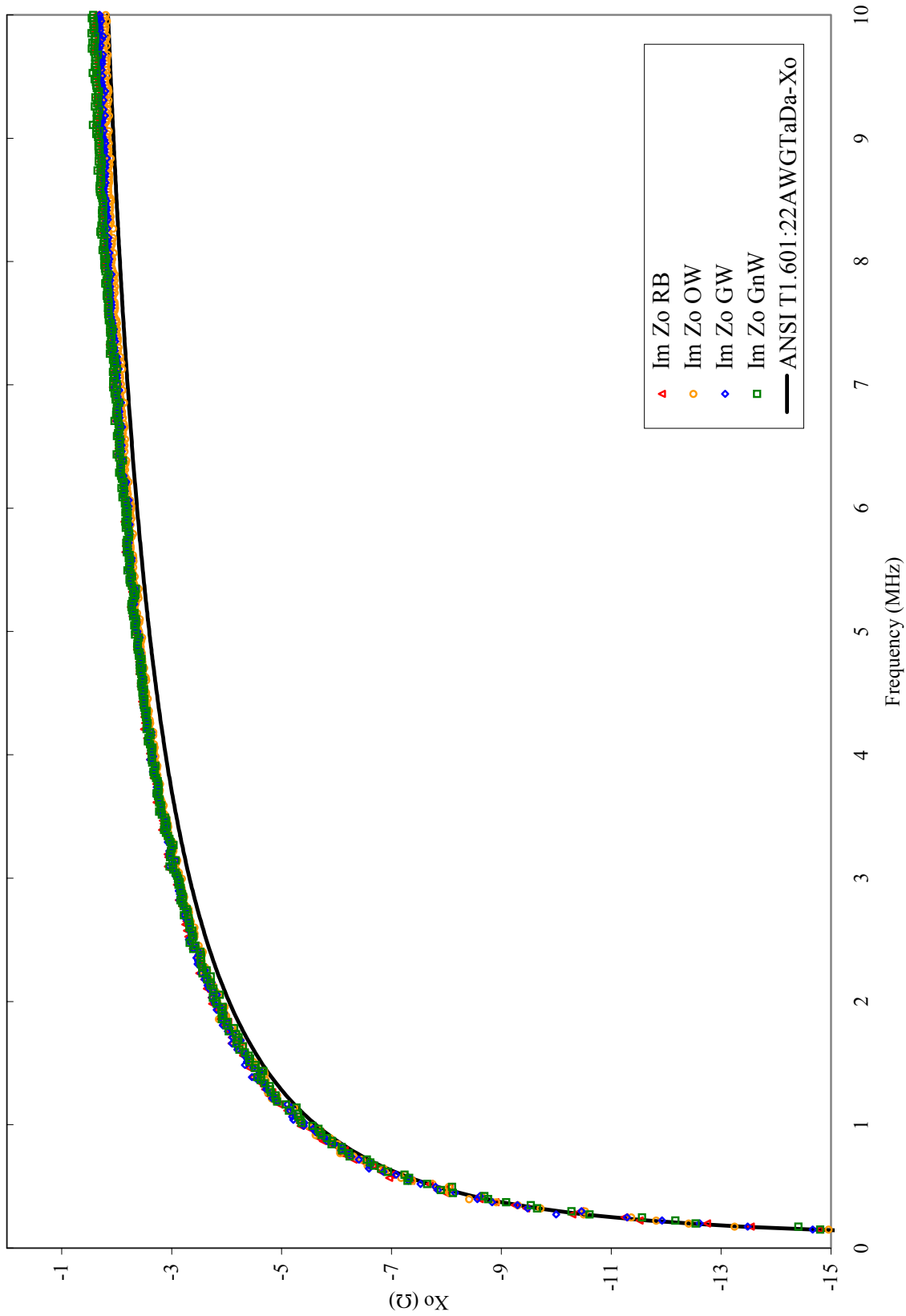


Figure D-18: Imaginary Intrinsic Impedance of Tabulated and Measured Data for Different Twisted-Pairs of a 22 AWG Cable.

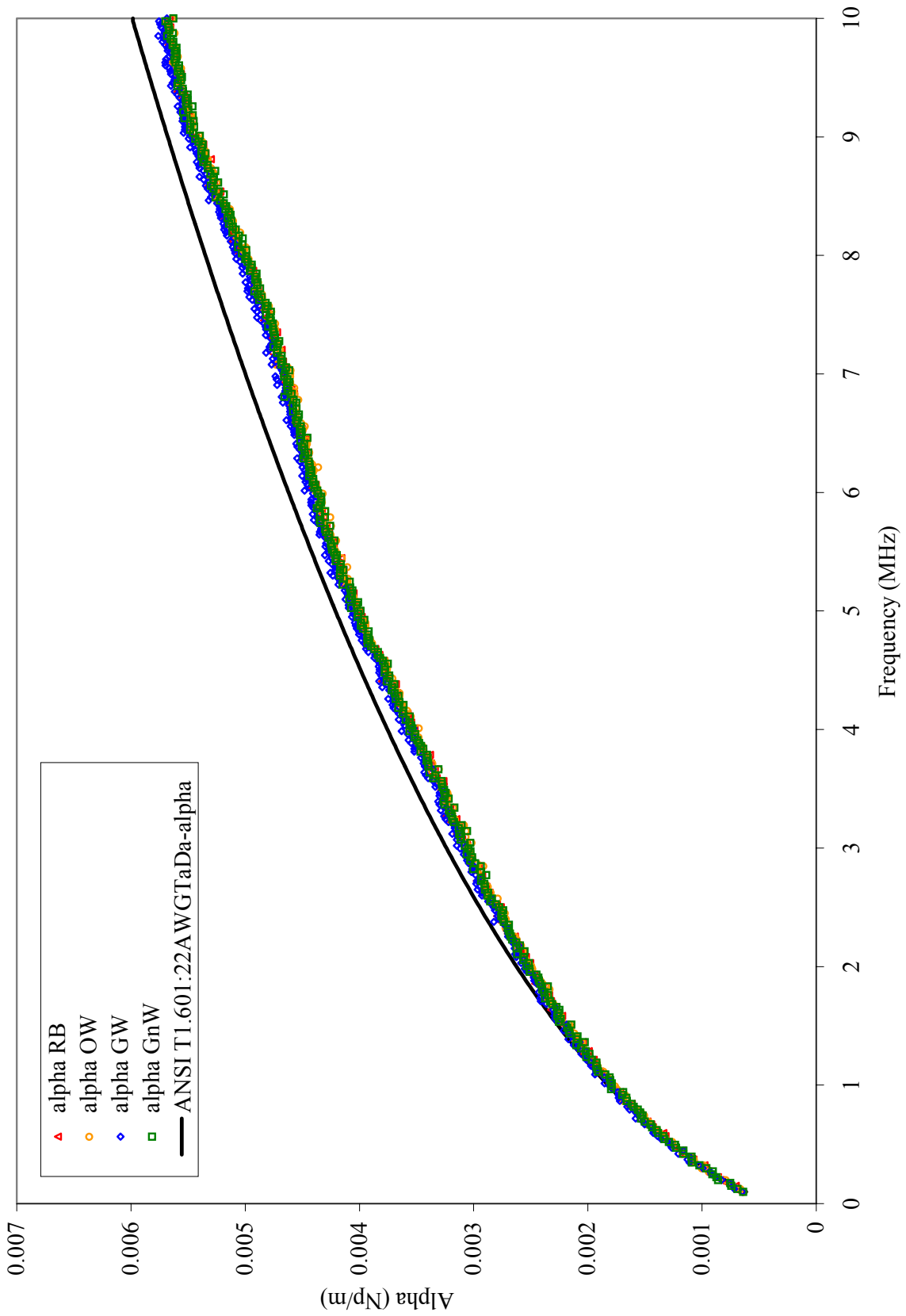


Figure D-19: Attenuation Constant of Tabulated and Measured Data for Different Twisted-Pairs of a 22 AWG Cable.

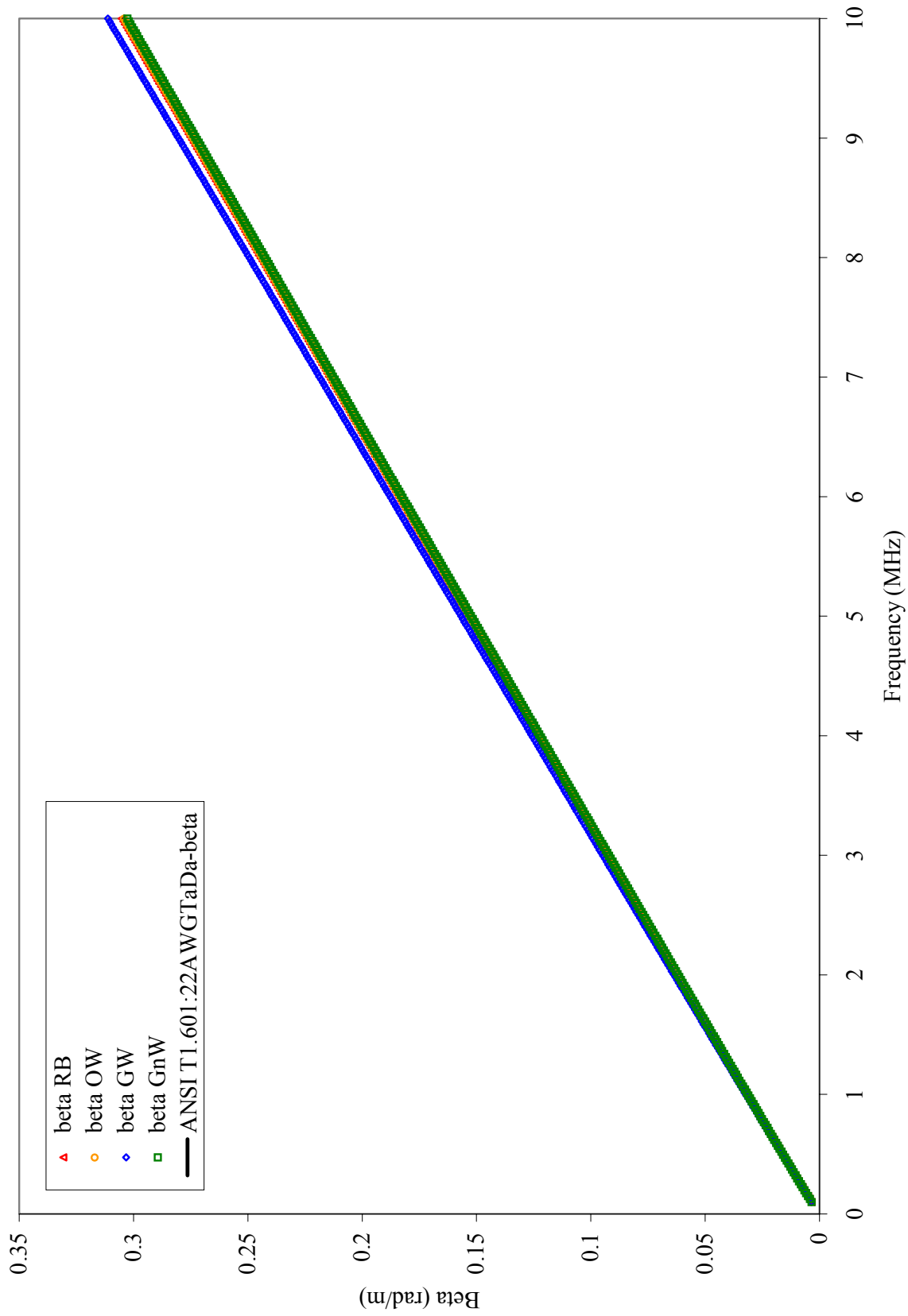


Figure D-20: Phase Constant of Tabulated and Measured Data for Different Twisted-Pairs of a 22 AWG Cable.

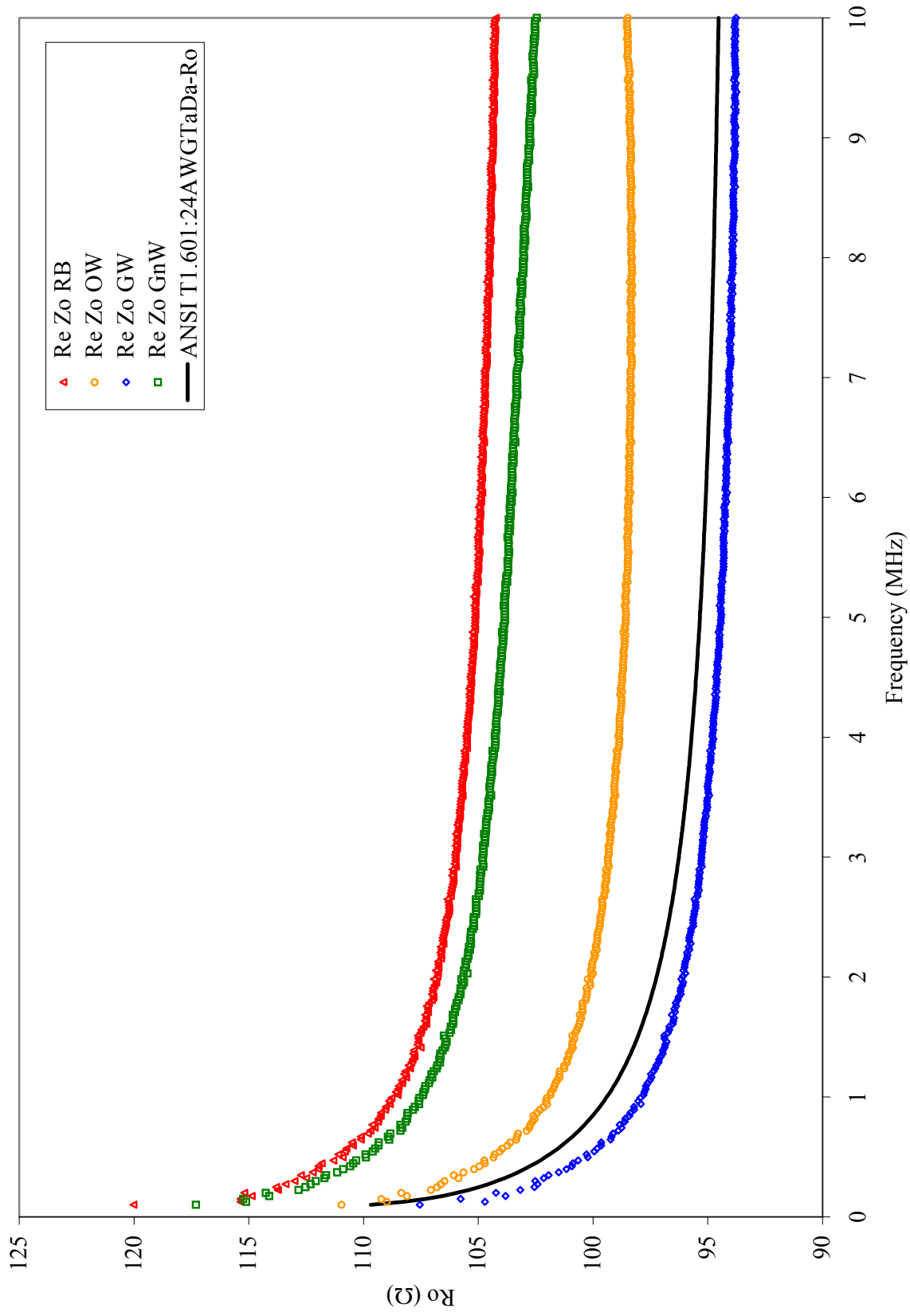


Figure D-21: Real Intrinsic Impedance of Tabulated and Measured Data for Different Twisted-Pairs of a 24 AWG Cable.

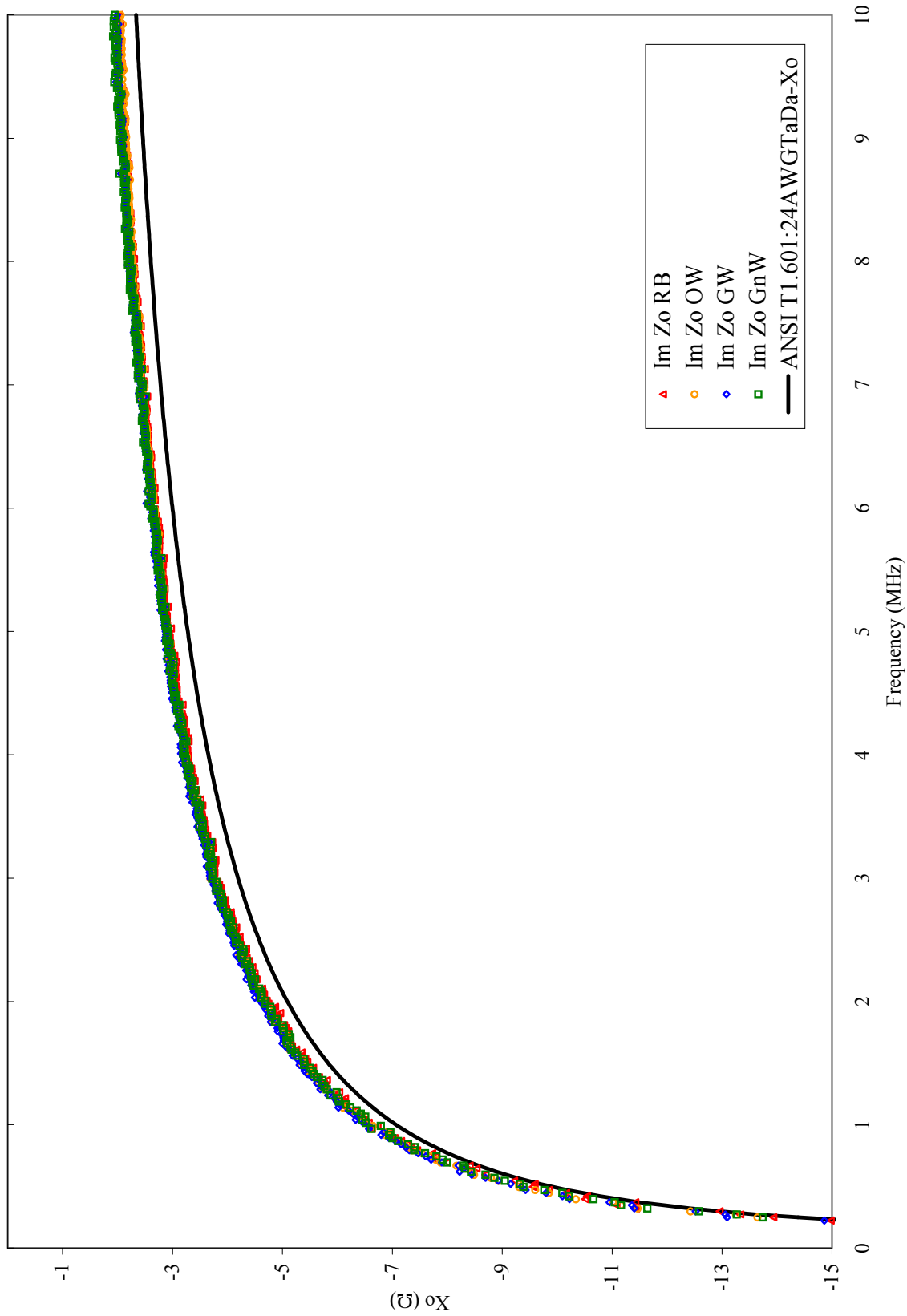


Figure D-22: Imaginary Intrinsic Impedance of Tabulated and Measured Data for Different Twisted-Pairs of a 24 AWG Cable.

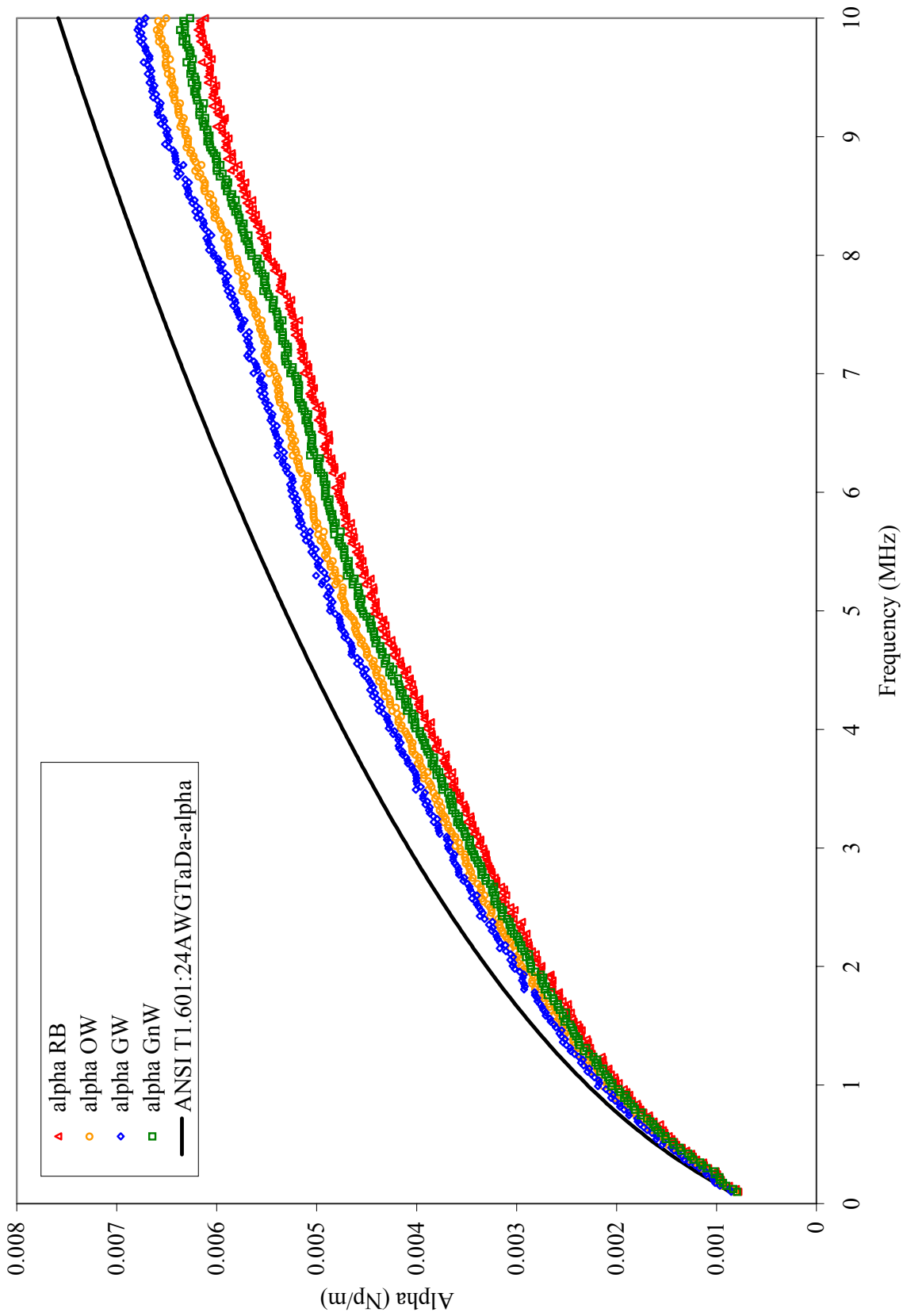


Figure D-23: Attenuation Constant of Tabulated and Measured Data for Different Twisted-Pairs of a 22 AWG Cable.

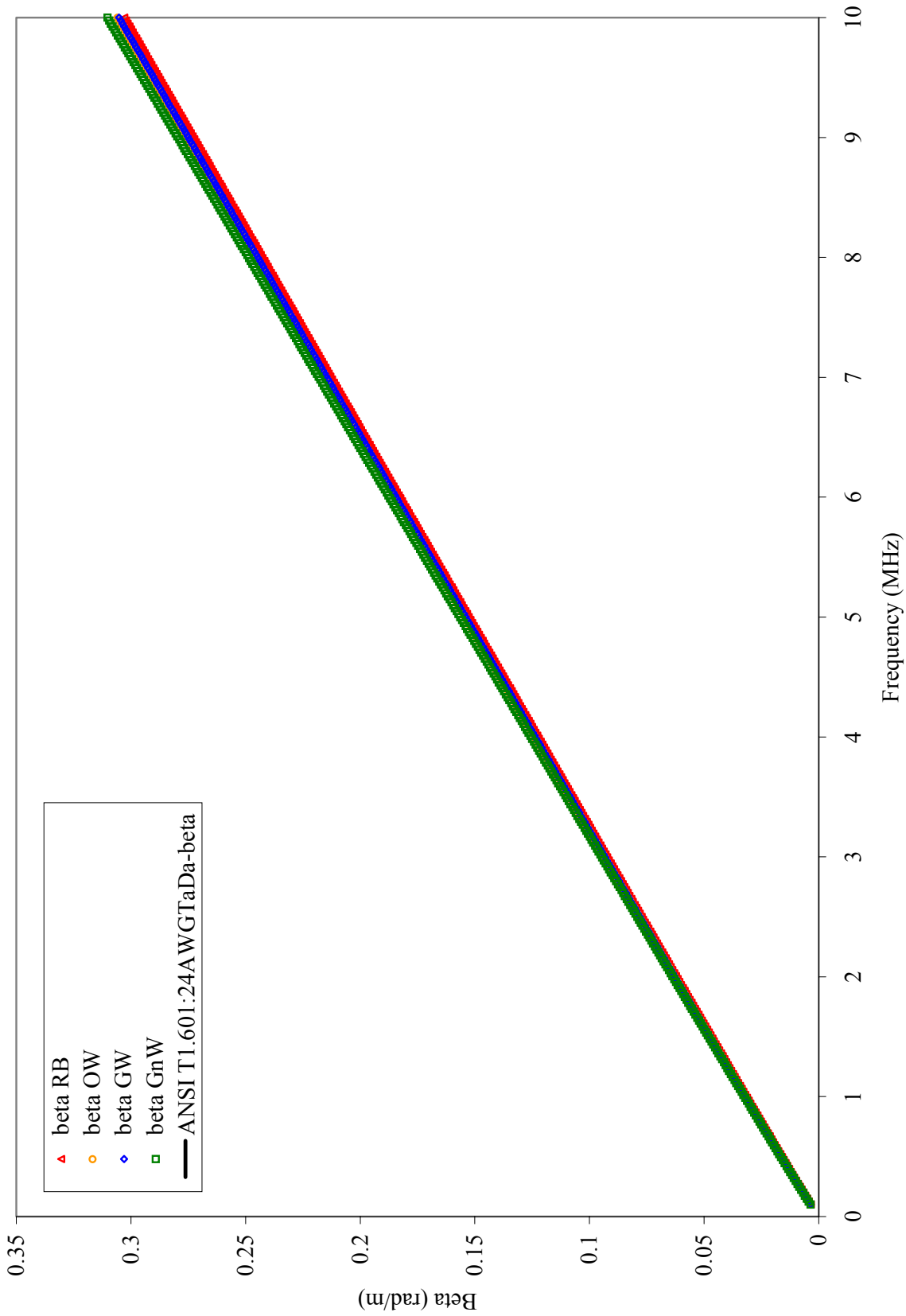


Figure D-24: Phase Constant of Tabulated and Measured Data for Different Twisted-Pairs of a 22 AWG Cable.

## **Vita**

**Jason Jon Yoho** received his B.S. degree in Electrical Engineering from Clemson University in 1996 and his M.S. degree in Electrical Engineering from Virginia Polytechnic Institute and State University in 1998. He has been a member of the Time Domain and RF Measurement Laboratory in the Department of Electrical Engineering at Virginia Tech since 1996.

Jason Yoho's research interests include microwave and RF measurements (performed in the time and frequency domains) for the purpose of material and circuit characterization, microwave and RF device modeling, and microwave and RF structure simulations. He has also performed research in the area of RF system calibration. Jason Yoho has worked as a teaching and research assistant for the Electrical Engineering Department while attending Virginia Tech while also functioning as the manager of the Time Domain and RF Measurement Laboratory. He was awarded a Bradley Fellowship by the Electrical Engineering Department at Virginia Tech in 1998.

Upon completion of his Ph.D degree., he will enter the industrial sector with Picosecond Pulse Laboratories Inc. in Boulder, CO. There he will hold the position of a design engineer.

He is a member of the Institute of Electrical and Electronics Engineers (IEEE) society and also a member of the International Microelectronics and Electronics Packaging Society (IMAPS). He is also a member of the National Society of Professional Engineers (NSPE).

He was born in Fairmont, WV on June 2<sup>nd</sup>, 1973.